frontiers | Research Topics

Evaluation of quality and safety of agricultural products by non-destructive sensing technology

Edited by
Jiangbo Li, Yuzhen Lu and Jianwei Qin

Published in
Frontiers in Plant Science

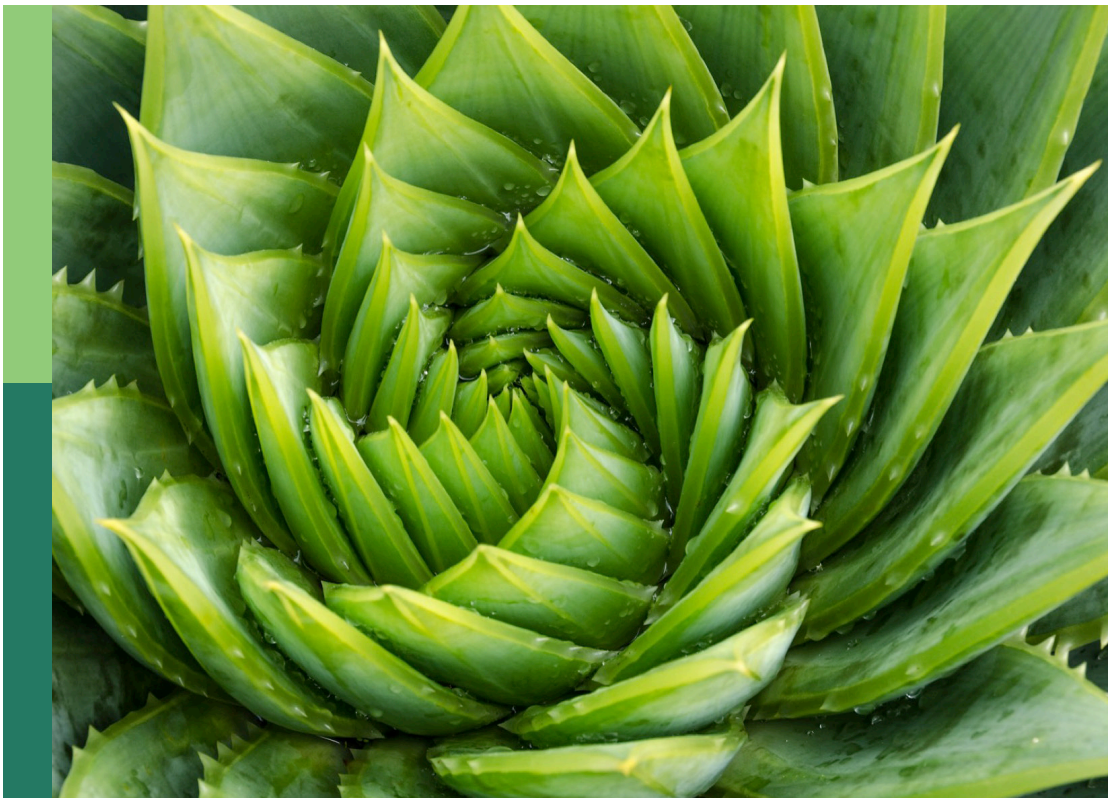

ISSN 1664-8714
ISBN 978-2-8325-2673-6
DOI 10.3389/978-2-8325-2673-6

About Frontiers

Frontiers is more than just an open access publisher of scholarly articles: it is a pioneering approach to the world of academia, radically improving the way scholarly research is managed. The grand vision of Frontiers is a world where all people have an equal opportunity to seek, share and generate knowledge. Frontiers provides immediate and permanent online open access to all its publications, but this alone is not enough to realize our grand goals.

Frontiers journal series

The Frontiers journal series is a multi-tier and interdisciplinary set of open-access, online journals, promising a paradigm shift from the current review, selection and dissemination processes in academic publishing. All Frontiers journals are driven by researchers for researchers; therefore, they constitute a service to the scholarly community. At the same time, the *Frontiers journal series* operates on a revolutionary invention, the tiered publishing system, initially addressing specific communities of scholars, and gradually climbing up to broader public understanding, thus serving the interests of the lay society, too.

Dedication to quality

Each Frontiers article is a landmark of the highest quality, thanks to genuinely collaborative interactions between authors and review editors, who include some of the world's best academicians. Research must be certified by peers before entering a stream of knowledge that may eventually reach the public - and shape society; therefore, Frontiers only applies the most rigorous and unbiased reviews. Frontiers revolutionizes research publishing by freely delivering the most outstanding research, evaluated with no bias from both the academic and social point of view. By applying the most advanced information technologies, Frontiers is catapulting scholarly publishing into a new generation.

What are Frontiers Research Topics?

Frontiers Research Topics are very popular trademarks of the *Frontiers journals series*: they are collections of at least ten articles, all centered on a particular subject. With their unique mix of varied contributions from Original Research to Review Articles, Frontiers Research Topics unify the most influential researchers, the latest key findings and historical advances in a hot research area.

Find out more on how to host your own Frontiers Research Topic or contribute to one as an author by contacting the Frontiers editorial office: frontiersin.org/about/contact

Evaluation of quality and safety of agricultural products by non-destructive sensing technology

Topic editors

Jiangbo Li — Intelligent Equipment Research Center, Beijing Academy of Agriculture and Forestry Sciences, China

Yuzhen Lu — Michigan State University, United States

Jianwei Qin — Beltsville Agricultural Research Center, Agricultural Research Service (USDA), United States

Citation

Li, J., Lu, Y., Qin, J., eds. (2023). *Evaluation of quality and safety of agricultural products by non-destructive sensing technology*. Lausanne: Frontiers Media SA. doi: 10.3389/978-2-8325-2673-6

Table of contents

frontiers | Frontiers in Plant Science

TYPE Editorial
PUBLISHED 26 May 2023
DOI 10.3389/fpls.2023.1203029

OPEN ACCESS

EDITED AND REVIEWED BY
Leo Marcelis,
Wageningen University and Research, Netherlands

*CORRESPONDENCE
Jiangbo Li
jbli2011@163.com
Yuzhen Lu
luyuzhen@msu.edu
Jianwei Qin
jianwei.qin@usda.gov

RECEIVED 10 April 2023
ACCEPTED 02 May 2023
PUBLISHED 26 May 2023

CITATION
Li J, Lu Y and Qin J (2023) Editorial: Evaluation of quality and safety of agricultural products by non-destructive sensing technology.
Front. Plant Sci. 14:1203029.
doi: 10.3389/fpls.2023.1203029

Editorial: Evaluation of quality and safety of agricultural products by non-destructive sensing technology

Jiangbo Li[1]*, Yuzhen Lu[2]* and Jianwei Qin[3]*

[1]Intelligent Equipment Research Center, Beijing Academy of Agriculture and Forestry Sciences, Beijing, China, [2]Department of Biosystems & Agricultural Engineering, Michigan State University, East Lansing, MI, United States, [3]Environmental Microbial and Food Safety Laboratory, Agricultural Research Service, U.S. Department of Agriculture, Beltsville, MD, United States

KEYWORDS

agricultural products, crop phenotype, non-destructive sensing techniques, quality assessment and control, smart agriculture-food systems

Editorial on the Research Topic
Evaluation of quality and safety of agricultural products by non-destructive sensing technology

Quality assessment is an essential task in post-harvest processing of agricultural products and important for improving their economic value. Advanced non-destructive sensing technologies, in conjunction with data analytics and control and automation technology, have evolved as a potent means for augmenting food quality control efforts. This research topic covers the latest applications of various sensing technologies, including machine vision, near-infrared spectroscopy, hyperspectral imaging, spatial-frequency domain imaging and ultrasound technology, in the quality assessment of fruits, vegetables, edible oils and seeds as well as the analysis of crop phenotypes.

Fruits are important agricultural products. Rapid, non-destructive, and accurate quality evaluation and grading can add value to the commodities when delivered to the marketplace. The soluble solids content (SSC) is one of the key internal quality characteristics of fruits. Yang et al. used the visible and near-infrared spectroscopy to assess SSC in Korla fragrant pears. A combination of bootstrapping soft shrinkage (BOSS) and successive projections algorithm (SPA) was used to extract important wavelengths from full-spectrum data. The partial least squares (PLS), least squares support vector machine (LS-SVM) and multiple linear regression (MLR) models were built for SSC predictions. The study showed that the PLS model based on 17 wavelengths selected by BOSS-SPA obtained the best prediction with r_p of 0.94 and RMSEP (root mean square error of prediction) of 0.27%. In fruit quality prediction, the model robustness is crucial for practical implementation. Traditional near-infrared spectroscopy that performs aggregated measurements is limited in decoupling absorption and scattering effects of biological tissues. Spatial-frequency domain imaging (SFDI) has emerged as a means for quantifying and mapping tissues optical properties, which can be useful for fruit quality assessment. By demodulating the reflectance images under structured illuminations with changed

frequencies and phases, the absorption coefficient and reduced scattering coefficients of biological samples can be estimated by an inversion algorithm based on appropriate light transfer models. Peng et al. reported on the measurement of optical properties of apples at the wavelengths of 460, 527, 630 and 710 nm using the SFDI technique, for assessing the SSC, firmness, and color parameters. The resultant absorption coefficient and reduced scattering coefficients were utilized for building models of SVM, MLR and PLS to predict apple quality attributes. The monitoring of quality changes during postharvest is important to quality control. Fruit usually undergoes certain periods of storage and transportation after harvest and before sale, in which they may be susceptible to spoilage and quality deterioration. The rapid, *in situ* identification of fruit spoilage is beneficial for minimizing product and financial losses. The volatile compounds (e.g., alcohols, esters, terpenes, and ethylene) released from fruit reflect fruit quality status during storage. The qualitative and quantitative analyses of these volatile compounds provide valuable insights into fruit quality. Zhou et al. used a spiral silver halide fiber optic evanescent wave spectroscopy (FOEW) sensor to explore the feasibility of identifying volatile compounds released from grapes *in situ*. The absorption peaks of ethanol in the volatile compounds were found in the FOEW spectra and their intensity gradually increased as the storage time of the grapes increased. Principal component analysis (PCA) of the spectra showed the clustering at different storage times, revealing that the concentration of the ethanol released from the grapes changed significantly with time. They built PLS discriminant analysis model for classifying grape samples as "fresh", "slight spoilage" or "severe spoilage", achieving the validation accuracy of 100%. This study can provide a reference for rapid identification of fruit deterioration.

In vegetable quality testing, cabbage is one of the economically important vegetable products worldwide. The dents and cracks of cabbage caused by extrusion and collection during transportation negatively impact both the commercial value and storage time of the commodity. Consumer-grade RGB-D (red-green-blue-depth) cameras are being increasingly used in the agriculture and food domain, which integrate the functionality of color (RGB) and depth (or range) sensing to provide richer information, and particularly the 3D point cloud from depth channel data enables the reconstruction of object surface geometry and shape, which can be useful for quality assessment of agricultural produce. Curvature is an important feature in shape analysis and can be used for the detection of shape defects. Gu et al. used an Intel RealSense-D455 depth camera to obtain the 3D point cloud cabbage segmented from the background noise through preprocessing and region of interest extraction. The normal vector was estimated based on a least-squares plane fitting method, and the curvature threshold was defined in agreement with the curvature character parameters. The surface defect detection was realized according to the curvature difference between the normal area and the defective area on the cabbage surface.

Seed quality is crucial for the productivity and eventual products quality of crops. Aged seeds generally have low plant vigor and growth, which need to be identified and segregated out. Wang et al. employed short wave-near infrared hyperspectral reflectance imaging to identify aged maize seeds. ANOVA was used to reduce data dimensionality. The band ratio (1987 nm/1079 nm) selected by ANOVA from embryo-side spectra achieved 95% classification accuracy. The image texture features, including histogram statistics and gray-level co-occurrence matrix, were extracted from the band ratio image to establish fusion models, yielding the accuracy of 97.5%. This study indicated that imaging at two wavelengths combined with the extraction and modeling of image textural features could detect aged maize seeds effectively. Cracks of cottonseeds negatively influence the germination rate of the crop. It can be a challenging task for techniques such as machine vision, spectroscopy, and thermal imaging, to detect slight cracks in the cottonseeds. An acoustic method is potentially sensitive to localizing fine structure defects. Zhang et al. presented a novel methodology to detect slightly cracked cottonseed using air-coupled ultrasound with a lightweight vision transformer and a sound-to-image encoding method. The echo signal of air-coupled ultrasound from cottonseeds was obtained in a non-contact way. The intrinsic mode functions of the ultrasound signal were obtained as the sound features through variational mode decomposition, which were further converted into color images by a color encoding method. A lightweight MobileViT model was trained with the resultant color image to discriminate between the slightly cracked and normal cottonseeds, resultant in an overall recognition accuracy of 90.7%.

In addition to quality assessment of raw or fresh-market commodities, the non-destructive sensing technology can also be applied to processed products. Pomegranate kernel oil has gained global attention due to the health benefits associated with its consumption, especially fatty acid composition. Various analytical methods have been used for quality control of edible fats and oils. However, these methods are expensive, labor-intensive, and often require specialized sample preparation, restricting their applicability on a commercial scale. Okere et al. used Fourier transform near-infrared and mid-infrared spectroscopy to qualitatively and quantitatively predict quality attributes of the pomegranate kernel oil. PCA and orthogonal partial least squares discriminant analysis were applied for qualitative analysis, and PLS regression was used for developing quantitative models. Their results demonstrated the potential of near- and mid-infrared spectroscopy for rapid screening of pomegranate oil quality.

In addition to aforementioned studies, this research topic also includes two articles pertaining to crop phenotypic analysis. Watermelon is a widely consumed and nutritious fruit with rich sugars. Abiotic stresses caused by changes in temperature, moisture, etc., pose a threat to crop production and product quality. Stress diagnosis based on monitoring plant morphological features (e.g., shape, color, and texture) is important for optimizing management practices for yield and quality protection. Nabwire et al. classified watermelon plants exposed to low-temperature stress conditions from the normal ones using features extracted by image analysis, which achieved 100% accuracy in discriminating between normal and low-temperature stressed watermelon plants. They also built models for estimating the number of leaves and plant age using the extracted features, resulting in R_2, RMSE and mean absolute difference (MAD) of 0.94, 0.87 and 0.88, respectively for the

number of leaves and the R_2 and RMSE of 0.92 and 0.29 (weeks), respectively, for estimating the plant age. The models developed can be utilized for monitoring and analysis of phenotypic traits during watermelon growth. The segregation of plug seedlings by quality is important for planting high-quality seedlings for wide-scale production. Du et al. used a color vision system to acquire images of the tops of pepper plug seedlings and built an EfficientNet based convolutional neural network (CNN) model for classifying the plug seedlings into three classes (strong seedlings, week seedlings, and empty plug cells). The CCN model, structured by adding a convolutional block attention module (CBAM) to EfficientNet-B7, alongside transfer learning and Adam optimization, achieved an accuracy of about 98%. The proposed method had high accuracy for the plug seedling quality classification task.

Non-destructive sensing technologies reported in the above studies provide useful tools for the assessment of agricultural product quality and analysis of crop phenotypes. These studies provide valuable references for further research and developments of advanced sensing technologies for enhanced quality assessment and control. Based on these technologies, the advanced detection and monitoring equipment for real-time, high-volume application has been and is being developed to propel the production of smart agriculture-food systems.

Author contributions

All authors have made substantial contributions to the work reported in the Editorial. Specific contributions are as follows: JL: Original Editorial writing. YL: Editing. JQ: Editing. All authors contributed to the article and approved the submitted version.

Acknowledgments

The authors grateful for the opportunity to serve as the guest editors of the Research Topic, "Evaluation of Quality and Safety of Agricultural Products by Non-destructive Sensing Technology", as well as the contribution of all the authors to this Research Topic. The dedicated work of Research Topic Editor and the editorial and publishing staff of Frontiers in Plant Science are greatly appreciated.

Conflict of interest

The authors declare that the research was conducted in the absence of any commercial or financial relationships that could be construed as a potential conflict of interest.

Publisher's note

frontiers in Plant Science

ORIGINAL RESEARCH
published: 18 February 2022
doi: 10.3389/fpls.2022.847225

Estimation of Cold Stress, Plant Age, and Number of Leaves in Watermelon Plants Using Image Analysis

*Shona Nabwire[1], Collins Wakholi[1], Mohammad Akbar Faqeerzada[1], Muhammad Akbar Andi Arief[2], Moon S. Kim[3], Insuck Baek[3] and Byoung-Kwan Cho[1,2]**

[1] Department of Biosystems Machinery Engineering, Chungnam National University, Daejeon, South Korea, [2] Department of Smart Agriculture Systems, Chungnam National University, Daejeon, South Korea, [3] Environmental Microbial and Food Safety Laboratory, Agricultural Research Service, United States Department of Agriculture, Beltsville, MD, United States

Watermelon (*Citrullus lanatus*) is a widely consumed, nutritious fruit, rich in water and sugars. In most crops, abiotic stresses caused by changes in temperature, moisture, etc., are a significant challenge during production. Due to the temperature sensitivity of watermelon plants, temperatures must be closely monitored and controlled when the crop is cultivated in controlled environments. Studies have found direct responses to these stresses include reductions in leaf size, number of leaves, and plant size. Stress diagnosis based on plant morphological features (e.g., shape, color, and texture) is important for phenomics studies. The purpose of this study is to classify watermelon plants exposed to low-temperature stress conditions from the normal ones using features extracted using image analysis. In addition, an attempt was made to develop a model for estimating the number of leaves and plant age (in weeks) using the extracted features. A model was developed that can classify normal and low-temperature stress watermelon plants with 100% accuracy. The R^2, RMSE, and mean absolute difference (MAD) of the predictive model for the number of leaves were 0.94, 0.87, and 0.88, respectively, and the R^2 and RMSE of the model for estimating the plant age were 0.92 and 0.29 weeks, respectively. The models developed in this study can be utilized in high-throughput phenotyping systems for growth monitoring and analysis of phenotypic traits during watermelon cultivation.

Keywords: chilling stress, phenomics, image processing, morphological traits, leaf count, plant age

OPEN ACCESS

Edited by:
Jiangbo Li, Intelligent Equipment Research Center, Beijing Academy of Agriculture and Forestry Sciences, China

Reviewed by:
Dimitrios Fanourakis, Technological Educational Institute of Crete, Greece
Mohsen Yoosefzadeh Najafabadi, University of Guelph, Canada

***Correspondence:**
Byoung-Kwan Cho
chobk@cnu.ac.kr

Specialty section:
This article was submitted to Crop and Product Physiology, a section of the journal Frontiers in Plant Science

Received: *01 January 2022*
Accepted: *28 January 2022*
Published: *18 February 2022*

Citation:
Nabwire S, Wakholi C, Faqeerzada MA, Arief MAA, Kim MS, Baek I and Cho B-K (2022) Estimation of Cold Stress, Plant Age, and Number of Leaves in Watermelon Plants Using Image Analysis. Front. Plant Sci. 13:847225. doi: 10.3389/fpls.2022.847225

INTRODUCTION

Watermelon (*Citrullus lanatus*) is a highly nutritious fruit comprised of 93% water with small quantities of protein, fat, minerals, and vitamins. It is widely considered a functional food, thus contributing to its widespread consumption around the world (Assefa et al., 2020). Watermelon is a member of the cucurbit family (*Curcurbitaceae*), which are chill-sensitive plants that are native to subtropical and tropical regions around the world. There are four main cucurbit crops, namely cucumber, watermelon, melon, and squash. Of these main crops, watermelon has the highest worldwide consumption (Wehner et al., 2020).

Watermelon plants are characterized by big leaves, long, and thin hairy stems that can grow up to 10 m long with branched coiled tendrils at the nodes and yellow flowers. Its leaves are green,

with blades of about 20 × 20 cm, pinnately lobed, and usually divided into three to five pairs of lobes. Its growth habit is a long trailing vine, due to which the plants are usually grown at a wide spacing (Aruna et al., 2016). Watermelons are mainly grown in tropical and subtropical climates and require a warm growing season of 75–95 days from planting to harvesting. While the optimum growth temperature for watermelons ranges from 21 to 29°C, they can tolerate a minimum of 18°C and a maximum of 32°C (Noh et al., 2013; Shirani Bidabadi and Mehralian, 2020). Watermelons are highly temperature sensitive depending on the growth stage. In the early stages of plant growth, 25°C is optimal and growth has been observed to stop at 10°C. Below temperatures of 13°C, flowering does not occur and above 45°C only mature plants can survive (Noh et al., 2013).

Plants are vulnerable to a wide range of physical and chemical variables, including low and high temperatures, insufficient or excessive water, high salinity, heavy metals, and ultraviolet (UV) exposure, among others. These stresses, known collectively as abiotic stresses, pose a danger to agriculture and the ecosystem, accounting for significant crop production loss. In watermelon plants, abiotic stresses caused by temperature extremes (Rivero et al., 2001; Shirani Bidabadi and Mehralian, 2020), water stress (Yoosefzadeh Najafabadi et al., 2018), salinity stress (Yetişir and Uygur, 2009; Li et al., 2017), etc., are the most prevalent. In the watermelon plant life cycle, both reproductive and vegetative stages are negatively affected by low temperature stress (Nishiyama, 1970; Shirani Bidabadi and Mehralian, 2020). During reproductive development, low temperature stress can delay flowering and induce flower abscission, pollen sterility, pollen tube shortening and distortion, and reduced fruit set, which lowers yield (Waraich et al., 2012). The effects of cold stress on the reproductive stage have important economic and social effects since the products of this stage are the source of food supply (Thakur et al., 2010; Zinn et al., 2010). At the vegetative development stage, low temperatures can cause a reduction in stomatal conductance and leaf water content, therefore resulting in smaller leaves and shoots (Rodríguez et al., 2015). Collectively, these stress responses reduce fruit yield and quality, which has negative economic and nutritional impacts (Lu et al., 2003; Taylor et al., 2003).

In climates with short warm seasons, seeds are sown in growth chambers and transplanted into the field or protective structures after 3–4 weeks (Wehner et al., 2020). The largest protective structures for commercial watermelon production in non-tropical climates are glasshouses (greenhouses). These have systems that control lighting, shading, heating and cooling, ventilation, humidity, and carbon dioxide concentration. Due to the temperature sensitivity of the watermelon plants, temperatures must be closely monitored in the controlled environments. It is necessary to understand plant responses to temperature stresses to improve management within the controlled environments. Studies have found that immediate plant morphological responses to these stresses include reductions in leaf size, number of leaves, and plant size (Bismillah Khan et al., 2015; Fahad et al., 2017).

Plant morphological studies involve a detailed study of vegetative and reproductive plant structures that can be used to make comparisons between species, identify different varieties, or study plant responses to stimuli (Wyatt, 2016). Some of the key morphological features relevant to plant morphological studies are leaf shape, size, color, texture, angle, and volume. In the shoot system, leaves experience significant changes in morphology in response to the environment that can be easily observed (Yang et al., 2015). Leaf morphological features can be important determinants of plant performance because leaf size and shape influence key plant productivity processes such as photosynthesis, stomatal conductance, and transpiration efficiency (An et al., 2017). In studies involving morphological feature analysis of plants, some key features measured include plant leaf length, width, angle, diameter, perimeter area, and volume (Harish et al., 2013). Leaf morphological features are useful for plant recognition, identification, classification, and disease identification and classification (Aptoula and Yanikoglu, 2013; Ramcharan et al., 2017, 2019; Kumar et al., 2019; Tan et al., 2020).

Image analysis has found wide application in various domains of science. The image analysis workflow consists of image capture, preprocessing, feature extraction, and analysis. In plant studies, imaging techniques and analysis have the advantage of being non-destructive and able to extract intricate information that can be used to analyze biological patterns of plant growth (Nabwire et al., 2021). The application of image analysis in morphological studies has been done to automate plant recognition tasks (Aptoula and Yanikoglu, 2013; Kumar et al., 2019), classification of plant leaves using leaf shape feature extraction techniques (Manik et al., 2016), automation of plant classification systems (Harish et al., 2013), and development of leaf disease detection and diagnosis systems (Jagtap and Hambarde, 2014). Specifically, image analysis has been applied in cold stress response classification in maize plants (Enders et al., 2019), drought and heat stress tolerance screening in wheat (Schmidt et al., 2020), weed growth stage estimation (Teimouri et al., 2018), and leaf counting in *Arabidopsis* using deep learning (Aich and Stavness, 2017). These studies achieved acceptable results, however there have been no studies that have applied image analysis to identify cold stress plants, estimate leaf count, and plant age in watermelon plants.

High throughput plant phenotyping (HTPP) systems are useful for quantifying/estimating the effects of exposure to sub optimal conditions (temperature, water, etc.) on individual plant through estimating various plant characteristics. The data from such systems is useful for making comparisons between plant species, identifying varieties, or study plant responses to stimuli. This information is useful for research and in decision making. Therefore, the objective of this study was to extract and analyze the morphological features (relating to form, structure, texture, and color) of watermelon plants using image analysis. The features were used to develop a model for prediction of cold stress condition of the plants and determination of the number of leaves and plant age. The models developed in this study can be utilized in high-throughput phenotyping systems for growth monitoring and analysis of phenotypic characteristics (such as number of leaves, plant age) during watermelon cultivation.

MATERIALS AND METHODS

Dataset

The watermelon seed samples were acquired from Partner seed (Gimje, Jeollabuk-do, South Korea). Four test varieties, namely, DAPCT, PI482261, DAP, and 45NC, as defined by the seed company, were used for this study. A total of 128 seeds were used, including 12 from the PI482261, 16 from the 45NC, 52 from the DAP, and 48 from the DAPCT variety. The seeds were planted in a container in individual cells and placed in a growing chamber maintained at 28°C and 70% relative humidity to ensure germination. After 2 weeks, the seedlings were transplanted into individual cylindrical pots (12 cm diameter, 11 cm height) with porous bases and transferred to the growing chamber that was reserved for this experiment. A nutrient mixture called "Mulfuresiriz" from Daeyu company limited (Seoul, Gyeonggi-do, South Korea) used in hydroponics was applied equally (concentration of 4 ml of nutrient mixture per liter of water) to all the pots at the start of the experiment.

Experiment Design

The experiment design for this study was based on the growth stages of watermelon plants. Data collection was done weekly between the 2nd and 5th week (seedling to flowering stage of watermelon plants) at total of 4 weeks (week 2, 3, 4 and 5). This is because at less than 13°C flowering will not occur; however, after flowering and fruit set, temperatures greater than 14°C have no significant effect on plant growth (Noh et al., 2013). The watermelon plants were separated in two groups, the normal group (plants grown in optimum growth conditions), and the stressed group (plants grown in cold stress conditions). A total of 10% of the plants from each variety were stressed each week. The plants to be considered for the stress group were selected using random numbers to eliminate bias. The growth temperature considered for the control (normal) and the stressed group in this study were as detailed in **Table 1**. The plants in each group were grown in separate chambers that were both maintained at a relative humidity of 70% for the entire growth period. The lighting used for both growth chambers was 15,000 lux intensity, 6,500K color temperature for the simulated day hours and no lights for the simulated night hours. The concentration of carbon dioxide gas was maintained at 700 ppm for both growth chambers. Both the normal and stressed group plants followed the same watering regime, which was done after every 2 days. During watering, the plant pots were soaked in 2 cm deep pure water for 4 h to allow time for water to percolate into the soil.

Data Collection

Image data collection was done using a multi-camera system (**Figure 1**). The system specifications are detailed in **Table 2**. The reason for the multiple camera setup was to capture more views of the plant from which to choose when extracting consistent and representative morphological features. The target field of view (FOV) for the cameras was 32 × 27 cm (enough to cover the entire watermelon plant), therefore the camera-to-sample distance for the system was 60 cm to accommodate the FOV. The cameras were set up with the same angle, distance, aperture, and exposure time (10,000 μs). Color calibration was done during data collection to compensate for variations in color channel values, aperture opening, and manufacturing tolerances that can result in varying camera color signatures. Color calibration was done by taking images of the standard X-Rite color chart, extracting the color values of the patches, and finding the best transform matrix that maps the resultant color values with their respective reference values. The resultant color correction matrix was then used to transform the images taken from the cameras to their true color (Sunoj et al., 2018).

One camera was set up at the top of the system to capture the top view image of the plant, while the other six cameras were set up to capture the side view of the plant at 60 degree intervals from each other.

Reference data, which include number of leaves, plant age (weeks), and stress condition (control or stressed), were recorded for each plant every week after image data collection.

Thresholding/Background Removal

For the analysis, three images were selected from the top view camera and cameras at 0 and 60 degrees. The image views were labeled image 1, image 2, and image 3, corresponding to the 0-degree, 60-degree, and top view image, respectively. A summary of the data analysis workflow for this study is shown in **Figure 2**.

Background removal was carried out using two methods to define the region of interest (the plant) for further processing. Initially, it was carried out using conventional image processing. This involved conversion of the image from RGB to the CIELAB color space. An analysis of the histograms of each channel resulted in a necessity to keep all pixels below the local minima in the "*a*" channel and above the local minima in the "*b*" channel (**Figure 3**). Since these local minima (for both channels) varied for each image, a search algorithm that automatically determines the position of the local minima in a predefined range was used. The determined position values were used as thresholds to make two binary images, which were then combined to create the watermelon plant mask.

Deep learning was also applied for background removal using U-Net, a network commonly used for image segmentation. It can work with few images and give accurate segmentation results. The network does not have fully connected layers and uses the pixels in the segmentation map whose full context is available in the input image. It uses successive layers with pooling layers replaced by upsampling layers therefore increasing the output resolution. The upsampling section of the network has many feature channels that enable the network to propagate context information into the higher resolution layers. This makes the expansive path symmetric with the contracting path and gives the architecture its characteristic U-shape (Ronneberger et al., 2015). Although U-Net was originally developed for application to biomedical images, it has been applied in various domains of science, including audio signal source separation and satellite imagery (Stephan and Santra, 2019).

The network was trained on 830 images with a ratio of 7:2:1 for the training, validation, and test datasets, respectively. The

TABLE 1 | Plant growth conditions and weekly stress plan.

Plant condition	Number of plants				Optimal temperature	Growth temperature	
	Week 2	Week 3	Week 4	Week 5		Day (16 h)	Night (8 h)
Control group	128	116	104	92	20–30°C	28°C	21°C
Stress group	0	12	24	36	≤15°C	15°C	10°C

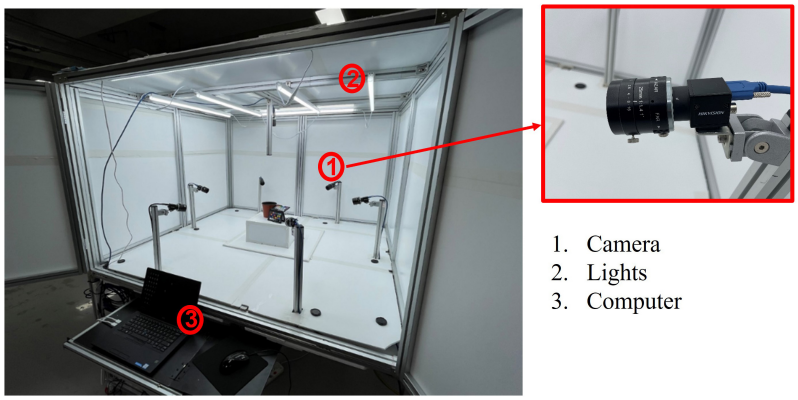

FIGURE 1 | System for data collection.

input image size for the network was 512 × 512 × 3 and the output image size was 512 × 512. The network was trained for 100 epochs using Adam optimizer, mini-batch size of 8, learning rate of 0.001, drop factor of 0.9, and drop period of 5.

Feature Extraction

Color Feature Extraction

The color features considered for this study were extracted from four color spaces (RGB, HSV, CIELAB, and YCbCr). The color space suitable for an application is selected based on the acquisition setup. While HSV and CIELAB represent colors in a format closer to human vision, CIELAB has the advantage of being able to detect small differences in color and is device independent. YCbCr is suitable for image/video data compression. The color components are represented by coefficients of the three colors depending on the selected color space. They are extracted by conversion of the image to the desired color space and averaging the color values in each component (Kavitha and Suruliandi, 2016). Color feature extraction was done by conversion of the images from RGB to the major color spaces: HSV, LAB, and YCbCr. The average value of the color channels in each of the color spaces was computed to extract the color features – in total 12 feature values for each image.

Shape-Based Feature Extraction

Shape-based feature extraction is carried out to extract features that describe the shape and size of a region of interest in an image. Shape and size parameters, sometimes referred to as region properties, quantify the shape of the region depending on the requirements of the image processing task (Mingqiang et al., 2008). The region properties of the region of interest (**Table 3**) were extracted from the resultant mask from the image segmentation process. These amounted to a total of 30 feature values for each image.

Texture Feature Extraction

Texture can be defined as the surface quality of a region of interest. In image processing, texture is analyzed based on the variations in the gray tone values extracted from an image (Metre and Ghorpade, 2013). Texture features are commonly extracted using Gray Level Co-occurrence Matrix (GLCM) to find symmetry in the texture in an image (Hu and Ensor, 2019). It is based on the occurrence of the gray level configuration and measures the spatial relationships between pixels to infer texture information (Ehsanirad and Sharath, 2010). Haralick texture features are derived from the GLCM (Haralick et al., 1973). They consist of 14 statistical features, which include autocorrelation, contrast, cluster prominence, cluster shade, correlation, etc. For this analysis, four properties were extracted using the GLCM, namely contrast, correlation, energy, and homogeneity.

TABLE 2 | System specifications.

System dimensions	Camera specifications	Lights
Width: 160 cm Length: 168 cm Height: 107 cm	Name: HIKVISION MV-CA050-20UC Type: 5MP 1" CMOS USB3.0 Resolution: 2592 × 2048 Lens: 25 mm lens Variable aperture: f/1.4 to f/16 (fixed to f/8) Number: 7 cameras	Type: D65 White LED Power: 15W Quantity: 6 lights

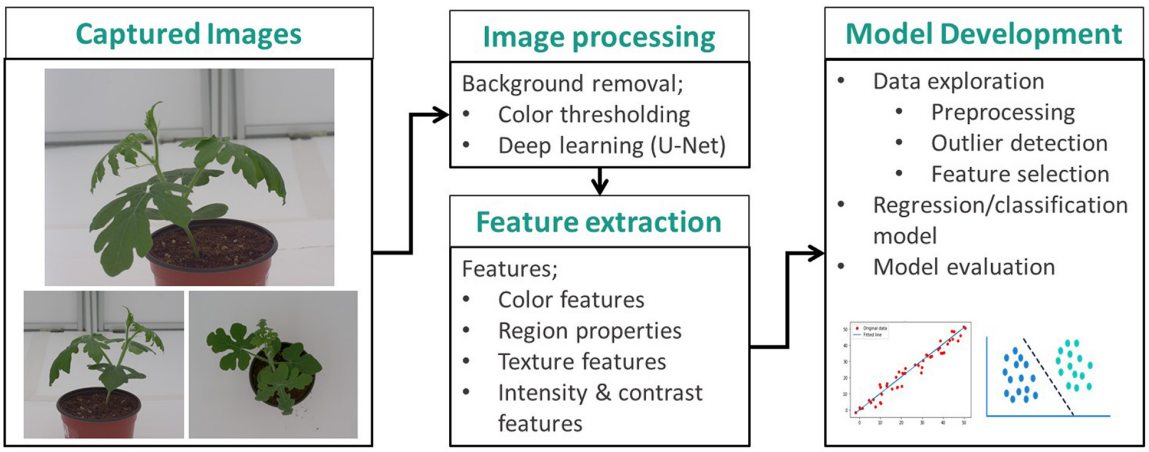

FIGURE 2 | Data analysis workflow.

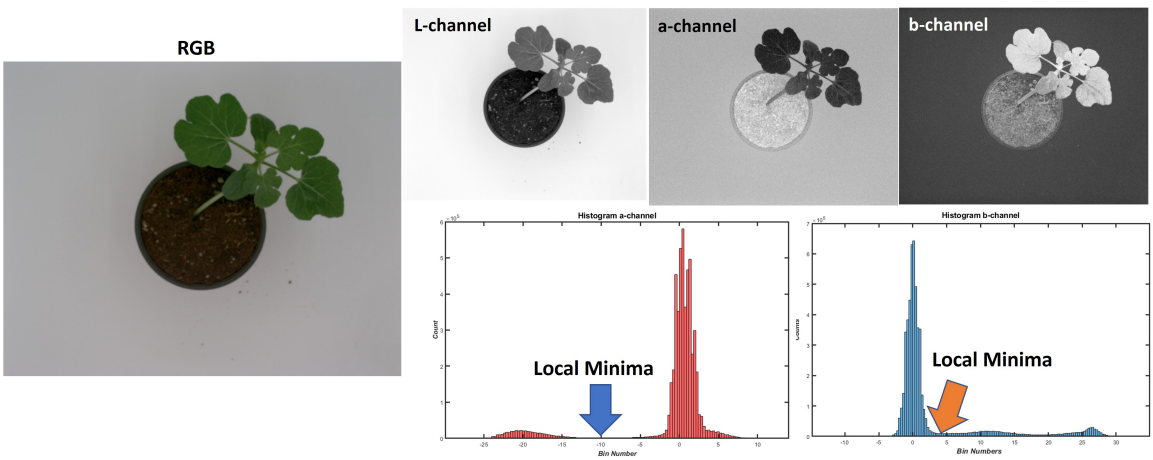

FIGURE 3 | Summary of conventional image processing background removal algorithm.

Using a Haralick distance of 3, 28 texture feature values were extracted for each image.

Additionally, other texture feature extraction methods, including local binary patterns (LBP), discrete cosine transform (DCT), Fourier descriptors, and Gabor features, were used. These features were extracted using the BALU toolbox in MATLAB (Mery, 2011).

Local binary patterns (LBP) are generated by the best matching pattern in the image and are responsive to edges, lines, spots, and flat areas, whose distribution is estimated by the occurrence histogram. They are key texture properties and provide most patterns in observed textures. LBP features derive their name from the functionality of the LBP operator $LBP_{P,R}$, whereby the threshold of the local neighborhood is determined at the gray value of the center pixel in a binary pattern (Ojala et al., 2002). LBP features address the challenge of non-uniformity of textures due to variations in orientation, scale, or resolution of an image. For each image, a uniform LBP operator was applied with eight neighborhood pixels and one vertical and horizontal division. This resulted in 59 LBP feature values for each image.

Discrete Cosine Transform (DCT) is a unitary image transform that transforms the image from the spatial domain to the frequency domain. Unitary transformations are useful in image processing in that they preserve the length of the vector and pack a large fraction of the mean energy of an image into a few transform coefficients, allowing for the preservation of feature information (Jain, 1989; Kumar and Bhatia, 2014). DCT separates the image into parts of varying importance depending on the image visual quality. It gives coefficients that are both local and global features. DCT is a popular feature extraction transform in terms of its compact feature representation and computational complexity arising from its data independent nature (Chadha et al., 2011). For this study, a vertical and horizontal resize of 64 and frequency of 2 were applied to each image to extract four DCT coefficients.

Fourier-based feature extraction involves the transformation of the image from the spatial to the frequency domain and has the

TABLE 3 | Region properties used for shape-based feature extraction.

Parameter	Description
Area	The number of pixels in the selected region of the image.
Bounding box	The rectangle that contains every point in the selected region.
Major axis length	The length of the line connecting the base point to the tip of the leaf.
Minor axis length	The length of the line perpendicular to the major axis.
Centroid	The center of mass of the region being analyzed.
Solidity	The ratio of the leaf area to the area of the convex hull. This is useful for measuring the density of the region.
Perimeter	The length of the external shape of the region being analyzed.
Circularity	A measure that describes the roundness of an object.
Convex hull	This is the smallest convex polygon that contains the selected region.
Equivalent diameter	A measure of the diameter of a circle that has the same area as the region of interest.
Eccentricity	The ratio of the distance between the foci of an ellipse that has the same second-moment as the region of interest and the length of its major axis.
Maximum Feret diameter	The maximum distance between two boundary points on the antipodal vertices of the convex hull.
Minimum Feret diameter	The smallest distance between two boundary points on the antipodal vertices of the convex hull.
Extent	The ratio of pixels in the region of interest to the pixels in the bounding box.

advantage of eliminating noise that occurs at higher frequencies. Using this technique, a spectrum of texture is obtained using a Fourier transform. Local and global texture feature descriptors are obtained from the spectrum. Fourier spectrum descriptors describe the direction and formation of texture patterns (Hu and Ensor, 2019). For this study, a frequency of 2 was applied to each image to generate 8 spectral peaks and 16 texture descriptors.

Gabor feature extraction method extracts the Gabor features of an image using a Gabor filter function. The Gabor filter function is useful in texture analysis where texture is non-uniform (Kumar and Pang, 2002). They extract local pieces of information that are combined to recognize the object of interest, making this method one of the superior methods for complex tasks such as facial recognition (Kamarainen, 2012). Eight rotations and dilations were applied to each image with a frequency ranging from 0.1 to 2 to generate 19 Gabor feature values.

Intensity-Based Feature Extraction

Other features extracted include intensity and contrast features. Intensity-based feature extraction extracts the color intensity values for each pixel (Sabrol and Kumar, 2016). Contrast measures the differences in brightness levels between the light and dark areas of an image (Chen et al., 2019). The parameters extracted in this feature extraction method include, but are not limited to, maximum intensity – the intensity value of the pixel with the greatest intensity in the region of interest, mean intensity – the average intensity of all the intensity values in the region of interest, minimum intensity – the intensity value of the pixel with the lowest intensity in the region of interest, and the weighted centroid – the center of the region of interest based on intensity values. Intensity features were extracted from the green channel – a total of six feature values from each image. Contrast features were similarly extracted from the green channel image resulting in five feature values. Both functions were inherited from the MATLAB BALU toolbox (Mery, 2011).

TABLE 4 | Total number of features extracted for each watermelon plant.

Feature type	Number of features	Remarks
Region properties	30	Extracted from mask image
Color features	12	Average color values
Texture features	138	Sum of all the texture features
Other features	11	Including contrast and intensity features
Total for each image	191	Number of features extracted per image
Total for three images	573	Total number of features extracted per plant

The resultant features (**Table 4**) were concatenated horizontally for each watermelon plant sample. The resulting features from each plant were concatenated vertically, resulting in a data matrix (rows = sample, columns = features), which was used for modeling the phenotypic traits.

Data Analysis and Model Development

Feature Preprocessing

Feature extraction methods use different formulae and conventions and therefore output feature values are of varying magnitudes. Preprocessing of the features is necessary before data analysis to enhance the features, remove noise that may result from intensity variations in the image, and standardize the ranges of feature values. For this reason, a normalization vector was applied using min–max normalization (Patro and Sahu, 2015), which resulted in values ranging between 1 and 0.

Outlier Detection

Outliers are extreme data points that deviate from other observations of the data and may indicate experimental errors, data processing errors, or variability in measurements (Wang et al., 2019). The outliers in the extracted dataset were likely caused by misdetections during feature extraction. Outliers are bound to exist and can influence the model development process and overall model performance.

To remove outliers from the data, two steps were followed:

(1) Computation of principal component analysis (PCA) of the data, followed by extraction scores of the first five PC (representing more than 90% of variance in the data);

(2) Use of robust multivariate dispersion algorithm (Olive and Hawkins, 2010) on the extracted scores to determine which samples are outliers and which are inliers.

Feature Cleaning and Selection

Feature selection is usually done to select a group of features from the original set that contain accurate distinguishing information

of one object from another for accurate predictions in the model (Kumar and Bhatia, 2014). It may consist of feature cleaning, where features that are redundant and those that contain little or no information are removed from the feature set. The decision to remove some features is subjective depending on the parameters being predicted by the model. The removal of some features that contain noise may compromise prediction accuracy in cases where they contain valuable information for the prediction of some parameters (Tallón-Ballesteros and Riquelme, 2015).

Due to the many features extracted from the image data, it is likely that the data contained irrelevant features possibly due to noise or redundancy/collinearity in the data. To reduce the effects of these irrelevant features, feature cleaning and a feature selection algorithm called sequential feature selection (SFS) were used to find relevant features. The feature cleaning algorithm was used to eliminate constant and correlated features. The SFS algorithm searches for the linear combinations of features that best correlate with the responses (Pudil et al., 1994). Both the feature cleaning and SFS algorithms used are available in the MATLAB BALU toolbox (Mery, 2011). The resultant few features were used to develop the final models.

Model Development

After the feature cleaning and selection process, a few important features were retained. Depending on the phenotypic trait, a classification or regression model was developed. In the model development process, 70% of the data were used for model calibration (implemented with fivefold, k-fold cross validation) and 30% were used to test the resultant models.

Linear discriminant analysis (LDA), a commonly used technique for classification and dimensionality reduction (Varmuza and Filzmoser, 2009), was used to develop a model for discriminating between normal (control) and cold-stressed watermelon plants. Plants that belong to the control group were labeled 1 while all stressed plants (1, 2, and 3-week stressed plants) were labeled 2.

Multiple linear regression (MLR) is known for its simplicity in finding correlations between multiple variables and responses (in this case number of leaves and plant age). The MLR algorithm is known to fail with high-dimensional data and highly correlated data (Marill, 2004). However, due to the reduced number of variables after SFS variable selection (reduction to less than 40 features), applying MLR was sufficient for this study to develop models for prediction of number of leaves and plant age.

Model Evaluation

The performance of the LDA model(s) developed for classifying normal from cold-stressed plants was evaluated using classification accuracy and confusion matrix (which shows the specificity and precision of the model) for both the calibration and prediction sets (Visa et al., 2011; Raschka, 2018).

The performance of the MLR models developed for predicting number of leaves and plant age was tested using the goodness of fit criteria, including root-mean-square error (RMSE) and coefficient of determination (R^2) for the calibration and prediction sets (Zhou and Bovik, 2009; Chai and Draxler, 2014). The best models should have R^2 values close to 1, and RMSE values close to zero.

Finally, tests were carried out on the results to evaluate and find optimum conditions. These tests include:

(1) Analysis of the composition of the selected features to determine the most relevant and abundant features and image view from whence most features are extracted;

(2) Testing the results using 1, 2, and 3 image views to determine the most suitable number of images to be used for predicting the phenotypic traits.

RESULTS

Image Data

Using the data collection system setup, the seven cameras each captured one image for each watermelon plant sample placed at the center of the system. The captured images (**Figure 4**) were then saved in a specified directory in a portable network graphics (PNG) format. The images were later fed into an image analysis pipeline to estimate the phenotypic traits of the watermelon plants.

Background Detection

The results of the two methods used for background removal showed that U-Net performed better than the conventional image processing algorithm (**Figure 5**). The less-than-pristine performance of the conventional image processing-based algorithm was due to of the poorly handled variances that existed in the data caused by inter-image intensity differences due to sample color/intensity variances. From these results, U-Net background removal was used for segmenting the watermelon plant from the background scene.

Discrimination of Stressed and Non-stressed Plants

Results of the LDA classifier for classification between normal and cold-stressed plants resulted in 100% classification accuracy both on the calibration and test data set (**Figure 6**).

The reason for the clear discrimination is because of the clear differences (in size, texture, and color) between the normal and stressed plants (**Figure 7**). An analysis of the features selected for classifying normal and cold-stressed plants revealed that 68.2, 18.2, 4.5, and 9.1% belonged to texture, region properties, color, and other features, respectively (**Table 5**). Texture features (describe plant texture) and region properties (describe plant shape and size) constituted more than 86% of the selected features and thus contributed more to the classification between normal and stressed watermelon plants.

The predominant texture features in the analysis were the DCT, LBP, Haralick, Gabor, and Fourier descriptor features. Further analysis established that features from image 2 (60-degree view image, 50% of the selected features) were more abundant, followed by those from image 3 (top view image, 27.3% of the selected features) and image 1 (0-degree view image, 22.7% of the selected features).

FIGURE 4 | Watermelon plant images captured using the data collection setup.

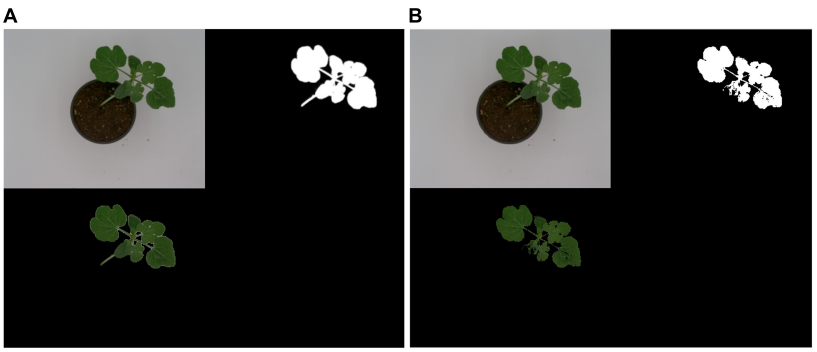

FIGURE 5 | Comparison of watermelon plant background segmentation using **(A)** U-Net and **(B)** a conventional image processing algorithm.

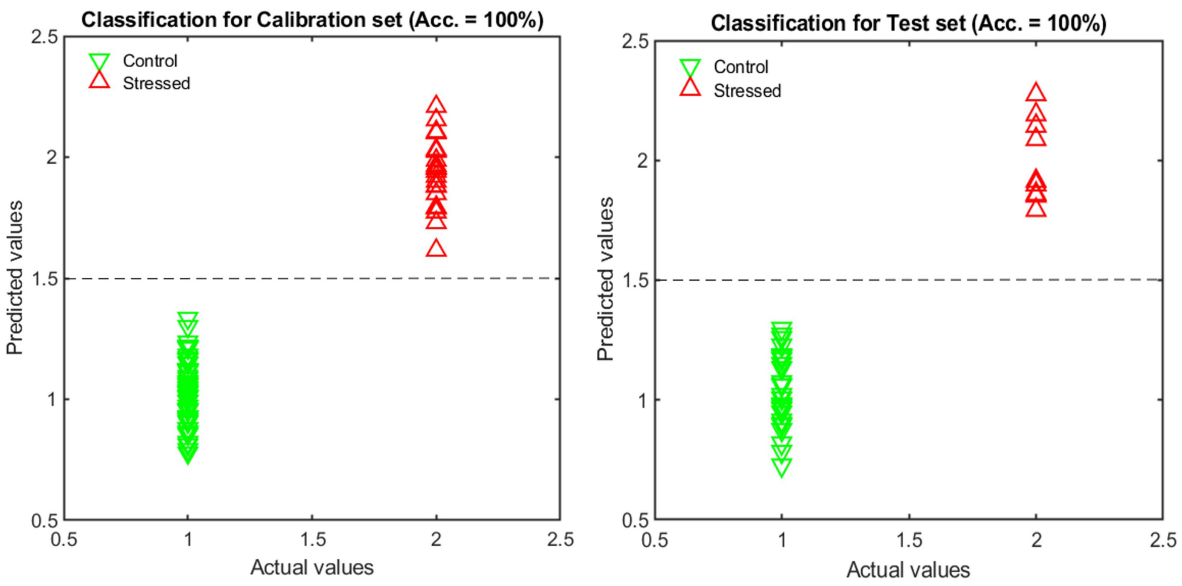

FIGURE 6 | Classification results for normal and stressed plants using three images.

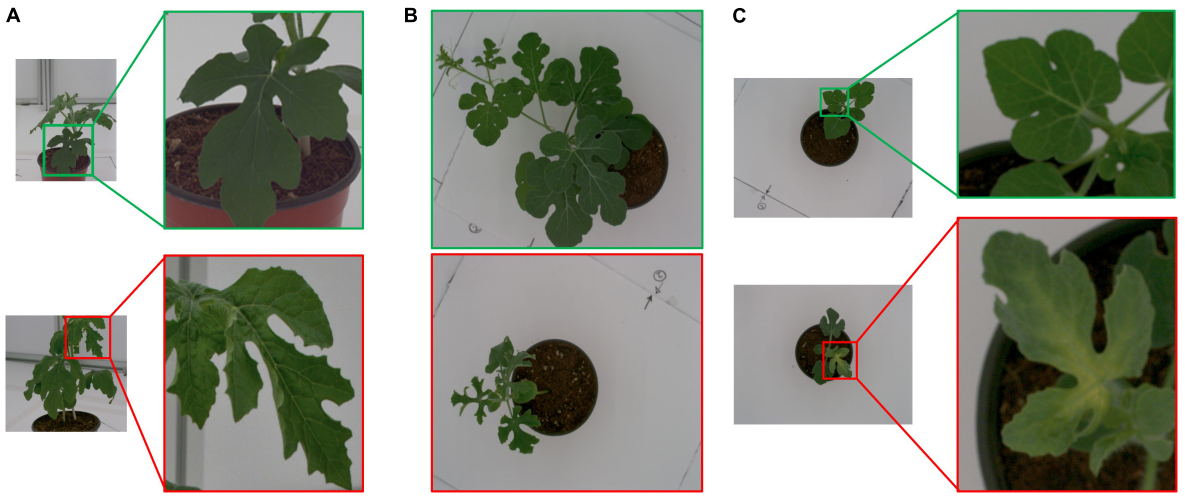

FIGURE 7 | (A) Textural difference between a normal (top) and stressed (bottom) plant at week 4. **(B)** Size difference between a normal (top) and stressed (bottom) plant at week 5. **(C)** Color difference between a normal (top) and stressed (bottom) plant at week 3.

The classification model development was repeated using features extracted from two images and one image, and a comparison was made to find out which number of image views is most suitable. The results show a slight reduction in model precision and accuracy as the number of images is reduced (**Table 6**), though not significantly different when using two or three images. However, the smaller the number of images used, the more complex the resultant classification, requiring more features to make a reliable classification. These results show that a minimum of two images are required for 100% classification accuracy.

Leaf Counting

Of the 573 features from the feature extraction process, 21 features were selected using the SFS algorithm and were used to estimate the leaf count of the watermelon plants. The number of leaves detected using the morphological features was correlated with the real number of leaves in the corresponding plants. The R^2, RMSE, and mean absolute difference (MAD) values achieved during prediction were 0.94, 0.97 leaves, and 0.88 leaves, respectively (**Figure 8**).

TABLE 5 | Selected features for classification of plant stress condition.

Features		Number of features	Percentage
Texture	LBP features	5	68.2%
	Haralick features	2	
	Fourier features	3	
	DCT coefficients	2	
	Gabor features	2	
Region properties	Feret properties	2	18.2%
	Euler Number	1	
	Orientation	1	
Color		1	4.5%
Others	Contrast	2	9.1%
Total		21	

Plant Age Estimation

For plant age estimation, number of weeks was used as the reference information since image data was collected every week for 4 weeks. Using the extracted features, 15 features were selected using the SFS feature selection algorithm and a regression model using MLR was developed to find a correlation between the selected features and the normal/control plant age in weeks. The performance of the model for predicting watermelon plant age was found to have R^2 and RMSE values of 0.92 and 0.29 weeks, respectively (**Figure 8**). This model was developed for all four watermelon varieties. However, using data from the individual watermelon varieties resulted in higher model performance in prediction (**Table 7**).

DISCUSSION

Discrimination Between Stressed and Non-stressed Plants

Temperature stress is a significant challenge to agricultural production. Extreme changes in temperature that deviate from a plant's optimal growth temperature range restrict plant metabolism, growth, and development (Yadav, 2010; Ding et al., 2019). In non-tropical climates, watermelon plants are cultivated in controlled environments where the plants are closely monitored to prevent the effects adverse temperature changes. Plants that are exposed to cold stress show symptoms including retarded growth, yellowing of leaves (chlorosis), wilting and reduced leaf expansion after 48 h of exposure (Yadav, 2010). Previous studies that used image analysis to assess cold stress in plants focused on variety performance comparison (Enders et al., 2019), and chilling stress injury classes (Dong et al., 2019).

TABLE 6 | Comparison of classification results for normal and stressed watermelon plants using features from three-view, two-view, and one-view images.

Number of Images	Calibration					Test					Selected features	Outliers
	TP	FP	TN	FN	Acc. (%)	TP	FP	TN	FN	Acc. (%)		
3 images	62	0	23	0	100	27	0	9	0	100	21	1
2 images	61	0	23	0	100	27	0	9	0	100	22	2
1 image	61	0	22	0	100	24	1	9	0	98	26	4

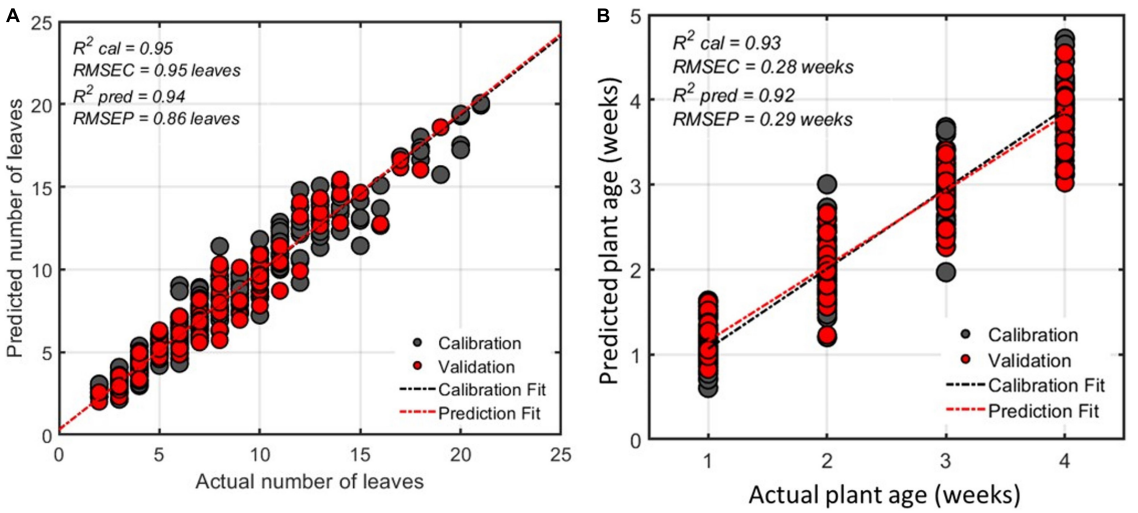

FIGURE 8 | Regression plot from model for estimating number of leaves of watermelon plant **(A,B)** watermelon plant age for all varieties estimated using 21 selected features.

However, none of these studies attempt to classify cold stressed plants from normal ones.

This study results demonstrated the possibility of classification of cold-stressed watermelon plants from normal plants and determination of some phenotypic traits based on image analysis. The classification model was able to distinguish the stressed plants after 1 week of exposure to stress conditions from the normal plants. Analysis of the selected features showed that texture was most important for the classification (**Table 5**). This is because during cold stress, the leaf shape of the plants is shriveled at the edges, causing a change from a smooth hairy texture to a coarser rough texture (**Figure 7**).

Similarly, the stressed plants were smaller in size than normal plants because plant growth is stunted during the cold stress spell (**Figure 7**). This was clearly seen in the plant image data resulting in a high feature importance for the shape-based features (region properties). This is because cold stress disrupts bio-energetic processes, causes changes in metabolism, and contributes to damage to cellular structures, hence the stunted growth and shriveled leaves (Korkmaz and Dufault, 2001; Staniak et al., 2021).

These clear differences in the image data resulted in a distinct classification between cold-stressed watermelon plants from normal ones regardless of the age and variety. A further analysis into the number of image views required for extraction of morphological features resulted in a minimum requirement of two image views (**Table 6**). Using one image-view to extract morphological features required a larger feature set of 26 features and achieved a lower classification accuracy. This is because of occlusion of plant leaves using one image view that was alleviated by using multiple views.

TABLE 7 | Multiple linear regression model performance based on all and individual watermelon varieties.

Varieties	Calibration		Test		Selected features	Outliers
	R^2	RMSE	R^2	RMSE		
All varieties	0.93	0.28	0.92	0.29	15	5
DAP	0.98	0.15	0.98	0.15	18	2
DAPCT	0.98	0.12	0.97	0.17	18	5
PI482261	1.00	0.02	0.99	0.04	14	1
45NC	1.00	0.03	1.00	0.05	18	1

Leaf Counting

Over the duration of the data collection period, it was noted that the watermelon plants exposed to stress were stunted and had a lower leaf count compared to the normal plants. This signifies the importance of counting the number of leaves as a phenotypic trait in plant monitoring to determine plant health alongside other traits. The leaf counting task is specialized and requires a new model to be developed for each plant due to variations among species. Similar to this study, Pape and Klukas (2015)

used a few geometric features to carry out the leaf counting task for *Arabidopsis thaliana* and tobacco plants. This study achieved comparable results to theirs using geometric as well as texture features to carry out leaf counting for watermelon plants which, to the best of our knowledge, has not been done in previous studies.

Similar results to ours have been obtained in previous studies using DL algorithms for the leaf counting task (Aich and Stavness, 2017; Ubbens and Stavness, 2017). However, the use of deep learning requires the annotation of each leaf in a plant image to generate a training dataset from which the algorithm learns and can then make accurate predictions of leaf counts from new images. This requires precise delineations, the acquisition of which is time-consuming and sensitive to the arrangement of leaves (Giuffrida et al., 2018). The model in this study attempted to overcome this challenge with the extraction and application of morphological features from images, which resulted in superior results for leaf counting that are comparable to previous studies that have used DL algorithms.

Plant Age Estimation

The sensitivity of watermelon plants to temperature stress varies depending on the age of the plant. The adverse effects of temperatures below 13°C can be seen before the flowering stage and plants that are subject to temperatures greater than 14°C beyond the flowering stage do not experience significant cold stress effects. This was the basis for the experimental design of this study. Estimation of the plant age can be done based on the number of leaves and tillers (Girma et al., 2007; Teimouri et al., 2018). For this study, the plant age was determined based on the number of weeks from the 2nd week (seedling stage) to the 5th week (flowering stage) i.e., for week 2, 3, 4, and 5.

The regression results (**Table 7**) showed distinct predictions of the age of the plants from all four varieties. A further analysis of plant age prediction for individual varieties resulted in better prediction performance. Because of the differences between the watermelon varieties, data from a single variety is more homogenous and subject to less variation compared to data from all the watermelon varieties, resulting in better model performance. This is consistent with the phenomenon of intraspecific variation that accounts for the phenotypic and genotypic variation within a species (des Roches et al., 2018). This phenomenon influences models that are used for estimating the watermelon plant age.

In summary, a simple plant-to-sensor system was developed that can identify cold stressed watermelon plants and additionally estimate plant characteristics including leaf count and plant age. This study applies an image analysis pipeline (image processing, feature detection, extraction, and selection) on the captured watermelon plant images to identify cold stressed plants and estimate leaf count and plant age.

The movement of plants to the data collection system disturbs the growth conditions, may induce mechanical damage, and is limited by the size of the plants. This method works well for small plants and becomes increasingly troublesome, as the plants grow. Similarly, since color information is employed in the image analysis pipeline, stable lighting conditions during image acquisition are required. Because of inconsistent lighting in fields or growth chambers, *in situ* measurements are not possible.

For this study, approximately 120 watermelon samples from four varieties were used. To develop more robust classification and regression models, more varieties are needed.

CONCLUSION

This study established that it is possible to classify cold-stressed watermelon plants from normal ones and predict phenotypic traits such as the number of leaves and plant age using selected morphological features from image analysis. The classification model achieved a test accuracy of 100% while using features from two and three different view images, indicating a minimum requirement of two images for 100% classification. An analysis of the few select features used for model development established that texture features and region properties (related to shape and size) were the most important features for classifying normal from stressed watermelon plants.

The models developed for additional phenotypic traits, i.e., plant age and number of leaves, achieved good prediction performance. Overall, this study was able to determine that it is possible to use image analysis to extract morphological features and accurately predict the stress condition and some key phenotypic traits for watermelon plants. This study can serve as a basis for the development of a real-time system for monitoring watermelon plants in high-throughput plant phenotyping facilities. Further studies can be carried out to develop wide-range models for the prediction of multiple phenotypic traits, which would be advantageous for high-throughput phenotyping systems.

DATA AVAILABILITY STATEMENT

The original contributions presented in the study are included in the article/supplementary material, further inquiries can be directed to the corresponding author.

AUTHOR CONTRIBUTIONS

B-KC contributed to the conceptualization, funding acquisition, and supervision of the study and made substantial contributions to the revision of the manuscript. SN, CW, MF, MA, MK, and IB performed the data acquisition and analysis. SN and CW wrote the manuscript. All authors contributed to the article and approved the submitted version.

FUNDING

This work was supported by the Korea Institute of Planning and Evaluation for Technology in Food, Agriculture, and Forestry (IPET) through Smart Farm Innovation Technology Development Program, funded by the Ministry of Agriculture, Food and Rural Affairs (MAFRA) (421005-04).

REFERENCES

Aich, S., and Stavness, I. (2017). "Leaf counting with deep convolutional and deconvolutional networks," in *Proceedings - 2017 IEEE International Conference on Computer Vision Workshops, ICCVW 2017*, (Piscataway: IEEE), 2080–2089. doi: 10.1109/ICCVW.2017.244

An, N., Welch, S. M., Markelz, R. J. C., Baker, R. L., Palmer, C. M., Ta, J., et al. (2017). Quantifying time-series of leaf morphology using 2D and 3D photogrammetry methods for high-throughput plant phenotyping. *Comput. Electr. Agric.* 135, 222–232. doi: 10.1016/j.compag.2017.02.001

Aptoula, E., and Yanikoglu, B. (2013). "Morphological features for leaf based plant recognition," in *2013 IEEE International Conference on Image Processing, ICIP 2013 - Proceedings*, (Piscataway: IEEE), 1496–1499. doi: 10.1109/ICIP.2013.6738307

Aruna, K. V., Vijayalakshmi, K., and Karthikeyan, V. (2016). Water Melon Plant (Citrullus lanatus): pharmacognostical standardization and phytochemical screening of its leaves. *Int. J. Adv. Pharm. Sci. Pharmanest* 5, 2184–2191.

Assefa, A. D., Hur, O., Ro, N., Lee, J., Hwang, A., Kim, B., et al. (2020). Fruit morphology, citrulline, and arginine levels in diverse watermelon (Citrullus lanatus) germplasm collections. *Plants* 9:1054. doi: 10.3390/plants9091054

Bismillah Khan, M., Hussain, M., Raza, A., Farooq, S., and Jabran, K. (2015). Seed priming with CaCl2 and ridge planting for improved drought resistance in maize. *Turk. J. Agric. For.* 39, 193–203. doi: 10.3906/tar-1405-39

Chadha, A. R., Vaidya, P. P., and Roja, M. M. (2011). "Face recognition using discrete cosine transform for global and local features," in *2011 International Conference on Recent Advancements in Electrical, Electronics and Control Engineering, IConRAEeCE'11 - Proceedings*, (Piscataway: IEEE), 502–505. doi: 10.1109/ICONRAEeCE.2011.6129742

Chai, T., and Draxler, R. R. (2014). Root mean square error (RMSE) or mean absolute error (MAE)? -Arguments against avoiding RMSE in the literature. *Geosci. Model Dev.* 7, 1247–1250. doi: 10.5194/gmd-7-1247-2014

Chen, M., Jin, L., Yuan, Z., and Rong, H. (2019). "Study on the extraction method for the contrast feature of ship wake images based on human visual characteristics," in *Proceedings of the 2019 International Conference on Image, Video and Signal Processing - IVSP 2019, Part F147767*, (New York, NY: Association of Computing Machinery), 33–39. doi: 10.1145/3317640.3317642

des Roches, S., Post, D. M., Turley, N. E., Bailey, J. K., Hendry, A. P., Kinnison, M. T., et al. (2018). The ecological importance of intraspecific variation. *Nat. Ecol. Evol.* 2, 57–64. doi: 10.1038/s41559-017-0402-5

Ding, Y., Shi, Y., and Yang, S. (2019). Advances and challenges in uncovering cold tolerance regulatory mechanisms in plants. *New Phytol.* 222, 1690–1704. doi: 10.1111/nph.15696

Dong, Z., Men, Y., Li, Z., Zou, Q., and Ji, J. (2019). Chlorophyll fluorescence imaging as a tool for analyzing the effects of chilling injury on tomato seedlings. *Sci. Hortic.* 246, 490–497.

Ehsanirad, A., and Sharath, K. Y. (2010). Leaf recognition for plant classification using GLCM and PCA Methods. *Oriental J. Comput. Sci. Technol.* 3, 31–36.

Enders, T. A., st. Dennis, S., Oakland, J., Callen, S. T., Gehan, M. A., Miller, N. D., et al. (2019). Classifying cold-stress responses of inbred maize seedlings using RGB imaging. *Plant Direct* 3:e00104. doi: 10.1002/pld3.104

Fahad, S., Bajwa, A. A., Nazir, U., Anjum, S. A., Farooq, A., Zohaib, A., et al. (2017). Crop production under drought and heat stress: plant responses and management options. *Front. Plant Sci.* 8:1147. doi: 10.3389/fpls.2017.01147

Girma, K., Martin, K. L., Freeman, K. W., Mosali, J., Teal, R. K., Raun, W. R., et al. (2007). Determination of optimum rate and growth stage for foliar-applied phosphorus in corn. *Commun. Soil Sci. Plant Anal.* 38, 1137–1154.

Giuffrida, M. V., Doerner, P., and Tsaftaris, S. A. (2018). Pheno-deep counter: a unified and versatile deep learning architecture for leaf counting. *Plant J.* 96, 880–890. doi: 10.1111/tpj.14064

Haralick, R. M., Dinstein, I., and Shanmugam, K. (1973). Textural Features for Image Classification. *Stud. Media Commun.* 3, 610–621. doi: 10.1109/TSMC.1973.4309314

Harish, B. S., Hedge, A., Venkatesh, O., Spoorthy, D. G., and Sushma, D. (2013). "Classification of plant leaves using Morphological features and Zernike moments," in *Proceedings of the 2013 International Conference on Advances in Computing, Communications and Informatics, ICACCI 2013*, (Piscataway: IEEE), 1827–1831. doi: 10.1109/ICACCI.2013.6637459

Hu, X., and Ensor, A. (2019). "Fourier spectrum image texture analysis," in *International Conference Image and Vision Computing New Zealand*, (Piscataway: IEEE), doi: 10.1109/IVCNZ.2018.8634740

Jagtap, S. B., and Hambarde, S. M. (2014). Agricultural plant leaf disease detection and diagnosis using image processing based on morphological feature extraction. *IOSR J. VLSI Signal Process.* 4, 24–30. doi: 10.9790/4200-04512430

Jain, A. K. (1989). "Image transforms," in *Fundamentals of Digital Image Processing*, ed. T. Kailath (Hoboken: Prentice-Hall Inc), 132–187.

Kamarainen, J. K. (2012). "Gabor features in image analysis," in *2012 3rd International Conference on Image Processing Theory, Tools and Applications, IPTA 2012*, (Piscataway: IEEE), 13–14. doi: 10.1109/IPTA.2012.6469502

Kavitha, J. C., and Suruliandi, A. (2016). Texture and color feature extraction for classification of melanoma using SVM. *2016 Int. Conf. Comput. Technol. Intell. Data Eng.* 2016, 1–6. doi: 10.1109/ICCTIDE.2016.7725347

Korkmaz, A., and Dufault, R. J. (2001). Developmental consequences of cold temperature stress at transplanting on seedling and field growth and yield. I. watermelon. *J. Am. Soc. Hortic. Sci.* 126, 404–409. doi: 10.21273/JASHS.126.4.404

Kumar, A., and Pang, G. K. H. (2002). Defect detection in textured materials using optimized filters. *IEEE Trans. Syst. Man Cybern. B Cybern.* 32, 553–570. doi: 10.1109/TSMCB.2002.1033176

Kumar, G., and Bhatia, P. K. (2014). "A detailed review of feature extraction in image processing systems," in *2014 Fourth International Conference on Advanced Computing & Communication Technologies*, (Piscataway: IEEE), 5–12. doi: 10.1109/ACCT.2014.74

Kumar, M., Gupta, S., Gao, X. Z., and Singh, A. (2019). Plant species recognition using morphological features and adaptive boosting methodology. *IEEE Access* 7, 163912–163918. doi: 10.1109/ACCESS.2019.2952176

Li, H., Chang, J., Chen, H., Wang, Z., Gu, X., Wei, C., et al. (2017). Exogenous melatonin confers salt stress tolerance to watermelon by improving photosynthesis and redox homeostasis. *Front. Plant Sci.* 8:295. doi: 10.3389/fpls.2017.00295

Lu, W., Edelson, J. V., Duthie, J. A., and Roberts, B. W. (2003). A comparison of yield between high-and low-intensity management for three watermelon cultivars. *HortScience* 38, 351–356. doi: 10.21273/hortsci.38.3.351

Manik, F. Y., Herdiyeni, Y., and Herliyana, E. N. (2016). Leaf morphological feature extraction of digital image anthocephalus cadamba. *Telkomnika* 14, 630–637. doi: 10.12928/telkomnika.v14i2.2675

Marill, K. A. (2004). Advanced statistics: linear regression, part II: multiple linear regression. *Acad. Emerg. Med.* 11, 94–102. doi: 10.1197/j.aem.2003.09.006

Mery, D. (2011). *BALU: A Matlab Toolbox For Computer Vision, Pattern Recognition and Image Processing*. Available online at: http://dmery.ing.puc.cl/index.php/balu (accessed October 12, 2021).

Metre, V., and Ghorpade, J. (2013). An overview of the research on texture based plant leaf classification. *arXiv* [Preprint]. Available online at: https://arxiv.org/abs/1306.4345v1

Mingqiang, Y., Kidiyo, K., and Joseph, R. (2008). "A survey of shape feature extraction techniques," in *Pattern Recognition Techniques, Technology and Applications*, ed. P. Y. Yin (London: IntechOpen), 43–90. doi: 10.5772/6237

Nabwire, S., Suh, H. K., Kim, M. S., Baek, I., and Cho, B. K. (2021). Review: application of artificial intelligence in phenomics. *Sensors* 21:4363. doi: 10.3390/s21134363

Nishiyama, I. (1970). Male sterility caused by cooling treatment at the meiotic stage in rice plants. IV: respiratory activity of anthers following cooling treatment at the meiotic stage. *Jpn. J. Crop Sci.* 39, 65–70.

Noh, J., Kim, J. M., Sheikh, S., Lee, S. G., Lim, J. H., Seong, M. H., et al. (2013). Effect of heat treatment around the fruit set region on growth and yield of watermelon [Citrullus lanatus (Thunb.) Matsum. and Nakai]. *Physiol. Mol. Biol. Plants* 19, 509–514. doi: 10.1007/s12298-013-0174-6

Ojala, T., Pietikäinen, M., and Mäenpää, T. (2002). Multiresolution gray-scale and rotation invariant texture classification with local binary patterns. *IEEE Trans. Pattern Anal. Mach. Intell.* 24, 971–987. doi: 10.1109/TPAMI.2002.1017623

Olive, D., and Hawkins, D. (2010). *Robust Multivariate Location And Dispersion*. Available online at: https://www.researchgate.net/publication/228434748

Pape, J.-M., and Klukas, C. (2015). "Utilizing machine learning approaches to improve the prediction of leaf counts and individual leaf segmentation of rosette plant images," in *Proceedings of the Computer Vision Problems in Plant*

Phenotyping (CVPPP), eds S. A. Tsaftaris, H. Scharr, and T. Pridmore (London: BMVA Press), 3.1–3.12. doi: 10.5244/c.29.cvppp.3

Patro, S. G. K., and Sahu, K. K. (2015). Normalization: a preprocessing stage. *ArXiv* [Preprint]. Available online at: http://arxiv.org/abs/1503.06462 (accessed October 12, 2021).

Pudil, P., Novovièová, J., and Kittler, J. (1994). Floating search methods in feature selection. *Pattern Recognit. Lett.* 15, 1119–1125. doi: 10.1016/0167-8655(94)90127-9

Ramcharan, A., Baranowski, K., McCloskey, P., Ahmed, B., Legg, J., and Hughes, D. P. (2017). Deep learning for image-based cassava disease detection. *Front. Plant Sci.* 8:1852. doi: 10.3389/fpls.2017.01852

Ramcharan, A., McCloskey, P., Baranowski, K., Mbilinyi, N., Mrisho, L., Ndalahwa, M., et al. (2019). A mobile-based deep learning model for cassava disease diagnosis. *Front. Plant Sci.* 10:272. doi: 10.3389/fpls.2019.00272

Raschka, S. (2018). Model evaluation, model selection, and algorithm selection in machine learning. *Arxiv* [Preprint]. Available online at: http://arxiv.org/abs/1811.12808 (accessed October 12, 2021).

Rivero, R. M., Ruiz, J. M., Garcıa, P. C., Lopez-Lefebre, L. R., Sánchez, E., and Romero, L. (2001). Resistance to cold and heat stress: accumulation of phenolic compounds in tomato and watermelon plants. *Plant Sci.* 160, 315–321. doi: 10.1016/s0168-9452(00)00395-2

Rodríguez, V. M., Soengas, P., Alonso-Villaverde, V., Sotelo, T., Cartea, M. E., and Velasco, P. (2015). Effect of temperature stress on the early vegetative development of Brassica oleracea L. *BMC Plant Biol.* 15:145. doi: 10.1186/s12870-015-0535-0

Ronneberger, O., Fischer, P., and Brox, T. (2015). U-Net: convolutional networks for biomedical image segmentation. *IEEE Access* 9, 16591–16603. doi: 10.1109/ACCESS.2021.3053408

Sabrol, H., and Kumar, S. (2016). Intensity based feature extraction for tomato plant disease recognition by classification using decision tree. *Int. J. Comput. Sci. Inform. Security* 14, 622–626.

Schmidt, J., Claussen, J., Wörlein, N., Eggert, A., Fleury, D., Garnett, T., et al. (2020). Drought and heat stress tolerance screening in wheat using computed tomography. *Plant Methods* 16, 1–12. doi: 10.1186/s13007-020-00565-w

Shirani Bidabadi, S., and Mehralian, M. (2020). Arbuscular Mycorrhizal Fungi Inoculation to Enhance Chilling Stress Tolerance of Watermelon. *Gesunde Pflanzen* 72, 171–179. doi: 10.1007/s10343-020-00499-2

Staniak, M., Czopek, K., Stêpień-Warda, A., Kocira, A., and Przybyś, M. (2021). Cold stress during flowering alters plant structure, yield and seed quality of different soybean genotypes. *Agronomy* 11:2059. doi: 10.3390/agronomy11102059

Stephan, M., and Santra, A. (2019). "Radar-based human target detection using deep residual u-net for smart home applications," in *2019 18th IEEE International Conference On Machine Learning And Applications (ICMLA)*, (Piscataway: IEEE), 175–182.

Sunoj, S., Igathinathane, C., Saliendra, N., Hendrickson, J., and Archer, D. (2018). Color calibration of digital images for agriculture and other applications. *ISPRS J. Photogram. Remote Sens.* 146, 221–234. doi: 10.1016/j.isprsjprs.2018.09.015

Tallón-Ballesteros, A. J., and Riquelme, J. C. (2015). "Data cleansing meets feature selection: a supervised machine learning approach," in *International Work-Conference on the Interplay Between Natural and Artificial Computation*, eds J. Ferrández Vicente, J. Álvarez-Sánchez, F. de la Paz López, F. Toledo-Moreo, and H. Adeli (Cham: Springer), 369–378. doi: 10.1007/978-3-319-18833-1_39

Tan, J. W., Chang, S. W., Abdul-Kareem, S., Yap, H. J., and Yong, K. T. (2020). Deep learning for plant species classification using leaf vein morphometric. *IEEE/ACM Trans. Comput. Biol. Bioinform.* 17, 82–90. doi: 10.1109/TCBB.2018.2848653

Taylor, M. J., Lu, W., Duthie, J. A., Roberts, B. W., and Edelson, J. V. (2003). "Effect of high and low management intensity on profitability for three watermelon genotypes," in *Proceedings of the Southern Agricultural Economics Associaltion, Annual Meeting, Mobile, Alabama*. (Alabama: Southern Agricultural Economics Association).

Teimouri, N., Dyrmann, M., Nielsen, P. R., Mathiassen, S. K., Somerville, G. J., and Jørgensen, R. N. (2018). Weed growth stage estimator using deep convolutional neural networks. *Sensors* 18:1580. doi: 10.3390/s18051580

Thakur, P., Kumar, S., Malik, J. A., Berger, J. D., and Nayyar, H. (2010). Cold stress effects on reproductive development in grain crops: an overview. *Environ. Exp. Bot.* 67, 429–443. doi: 10.1016/j.envexpbot.2009.09.004

Ubbens, J. R., and Stavness, I. (2017). Deep plant phenomics: a deep learning platform for complex plant phenotyping tasks. *Front. Plant Sci.* 8:1190. doi: 10.3389/fpls.2017.01190

Varmuza, K., and Filzmoser, P. (2009). *Introduction to Multivariate Statistical Analysis in Chemometrics*, 1st Edn. Boca Raton: CRC Press, doi: 10.1201/9781420059496

Visa, S., Ramsay, B., Ralescu, A. L., and van der Knaap, E. (2011). Confusion matrix-based feature selection. *MAICS* 710, 120–127.

Wang, H., Bah, M. J., and Hammad, M. (2019). Progress in outlier detection techniques: a survey. *IEEE Access* 7, 107964–108000. doi: 10.1109/ACCESS.2019.2932769

Waraich, E. A., Ahmad, R., Halim, A., and Aziz, T. (2012). Alleviation of temperature stress by nutrient management in crop plants: a review. *J. Soil Sci. Plant Nutr.* 12, 221–244. doi: 10.4067/S0718-95162012000200003

Wehner, T. C., Naegele, R. P., Myers, J. R., Narinder, P. S. D., and Crosby, K. (2020). *Curcubits*, 2nd Edn, Vol. 32. Wallingford: CABI.

Wyatt, J. (2016). "Grain and plant morphology of cereals and how characters can be used to identify varieties," in *Encyclopedia of Food Grains*, eds C. Wrigley, H. Corke, K. Seetharaman, and J. Faubion (Cambridge: Academic Press), 51–72. doi: 10.1016/B978-0-12-394437-5.00009-7

Yadav, S. K. (2010). Cold stress tolerance mechanisms in plants. A review. *Agron. Sustain. Dev.* 30, 515–527. doi: 10.1051/agro/2009050

Yang, J., Spicer, R. A., Spicer, T. E. V., Arens, N. C., Jacques, F. M. B., Su, T., et al. (2015). Leaf form-climate relationships on the global stage: an ensemble of characters. *Glob. Ecol. Biogeogr.* 24, 1113–1125. doi: 10.1111/geb.12334

Yetişir, H., and Uygur, V. (2009). Plant growth and mineral element content of different gourd species and watermelon under salinity stress. *Turk. J. Agric. For.* 33, 65–77.

Yoosefzadeh Najafabadi, M., Soltani, F., Noory, H., and Díaz-Pérez, J. C. (2018). Growth, yield and enzyme activity response of watermelon accessions exposed to irrigation water déficit. *Int. J. Veg. Sci.* 24, 323–337.

Zhou, W., and Bovik, A. C. (2009). Mean squared error: love it or leave it? A new look at signal fidelity measures. *IEEE Signal Process. Mag.* 26, 98–117. doi: 10.1109/MSP.2008.930649

Zinn, K. E., Tunc-Ozdemir, M., and Harper, J. F. (2010). Temperature stress and plant sexual reproduction: uncovering the weakest links. *J. Exp. Bot.* 61, 1959–1968. doi: 10.1093/jxb/erq053

Conflict of Interest: The authors declare that the research was conducted in the absence of any commercial or financial relationships that could be construed as a potential conflict of interest.

Publisher's Note: All claims expressed in this article are solely those of the authors and do not necessarily represent those of their affiliated organizations, or those of the publisher, the editors and the reviewers. Any product that may be evaluated in this article, or claim that may be made by its manufacturer, is not guaranteed or endorsed by the publisher.

frontiers | Frontiers in Plant Science

ORIGINAL RESEARCH
published: 25 April 2022
doi: 10.3389/fpls.2022.873065

Optical Property Mapping of Apples and the Relationship With Quality Properties

Hehuan Peng[1], Chang Zhang[2], Zhizhong Sun[3], Tong Sun[1], Dong Hu[1], Zidong Yang[1] and Jinshuang Wang[4]*

[1] College of Optical, Mechanical and Electrical Engineering, Zhejiang A&F University, Hangzhou, China, [2] Office of Educational Administration, Zhejiang A&F University, Hangzhou, China, [3] College of Mathematics and Computer Science, Zhejiang A&F University, Hangzhou, China, [4] Key Laboratory of Crop Harvesting Equipment Technology of Zhejiang Province, Jinhua, China

This paper reports on the measurement of optical property mapping of apples at the wavelengths of 460, 527, 630, and 710 nm using spatial-frequency domain imaging (SFDI) technique, for assessing the soluble solid content (SSC), firmness, and color parameters. A laboratory-based multispectral SFDI system was developed for acquiring SFDI of 140 "Golden Delicious" apples, from which absorption coefficient (μ_a) and reduced scattering coefficient (μ_s') mappings were quantitatively determined using the three-phase demodulation coupled with curve-fitting method. There was no noticeable spatial variation in the optical property mapping based on the resulting effect of different sizes of the region of interest (ROI) on the average optical properties. Support vector machine (SVM), multiple linear regression (MLR), and partial least square (PLS) models were developed based on μ_a, μ_s' and their combinations ($\mu_a \times \mu_s'$ and μ_{eff}) for predicting apple qualities, among which SVM outperformed the best. Better prediction results for quality parameters based on the μ_a were observed than those based on the μ_s', and the combinations further improved the prediction performance, compared to the individual μ_a or μ_s'. The best prediction models for SSC and firmness parameters [slope, flesh firmness (FF), and maximum force (Max.F)] were achieved based on the $\mu_a \times \mu_s'$, whereas those for color parameters of b* and C* were based on the μ_{eff}, with the correlation coefficients of prediction as 0.66, 0.68, 0.73, 0.79, 0.86, and 0.86, respectively.

Keywords: optical property mapping, spatial-frequency domain imaging, apple, quality, correlation, prediction

OPEN ACCESS

Edited by:
Jiangbo Li,
Beijing Academy of Agriculture and Forestry Sciences, China

Reviewed by:
Yanru Zhao,
Northwest A&F University, China
Xiongzhe Han,
Kangwon National University, South Korea

***Correspondence:**
Dong Hu
20180047@zafu.edu.cn

Specialty section:
This article was submitted to Crop and Product Physiology, a section of the journal Frontiers in Plant Science

Received: *10 February 2022*
Accepted: *03 March 2022*
Published: *25 April 2022*

Citation:
Peng H, Zhang C, Sun Z, Sun T, Hu D, Yang Z and Wang J (2022) Optical Property Mapping of Apples and the Relationship With Quality Properties. Front. Plant Sci. 13:873065. doi: 10.3389/fpls.2022.873065

INTRODUCTION

The apple, famous for its rich vitamin and mineral with high-nutritional value, is one of the most consumed fruits worldwide. Apples are available throughout the year due to the advanced and strict storage control. After harvesting, apples are transported immediately from the orchard to the shed storage. Alternatively, apples are graded and sorted first in the warehouse, after which they are directly moved to the cold shed storage (Zhang et al., 2020, 2021). The latter case is more popular because it can meet the increasing and diverse demands of consumers for apple quality. Quality evaluation on intact apple fruit, which is the key step in the process of grading and sorting, is gaining tremendous interest and attention in the field of non-destructive inspection. In the past decades, visible and near-infrared (Vis/NIR) spectroscopy has been widely developed and adopted

for quality assessment of plant and food products (Zhao et al., 2020; Daniels et al., 2021; Li and Zhang, 2021; van Wyngaard et al., 2021; Wan et al., 2021), thanks to its rapid and non-invasive character. A large number of statistical models based on Vis/NIR spectroscopy have been built for predicting apple quality properties, such as firmness, crispness, soluble solid content (SSC), and acidity (Gao et al., 2016; Fan et al., 2020; Huang et al., 2020; Tian et al., 2020). However, these models are often valid for the conditions under which they were trained and are not applicable under very variable conditions, such as different cultivars, batches, and places of origin. The main reason causing the weak robustness and applicability of the statistical models is that conventional Vis/NIR spectroscopy typically relates the spectra to the chemical and/or physical properties using a "black-box" method directly and it cannot offer separate information on the absorption and scattering properties of plant and food tissues. It is thus desirable to reveal the insight into light-tissue interaction (mainly absorption and multiple scattering), which is expected to provide more reliable prediction of quality properties under very variable conditions.

In the last decade, optical properties of fruits and vegetables, mainly referring to absorption coefficient (μ_a, mm^{-1}) and reduced scattering coefficient (μ_s', mm^{-1}), have been measured by different researchers using diverse optical sensing techniques (Hu et al., 2015; Lu et al., 2020), such as integrating sphere (IS), time-resolved (TR), spatially resolved (SR) and spatial-frequency domain imaging (SFDI). Sun C. et al. (2020) used IS coupled with inverse adding-doubling algorithm for extracting the μ_a and μ_s' of citrus fruit. Huang et al. (2018) measured the μ_a and μ_s' of tomatoes at six maturity stages from multichannel hyperspectral imaging-based SR spectra. Vanoli et al. (2020) applied TR and SR spectroscopy to determine the μ_a and μ_s' of apples after ripening in shelf life. The measured optical properties were used for evaluating the physiochemical properties, such as water content, oil gland size, total soluble solids, titratable acidity, and firmness. All these studies are limited to point measurement, which means the measured optical property is from single point (usually one pixel), and it cannot attain the spatial distribution of optical properties through single measurement. Since plant and food tissues present heterogeneity to some extent, some researchers measured several tissue points and took the average value as the optical property (He et al., 2016). This attempt might partly weaken the effect of measurement location on the intrinsic optical property, but it could not address the issue fundamentally.

Spatial-frequency domain imaging, as an emerging modality for measuring optical properties, is capable of mapping μ_a and μ_s' on a pixel-by-pixel fashion, which enables to attain 2-D optical property distribution through single measurement. By demodulating the emitted images under structured illuminations with changed frequencies and phases, the μ_a and μ_s' can be estimated using inverse algorithm based on appropriate light transfer models (Hu et al., 2016). Owing to the capabilities of wide-field and non-contact imaging, and depth-varying and signal-enhanced characterization (Gigan, 2017), SFDI has been applied for measuring the optical property mappings of apple, kiwi, mango, and pear (Hu et al., 2020a; He et al., 2021; Lohner et al., 2021; Sun et al., 2021). However, no reports were found on the prediction of apple quality properties based on the measured optical property mappings. In addition, in the SFDI, one can extract the optical property of single pixel, as well as do the measurements of multiple pixels in a preselected ROI, but the results would present difference to some extent. It is thus necessary to quantify the effect of ROI size (i.e., number of pixels) on optical property measurement. Therefore, the objectives of this research were as (1) to measure the optical property (μ_a and μ_s') mappings of apples and compare the optical property difference among different sizes of ROI; (2) to relate the average optical properties to apple SSC, firmness, and color parameters; and (3) to evaluate prediction performance of apple quality properties based on the optical properties using different models.

MATERIALS AND METHODS

Apple Preparation

A total of 140 "Golden Delicious" apples with similar size and being free of visible defects were purchased from a local fruit supermarket at the city of Hangzhou. Physical properties (i.e., weight, diameter, and height) of the apples are measured and summarized in **Table 1**. To complete the acquisition of SFDI and the measurement of quality attributes for all the apples, the experiments were designed and conducted, with the flowchart shown in **Figure 1**. The intact apples were cut lengthwise to generate a slice with the thickness of about 15 mm. The slice (left in **Figure 1**) was used for juicing measurement to get the corresponding SSC value, while the other part (right in **Figure 1**) was subjected to the color measurement, SFDI measurement, and puncture test, respectively, from which the color parameters (L*, a*, b*, C*, and H°), optical property mapping, and firmness parameters [slope, flesh firmness (FF), and maximum force (Max.F)] were obtained. The measured optical property mapping was then used for data interpretation, correlation analysis, and quality prediction. During the experiment, apples were kept at room temperature (∼22°C) with no humidity control and the experiment was completed within 5 days.

Acquisition of Spatial-Frequency Domain Imaging and Optical Property Mapping

Spatial-frequency domain imaging of the apples was acquired using a laboratory-developed SFDI system, as shown in **Figure 2**. A detailed description of the SFDI system and its calibration procedure were given in our previous study (Hu et al., 2016). The SFDI system mainly consists of a light source, a digital projector, and a color camera. The light source, combined with the DLP-based projector, is used to generate structured patterns for illuminating the apples. The reflected light is received by the camera, which produces SFDI under different frequencies and phases. The neutral density filter mounted with the projector could reduce light intensity uniformly to avoid burning on the apples, while the bandpass filter placed in front of the camera is used for wavelength dispersion, constituting a multispectral SFDI system. A number of two crossed linear polarizers are mounted in the projection and detection arms to reduce specular reflection from the apple surface. In this study, four wavelengths of 460,

TABLE 1 | Statistics of physical and quality parameters for 140 "Golden Delicious" apples.

Test method	Parameter	Mean	*SD*	Max	Min	CV (%)
Auncel	Weight (g)	226.8	17.9	270.0	190	7.9
Vernier caliper	Diameter (mm)	80.4	2.4	84.9	74.9	2.9
	Height (mm)	68.0	3.7	77.4	59.4	5.4
	Slice thickness (mm)	14.8	0.9	17.2	12.1	5.6
Refractometer	SSC (%)	15.0	1.3	18.6	11.5	8.5
Puncture	Slope (N/mm)	7.3	1.7	11.1	3.4	22.9
	FF (N)	14.0	1.6	17.4	9.5	11.4
	Max.F (N)	16.7	1.2	19.8	13.6	17.5
Colorimeter	L*	76.8	1.1	79.2	74.1	1.4
	a*	−2.9	0.8	−1.1	−5.0	−7.8
	b*	27.3	1.8	34.3	22.6	10.2
	C*	27.4	1.8	34.6	22.8	10.2
	H°	96.1	1.7	100.0	92.4	1.7

SD, standard deviation; CV, coefficient of variation; FF, flesh firmness; Max.F, maximum force.

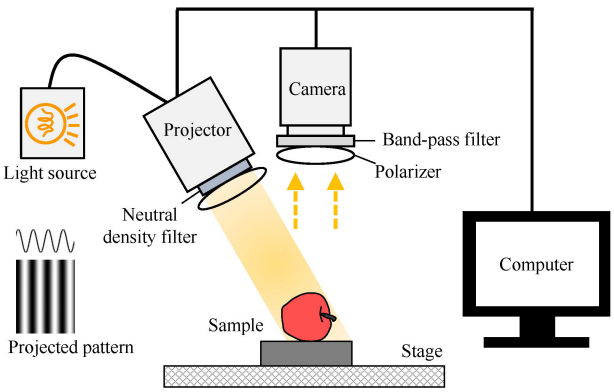

FIGURE 2 | Schematic of a multispectral spatial-frequency domain imaging system for measuring optical property mappings of apples.

527, 630, and 710 nm are used. When spatial frequency of the structured illumination is 0.20 mm^{-1}, the light penetration depth within apple tissue is approaching 1 mm (Hu et al., 2021). High-frequency illumination has a relatively shallow light penetration depth, which could be interpreted by the depth-varying feature (Hayakawa et al., 2018; Lu and Lu, 2019). To remove the effect of apple peel (with the thickness about 1 mm) on optical property mapping, six spatial frequencies with the values of 0, 0.04, 0.08, 0.12, 0.16, and 0.20 mm^{-1} were utilized in this study.

The captured SFDI of apples was processed using appropriate algorithms for extracting optical property mapping, among which image demodulation and inverse estimation are the two key steps (**Figure 3A**). Great efforts have been made to develop and improve the demodulation and inverse estimation methods (Lu et al., 2016; Hu et al., 2018, 2019; Sun et al., 2022). In this study, the conventional three-phase demodulation coupled with non-linear curve-fitting (TP-CF) method was applied for extracting optical property mapping of apples due to its high accuracy. To implement the TP-CF method, three-phase images at the same frequency were first demodulated to generate one alternative component (AC) image. Then, the non-linear curve-fitting method was used to extract the optical property (μ_a and μ_s') mappings of apples on a pixel-by-pixel fashion. It should be noted that two AC images are at least needed for curve fitting. The essential nature of the curve fitting is continuously iterative computing until the difference between the measured reflectance from the AC image and the computed reflectance based on the initially guessed optical properties is within the preset threshold

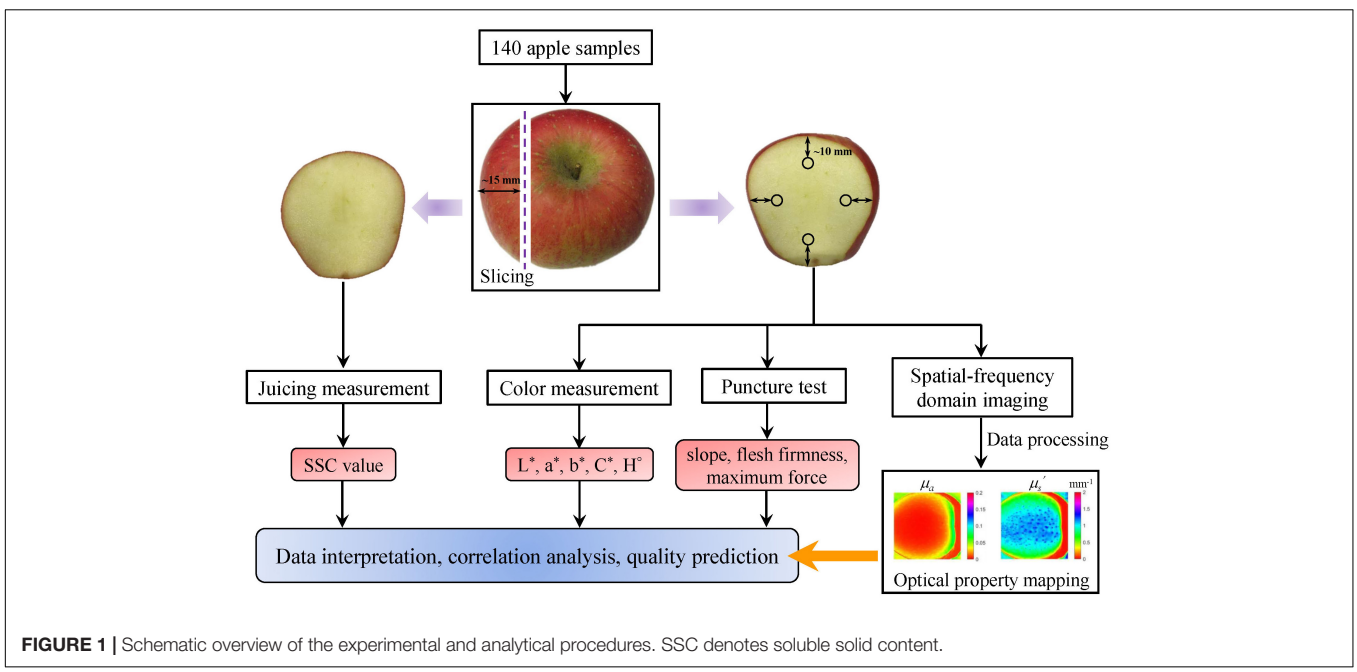

FIGURE 1 | Schematic overview of the experimental and analytical procedures. SSC denotes soluble solid content.

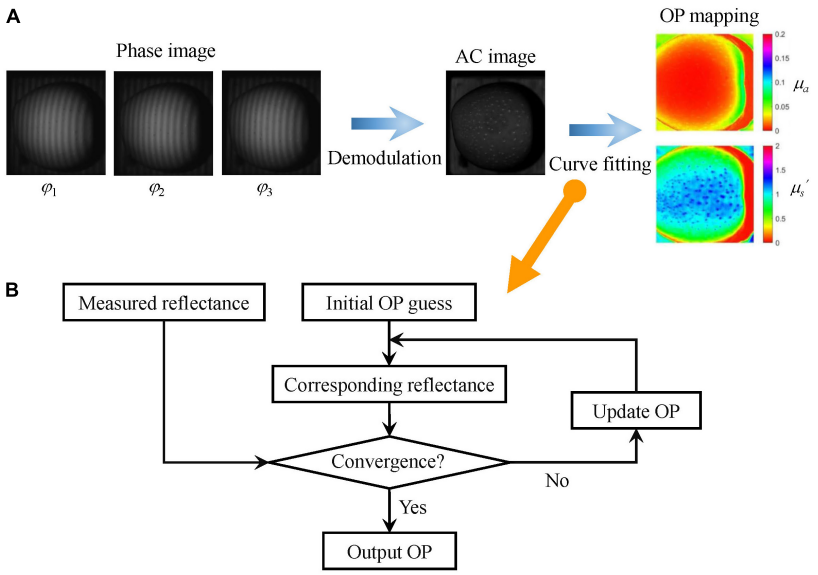

FIGURE 3 | Schematic of optical property mapping using three-phase demodulation coupled with curve fitting **(A)** and flowchart of the curve-fitting algorithm **(B)**. AC and OP denote alternative component and optical property, respectively.

(**Figure 3B**). In this occasion, dynamic adjustment is carried out to update the initial optical properties until the reflectance present a convergent pattern. To investigate the effect of ROI size on the optical property measurement, four ROIs with different sizes (i.e., 10 × 10, 30 × 30, 60 × 60, and 100 × 100 pixels, corresponding to 3 × 3 mm^2, 9 × 9 mm^2, 18 × 18 mm^2, and 30 × 30 mm^2 approximately) were selected, and the average value was taken as the optical property.

Measurement of Apple Quality Attributes

All the 140 apples were subjected to the measurement for different quality attributes. Juice of apple fruit was extracted from the apple slice (left in **Figure 1**), and SSC was measured using a handheld digital refractometer (model PR-101, Atago Co., Tokyo, Japan). Apple color was measured from the other part (right in **Figure 1**) using a colorimeter (CR-400, Konica Minolta Sensing, Inc., Tokyo, Japan) for the L*, a*, b*, C*, and H° values in triplicate, and average values were recorded for further analysis. As shown in **Figure 1**, apple firmness was measured from the surface area in quadruplicate with the distance between the center of puncture points and the external contour of apple about 10 mm, and the average values were recorded. Puncture tests were carried out using the texture analyzer (Model TA.XT plus, Stable Micro System, United Kingdom) equipped with a 5-mm cylindrical Magness-Taylor probe at a test speed of 4 mm/s and the penetration depth was set as 8 mm. A number of three parameters related to the firmness, which include slope in N/mm, FF in N, and Max.F in N, were then determined from the force–displacement curve. The slope was measured between the point of initial displacement and the point corresponding to the Max.F, while the FF was defined as the average force over the puncture distances between the rupture point and maximum puncture depth (8 mm).

Correlation Analysis and Prediction Modeling

Pearson's linear correlation analysis was performed on the relationship among all quality parameters and the absorption and reduced scattering coefficients as well as their combinations (i.e., μ_a, μ_s', $\mu_a \times \mu_s'$, and $\mu_{eff} = [3\mu_a\ (\mu_a + \mu_s')]^{1/2}$) using the software of IBM SPSS Statistics 25. $\mu_a \times \mu_s'$ is the multiplication of μ_a and μ_s', and it was reported to be more effective for predicting quality of tomatoes than using individual μ_a and μ_s' (Huang et al., 2018). μ_{eff} is a useful parameter for comparing light transmittance characteristics of different tissues and their wavelength dependence (Flock et al., 1987). To further explore the relationship between optical properties and quality parameters of apples (i.e., SSC, firmness and color), prediction models were established based on μ_a, μ_s', $\mu_a \times \mu_s'$, and μ_{eff} using support vector machine (SVM), multiple linear regression (MLR), and partial least squares (PLS) at the four wavelengths. The models of SVM, MLR, and PLS were developed by the Unscrambler X 10.4 software. All the 140 apple samples were randomly divided with 75% for the calibration set and the remaining 25% for the validation set. The performance of the prediction models was evaluated using the statistic parameters of correlation coefficient of prediction (r_p) and root mean square error of prediction (RMSEP).

RESULTS AND DISCUSSION

Statistics of Measured Quality Parameters

The statistical data of SSC, firmness (slope, FF, Max.F), and color (L*, a*, b*, C*, and H°) for all tested apples are summarized

in **Table 1**. There was no relatively large variation for all the nine quality indexes based on the standard deviation (SD) and coefficient of variation (CV), since all the 140 apples were purchased from the same batch with similar properties. It was observed that the distributions of apple SSC and color were relatively narrow than the firmness, with the CV values close to or smaller than 10%. This observation brought great challenges for predicting SSC and color parameters, which will be discussed in the following section.

Correlations among the SSC, firmness, and color parameters for all apples are summarized in **Table 2**. It was observed that the overall correlation among these quality parameters was not strong, with most of the coefficients smaller than 0.50. This might be due to the fact that the apples used in this study were similar in appearance and had no difference in maturation stage or shelf life, thus causing narrow distribution of quality attributes. It should be noted that the correlation coefficient between the Max.F and FF was as high as 0.80, because the FF was defined as the average force over the puncture distances between the rupture point (Max.F) and puncture depth. This phenomenon was also reported by Huang et al. (2018) when studying tomato fruit based on spatially resolved spectroscopy. The correlation coefficient between b* and C* was 1.00, because the two parameters were very close to each other.

Optical Property Mappings of Apples

To determine the optical property mappings of apples, the TP-CF method was carried out, and the resulting absorption and scattering properties are displayed in **Figures 4A,B**, respectively. The numbers labeled below the sub-pictures are the average values of μ_a or μ_s' for the marked ROI with the size of 30 × 30 pixels. It should be noted that the circular part is sliced apple tissue with relatively flat surface, while the surrounding part, which has a more uniform color distribution, is the sample holder made of aluminum material with blackening treatment. There was a decreased tendency of the μ_a and μ_s' along the four wavelengths. Comparing the scattering properties at a wavelength, like 527 nm in **Figure 4B**, a spatial variation of μ_s' for the apple tissue between 0.996 and 1.152 mm^{-1} was noticed. The complex apple tissue formed by different components with different physicochemical characteristics and the performance of structured illumination (e.g., non-uniformity), as well as data processing algorithm for optical property estimation, are the potential factors that cause the variation. A similar variation also occurs for the μ_a mappings in **Figure 4A**. It was observed that the spatial variation of optical properties at 710 nm was less pronounced than the other three wavelengths, which demonstrates that wavelength plays a non-negligible role when estimating apple optical properties.

Figure 5 shows the average optical properties of four different ROI with the sizes of 10 × 10, 30 × 30, 60 × 60, and 100 × 100 along the four wavelengths. The μ_a and μ_s' for different sizes of ROI are quite similar, but still, a difference can be observed. In general, the optical property value in small size ROI (10 × 10) was slightly different from the value in large size ROI, which might be caused by the spatial variation mentioned above. For the three larger ROIs, the average optical properties were close to each other, with the differences of 6.94–19.0% and 1.56–3.51% for μ_a and μ_s', respectively. Considering the fact that larger-size ROI means more cost of time, the ROI with the size of 30 × 30 was chosen for averaging the μ_a and μ_s' and would be used in the following sections.

To our knowledge, this is the first time that the optical properties of apple tissue were determined from different sizes of ROI. Based on SFDI measurements of "Braeburn" apples, Lohner et al. (2021) recently observed that μ_a was about 0.01–0.04 mm^{-1} for the cortex tissue at 656 nm, which covers the μ_a range at 630 nm in this study (0.021–0.024 mm^{-1}), if the value from the ROI of 10 × 10 is excluded. As known from the previous work, the wavelength of 656 nm is mainly related to the presence of chlorophyll *b* (Merzlyak and Solovchenko, 2002), and it is thus reasonable that the μ_a value is larger than the present results. Our results are also comparable to the published integrating sphere measurements by other researchers. For example, Wei et al. (2020) measured the optical properties of cold-stored "Fuji" apples over 400–1,100 nm and reported that the μ_a was in the range of about 0.02–0.13 mm^{-1}, whereas the μ_s' was between 1.0 and 1.75 mm^{-1} for the flesh tissue, which are comparable with the present results.

TABLE 2 | Pearson's linear correlation coefficients among apple quality parameters.

Parameter	SSC	Slope	FF	Max.F	L*	a*	b*	C*	H°
SSC	1.00								
Slope	0.46	1.00							
FF	**0.51**	0.38	1.00						
Max.F	**0.69**	**0.51**	**0.80**	1.00					
L*	0.32	0.36	0.36	0.36	1.00				
a*	**0.77**	−0.45	−0.32	0.31	−0.48	1.00			
b*	**0.51**	0.48	0.42	**0.53**	**−0.50**	**−0.50**	1.00		
C*	0.49	0.48	0.42	**0.52**	−0.49	**−0.52**	**1.00**	1.00	
H°	**−0.86**	0.38	−0.34	−0.40	**0.57**	**−0.91**	−0.49	−0.46	1.00

Significant correlations are in bold (n = 140, r ≥ 0.5, p-value ≤ 0.05).
SSC, soluble solid content; FF, flesh firmness; Max.F, maximum force.

Correlations Between Optical Properties and Apple Quality Attributes

Table 3 presents the relationships between the average optical properties and apple quality parameters. The correlations between the optical properties and their combinations at 527 and 630 nm measured by SFDI and apple quality parameters are not reported as non-significant. Better correlations were observed between μ_a and quality parameters, compared with μ_s', which is in general agreement with the previous studies for apples, tomatoes, and peaches (Do Trong et al., 2014; Huang et al., 2018; Sun Y. et al., 2020). The μ_{a_460} was negatively related to a* and C* and positively related to b*, slope, FF, and Max.F, whereas μ_{a_710} was only positively related to b* and negatively related to a*, C*, slope, FF, and Max.F. As for scattering, no significant correlations were found between $\mu_s'_{\_460}$ and quality parameters, whereas $\mu_s'_{\_710}$ was positively

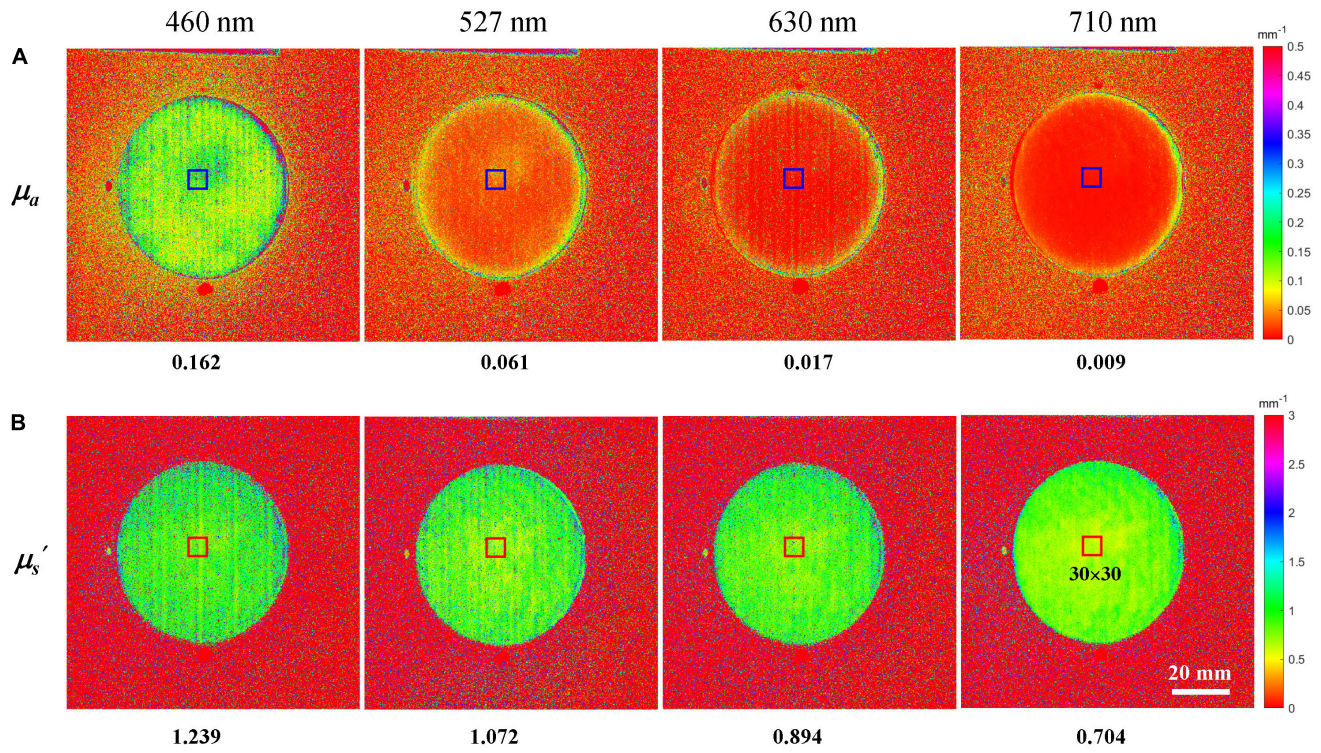

FIGURE 4 | Absorption coefficient **(A)** and reduced scattering coefficient **(B)** mappings of a representative apple at the wavelengths of 460, 527, 630, and 710 nm.

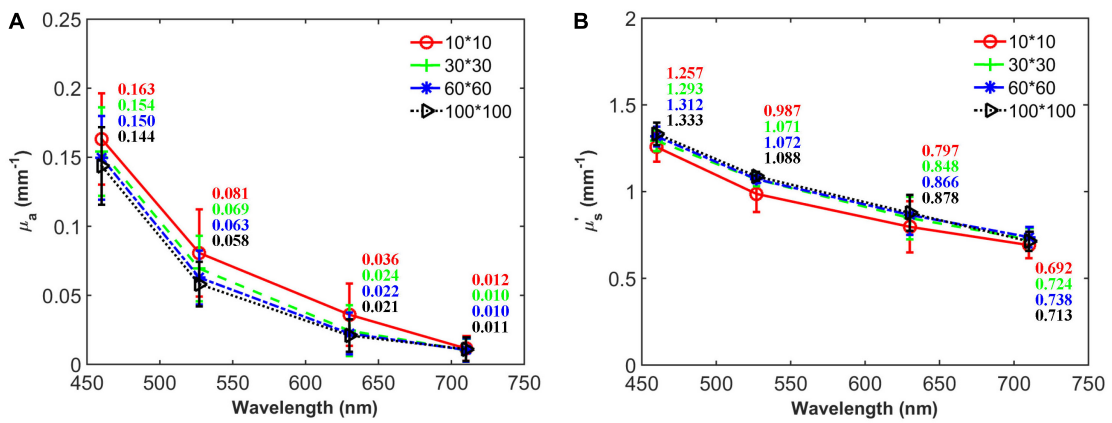

FIGURE 5 | Average absorption coefficient **(A)** and reduced scattering coefficient **(B)** of a representative apple with different sizes of ROI at the wavelengths of 460, 527, 630, and 710 nm.

and negatively related to b* and C*, respectively. It was observed that the combinations of $\mu_a \times \mu_s'\_460$, $\mu_a \times \mu_s'\_710$, μ_{eff}_460, and μ_{eff}_710 resulted in better correlation results, compared with the individual optical properties. This is especially true for the correlations between the color parameters of a*, b*, C*, and $\mu_a \times \mu_s'\_460$, $\mu_a \times \mu_s'\_710$. For example, using $\mu_a \times \mu_s'\_710$ improved correlation coefficients of a*, b*, and C* by 14.8, 25.4, and 25.4%, compared with the correlation analysis based on the μ_a_710. Moreover, a noticeable improvement was found for SSC when using the combinations of optical properties (**Table 3**). These results demonstrated that optical property measurement can provide useful information about the apple quality.

Prediction for Apple Quality Attributes

The resulting r_p and RMSEP from SVM, MLR, and PLS based on μ_a, μ_s', $\mu_a \times \mu_s'$, and μ_{eff} are summarized in **Table 4**. Overall, the prediction result performs not well with the r_p-values of 0.24–0.86 and 0.19–0.82 for the SVM and MLR, respectively. The result predicted by PLS is worse and not reported. It could be

TABLE 3 | Pearson's linear correlation coefficients between optical properties and apple quality parameters.

	μ_a_460	μ_a_710	μ_s'_460	μ_s'_710	$\mu_a \times \mu_s'$_460	$\mu_a \times \mu_s'$_710	μ_{eff}_460	μ_{eff}_710
SSC	−0.42	−0.45	−0.31	−0.39	**−0.61**	**−0.65**	**−0.61**	**−0.64**
Slope	**0.64**	**−0.55**	0.40	0.45	**0.63**	**−0.52**	**0.64**	**−0.53**
FF	**0.61**	**−0.56**	0.33	0.34	**0.69**	**−0.65**	**0.69**	**−0.65**
Max.F	**0.62**	**−0.59**	0.40	0.38	**0.62**	**−0.60**	**0.63**	**−0.59**
L*	0.39	0.32	0.21	0.32	0.49	0.37	0.30	0.28
a*	**−0.57**	**−0.54**	−0.23	−0.20	**−0.65**	**−0.62**	**−0.57**	**−0.61**
b*	**0.59**	**0.59**	0.32	**0.52**	**0.67**	**0.74**	**0.60**	**0.67**
C*	**−0.59**	**−0.59**	−0.32	**−0.52**	**−0.67**	**−0.74**	**−0.60**	**−0.66**
H°	0.36	0.26	0.15	0.11	0.45	**0.50**	0.26	0.28

Significant correlations are in bold (n = 140, r ≥ 0.5, p-value ≤ 0.05).
SSC, soluble solid content; FF, flesh firmness; Max.F, maximum force.

observed that color parameters of b* and C* achieved the best prediction performance (r_p = 0.86), followed by the firmness parameters with the r_p-values of 0.68, 0.73, and 0.79 for slope, FF, and Max.F, and finally, SSC was the most challenging for the prediction (r_p = 0.66). The prediction results for all the apple quality parameters based on μ_a were far better than that based on μ_s', which is consistent with the findings of Pearson's correlation analysis above. The combinations of $\mu_a \times \mu_s'$ and μ_{eff} gave better prediction results, compared to the individual μ_a or μ_s'. For example, using $\mu_a \times \mu_s'$ for predicting the parameter of slope by the SVM resulted in r_p of 0.68, which represents 17.2% improvement, compared with the individual μ_a. It should be mentioned that the combinations improved the prediction of SSC significantly (> 34.0%), which also agrees well with the correlation analysis.

DISCUSSION

Optical property measurement, as a powerful tool for interpreting light-tissue interaction, as well as an alternative solution for quality assessment of plant and food products by quantitatively separating absorption and scattering information from spectroscopic and/or image signals, has received increasing interests. Many fruits and vegetables, such as apple, pear, peach, citrus fruit, tomato, onion, and sweet potato, have been tested using diverse optical measurement techniques (Hu et al., 2015, 2020b; Lu et al., 2020). However, most of the efforts were made to obtain the optical property of single point (usually one pixel in the tissue). To our knowledge, SFDI is the sole technique which is capable of measuring the optical property mappings (in the axial and transverse directions), and till now, only apple and pear fruit have been studied (Hu et al., 2020a; He et al., 2021; Lohner et al., 2021). The apple flesh, as a relatively uniform tissue, should present homogeneous optical property mapping, which was confirmed by the results observed in this paper. For non-uniform samples, such as apple with peel, optical property mapping is critical to elaborate the spatial distribution of optical properties, which, in turn, would help to select the optimal location in optical inspection for quality evaluation.

It is well known that there are several peaks in apple absorbance spectra, which can be attributed to carotenoids around 500 nm, chlorophyll around 670 nm, and water around 980 nm (Vanoli et al., 2020). The wavelengths of 460 and 710 nm, under which better correlations between the optical properties and apple quality parameters were obtained, are close to the absorption peaks of carotenoids and chlorophyll, respectively. However, apple preparation in this study is destructive by removing a slice of about 15 mm, and the color parameters are all measured from the flesh tissues. Though pigments could contribute to flesh coloration, the amounts of carotenoids and chlorophylls in the flesh are very low (Delgado-Pelayo et al., 2014), which could partly explain why the correlations between optical property and color parameters were not high enough.

TABLE 4 | SVM and MLR prediction results for apple quality parameters based on absorption coefficient (μ_a), reduced scattering coefficient (μ_s'), and their combinations.

Quality parameter	Statistic parameter	SVM prediction				MLR prediction			
		μ_a	μ_s'	$\mu_a \times \mu_s'$	μ_{eff}	μ_a	μ_s'	$\mu_a \times \mu_s'$	μ_{eff}
SSC	r_p	0.47	0.30	0.66	0.63	0.40	0.31	0.59	0.60
	RMSEP	1.28	1.27	1.28	1.28	1.32	1.34	1.32	1.32
Slope	r_p	0.58	0.32	0.68	0.67	0.54	0.27	0.60	0.61
	RMSEP	1.65	1.63	1.66	1.66	1.70	1.72	1.71	1.71
FF	r_p	0.64	0.24	0.73	0.72	0.53	0.20	0.63	0.62
	RMSEP	2.24	2.29	2.24	2.25	2.25	2.29	2.25	2.25
Max.F	r_p	0.72	0.25	0.79	0.78	0.56	0.21	0.64	0.64
	RMSEP	1.20	1.27	1.21	1.22	1.28	1.31	1.29	1.29
L*	r_p	0.34	0.35	0.41	0.42	0.31	0.33	0.38	0.40
	RMSEP	1.06	1.01	1.07	1.07	1.09	1.09	1.10	1.10
a*	r_p	0.57	0.35	0.66	0.57	0.52	0.28	0.58	0.50
	RMSEP	0.84	0.82	0.84	0.84	0.86	0.85	0.87	0.87
b*	r_p	0.80	0.61	0.85	0.86	0.75	0.57	0.78	0.82
	RMSEP	2.32	2.42	2.16	2.28	2.52	2.53	2.35	2.44
C*	r_p	0.81	0.61	0.85	0.86	0.75	0.58	0.77	0.82
	RMSEP	2.32	2.42	2.16	2.28	2.53	2.53	2.35	2.44
H°	r_p	0.33	0.26	0.38	0.37	0.31	0.19	0.33	0.32
	RMSEP	1.73	1.71	1.70	1.71	1.76	1.78	1.75	1.76

SSC, soluble solid content; FF, flesh firmness; Max.F, maximum force; r_p, correlation coefficient of prediction; RMSEP, root mean square error of prediction.

This study showed that absorption properties provided useful information for apple SSC, firmness, and color prediction, while the prediction performance based on the scattering properties was much worse. This observation is general agreement with the previous studies for apple, peach, and tomato using the spatially resolved technique (Do Trong et al., 2014; Huang et al., 2018; Sun Y. et al., 2020). For SSC and color parameters, they are closely related to the chemical compositions and pigment contents in apples, which have direct relationships with the absorption properties. On the other hand, and surprisingly enough, the prediction of firmness parameters based on the absorption properties was far better than that based on the scattering properties. This unexpected outcome could be attributed to the fact that SFDI is limited to light penetration depth (2–3 mm) (Lu and Lu, 2019; Hu et al., 2021), while the firmness measurement by the texture analyzer probed the flesh much deeper (8 mm). In addition, the wavelengths used in this study are near to the characteristic wavelengths with absorption peaks, while the scattering properties have no features in those wavelengths. This may also explain why absorption properties performed better correlations with apple quality parameters than scattering properties. Since the apple quality is accompanied with both chemical compositions and tissue microstructures, the combinations of optical properties could improve the prediction performance.

The prediction models based on SVM were superior to the models established by MLR and PLS. This may be attributed to the fact that four wavelengths are not adequate to establish the stable and adaptable MLR and PLS models, while SVM is one of machine-learning methods, which is more powerful in dealing with this issue. This observation suggests that other machine-learning and deep learning methods, such as artificial neural network and convolutional neural network, can be tested for quality prediction based on optical properties in the future. Overall, the correlation and prediction performance between the optical properties and quality parameters were comparable to the results of some published work. For instance, He et al. (2016) and Sun C. et al. (2020) showed that the prediction models for SSC of pear and citrus fruit based on the μ_a spectra measured by integrating sphere technique gave the r_p-values of 0.63 and 0.67, respectively, while the r_p for SSC of tomato fruit based on the absorption properties estimated from spatially resolved diffuse reflectance was 0.62 (Huang et al., 2018), which are all comparable to the r_p of 0.66 in this study. As for the firmness prediction, He et al. (2016) reported that the PLS model gave r_p-value of 0.66, which was less satisfied than the results of Do Trong et al. (2014) (r_p = 0.84). The apple color prediction in this study was much better than the result reported by Vanoli et al. (2020) based on time- and spatially resolved techniques. Though the prediction performance of these results showed great differences, which may be in part caused by the factors of cultivar, growing, maturity and storage conditions, and measuring technique, they all demonstrated that there was a great potential for quality prediction based on the measured optical properties. However, in this paper, the results are still far away from practical application in the field of non-destructive inspection. Very few samples and characteristic wavelengths, as well as the narrow distribution of quality attributes (SSC, firmness, and color) for the apple samples used in this study, are the critical factors that result in low r_p-values. Furthermore, relatively low correlation for SSC could also be caused by the different locations (i.e., the left and right pieces in **Figure 1**) for juicing and SFDI measurements. Apples were cut into two parts in the sample preparation to generate a relatively smooth surface, which is critical to keep the distance between camera and sample surface consistent during SFDI measurement. However, this operation could not meet the requirement of non-destructive inspection in practical applications. Apple contour has non-negligible effect on optical property mapping, and thus, the contour correction is worth studying in the future research.

CONCLUSION

The optical property mappings of "Golden Delicious" apples were measured using the SFDI technique at the wavelengths of 460, 527, 630, and 710 nm. Spatial variations in the absorption coefficient (μ_a) and reduced scattering coefficient (μ_s') mappings for the sliced flesh tissue were noticed, but overall, the μ_a and μ_s' distributions were relatively uniform. Different sizes of ROI (10 × 10, 30 × 30, 60 × 60, and 100 × 100 pixels) had less effect on the average μ_a and μ_s', except for the 10 × 10 that was too small. The average μ_a and μ_s' showed a decreased tendency along the four wavelengths. Correlations between apple quality parameters and μ_a and μ_s', as well as their combinations ($\mu_a \times \mu_s'$ and μ_{eff}) at 460 and 710 nm, were superior to those at 527 and 630 nm, since the former two wavelengths were close to the absorption peaks. The prediction for quality parameters (SSC, firmness, and color) based on the μ_a was far better than that based on the μ_s', and the combinations of $\mu_a \times \mu_s'$ and μ_{eff} improved the prediction performance, compared to the individual μ_a or μ_s'. The prediction models established based on SVM outperformed those by MLR and PLS. The best prediction models for SSC, slope, FF, and Max.F were all achieved based on the $\mu_a \times \mu_s'$, with the correlation coefficients of prediction (r_p) of 0.66, 0.68, 0.73, and 0.79, respectively, whereas the μ_{eff} gave the best prediction for most of the color parameters, with the r_p-value of 0.86 for both of the parameters of b* and C*.

DATA AVAILABILITY STATEMENT

The original contributions presented in the study are included in the article/supplementary material, further inquiries can be directed to the corresponding author/s.

AUTHOR CONTRIBUTIONS

HP: conceptualization, data analysis, writing, reviewing, editing, and project administration. CZ: data collection,

methodology, reviewing, and editing. ZS: data analysis, reviewing, and editing. TS and JW: reviewing and editing. DH: conceptualization, methodology, data collection, final analysis, writing—original draft preparation, reviewing, and editing. ZY: resources, reviewing, and editing. All authors contributed to the article and approved the submitted version.

FUNDING

This work was supported by Zhejiang Basic Public Welfare Research Project (grant no. LGN18B060001), the Natural Science Foundation of Zhejiang Province (grant no. LQ20C130002), and the National Natural Science Foundation of China (grant no. 32001414).

REFERENCES

Daniels, A. J., Poblete-Echeverría, C., Nieuwoudt, H. H., Botha, N., and Opara, U. L. (2021). Classification of browning on intact table grape bunches using near-infrared spectroscopy coupled with partial least squares-discriminant analysis and artificial neural networks. *Front. Plant Sci.* 12:768046. doi: 10.3389/fpls.2021.768046

Delgado-Pelayo, R., Gallardo-Guerrero, L., and Hornero-Méndez, D. (2014). Chlorophyll and carotenoid pigments in the peel and flesh of commercial apple fruit varieties. *Food Res. Int.* 65, 272–281. doi: 10.1016/j.foodres.2014.03.025

Do Trong, N. N., Erkinbaev, C., Tsuta, M., De Baerdemaeker, J., Nicolaï, B., and Saeys, W. (2014). Spatially resolved diffuse reflectance in the visible and near-infrared wavelength range for non-destructive quality assessment of 'Braeburn'apples. *Postharv. Biol. Technol.* 91, 39–48. doi: 10.1016/j.postharvbio.2013.12.004

Fan, S., Wang, Q., Tian, X., Yang, G., Xia, Y., Li, J., et al. (2020). Non-destructive evaluation of soluble solids content of apples using a developed portable Vis/NIR device. *Biosyst. Eng.* 193, 138–148. doi: 10.1016/j.biosystemseng.2020.02.017

Flock, S. T., Wilson, B. C., and Patterson, M. S. (1987). Total attenuation coefficients and scattering phase functions of tissues and phantom materials at 633 nm. *Med. Phys.* 14, 835–841. doi: 10.1118/1.596010

Gao, F., Dong, Y., Xiao, W., Yin, B., Yan, C., and He, S. (2016). LED-induced fluorescence spectroscopy technique for apple freshness and quality detection. *Postharv. Biol. Technol.* 119, 27–32. doi: 10.1016/j.postharvbio.2016.04.020

Gigan, S. (2017). Optical microscopy aims deep. *Nat. Phot.* 11, 14–16. doi: 10.1038/nphoton.2016.257

Hayakawa, C. K., Karrobi, K., Pera, V. E., Roblyer, D. M., and Venugopalan, V. (2018). Optical sampling depth in the spatial frequency domain. *J. Biomed. Opt.* 24:071603. doi: 10.1117/1.JBO.24.7.071603

He, X., Fu, X., Rao, X., and Fang, Z. (2016). Assessing firmness and SSC of pears based on absorption and scattering properties using an automatic integrating sphere system from 400 to 1150 nm. *Postharv. Biol. Technol.* 121, 62–70. doi: 10.1016/j.postharvbio.2016.07.013

He, X., Hu, D., Fu, X., and Rao, X. (2021). Spatial frequency domain imaging for determining absorption and scattering properties of bruised pears based on profile corrected diffused reflectance. *Postharv. Biol. Technol.* 179:111570. doi: 10.1016/j.postharvbio.2021.111570

Hu, D., Fu, X., He, X., and Ying, Y. (2016). Noncontact and wide-field characterization of the absorption and scattering properties of apple fruit using spatial-frequency domain imaging. *Sci. Rep.* 6:37920. doi: 10.1038/srep37920

Hu, D., Fu, X., Wang, A., and Ying, Y. (2015). Measurement methods for optical absorption and scattering properties of fruits and vegetables. *Trans. ASABE* 58, 1387–1401. doi: 10.13031/trans.58.11103

Hu, D., Huang, Y., Zhang, Q., Yao, L., Yang, Z., and Sun, T. (2021). Numerical simulation on spatial-frequency domain imaging for estimating optical absorption and scattering properties of two-layered horticultural products. *Appl. Sci.* 11:617. doi: 10.3390/app11020617

Hu, D., Lu, R., and Ying, Y. (2018). A two-step parameter optimization algorithm for improving estimation of optical properties using spatial frequency domain imaging. *J. Quantit. Spectrosc. Radiat. Transfer* 207, 32–40. doi: 10.1016/j.jqsrt.2017.12.022

Hu, D., Lu, R., and Ying, Y. (2020a). Spatial-frequency domain imaging coupled with frequency optimization for estimating optical properties of two-layered food and agricultural products. *J. Food Eng.* 277:109909. doi: 10.1016/j.jfoodeng.2020.109909

Hu, D., Sun, T., Yao, L., Yang, Z., Wang, A., and Ying, Y. (2020b). Monte Carlo: A flexible and accurate technique for modeling light transport in food and agricultural products. *Trends Food Sci. Technol.* 102, 280–290. doi: 10.1016/j.tifs.2020.05.006

Hu, D., Lu, R., Ying, Y., and Fu, X. (2019). A stepwise method for estimating optical properties of two-layer turbid media from spatial-frequency domain reflectance. *Opt. Expr.* 27, 1124–1141. doi: 10.1364/OE.27.001124

Huang, Y., Lu, R., and Chen, K. (2020). Detection of internal defect of apples by a multichannel Vis/NIR spectroscopic system. *Postharv. Biol. Technol.* 161:111065. doi: 10.1016/j.postharvbio.2019.111065

Huang, Y., Lu, R., Hu, D., and Chen, K. (2018). Quality assessment of tomato fruit by optical absorption and scattering properties. *Postharv. Biol. Technol.* 143, 78–85. doi: 10.1016/j.postharvbio.2018.04.016

Li, J., and Zhang, Z. (2021). *Nondestructive Evaluation of Agro-Products by Intelligent Sensing Techniques*. Sharjah: Bentham Science Publishers.

Lohner, S. A., Biegert, K., Nothelfer, S., Hohmann, A., McCormick, R., and Kienle, A. (2021). Determining the optical properties of apple tissue and their dependence on physiological and morphological characteristics during maturation. *Part 1: Spat. Frequency Domain Imaging. Postharvest Biol. Technol.* 181:111647. doi: 10.1016/j.postharvbio.2021.111647

Lu, R., Van Beers, R., Saeys, W., Li, C., and Cen, H. (2020). Measurement of optical properties of fruits and vegetables: A review. *Postharvest Biol. Technol.* 159:111003. doi: 10.1016/j.postharvbio.2019.111003

Lu, Y., Li, R., and Lu, R. (2016). Fast demodulation of pattern images by spiral phase transform in structured-illumination reflectance imaging for detection of bruises in apples. *Comput. Electr. Agricult.* 127, 652–658. doi: 10.1016/j.compag.2016.07.012

Lu, Y., and Lu, R. (2019). Structured-illumination reflectance imaging for the detection of defects in fruit: analysis of resolution, contrast and depth-resolving features. *Biosyst. Eng.* 180, 1–15. doi: 10.1016/j.biosystemseng.2019.01.014

Merzlyak, M. N., and Solovchenko, A. E. (2002). Photostability of pigments in ripening apple fruit: a possible photoprotective role of carotenoids during plant senescence. *Plant Sci.* 163, 881–888. doi: 10.1016/S0168-9452(02)00241-8

Sun, C., Van Beers, R., Aernouts, B., and Saeys, W. (2020). Bulk optical properties of citrus tissues and the relationship with quality properties. *Postharvest Biol. Technol.* 163:111127. doi: 10.1016/j.postharvbio.2020.111127

Sun, Y., Lu, R., and Wang, X. (2020). Evaluation of fungal infection in peaches based on optical and microstructural properties. *Postharvest Biology and Technol.* 165:111181. doi: 10.1016/j.postharvbio.2020.111181

Sun, Z., Hu, D., Xie, L., and Ying, Y. (2022). Detection of early stage bruise in apples using optical property mapping. *Comput. Electr. Agricult.* 194:106725. doi: 10.1016/j.compag.2022.106725

Sun, Z., Xie, L., Hu, D., and Ying, Y. (2021). An artificial neural network model for accurate and efficient optical property mapping from spatial-frequency domain images. *Comput. Electr. Agricult.* 188:106340. doi: 10.1016/j.compag.2021.106340

Tian, X., Wang, Q., Huang, W., Fan, S., and Li, J. (2020). Online detection of apples with moldy core using the Vis/NIR full-transmittance spectra. *Postharvest Biol. Technol.* 168:111269. doi: 10.1016/j.postharvbio.2020.111269

van Wyngaard, E., Blancquaert, E., Nieuwoudt, H., and Aleixandre-Tudo, J. L. (2021). Infrared spectroscopy and chemometric applications for the qualitative and quantitative investigation of grapevine organs. *Front. Plant Sci.* 12:723247. doi: 10.3389/fpls.2021.723247

Vanoli, M., Van Beers, R., Sadar, N., Rizzolo, A., Buccheri, M., Grassi, M., et al. (2020). Time-and spatially-resolved spectroscopy to determine the bulk optical

properties of 'Braeburn'apples after ripening in shelf life. *Postharvest Biol. Technol.* 168:111233. doi: 10.1016/j.postharvbio.2020.111233

Wan, L., Zhu, J., Du, X., Zhang, J., Han, X., Zhou, W., et al. (2021). A model for phenotyping crop fractional vegetation cover using imagery from unmanned aerial vehicles. *J. Exp. Bot.* 72, 4691–4707. doi: 10.1093/jxb/erab194

Wei, K., Ma, C., Sun, K., Liu, Q., Zhao, N., Sun, Y., et al. (2020). Relationship between optical properties and soluble sugar contents of apple flesh during storage. *Postharvest Biol. Technol.* 159:111021. doi: 10.1016/j.postharvbio.2019.111021

Zhang, Z., Igathinathane, C., Li, J., Cen, H., Lu, Y., and Flores, P. (2020). Technology progress in mechanical harvest of fresh market apples. *Comput. Electr. Agricult.* 175:105606. doi: 10.1016/j.compag.2020.105606

Zhang, Z., Lu, Y., and Lu, R. (2021). Development and evaluation of an apple infield grading and sorting system. *Postharvest Biol. Technol.* 180:111588. doi: 10.1016/j.postharvbio.2021.111588

Zhao, Y., Chu, B., Fang, S., Zhao, J., Zhang, H., and Yu, K. (2020). Potential of vibrational spectroscopy for rapid and accurate determination of the hydrogen peroxide treatment of plant leaves. *Spectrochim. Acta Part A: Mol. Biomol. Spectrosc.* 230:118048. doi: 10.1016/j.saa.2020.118048

Conflict of Interest: The authors declare that the research was conducted in the absence of any commercial or financial relationships that could be construed as a potential conflict of interest.

Publisher's Note: All claims expressed in this article are solely those of the authors and do not necessarily represent those of their affiliated organizations, or those of the publisher, the editors and the reviewers. Any product that may be evaluated in this article, or claim that may be made by its manufacturer, is not guaranteed or endorsed by the publisher.

frontiers | Frontiers in Plant Science

ORIGINAL RESEARCH
published: 10 May 2022
doi: 10.3389/fpls.2022.849495

Rapid and Non-destructive Classification of New and Aged Maize Seeds Using Hyperspectral Image and Chemometric Methods

*Zheli Wang[1,2], Wenqian Huang[1], Xi Tian[1], Yuan Long[1], Lianjie Li[1] and Shuxiang Fan[1]**

[1] Intelligent Equipment Research Center, Beijing Academy of Agriculture and Forestry Sciences, Beijing, China, [2] College of Information and Electrical Engineering, China Agricultural University, Beijing, China

OPEN ACCESS

Edited by:
Yuzhen Lu,
Mississippi State University,
United States

Reviewed by:
Nuwan Wijewardane,
Mississippi State University,
United States
Akinbode A. Adedeji,
University of Kentucky, United States
Dongyi Wang,
University of Arkansas, United States
Tantan Jin,
Henan Academy of Agricultural Sciences (HNAAS), China

***Correspondence:**
Shuxiang Fan
fanshuxiang@outlook.com

Specialty section:
This article was submitted to Crop and Product Physiology, a section of the journal Frontiers in Plant Science

Received: *06 January 2022*
Accepted: *05 April 2022*
Published: *10 May 2022*

Citation:
Wang Z, Huang W, Tian X, Long Y, Li L and Fan S (2022) Rapid and Non-destructive Classification of New and Aged Maize Seeds Using Hyperspectral Image and Chemometric Methods. Front. Plant Sci. 13:849495. doi: 10.3389/fpls.2022.849495

The aged seeds have a significant influence on seed vigor and corn growth. Therefore, it is vital for the planting industry to identify aged seeds. In this study, hyperspectral reflectance imaging (1,000–2,000 nm) was employed for identifying aged maize seeds using seeds harvested in different years. The average spectra of the embryo side, endosperm side, and both sides were extracted. The support vector machine (SVM) algorithm was used to develop classification models based on full spectra to evaluate the potential of hyperspectral imaging for maize seed detection and using the principal component analysis (PCA) and ANOVA to reduce data dimensionality and extract feature wavelengths. The classification models achieved perfect performance using full spectra with an accuracy of 100% for the prediction set. The performance of models established with the first three principal components was similar to full spectrum models, but that of PCA loading models was worse. Compared to other spectra, the two-band ratio (1,987 nm/1,079 nm) selected by ANOVA from embryo-side spectra achieved a better classification accuracy of 95% for the prediction set. The image texture features, including histogram statistics (HS) and gray-level co-occurrence matrix (GLCM), were extracted from the two-band ratio image to establish fusion models. The results demonstrated that the two-band ratio selected from embryo-side spectra combined with image texture features achieved the classification of maize seeds harvested in different years with an accuracy of 97.5% for the prediction set. The overall results indicated that combining the two wavelengths with image texture features could detect aged maize seeds effectively. The proposed method was conducive to the development of multi-spectral detection equipment.

Keywords: maize seeds, hyperspectral imaging, ANOVA, classification, SVM - support vector machine

INTRODUCTION

Maize, regarded as a primary source of food, feeds, fuel, and industrial materials, is one of the most extensively cultivated cereal crops worldwide (Guo et al., 2017). Seed is the key to agriculture production. High-quality maize seeds will increase the yield and ensure consistency of plant growth. It will be conducive to using drones to spray pesticides, emasculation, and other

mechanized operations (Feng et al., 2019). Seed quality can be determined by its germinability or physicochemical attributes. Due to the storage time and storage method, the aged maize seeds greatly influence the germination rate and corn growth. New maize seeds show a high germination rate, and the seedlings will grow strong and healthy. On the contrary, the germination rate of aged maize seeds is low, and the seedlings tend to be thin and weak because their nutrition is lost with long storage time.

Generally, the freshness of maize seeds can be judged by manual observation. The aged maize seeds are stored in a dry environment and consume their nutrients during storage, due to which the surface of the seeds lose luster, but the new maize seeds will appear brighter and fresher. In addition, chemical principles can be used to identify whether the maize seeds are new or old. The maize seeds are soaked in the red ink solution for 15 min, and the embryo of the maize seed is stained for different periods of time for aged and new seeds. However, these methods are time consuming and require experienced operators, and farmers cannot master this skill well. These methods are also inapplicable for the online detection of a single seed. In order to meet the requirement of consumers, it is necessary to develop a rapid, accurate, and non-destructive method for classifying aged maize seeds for the maize seed industry.

Currently, machine vision and near-infrared (NIR) spectroscopy have been applied widely for the detection of seed quality, such as variety (Tu et al., 2021; Xu et al., 2021), vigor (Wang et al., 2020), and defect (Huang et al., 2019). Ali et al. (2021) applied a machine vision approach combined with a support vector machine (SVM) classifier to achieve the classification of maize seed varieties, and the obtained accuracy on six varieties was over 99%. Lin et al. (2018) used the NIR spectroscopy to identify the maize haploid seeds. The results indicated that the average accuracy of the back-propagation neural network (BPNN) classifier is 96.16%. However, machine vision employs only phenotypic characteristics, such as color, size, shape, and surface texture, but it is unsuitable for predicting the chemical composition of samples (Huang and Chien, 2017). Thus, machine vision is not suitable to detect maize seeds harvested in different years because the chemical composition, such as starch and protein, will be changed by storage time. NIR spectroscopy can be used to assess the chemical composition of samples, but it is only used to obtain spectral information by using a single spot and is always influenced by the uniformity of sample distribution (ElMasry et al., 2019). Single-seed detection equipment using NIR spectroscopy is usually specially designed according to the different shapes and sizes of samples. Therefore, NIR spectroscopy is not the best choice for developing a single-seed detection system.

Hyperspectral imaging, as a non-destructive and reliable technique, has been widely used in different fields. This technology combines the advantages of machine vision and NIR spectroscopy (Chen et al., 2021). It obtains both image and spectral information, and collects spectral information not only from a single point but also at each pixel of an image, thereby overcoming the limitations of machine vision and NIR spectroscopy technology (Gabrielli et al., 2021). In recent years, several studies have used hyperspectral imaging as a powerful tool for the classification and identification of seed quality (Zhang et al., 2020a; Zhou et al., 2020). Wakholi et al. (2018) used a shortwave infrared hyperspectral imaging system with a range of 1,000–2,500 nm to assess the viability of maize seeds, and the result indicated the SVM model obtained the highest classification of 100%. Cui et al. (2020) employed the hyperspectral imaging system to predict the root and seeding length of sweet corn seed for the assessment of germination. The results demonstrated that the kernel principal component regression (KPCR) combined with several feature wavelengths can predict the root and seeding length with a correlation coefficient of 0.7805 and 0.6074, respectively. Ma et al. (2020) demonstrated that NIR-HSI, combined with the CNN approach using PC images and SVM mapping, is an effective method for classifying the naturally aged Japanese mustard spinach seeds, with the seed viability classification accuracies for the training set and the test set of approximately 90% and 83%, respectively. In addition, hyperspectral imaging is also used to detect variety (Xia et al., 2019; Liu et al., 2022), frostbite, heat damage (Zhang et al., 2020b,c), and fungal infection (Alisaac et al., 2019).

Previous research has demonstrated the potential of hyperspectral imaging and provided good references in the field of seed quality detection. However, the detection models still need to be established with several feature wavelengths. In the development of detection equipment, the fewer the number of feature wavelengths used for the model establishment, the lower the difficulty and cost of development. For instance, Qiao et al. (2022) applied the partial least squares regression (PLSR) and successive projection algorithm (SPA) to detect the hardness of maize kernels. Although this method used only six feature wavelengths for modeling, it is still not easy to develop online detection equipment using these wavelengths because the multiband camera of six wavelengths should be designed. Hence, a more convenient method should be proposed to identify the aged maize seeds to reduce the cost of equipment development and improve detection efficiency. In addition, some studies demonstrated the potential of using image textures to detect the seed quality (Lurstwut and Pornpanomchai, 2017; Long et al., 2022). Thus, several image textures, including histogram statistics (HS) and gray-level co-occurrence matrix (GLCM) based on feature wavelength images, were extracted for modeling in this study. Therefore, it is necessary to establish data fusion models based on spectral and image texture features to improve accuracy.

The overall goal of this study was to examine the potential of hyperspectral imaging for the detection of aged maize seeds using samples harvested in different years. Specific objectives were to (1) establish classification models for maize seed detection based on full spectra; (2) identify and evaluate optimal feature wavelengths and two-band ratio for maize seed detection; (3) extract the image texture features based on feature images; and (4) develop a simple model based on using spectral and image texture features. The ultimate purpose was to develop a faster and more efficient multi-spectral method for real-time inspection of maize seeds harvested in different years.

MATERIALS AND METHODS

Sample Preparation

JINGKE 968 is one of the typical varieties of maize seeds in China. In this study, a total of 360 samples of this variety with uniform sizes and without apparent defects were utilized. The samples (120 maize seeds from each year) were harvested in three different years (2018, 2019, and 2020). All the seeds were provided by a seed company in Gansu Province, China. The germination percentages were 85.5, 87.6, and 98% for the maize seeds harvested in 2018, 2019, and 2020. A subset of 240 kernels was selected randomly as the calibration set for training models, and the remaining 120 single maize seeds were used as the prediction set for testing.

Hyperspectral Image Collection and Processing

Hyperspectral Image Collection and Calibration

A line-scan reflectance hyperspectral imaging system with a near-infrared range (930–2,548 nm) was employed to acquire images of maize seeds. The system comprises an imaging spectrograph (ImSpector N25E, Spectral Imaging Ltd., Oulu, Finland) with a spectral range of 930–2,548 nm and a 6.2–6.5 nm slit, 150 Watt (W) halogen lamp with two-line lighting fibers (3900-ER, Illumination Technologies, Inc., United States) providing uniform lighting conditions for samples in the field of view (FOV), a 14-bit NIR charge-coupled device (CCD) camera (Xeva-2.5-320, Xenics Ltd., Belgium) with the spatial resolution of 320 × 256 pixels, a control platform moving horizontally (EZHR17EN, AllMotion, Inc., United States) driven by a stepping motor, and a computer (Dell OPTIPLEX 990, Intel (R) Core (TM) i5-2400 CPU at 3.10 GHZ) with specialized software programs, such as spectral data acquisition software and platform control software (Isuzu Optics Corp., Taiwan). Before collecting the hypercube of maize seed, the time of exposure of the spectrograph, the speed of the platform, and the object distance should be confirmed to avoid image distortion. Thus, the final guaranteed exposure, speed, and distance parameters were 3 ms, 25 mm/s, and 365 mm, respectively. The system was placed in a metal box painted with black matte ink, thus reducing the influence of stray light from outside.

In order to enhance the collection efficiency, every 60 maize seeds from the same year were placed on a dark-background sampling plate for the collection of hyperspectral images. First, the embryo side of the seed faced the camera, and hyperspectral images of the embryo side were collected; then, the seeds were flipped one by one so that the images of the endosperm side of the seeds were acquired. Because of the low single-noise ratio at the edges of the spectral region of 930–2,548 nm caused by the lower CCD response efficiency, the spectra within 1,000–2,000 nm (159 bands) were employed for further analysis. The uneven intensity of the light source in different bands and the dark current in the CCD camera could lead to increased noise of some bands. Therefore, the raw hyperspectral images should be corrected with white and dark references. The white reference image was collected with a white Teflon board (99% reflection efficiency) (Spectralon SRT-99-100, Labsphere Inc., North Sutton, NH, United States). The dark reference image was obtained by turning off the light sources and covering the lens with a black cap (99% reflection efficiency), thus removing the dark current influence in the CCD camera. The corrected image (R_c) is calculated using the following equation:

$$R_c = \frac{R_{raw} - R_{dark}}{R_{white} - R_{dark}}$$

where R_c indicates the corrected hyperspectral image and R_{raw} means the original hyperspectral image. R_{white} and R_{dark} represent the white and dark reference images, respectively.

Spectral Data Extraction

The corrected image was used to extract the average spectra of the single maize seed. The background segmentation is the critical step for extracting multi-spectral images. First, the gray-scale image at 1,098 nm, which can show the highest contrast between seeds and background among all the band images, was selected to be the mask. Then, the background data can be removed by applying the mask image in all band images, and the data of regions of all single seeds were retained. The spectra of each pixel in the regions of a single seed were averaged, and finally, 360 averaged spectra were acquired for future analysis.

In order to compare the performance of different spectral types extracted from a single maize seed for modeling, the average reflectance spectra of embryo and endosperm sides were extracted, respectively. Then, the average spectra of both sides were calculated by averaging the spectra of the embryo and endosperm sides.

Principal Component Analysis

Principal component analysis (PCA) is the classical method to reduce dimensionality and select feature in hyperspectral data. PCA could synthesize and simplify the multiple data (Yang et al., 2018). In the premise of keeping the vital spectral information, it uses a few new variables to replace the original data to eliminate overlapping information coexisting in the vast information (Dong et al., 2017). After PCA with original spectra, every sample could obtain a few new variables called PCs (principal components) by the linear combination of the original spectra, indicating the similarity and otherness between different samples (Wu et al., 2016). Since each PC is the linear sum of original spectra at individual wavelengths multiplied by the corresponding waveband weight coefficient, the wavelengths corresponding to the peak and valley of the curve of weight coefficient represent the feature wavelengths (Huang et al., 2015). In this study, PCs and weight coefficients of PCs were used to analyze the average spectral data for dimensionality reduction and feature selection.

ANOVA for Two-Band Ratio

This study used a two-band ratio method to exploit a detection algorithm for a low-cost and real-time system. A one-way ANOVA test was employed to determine the optimal two-band ratio combination. The ANOVA is one of the most robust and frequently used statistical comparison methods to analyze the

differences between groups (Lee et al., 2017; Torres et al., 2019). It was utilized to select the optimal two-band combination for seed classification between different harvested years. The F-values of a one-way ANOVA were used to select feature wavelengths representing statistically significant differences for three groups. The two-band ratio with the highest *F*-values indicated that the differences between different groups are the most significant under this two-band ratio (Tian et al., 2021). The optimal threshold was determined based on the highest classification accuracy. The data in the calibration set was used to select the optimal two-band ratio and threshold for identifying single maize seed harvested in different years.

Image Texture Extraction From Optimal Two-Band Ratio Images

Image texture plays a critical role in contributing to the classification system. In this study, the optimal two-band ratio image selected by the ANOVA test based on F-value was applied to extract the information about the texture of the hidden image. Two representative types of statistical image texture features were extracted in this study. One was histogram statistics (HS) and the other was gray-level co-occurrence matrix (GLCM).

Histogram statistics is a frequently used method in image processing. In HS, the number of pixels at each different gray intensity value is calculated, which could reflect the statistical feature of gray intensity value in an image (Hu et al., 2012; Pu et al., 2015). The difference in HS of different images can be used as a basis for recognition. In this study, the statistical features of histograms, including mean intensity, mean consistency, skewness, kurtosis, mean contrast, and entropy, were employed as one of the texture features of images and denoted as $H_{intensity}$, $H_{consistency}$, $H_{skewness}$, $H_{kurtosis}$, $H_{contrast}$, and $H_{entropy}$, respectively. The above-mentioned parameters can be calculated as follows:

Mean intensity

$$H_{intensity} = \sum_{i=0}^{L-1} z_i p(z_i)$$

Mean consistency

$$H_{consistency} = \sum_{i=0}^{L-1} p^2(z_i)$$

Skewness

$$H_{skewness} = \frac{1}{H_{contrast}^3} \sum_{i=0}^{L-1} (z_i - H_{intensity})^3 p(z_i)$$

Kurtosis

$$H_{kurtosis} = \frac{1}{H_{contrast}^4} \sum_{i=0}^{L-1} (z_i - H_{intensity})^4 p(z_i)$$

Mean contrast

$$H_{contrast} = \sqrt{\sum_{i=0}^{L-1} (z_i - H_{intensity})^2 p(z_i)}$$

Entropy

$$H_{entropy} = \sum_{i=0}^{L-1} p(z_i) \log_2 p(z_i)$$

where z_i is the random variable of gray level i and L is the largest gray level in images. The term $p(z_i)$ represents the probability of z_i in an image.

The gray-level co-occurrence matrix is a classical statistical texture analysis tool in which image texture features can be extracted by means of statistical approaches from the co-occurrence matrix (Khodabakhshian and Emadi, 2018; Ren et al., 2021). The GLCM measures the probability that a pixel of a particular gray level occurs at a specified direction and a distance from its neighboring pixels. In this study, image texture features were calculated from the gray co-occurrence matrix with 0 angles, and the distance between pixels was 1 pixel. Four image texture features, including contrast, correlation, energy, and homogeneity, were extracted for future research studies and denoted as $G_{contrast}$, $G_{correlation}$, G_{energy}, and $G_{homogeneity}$, respectively.

Contrast

$$G_{contrast} = \sum_{i=0}^{X} \sum_{i=0}^{Y} |i-j|^2 p(i,j)$$

Correlation

$$G_{correlation} = \sum_{i=0}^{X} \sum_{j=0}^{Y} \frac{(i - \mu_i i)(j - \mu_j j) p(i,j)}{\sigma_i \sigma_j}$$

Energy

$$G_{energy} = \sum_{i=0}^{X} \sum_{j=0}^{Y} p(i,j)^2$$

Homogeneity

$$G_{homogeneity} = \sum_{i=0}^{X} \sum_{i=0}^{Y} \frac{p(i,j)}{1 + |i-j|}$$

$$\mu_i = \sum_{i=0}^{X} i \sum_{j=0}^{Y} p(i,j)$$

$$\mu_j = \sum_{j=0}^{X} j \sum_{i=0}^{Y} p(i,j)$$

$$\sigma_i = \sqrt{\sum_{i=0}^{X} (i - \mu_i)^2 \sum_{j=0}^{Y} p(i,j)}$$

$$\sigma_j = \sqrt{\sum_{j=0}^{Y} (j - \mu_j)^2 \sum_{i=0}^{X} p(i,j)}$$

where X is the column number of GLCM, Y is the row number of GLCM, and $p\ (i, j)$ is the gray-level co-occurrence matrix.

Supervised Classification Method

The classification of the hyperspectral image can be divided into two main categories. One is the spectral-based classification, where the mean spectra derived by averaging reflectance or transmittance values of all pixels at different wavelengths could be regarded as spectral features (Shrestha et al., 2016). The other one is image-based classification, and it could employ the image texture features for the quality assessment of agriculture products (He et al., 2021). In this study, both spectral features and image texture features were used for the three-class classification. The widely used supervised classification algorithm, support vector machine (SVM), was employed for distinguishing the single maize seed harvested in different years. SVM can deal with linear and nonlinear problems by enabling an implicit mapping to transform inseparable linear data into a linear separable space (Gopinath et al., 2020; Li et al., 2021). The kernel function and parameters of SVM play an essential role in modeling. In this study, the radial basis function (RBF), the most commonly used kernel, was used as the kernel function of SVM. The penalty parameters (c) and kernel function parameters (g) were optimized by a grid search procedure in the range of 2^{-10}–2^{10} through five-fold cross-validation.

Software Tools

MATLAB R2016b (The math-Works, Natick, MA, United States) was used to extract the average spectra, select the spectral and image features, and establish classification models. Origin 2018 (Origin Lab Corporation, Northampton, MA, United States) was applied to construct the graphs. The Win 10 64-bit operating system, with Inter (R) Core (TM) i5-8300H CPU, 2.30 GHz, and 8G RAM as the software platform, carried out all software operations.

RESULTS AND DISCUSSION

Spectra Analysis

The raw average reflectance spectra with standard deviation (SD) of maize seeds harvested in three different years are shown in **Figure 1**. **Figures 1A–C** represent the spectra of the embryo, endosperm, and both sides, respectively. A similar trend is observed for different curves, but some differences still exist. The obvious peak and valley appeared at around 1,110 nm, 1,200 nm, 1,300 nm, and 1,467 nm. The peak and valley around 1,110 nm and 1,200 nm are caused by the second overtone of C–H stretching vibrations of carbohydrates (Marques et al., 2016; Alhamdan and Atia, 2018). The peak at around 1,300 nm mainly results from the combination of the first overtone of Amide B and the fundamental amid vibrations (Wu et al., 2019). The valley at around 1,467 nm is connected with the stretching vibration of the first overtone of the N–H contained in protein (Zhao et al., 2018). As shown in **Figure 1**, the overlap of embryo-side spectra of different year seeds is the lowest, followed by the spectra of both sides and the endosperm side. Complex changes might have occurred in maize seeds stored for different time periods, which is further reflected by the average spectra of seeds obtained from different years. It can be seen in **Figures 1A,C** that the spectra reflectance increases with the storage time of maize seeds. However, the spectral curves of maize seeds harvested in different

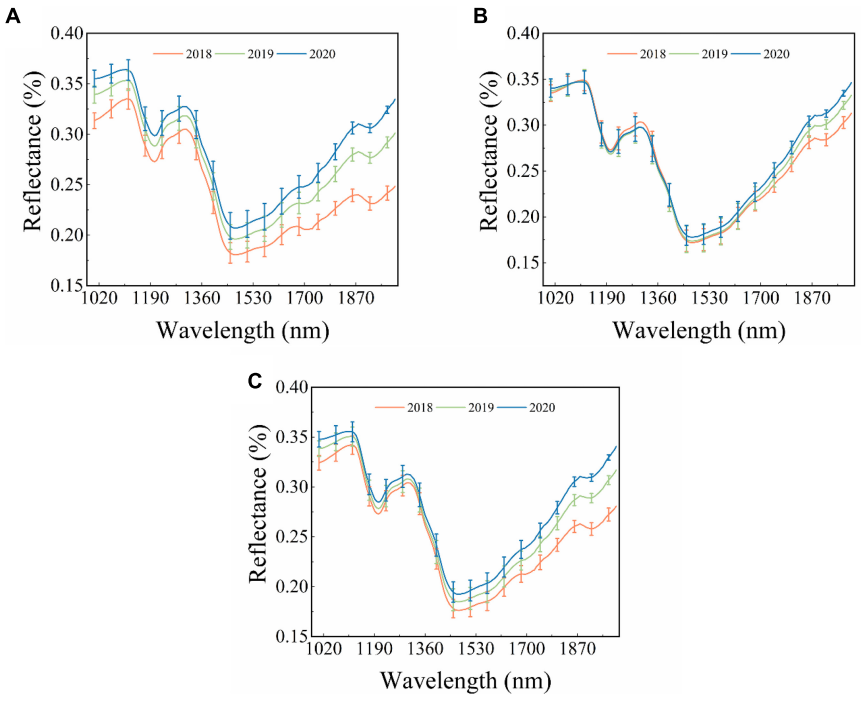

FIGURE 1 | The original reflectance spectra of different sides of single maize seed. **(A)** Embryo side, **(B)** endosperm side, and **(C)** both sides.

TABLE 1 | The classification results based on original spectra using SVM algorithm.

Spectral type	Parameters	Classification accuracy	
		Calibration set	Prediction set
Embryo side	c 0.5 g 4	100	100
Endosperm side	c 128 g 8	100	100
Both sides	c 0.25 g 64	100	100

Abbreviations: PCs: principal components. c: the penalty coefficient. g: the kernel function parameter.

TABLE 2 | The results of feature wavelength selection from different spectral types based on loading of PC3.

Spectral type	Feature wavelengths
Embryo side	1111 nm 1198 nm 1310 nm 1151 nm
Endosperm side	1104 nm 1197 nm 1304 nm 1518 nm
Both sides	1111 nm 1198 nm 1310 nm 1151 nm

years overlap sufficiently in **Figure 1B**, but they start to separate after around 1,400 nm. All these findings lay the foundation for the theoretical basis of the classification of the maize seeds of different years using spectral data. However, the classification of the maize seeds harvested from different years based on the difference in spectral curves is unreliable owing to the overlap problem. Thus, it is necessary to establish classification models to effectively extract and use features in hyperspectral images to classify new and aged maize seeds.

Classification Results Based on Full Spectra

The classification of harvested years was performed using SVM models based on the three types of spectra (embryo side, endosperm side, and both sides) acquired in the wavelength range of 1,000–2,000 nm. **Table 1** presents the performance of classification models built with different types of spectra. It can be seen clearly in the table that all the spectra achieved the perfect classification performance. The classification accuracy of the calibration and prediction set was 100%, respectively. This might be caused by the significant difference in the spectra of maize seeds harvested in different years after around 1,400 nm. These results demonstrated that hyperspectral imaging technology could classify new and aged maize seeds. However, the full spectrum models are unsuitable for developing online detection instruments due to the vast and high-dimensional data. Hence, selecting the optimal feature information from hyperspectral images is necessary to simplify the models for future study.

Feature Selection and Classification Results Based on Principal Component Analysis

In this study, PCA was used as one of the data dimension reduction methods for raw spectra. In the process of PCA, a few numbers of PCs could be used to replace the full spectra, or the loading of PCs can be applied to select feature wavelengths (Dong et al., 2017; He et al., 2019). The PCA results of the endosperm-side and both-side spectra are similar to that of the embryo-side spectra. **Figure 2** only shows the PCA results of embryo-side original reflectance spectra. It is clear from **Figure 2A** that the first three PCs explained the most of the variance in this situation (PC1 = 88.4%, PC2 = 9.2%, and PC3 = 1.9%). It can also be seen that there was a lot of overlap among sample points in the projections of the scatter plot in different directions, and a better classification can be obtained when the PC1, PC2, and PC3 work together. Thus, the first three PCs were applied to replace full spectra to build identification models.

The loading plots of the first three PCs are shown in **Figure 2B**. The peaks and valleys offer the dominant wavelengths. The loading plot of PC1 is flat, meaning the feature wavelengths could not be obtained from that of PC1. The loading plot of

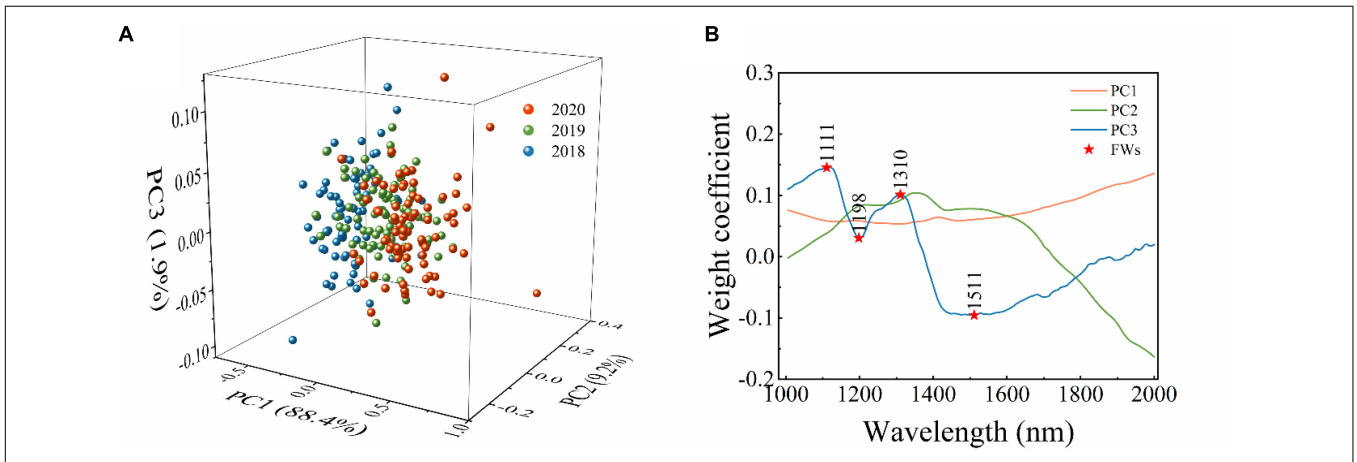

FIGURE 2 | The results of PCA analysis of embryo-side original reflectance spectra. **(A)** Scatter plot of first three principal components, and **(B)** loading plots for the first three principal components. Abbreviations: PC1: the first principal component. PC2: the second principal component. PC3: the third principal component. FWs: the feature wavelengths.

TABLE 3 | The classification results based on the first three PCs and the loading of PC3 using SVM algorithm.

Spectral type	Model	Parameters	Classification accuracy (%)	
			Calibration set	Prediction set
Embryo side	PCs	c 0.5 g 4	100	100
	Loading	c 1024 g 4	85.83	85.83
Endosperm side	PCs	c 512 g 0.5	99.17	99.17
	Loading	c 16 g 64	68.75	71.67
Both sides	PCs	c 0.5 g 16	100	100
	Loading	c 512 g 4	72.50	80.83

Abbreviations: PCs: principal components. c: the penalty coefficient. g: the kernel function parameter.

The above-mentioned results indicated that SVM combined with the first three PCs based on the embryo-side and both-side spectra could establish perfect classifiers to classify maize seeds harvested in different years. However, PCs are a linear combination of the full spectra. In terms of rapid detection equipment development, this method still needs to extract the full spectra to establish a classification model, which cannot effectively reduce the development cost and model complexity. Therefore, it is necessary to find a more effective data dimension reduction method for further study.

PC2 fluctuates gently, and the positions of peaks and valleys which have a value not equal to zero are similar to that of PC3. It can be seen clearly that the loading plot of PC3 fluctuates sharply, and the peaks and valleys can be observed at 1,111, 1,198, 1,310, and 1,511 nm. Thus, from the loading plot of PC3, these wavelengths (corresponding to peaks and valleys) were selected as feature wavelengths related to C–H, O–H, and N–H, respectively. The feature wavelengths selected from different spectral types based on the loading plot of PC3 are summarized in **Table 2**.

The first three PCs (PC model) and feature wavelengths selected from the loading of PC3 (loading model) were employed to build SVM classification models instead of full spectra, respectively. The performance of developed SVM models is presented in **Table 3**, indicating that the PC models performed better than the loading models. All PC models achieved perfect performance. The results indicated that PCA is an effective method for data dimension reduction, and the first three PCs could explain the most information and replace full spectra for identification in this study. The performance of loading models decreased sharply compared to the PC models, with a classification accuracy of prediction set of 85.83%, 71.67%, and 80.83%, respectively. The results indicated that the feature wavelengths selected from the loading of PC3 could be used to identify the maize seeds harvested in different years, but other critical wavelengths in spectra were ignored. It is interesting to observe that the peaks and valleys of the loading curve of PC3 are similar to the original spectra. The original spectra began to separate significantly after 1,400 nm (**Figure 1**). However, the feature wavelengths selected by the loading curve of PC3 only included one wavelength in the spectral range of 1,400–2,000 nm,

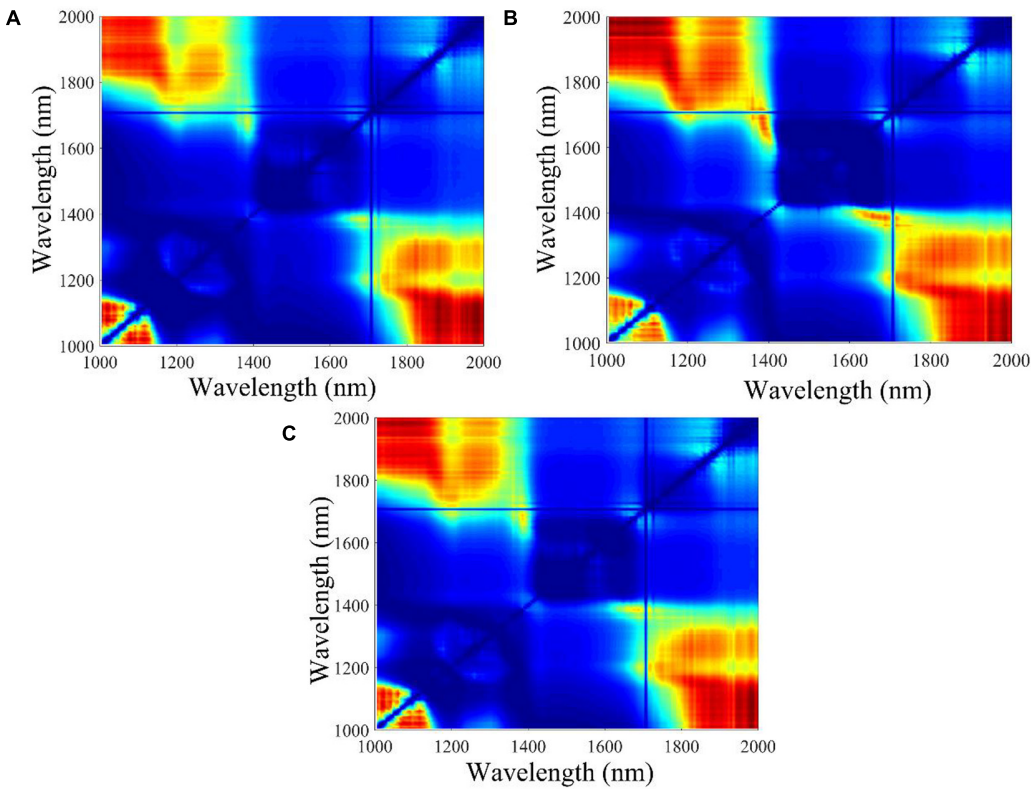

FIGURE 3 | The contour plots of F-value calculated from different waveband ratio combinations. The color change from blue to red represents the F-value increases from low to high. **(A)** Embryo side, **(B)** endosperm side, and **(C)** both sides.

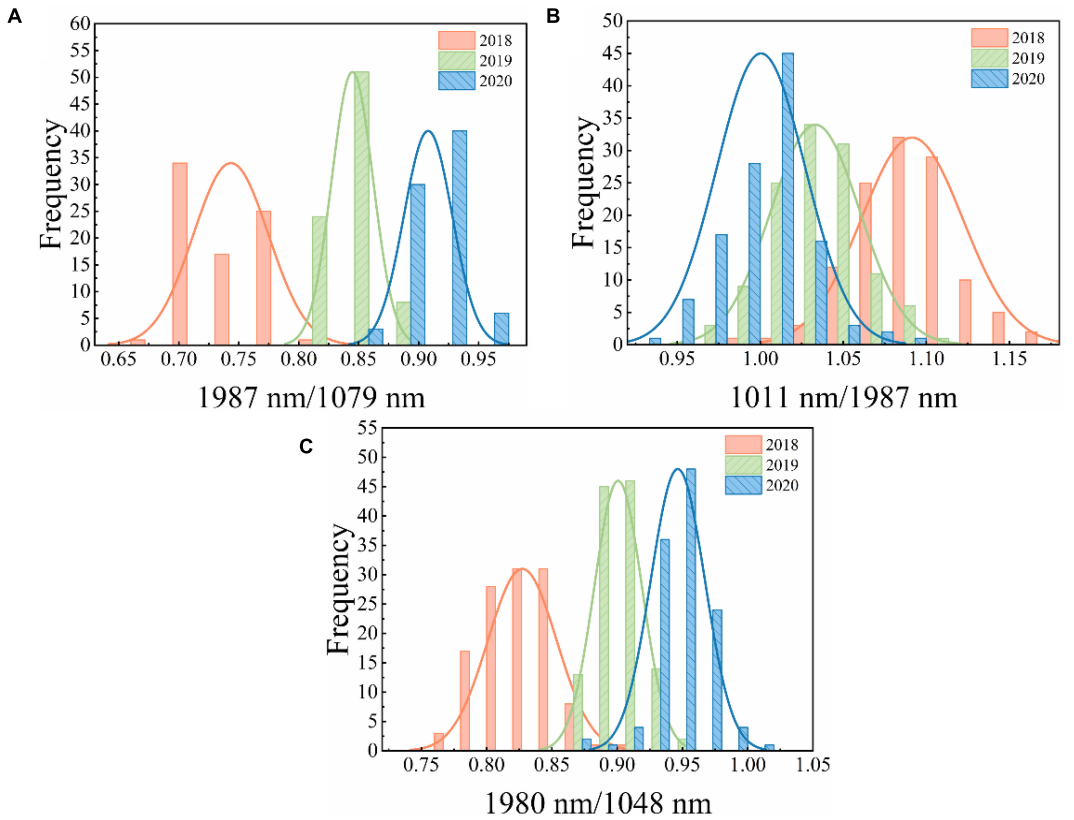

FIGURE 4 | The distribution of two-band ratio for different samples. **(A)** Embryo side, **(B)** endosperm side, and **(C)** both sides.

TABLE 4 | The classification results using threshold values based on the two-band ratio values.

Spectral type	Two-band ratio	Threshold	Classification accuracy (%)	
			Calibration set	Prediction set
Embryo side	1987 nm/1079 nm	t1 0.8046 t2 0.8784	95.83	95.00
Endosperm side	1011 nm/1987 nm	t1 1.0140 t2 1.0550	76.67	72.50
Both sides	1980 nm/1048 nm	t1 0.8631 t2 0.9174	91.67	89.17

Abbreviations: t1: the first threshold value; t2: the second threshold value.
Compared to the classification results obtained by PCA-SVM models, the number of wavelengths selected by ANOVA was significantly lower. The result provides a more efficient and cost-effective solution for the development of a maize seed classification approach based on hyperspectral imaging technology. However, a two-band ratio alone may not provide sufficient information, and it is necessary to explore more features to improve the classification accuracy.

which could explain why the performance of the loading model was not as good as expected.

Optimal Two-Band Ratio Selection From ANOVA

The F-values of ANOVA for all the two-band ratios of three classes were calculated, and the contour plots of F-values are shown in **Figure 3**. The ratio of 1,987 nm/1,079 nm, 1,011 nm/1,987 nm, and 1,980 nm/1,048 nm obtained the largest F-values in embryo-side, endosperm-side, and both-side spectra, respectively. The results indicated that three sets of samples at these band ratios demonstrated the most difference. It can be seen clearly that the wavelengths selected based on *F*-value are different from feature wavelengths selected from the loading curve of PC3. Obviously, the wavelengths selected by the two-band ratio were distributed around the beginning or end of the spectral range, and the spectra of maize seeds harvested in different years showed apparent differences in that range.

Classification Results Based on ANOVA

Classification Results Based on Optimal Two-Band Ratio Value

Figure 4 shows the distribution of two-band ratios for new and aged seeds. The overlap among the three classes could result in misclassification between different classes. Thus, a proper threshold value is required for discrimination.

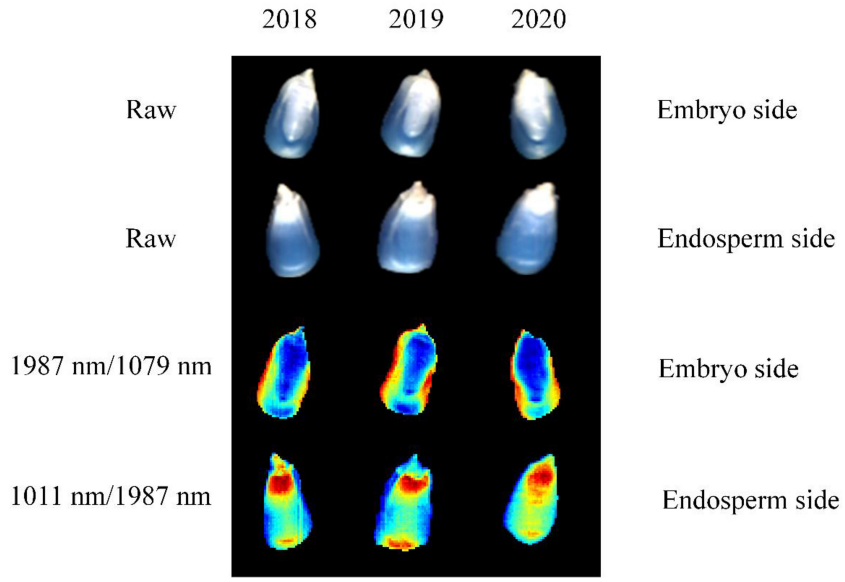

FIGURE 5 | Comparison of the images obtained by using the hyperspectral image.

TABLE 5 | The classification results based on various feature variables using SVM algorithm.

Spectral type	Two-band ratio	Model	Variable number	Classification accuracy (%)	
				Calibration set	Prediction set
Embryo side	1987 nm/1079 nm	Two-band ratio	1	96.67	95
		Image textures	10	65	59.17
		Data fusion	11	98.75	97.5
Endosperm side	1011 nm/1987 nm	Two-band ratio	1	75.83	73.33
		Image textures	10	58.33	44.17
		Data fusion	11	79.17	80

The above-mentioned results showed that the proposed method can be used to classify the maize seeds harvested in different years. However, only the new and aged seeds need to be identified for general production requirements. Therefore, the maize seeds harvested in 2020 were defined as new seeds, and the remaining were classified as aged seeds. Then, the classification model was built according to the proposed method. This model showed better performance with an accuracy of 99.17% in the prediction set. It is also clear from ***Figure 6B*** *that only one seed was misclassified. In brief, the SVM model combined with the two-band ratio and image textures extracted from the two-band ratio image of 1,987 nm/1,079 nm showed excellent performance for classifying new and aged maize seeds. It also demonstrated that ANOVA, HS, and GLCM algorithms were suitable for selecting the feature variables.*

The threshold values can be easily calculated based on the two-band ratios. **Table 4** shows the classification results using threshold values based on the two-band ratio values. The two-band ratio method based on embryo-side spectra (the first threshold value (t1) = 0.8046 and the second threshold value (t2) = 0.8784) obtained the best classification performance with the classification accuracy of 95.00%. The classification accuracy based on both-side spectra (t1 = 0.8631 and t2 = 0.9174) was less than that obtained by embryo-side spectra with 89.17% for prediction set. Due to the considerable overlap in the band ratio distribution among the three classes for the endosperm-side spectra, the two-band ratio based on endosperm-side spectra had a huge error in classifying the seeds of different harvest years.

Classification Results Based on Multiple Features

The advantage of hyperspectral imaging technology is that it combines both image features and spectral information. Thus, the band ratio images can be obtained according to the optimal two-band ratio selected by the largest *F*-values. **Figure 5** shows the color images of the maize seeds harvested in different years. It is clear from the figure that the maize seeds cannot be distinguished visually by using band ratio images of embryo and endosperm sides. Thus, 10 image textures, including mean intensity, mean consistency, skewness, kurtosis, mean contrast, entropy, contrast, correlation, energy, and homogeneity, were selected and extracted from band ratio images for seed identification. In order to standardize the image texture data, standard normalization was employed for each image texture.

In order to explore the robustness and reliability of prediction models, two-band ratio and information about image textures and their combination (two-band ratio and image textures were concatenated to create a single matrix) were used to establish SVM classification models, respectively. **Table 5** shows the classification results based on various feature variables by using

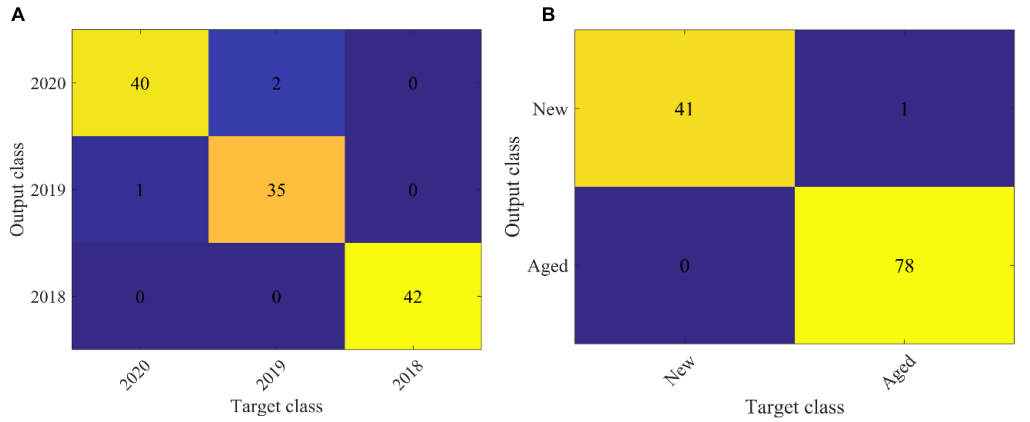

FIGURE 6 | The confusion matrix of the data fusion model based on embryo side spectra. **(A)** is the classification results of maize seed harvested in 2018, 2019 and 2020. **(B)** is the classification results of new (2020) and aged (2018 and 2019) maize seed.

the SVM algorithm. As for embryo-side spectra, the band ratio model obtained 95% classification accuracy for the prediction set, while the image texture model only yielded the classification accuracy of 59.17% for the prediction set. The fusion of band ratio and image features enhanced the model performance with 98.75% and 97.5% accuracy for calibration and prediction set, respectively. **Figure 6A** shows the confusion matrix of the data fusion model based on embryo-side spectra. In terms of the endosperm side, the image texture model obtained poor performance with the lowest classification accuracy of 44.17%. The performance of the band ratio model was a bit better than the image texture model with an accuracy of 73.33%. The data fusion model also obtained the best classification result with an accuracy of 80%, which also proved that the combined features improved the classification ability. However, it can be seen clearly that models built with embryo-side spectra presented better calibration and prediction accuracy than endosperm-side spectra, irrespective of the feature used to establish the identification model. The reason may be that the embryo side contains both embryo and endosperm structures, which could be used to extract more useful information. In addition, it also can be illustrated from the table that band ratio data provided more useful information than image texture data, and the band ratio had a higher contribution than the image texture in building SVM models. In particular, fusion information was more effective than the single feature for establishing SVM models, thus providing a more comprehensive understanding of the changes in components and textures and enhancing the model accuracy and reliability. The above results showed that the proposed method can be used to classify the maize seeds which were harvested in different years. However, only the new and aged seeds need to be identified for general production requirements. Therefore, the maize seeds harvested in 2020 were defined as new seeds, and the rest were aged seeds. Then, the classification model was built according to the proposed method. This model showed better performance with an accuracy of 99.17% in the prediction set. It is also clear from **Figure 6B** that only one seed was misclassified. In brief, the SVM model combined with the two-band ratio and image textures extracted from two-band ratio image of 1987 nm/1079 nm showed excellent performance for classifying new and aged maize seeds. It also demonstrated that ANOVA, HS, and GLCM algorithms were suitable for selecting the feature variables.

CONCLUSION

This study successfully applied a hyperspectral reflectance imaging system with the spectral range of 1,000–2,000 nm for rapid and non-destructive classification of maize seeds harvested in different years. In consideration of the issues caused by the discrepancies between the different sides of the maize seeds, the spectra of the different sides were analyzed. SVM algorithm was adopted for establishing classification models for maize seeds. PCA and ANOVA were used for the selection of feature variables to reduce redundant data and identify important information. The image texture features, including HS and GLCM, were applied to extract 10 texture features from two-band ratio images for data fusion. The results indicated that ANOVA was more suitable for data dimension reduction, where only two wavelengths were selected for modeling. Compared with the models using the single feature, the two-band ratio of 1,987 nm/1,079 nm combined with image texture features obtained the best classification accuracy with 97.5% for the prediction set. The results indicated that data fusion models were more advantageous than single feature models in maize seed classification. Moreover, the proposed two-band ratio (1,987 nm/1,079 nm) from the embryo side of maize seed has excellent potential for maize seed classification, which could be used to develop an imaging system for quality detection in the packing line. Further studies should be carried out to improve the classification capabilities of this technique at an industrial scale so that this proposed method can be used in the online evaluation of maize seed qualities.

DATA AVAILABILITY STATEMENT

The original contributions presented in the study are included in the article/supplementary material, further inquiries can be directed to the corresponding author.

AUTHOR CONTRIBUTIONS

ZW: data curation, writing-original draft, and methodology. WH: investigation and supervision. XT: resources. YL: validation. LL: hardware. SF: supervision, writing-review, and funding acquisition. All authors contributed to the article and approved the submitted version.

FUNDING

This work was supported by the financial support provided by the National Natural Science Foundation of China (31801262 and 31871523), Young Elite Scientists Sponsorship Program by CAST (2019QNRC001), Beijing Training Program Foundation for the Talents (2018000020060G184), and the National Engineering Laboratory for Agri-product Quality Traceability (PT2021-32).

REFERENCES

Alhamdan, A. M., and Atia, A. (2018). Non-destructive method to predict Barhi dates quality at different stages of maturity utilising near-infrared (NIR) spectroscopy. *Int. J. Food Prop.* 20, S2950–S2959. doi: 10.1080/10942912.2017.1387794

Ali, A., Mashwani, W. K., Tahir, M. H., Belhaouari, S. B., Alrabaiah, H., Naeem, S., et al. (2021). Statistical features analysis and discrimination of maize seeds utilizing machine vision approach. *J. Intell. Fuzzy Syst.* 40, 703–714. doi: 10.3233/jifs-200635

Alisaac, E., Behmann, J., Rathgeb, A., Karlovsky, P., Dehne, H. W., and Mahlein, A. K. (2019). Assessment of *Fusarium* infection and mycotoxin contamination of wheat kernels and flour using hyperspectral imaging. *Toxins* 11:18. doi: 10.3390/toxins11100556

Chen, Y., Xu, Z., Tang, W., Hu, M., and Li, Q. (2021). Identification of various food residuals on denim based on hyperspectral imaging system and combination optimal strategy. *Artif. Intell. Agric.* 5, 125–132. doi: 10.1016/j.aiia.2021.06.001

Cui, H., Cheng, Z., Li, P., and Miao, A. (2020). Prediction of sweet corn seed germination based on hyperspectral image technology and multivariate data regression. *Sensors* 20:4744. doi: 10.3390/s20174744

Dong, G., Guo, J., Wang, C., Liang, K., Lu, L., Wang, J., et al. (2017). Differentiation of storage time of wheat seed based on near infrared hyperspectral imaging. *Int. J. Agric. Biol. Eng.* 10, 251–258. doi: 10.3965/j.ijabe.20171002.1619

ElMasry, G., Mandour, N., Al-Rejaie, S., Belin, E., and Rousseau, D. (2019). Recent applications of multispectral imaging in seed phenotyping and quality monitoringan overview. *Sensors* 19:32. doi: 10.3390/s19051090

Feng, L., Zhu, S., Liu, F., He, Y., Bao, Y., and Zhang, C. (2019). Hyperspectral imaging for seed quality and safety inspection: a review. *Plant Methods* 15:91. doi: 10.1186/s13007-019-0476-y

Gabrielli, M., Lancon-Verdier, V., Picouet, P., and Maury, C. (2021). Hyperspectral imaging to characterize table grapes. *Chemosensors* 9:21. doi: 10.3390/chemosensors9040071

Gopinath, G., Sasidharan, N., and Surendran, U. (2020). Landuse classification of hyperspectral data by spectral angle mapper and support vector machine in humid tropical region of India. *Earth Sci. Inf.* 13, 633–640. doi: 10.1007/s12145-019-00438-4

Guo, D., Zhu, Q., Huang, M., Guo, Y., and Qin, J. (2017). Model updating for the classification of different varieties of maize seeds from different years by hyperspectral imaging coupled with a pre-labeling method. *Comp. Electron. Agric.* 142, 1–8. doi: 10.1016/j.compag.2017.08.015

He, X., Feng, X., Sun, D., Liu, F., Bao, Y., and He, Y. (2019). Rapid and non-destructive measurement of rice seed vitality of different years using near-infrared hyperspectral imaging. *Molecules* 24:2227. doi: 10.3390/molecules24122227

He, X. M., Yan, C., Jiang, X. S., Shen, F., You, J., and Fang, Y. (2021). Classification of aflatoxin B-1 naturally contaminated peanut using visible and near-infrared hyperspectral imaging by integrating spectral and texture features. *Infrared Phys. Technol.* 114:7. doi: 10.1016/j.infrared.2021.103652

Hu, J., Li, D., Duan, Q., Han, Y., Chen, G., and Si, X. (2012). Fish species classification by color, texture and multi-class support vector machine using computer vision. *Comp. Electron. Agric.* 88, 133–140. doi: 10.1016/j.compag.2012.07.008

Huang, K. Y., and Chien, M. C. (2017). A novel method of identifying paddy seed varieties. *Sensors* 17:8. doi: 10.3390/s17040809

Huang, S., Fan, X., Sun, L., Shen, Y., and Suo, X. (2019). Research on classification method of maize seed defect based on machine vision. *J. Sensors* 2019:9. doi: 10.1155/2019/2716975

Huang, W., Li, J., Wang, Q., and Chen, L. (2015). Development of a multi-spectral imaging system for online detection of bruises on apples. *J. Food Eng.* 146, 62–71. doi: 10.1016/j.jfoodeng.2014.09.002

Khodabakhshian, R., and Emadi, B. (2018). Application of Vis/SNIR hyperspectral imaging in ripeness classification of pear. *Int. J. Food Prop.* 20, S3149–S3163. doi: 10.1080/10942912.2017.1354022

Lee, H., Kim, M. S., Qin, J., Park, E., Song, Y. R., Oh, C. S., et al. (2017). Raman hyperspectral imaging for detection of watermelon seeds infected with *Acidovorax citrulli*. *Sensors (Basel)* 17:2188. doi: 10.3390/s17102188

Li, L. Q., Li, M. H., Liu, Y., Cui, Q. Q., Bi, K. Y., Jin, S. S., et al. (2021). High-sensitivity hyperspectral coupled self-assembled nanoporphyrin sensor for monitoring black tea fermentation. *Sensors Actuat. B Chem.* 346:10. doi: 10.1016/j.snb.2021.130541

Lin, J. C., Yu, L. N., Li, W. J., and Qin, H. (2018). Method for identifying maize haploid seeds by applying diffuse transmission near-infrared spectroscopy. *Appl. Spectrosc.* 72, 611–617. doi: 10.1177/0003702817742790

Liu, Q., Wang, Z., Long, Y., Zhang, C., Fan, S., and Huang, W. (2022). Variety classification of coated maize seeds based on Raman hyperspectral imaging. *Spectrochim. Acta Part A Mol. Biomol. Spectrosc.* 270:120772. doi: 10.1016/j.saa.2021.120772

Long, Y., Huang, W., Wang, Q., Fan, S., and Tian, X. (2022).). Integration of textural and spectral features of Raman hyperspectral imaging for quantitative determination of a single maize kernel mildew coupled with chemometrics. *Food Chem.* 372:131246. doi: 10.1016/j.foodchem.2021.131246

Lurstwut, B., and Pornpanomchai, C. (2017). Image analysis based on color, shape and texture for rice seed (*Oryza sativa* L.) germination evaluation. *Agric. Nat. Resourc.* 51, 383–389. doi: 10.1016/j.anres.2017.12.002

Ma, T., Tsuchikawa, S., and Inagaki, T. (2020). Rapid and non-destructive seed viability prediction using near-infrared hyperspectral imaging coupled with a deep learning approach. *Comp. Electron. Agric.* 177:105683. doi: 10.1016/j.compag.2020.105683

Marques, A. S., Castro, J. N. F., Costa, F. J., Neto, R. M., and Lima, K. M. G. (2016). Near-infrared spectroscopy and variable selection techniques to discriminate *Pseudomonas aeruginosa* strains in clinical samples. *Microchem. J.* 124, 306–310. doi: 10.1016/j.microc.2015.09.006

Pu, H., Sun, D.-W., Ma, J., and Cheng, J.-H. (2015). Classification of fresh and frozen-thawed pork muscles using visible and near infrared hyperspectral imaging and textural analysis. *Meat Sci.* 99, 81–88. doi: 10.1016/j.meatsci.2014.09.001

Qiao, M. M., Xu, Y., Xia, G. Y., Su, Y., Lu, B., Gao, X. J., et al. (2022). Determination of hardness for maize kernels based on hyperspectral imaging. *Food Chem.* 366:8. doi: 10.1016/j.foodchem.2021.130559

Ren, G. X., Wang, Y. J., Ning, J. M., and Zhang, Z. Z. (2021). Evaluation of Dianhongblack tea quality using near-infrared hyperspectral imaging technology. *J. Sci. Food Agric.* 101, 2135–2142. doi: 10.1002/jsfa.10836

Shrestha, S., Knapic, M., Zibrat, U., Deleuran, L. C., and Gislum, R. (2016). Single seed near-infrared hyperspectral imaging in determining tomato (*Solanum*

lycopersicum L.) seed quality in association with multivariate data analysis. *Sensors Actuat. B Chem.* 237, 1027–1034. doi: 10.1016/j.snb.2016.08.170

Tian, X., Zhang, C., Li, J., Fan, S., Yang, Y., and Huang, W. (2021). Detection of early decay on citrus using LW-NIR hyperspectral reflectance imaging coupled with two-band ratio and improved watershed segmentation algorithm. *Food Chem.* 360:130077. doi: 10.1016/j.foodchem.2021.130077

Torres, I., Sánchez, M.-T., Cho, B.-K., Garrido-Varo, A., and Pérez-Marín, D. (2019). Setting up a methodology to distinguish between green oranges and leaves using hyperspectral imaging. *Comp. Electron. Agric.* 167:105070. doi: 10.1016/j.compag.2019.105070

Tu, K. L., Wen, S. Z., Cheng, Y., Zhang, T. T., Pan, T., Wang, J., et al. (2021). A non-destructive and highly efficient model for detecting the genuineness of maize variety 'JINGKE 968 ' using machine vision combined with deep learning. *Comp. Electron. Agric.* 182:10. doi: 10.1016/j.compag.2021.106002

Wakholi, C., Kandpal, L. M., Lee, H., Bae, H., Park, E., Kim, M. S., et al. (2018). Rapid assessment of corn seed viability using short wave infrared line-scan hyperspectral imaging and chemometrics. *Sensors Actuat. B Chem.* 255, 498–507. doi: 10.1016/j.snb.2017.08.036

Wang, Y. L., Peng, Y. K., Zhuang, Q. B., and Zhao, X. L. (2020). Feasibility analysis of NIR for detecting sweet corn seeds vigor. *J. Cereal Sci.* 93:7. doi: 10.1016/j.jcs.2020.102977

Wu, N., Zhang, Y., Na, R., Mi, C., Zhu, S., He, Y., et al. (2019). Variety identification of oat seeds using hyperspectral imaging: investigating the representation ability of deep convolutional neural network. *RSC Adv.* 9, 12635–12644. doi: 10.1039/c8ra10335f

Wu, X., Song, X., Qiu, Z., and He, Y. (2016). Mapping of TBARS distribution in frozen–thawed pork using NIR hyperspectral imaging. *Meat Sci.* 113, 92–96. doi: 10.1016/j.meatsci.2015.11.008

Xia, C., Yang, S., Huang, M., Zhu, Q., Guo, Y., and Qin, J. (2019). Maize seed classification using hyperspectral image coupled with multi-linear discriminant analysis. *Infrared Phys. Technol.* 103:103077. doi: 10.1016/j.infrared.2019.103077

Xu, P., Yang, R. B., Zeng, T. W., Zhang, J., Zhang, Y. P., and Tan, Q. (2021). Varietal classification of maize seeds using computer vision and machine learning techniques. *J. Food Process Eng.* 44:e13846. doi: 10.1111/jfpe.13846

Yang, Y., Zhuang, H., Yoon, S.-C., Wang, W., Jiang, H., and Jia, B. (2018). Rapid classification of intact chicken breast fillets by predicting principal component score of quality traits with visible/near-infrared spectroscopy. *Food Chem.* 244, 184–189. doi: 10.1016/j.foodchem.2017.09.148

Zhang, J. N., Yang, Y., Feng, X. P., Xu, H. X., Chen, J. P., and He, Y. (2020a). Identification of bacterial blight resistant rice seeds using terahertz imaging and hyperspectral imaging combined with convolutional neural network. *Front. Plant Sci.* 11:15. doi: 10.3389/fpls.2020.00821

Zhang, L., Rao, Z., and Ji, H. (2020b). Hyperspectral imaging technology combined with multivariate data analysis to identify heat-damaged rice seeds. *Spectrosc. Lett.* 53, 207–221. doi: 10.1080/00387010.2020.1726402

Zhang, L., Sun, H., Rao, Z., and Ji, H. (2020c). Hyperspectral imaging technology combined with deep forest model to identify frost-damaged rice seeds. *Spectrochim. Acta Part A Mol. Biomol. Spectrosc.* 229:117973. doi: 10.1016/j.saa.2019.117973

Zhao, Y., Zhu, S., Zhang, C., Feng, X., Feng, L., and He, Y. (2018). Application of hyperspectral imaging and chemometrics for variety classification of maize seeds. *RSC Adv.* 8, 1337–1345. doi: 10.1039/c7ra05954j

Zhou, Q., Huang, W., Fan, S., Zhao, F., Liang, D., and Tian, X. (2020). Non-destructive discrimination of the variety of sweet maize seeds based on hyperspectral image coupled with wavelength selection algorithm. *Infrared Phys. Technol.* 109:103418. doi: 10.1016/j.infrared.2020.103418

Conflict of Interest: The authors declare that the research was conducted in the absence of any commercial or financial relationships that could be construed as a potential conflict of interest.

Publisher's Note: All claims expressed in this article are solely those of the authors and do not necessarily represent those of their affiliated organizations, or those of the publisher, the editors and the reviewers. Any product that may be evaluated in this article, or claim that may be made by its manufacturer, is not guaranteed or endorsed by the publisher.

frontiers | Frontiers in Plant Science

ORIGINAL RESEARCH
published: 06 July 2022
doi: 10.3389/fpls.2022.938162

Determination of the Soluble Solids Content in Korla Fragrant Pears Based on Visible and Near-Infrared Spectroscopy Combined With Model Analysis and Variable Selection

Xuhai Yang[1,2†], Lichun Zhu[1†], Xiao Huang[1], Qian Zhang[1], Sheng Li[1], Qiling Chen[2], Zhendong Wang[2] and Jingbin Li[1*]*

[1] Xinjiang Production and Construction Corps, Key Laboratory of Modern Agricultural Machinery, College of Mechanical and Electrical Engineering, Shihezi University, Shihezi, China, [2] Xinjiang Production & Construction Crops, Key Laboratory of Korla Fragrant Pear Germplasm Innovation and Quality Improvement and Efficiency Increment, Shihezi, China

OPEN ACCESS

Edited by:
Jiangbo Li,
Beijing Academy of Agriculture and Forestry Sciences, China

Reviewed by:
Du Xinwu,
Henan University of Science and Technology, China
Xudong Sun,
East China Jiaotong University, China

***Correspondence:**
Qian Zhang
zq_mac@shzu.edu.cn
Jingbin Li
ljb8095@163.com

[†] These authors have contributed equally to this work

Specialty section:
This article was submitted to Crop and Product Physiology, a section of the journal Frontiers in Plant Science

Received: 07 May 2022
Accepted: 30 May 2022
Published: 06 July 2022

Citation:
Yang X, Zhu L, Huang X, Zhang Q, Li S, Chen Q, Wang Z and Li J (2022) Determination of the Soluble Solids Content in Korla Fragrant Pears Based on Visible and Near-Infrared Spectroscopy Combined With Model Analysis and Variable Selection. Front. Plant Sci. 13:938162. doi: 10.3389/fpls.2022.938162

The non-destructive detection of soluble solids content (SSC) in fruit by near-infrared (NIR) spectroscopy has a good application prospect. At present, the application of portable devices is more common. The construction of an accurate and stable prediction model is the key for the successful application of the device. In this study, the visible and near-infrared (Vis/NIR) spectra of Korla fragrant pears were collected by a commercial portable measurement device. Different pretreatment methods were used to preprocess the raw spectra, and the partial least squares (PLS) model was constructed to predict the SSC of pears for the determination of the appropriate pretreatment method. Subsequently, PLS and least squares support vector machine (LS-SVM) models were constructed based on the preprocessed full spectra. A new combination (BOSS-SPA) of bootstrapping soft shrinkage (BOSS) and successive projections algorithm (SPA) was used for variable selection. For comparison, single BOSS and SPA were also used for variable selection. Finally, three types of models, namely, PLS, LS-SVM, and multiple linear regression (MLR), were constructed based on different input variables. Comparing the prediction performance of all models, it showed that the BOSS-SPA-PLS model based on 17 variables obtained the best SSC assessment ability with r_p of 0.94 and *RMSEP* of 0.27 °Brix. The overall result indicated that portable measurement with Vis/NIR spectroscopy can be used for the detection of SSC in Korla fragrant pears.

Keywords: portable spectral measurement, internal attribute evaluation, Korla fragrant pear, variable selection, quantitative analysis model

INTRODUCTION

Fruit is one of the most important foods in people's daily life. Fruit industry is a pillar industry in many countries and regions. The post-harvest quality detection and grading can realize the graded sales of fruit in the market, which not only greatly increases the profits but also improves the market competitiveness (Londhe et al., 2013). At present, many grading equipment manufacturers have successfully developed commercial systems for the quality detection of fruit. Fruit quality

includes external and internal qualities. Compared with external quality, such as size, color, and shape, consumers prefer fruits with good internal quality, because it is directly related to taste. Soluble solids content (SSC) is an important internal quality attribute that affects consumers' acceptance and price of fresh fruit. It is also an important index for determining fruit maturity and harvest time, as well as for evaluating and grading fruit post-harvest quality (Antonucci et al., 2011; Rajkumar et al., 2012). Non-destructive testing of SSC in fruit by refractometer is a standard detection way, which is destructive, cumbersome, and time-consuming (Li and Chen, 2017). This way is only suitable for detecting a small amount of fruit in specific circumstances, such as sampling inspection. However, for quality assessment of a large number of fruit, the rapid and non-destructive measurement techniques are more attractive.

In the past three decades, many technologies have been applied to detecting the SSC in fruits (Li et al., 2016; Walsh et al., 2020). Among them, the visible and near-infrared (Vis/NIR) spectroscopy is the most widely used technology. The detected fruits include apple (Ma et al., 2021), orange (Jamshidi et al., 2012), pear (Li et al., 2013), jujube (Wang et al., 2011), watermelon (Ali et al., 2017), melon (Zhang et al., 2019), banana (Zude, 2003), etc. For the detection of SSC in fruits by Vis/NIR spectroscopy, the way of measurement can be divided into static, online, and portable detection. In the early stage, the static detection was the most commonly used way using expensive testing instrument, which was mainly aimed at verifying the feasibility of Vis/NIR spectroscopy to detect the SSC of fruit and constructing appropriate prediction models. On this basis, many studies have proved that Vis/NIR spectroscopy was an effective technology for the SSC analysis of fruits (Walsh et al., 2020). Therefore, this study mainly focuses on the online SSC detection for developing a suitable prediction model for processing large quantities of fruit (Xia et al., 2020; Zhang et al., 2021). Different from the static and online detections, the portable detection is a rapid detection technique for assessing the internal quality of fruits based on portable measuring instruments (Neto et al., 2017). This way of detection has the unique advantages of convenient carrying and flexible use. This way is more suitable for the SSC inspection of fruit at anytime and anywhere in the process of storage and transportation and is also suitable for the detection of fruit maturity on trees and so on. In terms of these three ways of detection, no matter which way needs to build a special prediction model for different varieties of fruits to accurately predict the SSC, because of still many problems in the model transfer between different ways of detection and between prediction models of different varieties of fruits (Mishra et al., 2021).

The prediction model of SSC based on Vis/NIR spectroscopy contains linear [such as partial least squares (PLS) and multiple linear regression (MLR)] and non-linear [least squares-support vector machine (LS-SVM) and artificial neural network (ANN)] models, which can achieve the successful prediction of SSC in fruits (Walsh et al., 2020). Due to the different application objects and conditions, it is difficult to directly determine which model is better without actual verification. Generally, compared with non-linear models, the linear models are easier to explain and are simpler. However, the non-linear models may be more robust because they can deal with the linear and non-linear relationship between spectral data and prediction attributes at the same time (Li et al., 2013). However, this cannot be the judgment basis for using linear and non-linear models in actual SSC prediction. To find the best prediction model, it is necessary to build different models for analysis.

In the process of development, model optimization is the key to build a more efficient prediction model. Variable selection is a common model optimization strategy (Zou et al., 2010; Yun et al., 2019). By using appropriate variable selection methods, those uninformative variables and redundant variables are eliminated, and a small number of variables related to SSC prediction can be extracted, so as to achieve the purpose of model optimization. The variable selection can make the model simpler and improve the interpretation, modeling, and prediction rate of the model. For model optimization, many variable selection methods [such as successive projections algorithm (Araújo et al., 2001), competitive adaptive reweighted sampling (Li et al., 2009), and Monte Carlo uninformative variable elimination (Cai et al., 2008)] have been successfully applied. Compared with the variable selection using single method, some studies in fruit quality detection indicated that two complementary wavelength selection strategies may achieve a superimposed effect when combined together (Li et al., 2014). Therefore, in this study, a new combination (BOSS-SPA) of bootstrapping soft shrinkage (BOSS) and successive projections algorithm (SPA) will be applied to select the effective variables from full spectral data.

Pear is among the economically most important fruit in the world. The main objective of this study was to determine the best model for SSC prediction of Korla fragrant pears based on portable spectral detection technology. The specific purposes were given as follows: (1) To collect Vis/NIR spectral data of all pear samples using a commercially available portable spectroscopic device; (2) To establish the linear PLS and non-linear LS-SVM calibration models based on full-spectrum data and compare the performance of models; (3) To extract the effective variables that were most informative for SSC detection of Korla fragrant pears by using BOSS-SPA combination variable selection method; and (4) To determine the optimal predictive model, combined with prediction accuracy and stability, by comparing the performance of models established based on full spectra and effective variables.

MATERIALS AND METHODS

Fruit Samples

Korla fragrant pear, a unique variety in Xinjiang, China, was used in this study. A total of 120 intact pears were purchased from a grocery store. All samples were returned to the laboratory and stored at room temperature (20°C, relative humidity 60%) for 24 h, to avoid the influence of sample temperature on the accuracy of the prediction model (Xia et al., 2020). In this study, all samples were divided into calibration set and prediction set on the basis of Kennard-Stone (KS) sampling method (Galvão et al., 2005). The calibration set contained 80 samples, which were

mainly used for the construction of models. The prediction set contained 40 samples, which were mainly used to evaluate the performance of models. In the whole process of data analysis, the samples of calibration set and prediction set remain unchanged.

Portable Measurement Device for Spectral Data Acquisition

A commercial portable spectrometer (K-BA100R; Kubota Co., Osaka, Japan) was used to collect Vis/NIR spectral data of samples. This portable measurement device mainly contains halogen lamp light source, ring detection probe, optical fiber, display screen, processor, etc. The detection probe consists of two groups of ring optical fibers. One is the transmitting optical fiber, which is mainly used to transmit Vis/NIR light to the sample; and the other is the receiving optical fiber, which is mainly used to receive the diffuse reflectance light with fruit component information. Spectral data were acquired based on interactive mode. During spectral data collection, each sample was placed on the detection probe with its stem-calyx axis being horizontal. The collected spectral range was 500–1,010 nm with an interval of 2 nm. The integration time of spectrum acquisition was set to 300 ms for each sample. The final spectrum (*Rc*) was calculated automatically by using the raw sample spectrum (*R*), the dark reference spectrum (D), and the white reference spectrum (W), according to $Rc = [(R - D)/(W - D)]$. The dark spectrum and the white spectrum were obtained by turning off and turning on light sources (no sample information), respectively. Due to the noise at both ends of the original spectrum, only spectral data in the range of 550–1,000 nm were used.

Real Soluble Solids Content Measurement

After the spectral data of all samples were collected, the actual SSC was measured immediately. A commercial refractometer (Model: PR-101α, Atago Co., Ltd., Tokyo, Japan) with a refractive index accuracy of ±0.1 and the range of 0–45% with temperature correction was used for destructive measurement. For each sample, the whole fruit was juiced, and the SSC value of the juice was measured three times. The mean values of three measurements were recorded as the actual SSC value of the tested sample.

Wavelength Selection Methods

The original spectrum contains over 200 wavelengths (variables), not all of which are related to the prediction of SSC in pears, and moreover, too many wavelengths are not conducive to the construction of robust model. This study used the BOSS-SPA combination to extract the effective wavelengths from full spectral data. In terms of the BOSS-SPA combination, BOSS was first used to extract a set of effective wavelengths, and SPA was then used to optimize the extracted wavelengths. BOSS method, originally proposed by Deng et al. (2016), takes advantage of bootstrap sampling (BSS) and weighted bootstrap sampling (WBS) to generate random variable subsets for the construction of partial least squares regression (PLSR) sub-models. The regression coefficients of sub-models were analyzed, and the weights of variables were determined according to the absolute values of the regression coefficients. The informative variables with higher weights have a higher selection probability. Model population analysis (MPA), proposed by Deng et al. (2015), was used to analyze the sub-models to update the weight of variables. Variables were optimized according to the principle of soft shrinkage; in other words, less important variables were not eliminated directly, but assigned smaller weights. The algorithm iterates until the number of variables reaches 1. The subset with the lowest root mean square error of cross validation (RMSECV) was finally selected as the optimal variable set. SPA proposed by Araújo et al. (2001) is a forward wavelength selection algorithm, which aims to minimize the collinearity problem in variables. SPA uses a simple projection operation in a vector space to obtain a subset of wavelengths with minimal collinearity. The final selected variable set corresponds to the smallest root mean square error of prediction (RMSEP) in MLR analysis.

Modeling Algorithms

The PLS has become the most commonly used multivariate linear analysis method in spectral modeling and analysis. In the process of modeling, PLS can consider the target value matrix Y (SSC value in this study) and spectral matrix X at the same time and establish the basic relationship between X and Y. For the development of a PLS model, the spectral matrix X and the concentration matrix Y were first decomposed to obtain the corresponding score matrices T and U:

$$X = TP + E, Y = UQ + F \quad (1)$$

where P and Q are the loading matrices of X matrix and Y matrix, and E and F are the errors that come from the process of PLS. Then, MLR based on score matrix T and U was performed as follows:

$$U = BT + E \quad (2)$$

where B is the regression coefficient matrix of PLS. In linear regression, it is necessary to consider how many columns of data in the T matrix, i.e., the best factor or later variables (LVs), were used for modeling. In this study, the leave-one-out cross validation was used to determine the number of optimal LV.

The LS-SVM is an advanced statistical learning method, which can deal with linear and non-linear multivariate analysis and solve these problems in a relatively fast way. The LS-SVM regression model can be expressed as follows:

$$y(x) = \sum_{k=1}^{N} \alpha_k K(x, x_k) + b \quad (3)$$

where $K(x, x_k)$, x_k, α_k, and b are the kernel function, input vector, support value, and bias, respectively. The radial basis function (RBF) was used as kernel function $K(x, x_k)$ in this study and defined as follows:

$$K(x, x_k) = \exp(-||x_k - x||^2/(2\sigma^2)) \quad (4)$$

where $||x_k\text{-}x||$ represents the distance between the input vector and the threshold vector, and σ is a width vector.

The MLR is also a common calibration method for spectral quantitative analysis, which is easy to calculate and explain compared with PLS. The general form of the model is:

$$y = \beta x + b \quad (5)$$

where y represents an unknown concentration value (here, it was the SSC value), β represents a set of regression coefficients, x represents the spectral vector of a sample, and b is a constant. MLR is suitable for a simple system with good linear relationship. However, MLR also has the limitation. This method requires more samples than variables for modeling. In practical applications, the raw spectral variables obtained by spectrometers are often numerous. Therefore, before constructing MLR models, it is usually necessary to use the wavelength selection method to optimize the variables to meet the prerequisite condition of MLR modeling.

Model Evaluation

Four parameters, including calibration correlation coefficient (r_c) and root mean square error of calibration (*RMSEC*), and prediction correlation coefficient (r_p) and root mean square error of prediction (*RMSEP*), were used to assess the performance of models. The first two parameters were used to evaluate the prediction performance of models on the samples in the calibration set, and the last two parameters were used to evaluate the prediction performance of models on the samples in the prediction set. A good model usually has high r_c and r_p, low *RMSEC* and *RMSEP*, and a small difference between *RMSEC* and *RMSEP*. All parameters were calculated as follows:

$$r = \sqrt{1 - \frac{\sum_{i=1}^{n} \left(y_{i,actual} - y_{i,predicted}\right)^2}{\sum_{i=1}^{n} \left(y_{i,actual} - \bar{y}_{i,actual}\right)^2}} \quad (6)$$

$$RMSEC = \sqrt{\frac{1}{n_c} \sum_{i=1}^{n_c} \left(y_{i,predicted} - y_{i,actual}\right)^2} \quad (7)$$

$$RMSEP = \sqrt{\frac{1}{n_p} \sum_{i=1}^{n_p} \left(y_{i,predicted} - y_{i,actual}\right)^2} \quad (8)$$

where $y_{i,predicted}$ and $y_{i,actual}$ are the predictive SSC value and the real SSC value of the *i*th sample in the calibration set or prediction set, respectively. $\bar{y}_{i,actual}$ is the average SSC value of samples in the calibration or prediction set. n_c, n_p, and n correspond to the number of calibration samples, prediction samples, and all samples, respectively.

RESULTS AND DISCUSSION

Analysis of Soluble Solids Content Values of All Samples

Table 1 shows the statistical results of SSC values (°Brix) of all samples. It can be seen that the maximum, minimum, mean, and standard deviation (S.D.) of SSC values for 90 samples of calibration set were 14.5, 11.0, 12.6, and 0.6 °Brix, respectively, and for 30 samples of prediction set, these four values were 14.3, 11.2, 12.5, and 0.8 °Brix, respectively. The SSC range of the calibration set covers that of the prediction set, which is helpful to build a more robust prediction model.

TABLE 1 | The statistics of SSC (°Brix) of all samples.

Data set	No. of samples	Min.	Max.	Mean	S.D.
Total	120	11.0	14.5	12.6	0.8
Calibration set	90	11.0	14.5	12.6	0.8
Prediction set	30	11.2	14.3	12.5	0.6

TABLE 2 | Prediction results of SSC by PLS models combined with different preprocessing methods.

Preprocessing methods	LVs	Calibration set		Prediction set	
		r_c	*RMSEC*	r_p	*RMSEP*
None	7	0.97	0.19	0.86	0.32
SG	10	0.97	0.20	0.91	0.27
SG-MSC	11	0.97	0.20	0.92	0.25
SG-SNV	10	0.96	0.22	0.89	0.29
First derivative-SG-MSC	11	0.96	0.21	0.92	0.25
Second derivative-SG-MSC	12	0.93	0.25	0.90	0.27

Spectral Pretreatment and Spectral Features

The difference of sample size leads to large scattering in the original spectra, and the original spectra can also contain random noise, which negatively affects the prediction performance of the model. Therefore, the original spectrum was preprocessed before model construction. The pretreatments, including Savitzky-Golay smoothing (SG), first derivative and second derivative, combination of SG and standard normal variables (SG-SNV), combination of SG and multivariate scattering correction (SG-MSC), and combination of derivative and SG-MSC, were used for spectral pretreatment. **Table 2** shows the prediction results of SSC by PLS models combined with preprocessing and raw spectra. It can be seen that the prediction accuracy of all PLS models based on the preprocessed spectra was better than that of the PLS model based on the original spectra, indicating that the spectrum preprocessing can improve the prediction performance of the model. PLS models combined with SG-MSC and the first derivative-SG-MSC preprocessing achieved the best prediction results. Compared with the second derivative-SG-MSC preprocessing, the performance of the first derivative-SG-MSC is better, probably because the second derivative processing amplifies the noise in the original spectrum. For samples of the prediction set, the optimal r_p and *RMSEP* were 0.92 and 0.25, respectively. Considering that SG-MSC pretreatment is simpler than the first derivative-SG-MSC, the pretreatment spectra by SG-MSC were used for the subsequent analysis.

The preprocessed spectral curves of samples by SG-MSC are shown in **Figure 1**. It can be seen that all samples have a similar

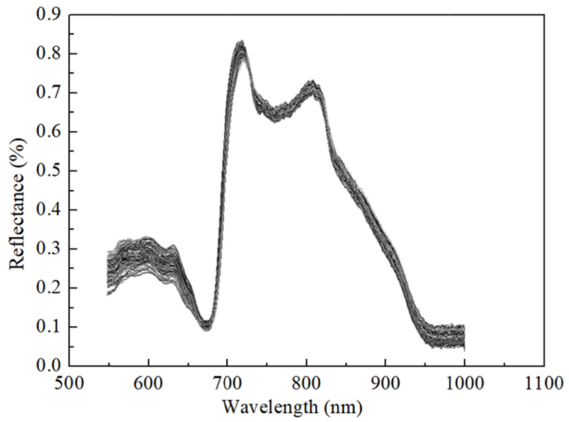

FIGURE 1 | Preprocessed spectral curves by SG-MSC.

TABLE 3 | Prediction results of SSC by PLS and LS-SVM with full spectral data, respectively.

Modeling methods	LVs/(γ/σ^2)	Calibration set		Prediction set	
		r_c	*RMSEC*	r_p	*RMSEP*
PLS	11	0.97	0.20	0.92	0.25
LS-SVM	$\gamma = 2.1 \times 10^5$; $\sigma^2 = 2.5 \times 10^4$	0.95	0.24	0.88	0.32

spectral trend in the Vis-NIR spectral region of 550–1,000 nm, and there are no abnormal samples. The spectral curve shows some obvious absorption and reflection peaks, which may be related to the internal chemical components of Korla fragrant pears. The first obvious absorption peak is about 680 nm, which is a typical chlorophyll absorption band. The central band of the second absorption peak is about 750 nm, which is a relatively wide absorption band associated with the fourth overtone of band C–H. The small absorption band around at 950 nm might be associated with the second overtone of band O–H. These results were similar to those of Li et al. (2018). In addition to the typical absorption characteristics, the spectral intensities of different samples were different, indicating that there were differences between chemical components, which was conducive to construct the SSC quantitative analysis model.

Full Spectra Models for Soluble Solids Content Prediction

In this study, two kinds of full-spectrum models, namely, linear PLS and non-linear LS-SVM were constructed to predict the SSC of pears. Prediction results are shown in **Table 3**. It can be seen that the prediction accuracy of PLS model was obviously better than that of LS-SVM model. For samples in the prediction set, the r_p and *RMSEP* of the latter were 0.92 and 0.25, respectively. The relatively high prediction accuracy indicated that the PLS model seems to be more suitable for the non-destructive evaluation of SSC of Korla fragrant pears, which may be due to the main linear relationship between the original spectral data and SSC of fragrant pears. For the PLS model, the optimal number of potential variables (LVs) was 11. Nevertheless, full variable modeling negatively influences the fast construction of the model and also reduces the prediction efficiency of the model.

Wavelength Selection by Bootstrapping Soft Shrinkage and Successive Projections Algorithm

The BOSS-SPA combination algorithm was used to select the most important wavelengths from all 450 spectral variables to build a more efficient SSC prediction model. The process of wavelength selection by the BOSS algorithm is shown in **Figure 2**. The evolution of wavelength number (nVAR), RMSECV, and weights in sub-models in each iteration of BOSS are shown in **Figures 2A–C**, respectively. As shown in **Figure 2A**, the number of variables shows a downward trend from fast to slow with the increase in the number of iterations. However, it is impossible to know how many variables are finally selected. It can be seen from **Figure 2B** that the number of the selected variables is directly related to the RMSECV value of the models. Observing the RMSECV curve, combined with **Figure 2A**, indicates that the prediction performance of the model gradually improves with the decrease in the number of selected variables. When the number of selected variables reaches 40 (the corresponding number of iterations is 13), the lowest RMSECV value was obtained. Afterward, the RMSECV value of the model begins to increase rapidly with the increase in the number of selected variables, indicating that the performance of the model gradually deteriorates. Therefore, the 40 variables corresponding to the lowest RMSECV value were considered as the most important wavelengths, which were selected by the BOSS algorithm. **Figure 2C** shows the change of each wavelength weight in different iterations. It can be seen that the extracted 40 wavelengths were distributed in the Vis/NIR spectrum region. This showed that the tissue color of Korla fragrant pears, especially the skin color, may have a certain correlation with SSC.

Although the selected 40 wavelengths account for only 8.9% of the full spectrum variable information, it can be seen from the weight figure that there is obvious collinearity between wavelengths, that is, there are more redundant variables in the selected variables. Thus, based on the selected 40 wavelengths, SPA was further used to optimize variables. During variable selection by SPA, the variation of RMSEP of the MLR model with the used variable number is shown in **Figure 3A**. The red solid block in the figure indicates the optimal number of the selected variables by SPA. It indicates that only 17 wavelengths are selected from 40 spectral variables. The number of variables is further reduced. The selected 17 wavelengths include 550, 565, 577, 636, 653, 664, 730, 739, 744, 765, 819, 854, 880, 902, 932, 966, and 997 nm, as shown in **Figure 3B**. In **Figure 3B**, the vertical line represents the positions of the corresponding 17 wavelengths. For these selected wavelengths, the first nine wavelengths are located in the visible spectrum region, which are mainly related to the color characteristics of the pear surface. The other eight wavelengths are located in the NIR spectral region of 750–1,000 nm. The absorbance of this region was related to the second and third overtones of oxygen–hydrogen (O–H) stretches

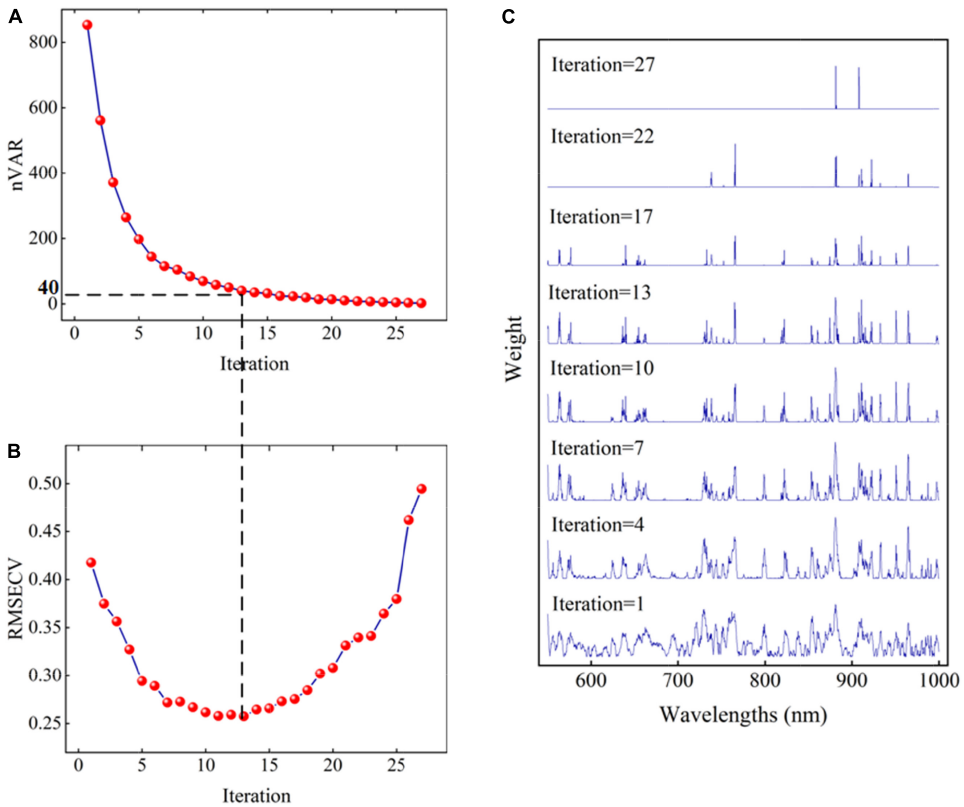

FIGURE 2 | The change of nVAR **(A)**, RMSECV **(B)**, and weights for variables **(C)** in each iteration of the BOSS algorithm.

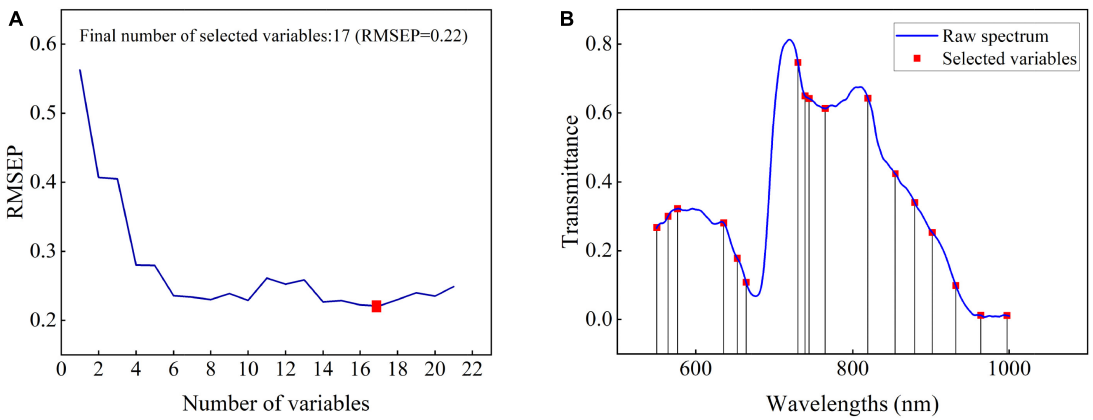

FIGURE 3 | The change of RMSEP with the selected variables by SPA **(A)** and distribution of 17 variables **(B)**.

and the third and fourth overtones of carbon–hydrogen (C—H) stretches of the organic molecules such as SSC (Liu et al., 2010; Jie et al., 2013; Li and Chen, 2017).

Effective Variable Models for Soluble Solids Content Prediction

Three kinds of models, namely, PLS, LS-SVM, and MLR, were established based on selected variables by BOSS-SPA for SSC prediction of Korla fragrant pears. For comparison, three types of models were also constructed based on those variables selected by only using BOSS or SPA method. Note that because the SPA variable selection process based on full spectrum is similar to SPA in the BOSS-SPA combination variable selection method, it is further introduced in this study; 24 variables were selected by only using SPA. Prediction results of all models are shown in **Table 4**. It can be seen that all models can effectively predict the SSC of pears, and the r_p and *RMSEP* ranges of models

TABLE 4 | Prediction results of SSC by PLS, LS-SVM, and MLR models with different effective wavelengths.

Models	Variable selection methods	LVs/(γ/σ^2)	No. of variables	Calibration set		Prediction set	
				r_c	*RMSEC*	r_p	*RMSEP*
PLS	BOSS-SPA	8	17	0.94	0.27	0.92	0.25
	BOSS	9	40	0.96	0.23	0.93	0.23
	SPA	14	24	0.92	0.28	0.90	0.27
LS-SVM	BOSS-SPA	$\gamma = 2.6 \times 10^4$; $\sigma^2 = 4.6 \times 10^3$	17	0.96	0.21	0.91	0.28
	BOSS	$\gamma = 5.3 \times 10^4$; $\sigma^2 = 5.1 \times 10^3$	40	0.98	0.17	0.92	0.26
	SPA	$\gamma = 7.3 \times 10^5$; $\sigma^2 = 8.6 \times 10^4$	24	0.90	0.35	0.89	0.29
MLR	BOSS-SPA	—	17	0.94	0.25	0.92	0.25
	BOSS	—	40	0.94	0.25	0.92	0.23
	SPA	—	24	0.92	0.24	0.89	0.32

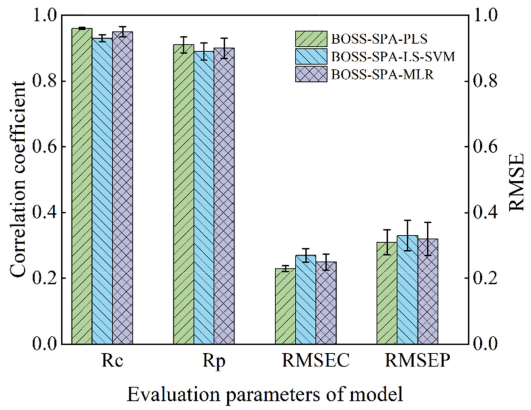

FIGURE 4 | Results of 20 predictions for BOSS-SPA-PLS, BOSS-SPA-LS-SVM, and BOSS-SPA-MLR models.

were 0.89–0.93 and 0.23–0.32 °Brix, respectively. Compared with full-spectrum PLS and LS-SVM models in **Table 3**, the models based on effective variables obtained similar or even better prediction performance. The results showed that the appropriate variable selection method can optimize the model. Comparing the three types of models (PLS, LS-SVM, and MLR) in **Table 4**, it can be found that the prediction accuracy of the two types of linear models for SSC was slightly better than that of the LS-SVM model based on the same inputs, indicating that the linear model was a better choice when a portable instrument was used to measure SSC of Korla fragrant pears. In terms of PLS and MLR models, the prediction accuracy of the two models was similar. For each type of model in PLS, MLR, and LS-SVM shown in **Table 4**, the models (i.e., BOSS-PLS, BOSS-LS-SVM, and BOSS-MLR) developed based on the variables selected by BOSS were the best, followed by the models (i.e., BOSS-SPA-PLS, BOSS-SPA-LS-SVM, and BOSS-SPA-MLR) developed based on the variables selected by BOSS-SPA. The prediction ability of the models (i.e., SPA-PLS, SPA-LS-SVM, and SPA-MLR) developed based on the variables extracted by the SPA algorithm was the worst, which may be because SPA can effectively reduce the collinearity between variables, but it is weak in the elimination of uninformative variables. Therefore, there may be uninformative variables in those variables selected by SPA. In contrast, the BOSS algorithm can effectively eliminate those uninformative variables.

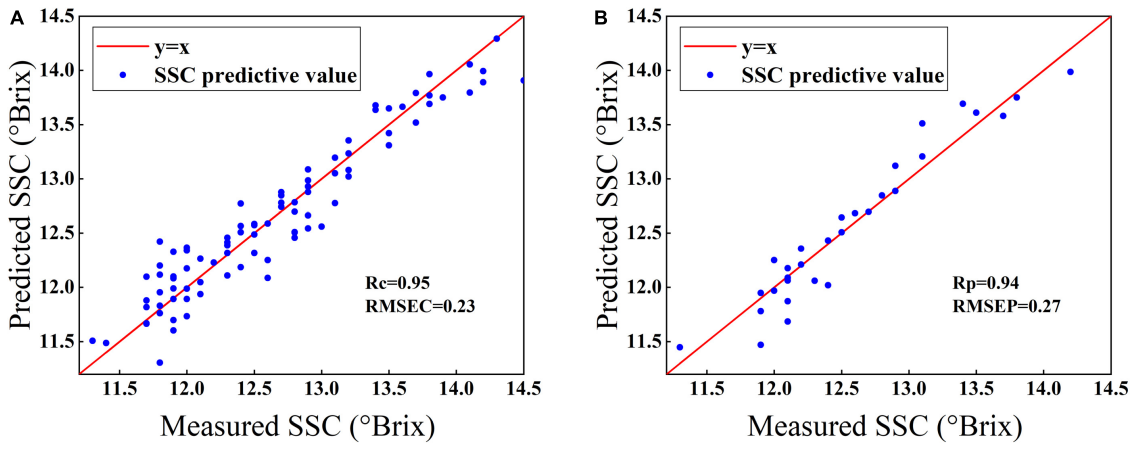

FIGURE 5 | Measured vs. predicted values for SSC prediction of Korla fragrant pears by BOSS-SPA-PLS models. **(A)** Samples in the calibration set and **(B)** samples in the prediction set.

The BOSS-SPA combination variable selection method takes into account the advantages of both BOSS and SPA. Based on BOSS-SPA, only 17 variables were selected, and the models based on these selected variables achieved high prediction accuracy for the SSC prediction of Korla fragrant pears. For samples in the calibration set, the r_c and *RMSEC* of BOSS-SPA-PLS, BOSS-SPA-LS-SVM, and BOSS-SPA-MLR models were 0.94 and 0.27 °Brix, 0.96 and 0.21 °Brix, and 0.94 and 0.25 °Brix, respectively. For samples in the prediction set, the r_p and *RMSEP* were 0.92 and 0.25 °Brix, 0.91 and 0.28 °Brix, and 0.92 and 0.25 °Brix, respectively, for the three models.

Determination of the Optimal Model

The analysis in the Section "Effective Variable Models for Soluble Solids Content Prediction" shows that BOSS-SPA-PLS, BOSS-SPA-LS-SVM, and BOSS-SPA-MLR models have high prediction accuracy and few input variables, which can be used for the SSC evaluation of Korla fragrant pears. To further compare the prediction performance of the three models, the stability of the models was analyzed. Specifically, all 120 samples were randomly divided into calibration set and prediction set according to the ratio of 3:1, and then, BOSS-SPA-PLS, BOSS-SPA-LS-SVM, and BOSS-SPA-MLR models were constructed, respectively, based on the new sample set to predict SSC. The sample set was divided 20 times, and accordingly, each type of model was also constructed 20 times. **Figure 4** shows the prediction results of 20 model calculations for the three types of models. For each type of model, the bar graph represents the average of the 20 predictions, and error bars from the 20 calculations were also shown on the bar graph. It can be observed from the figure that the BOSS-SPA-PLS model was optimal with the highest r_c/r_p average and the lowest *RMSEC*/*RMSEP*. Moreover, the correlation coefficient and root mean square error (RMSE) of the BOSS-SPA-PLS model have the smallest change of error bar, indicating that this model has the highest stability for the SSC prediction. Therefore, the BOSS-SPA-PLS model was finally confirmed as the optimal model for predicting the SSC of Korla fragrant pears based on portable Vis/NIR spectroscopy.

Figure 5 shows the scatterplots of the predicted vs. measured SSC values for calibration samples (**Figure 5A**) and prediction samples (**Figure 5B**) by the BOSS-SPA-PLS model. The red solid line is the regression line corresponding to the ideal prediction result. It can be observed that the samples were closely distributed around the regression line. The prediction accuracy of the model was 0.95 for r_c and 0.23 for *RMSEC* for samples in the calibration set and 0.94 for r_p and 0.27 for *RMSEP* for samples in the prediction set. Both *RMSEC* and *RMSEP* were low, and the difference between them was small, indicating that the BOSS-SPA-PLS model has a good prediction accuracy and stability, and it can be used to effectively predict the SSC of Korla fragrant pears.

Some similar studies have been carried out using portable Vis-NIR or NIR instruments. Sun et al. (2009) developed a portable NIR system to detect SSC of Nanfeng mandarin. The best results were obtained by the support vector machine model. The correlation coefficient (*R*) and *RMSEP* were 0.93 and 0.65 °Brix, respectively. Wang et al. (2017) achieved a prediction accuracy of 0.46 °Brix (*RMSEP*) for SSC analysis of the European pear based on the MLR model with 9 wavelengths. Fan et al. (2017) used Vis-NIR portable instrument to measure the SSC of apple and constructed a PLS model based on 50 wavelengths to obtain the best prediction performance, with r_p and *RMSEP* being 0.96 and 0.40 °Brix, respectively. Compared with these studies, satisfactory results were obtained in this study.

CONCLUSION

In this study, the portable Vis/NIR device was successfully used to evaluate the SSC of Korla fragrant pears. It was found that SGS-SNV spectral preprocessing can obviously improve the prediction performance of models developed using the raw spectra. The PLS and LS-SVM models with full spectra were constructed. For samples in the prediction set, the r_p and *RMSEP* of the two models were 0.92, 0.25 °Brix and 0.88, 0.32 °Brix, respectively. Furthermore, to reduce the number of variables involved in modeling, the BOSS-SPA combination method selected 17 optimal variables, which were used to develop BOSS-SPA-PLS, BOSS-SPA-LS-SVM, and BOSS-SPA-MLR models. Moreover, PLS, LS-SVM and MLR models were also constructed based on the variables selected by the only BOSS and SPA. The results showed that the prediction accuracy of models with effective variables was similar or better than that of the full-spectrum models, and the ranges of r_p and *RMSEP* of models were 0.89–0.93 and 0.23–0.32 °Brix, respectively, for SSC prediction. For each model of PLS, LS-SVM, and MLR established based on the selected variables, BOSS-SPA-PLS, BOSS-SPA-LS-SVM, and BOSS-SPA-MLR were optimal by considering the complexity and accuracy of the models. The *RMSEP* values of the three models for SSC prediction of Korla fragrant pears were 0.25, 0.28, and 0.25 °Brix, respectively. The stability of the three models was further compared based on 20 modeling calculations, which showed that BOSS-SPA-PLS was superior to BOSS-SPA-LS-SVM and BOSS-SPA-MLR models. Finally, the BOSS-SPA-PLS was determined to be the best model, and the BOSS-SPA combination method was proved to be an effective variable selection method. The model developed in this study, combined with portable measurement technology, has the potential to be used for the non-destructive evaluation of SSC in Korla fragrant pears.

DATA AVAILABILITY STATEMENT

The original contributions presented in this study are included in the article/supplementary material, further inquiries can be directed to the corresponding authors.

AUTHOR CONTRIBUTIONS

XY: methodology, original manuscript writing, and funding. LZ and SL: modeling. XH: spectrum processing. QZ: funding, supervision, revision, and editing. QC: spectral pretreatment. ZW: editing. JL: revision, editing, and supervision. All authors contributed to the article and approved the submitted version.

FUNDING

The authors were grateful for the Xinjiang Production and Construction Corps Financial Technology Plan Project under Grant (2021CB042); Xinjiang Production & Construction Crop Key Laboratory of Korla Fragrant Pear Germplasm Innovation and Quality Improvement and Efficiency Increment under Grant (2020DA004-202102); and Shihezi University Innovation and Development Special Project under Grant (CXFZ202107).

REFERENCES

Ali, M. M., Hashim, N., Bejo, S. K., and Shamsudin, R. (2017). Rapid and nondestructive techniques for internal and external quality evaluation of watermelons: a review. *Sci. Hortic.* 225, 689–699. doi: 10.1016/j.scienta.2017.08.012

Antonucci, F., Pallottino, F., Paglia, G., Palma, A., D'Aquino, S., and Menesatti, P. (2011). Nondestructive estimation of mandarin maturity status through portable VIS-NIR spectrophotometer. *Food Bioprocess Technol.* 4, 809–813. doi: 10.1007/s11947-010-0414-5

Araújo, M. C. U., Saldanha, T. C. B., Galvã, R. K. H., Yoneyama, T., Chame, H. C., and Visani, V. (2001). The successive projections algorithm for variable selection in spectroscopic multicomponent analysis. *Chemom. Intell. Lab. Syst.* 57, 65–73. doi: 10.1016/S0169-7439(01)00119-8

Cai, W. S., Li, Y. K., and Shao, X. G. (2008). A variable selection method based on uninformative variable elimination for multivariate calibration of near-infrared spectra. *Chemom. Intell. Lab. Syst.* 90, 188–194. doi: 10.1016/j.chemolab.2007.10.001

Deng, B. C., Yun, Y. H., and Liang, Y. Z. (2015). Model population analysis in chemometrics. *Chemom. Intell. Lab. Syst.* 149, 166–176. doi: 10.1016/j.chemolab.2015.08.018

Deng, B. C., Yun, Y. H., Cao, D. S., Yin, Y. L., Wang, W. T., Lu, H. M., et al. (2016). A bootstrapping soft shrinkage approach for variable selection in chemical modeling. *Anal. Chim. Acta* 908, 63–74. doi: 10.1016/j.aca.2016.01.001

Fan, S. X., Huang, W. Q., Li, J. B., Guo, Z. M., and Zhao, C. J. (2017). Application of characteristic NIR variables selection in portable detection of soluble solids content of apple by near infrared spectroscopy. *Spectrosc. Spectral Anal.* 34, 2707–2712.

Galvão, R. K. H., Araujo, M. C. U., José, G. E., Pontes, M. J. C., Silva, E. C., and Saldanha, T. C. B. (2005). A method for calibration and validation subset partitioning. *Talanta* 67, 736–740. doi: 10.1016/j.talanta.2005.03.025

Jamshidi, B., Minaei, S., Mohajerani, E., and Ghassemian, H. (2012). Reflectance Vis/NIR spectroscopy for nondestructive taste characterization of Valencia oranges. *Comput. Electron. Agric.* 85, 64–69. doi: 10.1016/j.compag.2012.03.008

Jie, D. F., Xie, L. J., Fu, X. P., Rao, X. Q., and Ying, Y. B. (2013). Variable selection for partial least squares analysis of soluble solids content in watermelon using near-infrared diffuse transmission technique. *J. Food Eng.* 118, 387–392. doi: 10.1016/j.jfoodeng.2013.04.027

Li, H. D., Liang, Y. Z., Xu, Q. S., and Cao, D. S. (2009). Key wavelengths screening using competitive adaptive reweighted sampling method for multivariate calibration. *Anal. Chim. Acta* 648, 77–84. doi: 10.1016/j.aca.2009.06.046

Li, J. B., and Chen, L. P. (2017). Comparative analysis of models for robust and accurate evaluation of soluble solids content in 'Pinggu' peaches by hyperspectral imaging. *Comput. Electron. Agric.* 142, 524–535. doi: 10.1016/j.compag.2017.11.019

Li, J. B., Huang, W. Q., Chen, L. P., Fan, S. X., Zhang, B. H., Guo, Z. M., et al. (2014). Variable selection in visible and near-infrared spectral analysis for noninvasive determination of soluble solids content of 'Ya' pear. *Food Anal. Methods* 7, 1891–1902. doi: 10.1007/s12161-014-9832-8

Li, J. B., Huang, W. Q., Zhao, C. J., and Zhang, B. H. (2013). A comparative study for the quantitative determination of soluble solids content, pH and firmness of pears by Vis/NIR spectroscopy. *J. Food Eng.* 116, 324–332. doi: 10.1016/j.jfoodeng.2012.11.007

Li, J. B., Wang, Q. Y., Xu, L., Tian, X., Xia, Y., and Fan, S. X. (2018). Comparison and optimization of models for determination of sugar content in pear by portable Vis-NIR spectroscopy coupled with wavelength selection algorithm. *Food Anal. Methods* 12, 12–22. doi: 10.1007/s12161-018-1326-7

Li, J. L., Sun, D. W., and Cheng, J. H. (2016). Recent advances in nondestructive analytical techniques for determining the total soluble solids in fruits: a review. *Compr. Rev. Food Sci. Food Saf.* 15, 897–911. doi: 10.1111/1541-4337.12217

Liu, Y. D., Sun, X. D., Zhang, H. L., and Ouyang, A. G. (2010). Nondestructive measurement of internal quality of Nanfeng mandarin fruit by charge coupled device near infrared spectroscopy. *Comput. Electron. Agric.* 71S, S10–S14. doi: 10.1016/j.compag.2009.09.005

Londhe, D., Nalawade, S., Pawar, G., Atkari, V., and Wandkar, S. (2013). Grader: A review of different methods of grading for fruits and vegetables. *Agric. Eng. Int.* 15, 217–230.

Ma, T., Xia, Y., Inagaki, T., and Tsuchikawa, S. (2021). Rapid and nondestructive evaluation of soluble solids content (SSC) and firmness in apple using Vis-NIR spatially resolved spectroscopy. *Postharvest Biol. Technol.* 173:111417. doi: 10.1016/j.postharvbio.2020.111417

Mishra, P., Klont, R., Verkleij, T., and Wisse, S. (2021). Translating near-infrared spectroscopy from laboratory to commercial slaughterhouse: existing challenges and solutions. *Infrared Phys. Technol.* 119:103918. doi: 10.1016/j.infrared.2021.103918

Neto, J. P. D. S., Assis, M. W. D. D., Casagrande, I. P., Júnior, L. C. C., and Teixeira, G. H. D. A. (2017). Determination of 'palmer' mango maturity indices using portable near infrared (vis-nir) spectrometer. *Postharvest Biol. Technol.* 130, 75–80. doi: 10.1016/j.postharvbio.2017.03.009

Rajkumar, P., Wang, N., EImasry, G., Raghavan, G. S. V., and Gariepy, Y. (2012). Studies on banana fruit quality and maturity stages using hyperspectral imaging. *J. Food Eng.* 108, 194–200. doi: 10.1016/j.jfoodeng.2011.05.002

Sun, X. D., Zhang, H. L., and Liu, Y. D. (2009). Nondestructive assessment of quality of Nanfeng mandarin fruit by a portable near infrared spectroscopy. *Int. J. Agric. Biol. Eng.* 2, 65–71.

Walsh, K. B., Blasco, J., Zude-Sasse, M., and Sun, X. D. (2020). Visible-NIR 'point' spectroscopy in postharvest fruit and vegetable assessment: the science behind three decades of commercial use. *Postharvest Biol. Technol.* 168:111246. doi: 10.1016/j.postharvbio.2020.111246

Wang, J. H., Wang, J., Chen, Z., and Han, D. H. (2017). Development of multi-cultivar models for predicting the soluble solid content and firmness of European pear (*Pyrus communis* L.) using portable vis-NIR spectroscopy. *Postharvest Biol. Technol.* 129, 143–151. doi: 10.1016/j.postharvbio.2017.03.012

Wang, J., Nakano, K., and Ohashi, S. (2011). Nondestructive evaluation of jujube quality by visible and near-infrared spectroscopy. *LWT Food Sci. Technol.* 44, 1119–1125. doi: 10.1016/j.lwt.2010.11.012

Xia, Y., Fan, S. X., Huang, W. Q., Tian, X., and Li, J. B. (2020). Multi-factor fusion models for soluble solid content detection in pear (*Pyrus bretschneideri* 'Ya') using Vis/NIR online half-transmittance technique. *Infrared Phys. Technol.* 100:103443. doi: 10.1016/j.infrared.2020.103443

Yun, Y. H., Li, H. D., Deng, B. C., and Cao, D. S. (2019). An overview of variable selection methods in multivariate analysis of near-infrared spectra. *TrAC Trends Anal. Chem.* 113, 105–115. doi: 10.1016/j.trac.2019.01.018

Zhang, D., Xu, L., Wang, Q., Tian, X., and Li, J. (2019). The optimal local model selection for robust and fast evaluation of soluble solid content in melon with thick peel and large size by Vis-NIR spectroscopy. *Food Anal. Methods* 12, 136–147. doi: 10.1007/s12161-018-1346-3

Zhang, Y., Yang, X., Cai, Z., Fan, S., Zhang, H., Zhang, Q., et al. (2021). Online detection of watercore apples by Vis/NIR full-transmittance spectroscopy coupled with ANOVA method. *Foods* 10:2983. doi: 10.3390/foods10122983

Zou, X. B., Zhao, J. W., Povey, M. J. W., Holmes, M., and Mao, H. P. (2010). Variables selection methods in near-infrared spectroscopy. *Anal. Chim. Acta* 667, 14–32. doi: 10.1016/j.aca.2010.03.048

Zude, M. (2003). Non-destructive prediction of banana fruit quality using VIS/NIR spectroscopy. *Fruits* 58, 135–142. doi: 10.1051/fruits:2003001

Conflict of Interest: The authors declare that the research was conducted in the absence of any commercial or financial relationships that could be construed as a potential conflict of interest.

Publisher's Note: All claims expressed in this article are solely those of the authors and do not necessarily represent those of their affiliated organizations, or those of the publisher, the editors and the reviewers. Any product that may be evaluated in this article, or claim that may be made by its manufacturer, is not guaranteed or endorsed by the publisher.

frontiers | Frontiers in Plant Science

ORIGINAL RESEARCH
published: 07 July 2022
doi: 10.3389/fpls.2022.867555

Non-destructive Evaluation of the Quality Characteristics of Pomegranate Kernel Oil by Fourier Transform Near-Infrared and Mid-Infrared Spectroscopy

*Emmanuel E. Okere[1,2], Ebrahiema Arendse[1], Helene Nieuwoudt[3], Willem J. Perold[2] and Umezuruike Linus Opara[1,4]**

[1]SARChI Postharvest Technology Research Laboratory, Africa Institute for Postharvest Technology, Faculty of AgriSciences, Stellenbosch University, Stellenbosch, South Africa, [2]Department of Electrical and Electronic Engineering, Stellenbosch University, Stellenbosch, South Africa, [3]Department of Viticulture and Oenology, Institute for Wine Biotechnology, Stellenbosch University, Stellenbosch, South Africa, [4]UNESCO International Centre for Biotechnology, Nsukka, Enugu State, Nigeria

OPEN ACCESS

Edited by:
Yuzhen Lu,
Mississippi State University,
United States

Reviewed by:
Changwen Du,
Institute of Soil Science (CAS), China
Mo Li,
Massey University, New Zealand

***Correspondence:**
Umezuruike Linus Opara
opara@sun.ac.za;
unesco.icb.nigeria@gmail.com

Specialty section:
This article was submitted to Crop and Product Physiology, a section of the journal Frontiers in Plant Science

Received: 01 February 2022
Accepted: 20 June 2022
Published: 07 July 2022

Citation:
Okere EE, Arendse E, Nieuwoudt H, Perold WJ and Opara UL (2022) Non-destructive Evaluation of the Quality Characteristics of Pomegranate Kernel Oil by Fourier Transform Near-Infrared and Mid-Infrared Spectroscopy. Front. Plant Sci. 13:867555. doi: 10.3389/fpls.2022.867555

The pomegranate kernel oil has gained global awareness due to the health benefits associated with its consumption; these benefits have been attributed to its unique fatty acid composition. For quality control of edible fats and oils, various analytical and calorimetric methods are often used, however, these methods are expensive, labor-intensive, and often require specialized sample preparation making them impractical on a commercial scale. Therefore, objective, rapid, accurate, and cost-effective methods are required. In this study, Fourier transformed near-infrared (FT-NIR) and mid-infrared (FT-MIR) spectroscopy as a fast non-destructive technique was investigated and compared to qualitatively and quantitatively predict the quality attributes of pomegranate kernel oil (cv. Wonderful, Acco, Herskawitz). For qualitative analysis, principal component analysis (PCA) and orthogonal partial least squares discriminant analysis (OPLS-DA) was applied. Based on OPLS-DA, FT-MIR spectroscopy resulted in 100% discrimination between oil samples extracted from different cultivars. For quantitative analysis, partial least squares regression was used for model development over the NIR region of 7,498–940 and 6,102–5,774 cm^{-1} and provided the best prediction statistics for total carotenoid content (R^2, coefficient of determination; RMSEP, root mean square error of prediction; RPD, residual prediction deviation; $R^2 = 0.843$, RMSEP = 0.019 g β-carotene/kg, RPD = 2.28). In the MIR region of 3,996–1,118 cm^{-1}, models developed using FT-MIR spectroscopy gave the best prediction statistics for peroxide value ($R^2 = 0.919$, RMSEP = 1.05 meq, RPD = 3.54) and refractive index ($R^2 = 0.912$, RMSEP = 0.0002, RPD = 3.43). These results demonstrate the potential of infrared spectroscopy combined with chemometric analysis for rapid screening of pomegranate oil quality attributes.

Keywords: *Punica granatum* L., oil quality, partial least squares regression, discriminant analysis, infrared spectroscopy

INTRODUCTION

Pomegranate and its co-products have gained traction in research and application for their nutraceutical and medicinal properties (Seeram et al., 2006; Opara et al., 2009). Pomegranate fruit can be divided into two fractions: edible and non-edible fractions. The edible portion contains arils and each aril contains a kernel (woody portion; O'Grady et al., 2014; Arendse et al., 2016). Pomegranate oil is derived from the kernel of the fruit and studies over the years have reported that the oil derived from the kernels have radical scavenging activity, anti-inflammatory, anti-tumoral and anti-diabetic properties (Lansky et al., 2005; Lansky and Newman, 2007; Jing et al., 2012; Fernandes et al., 2015; De Melo et al., 2016). These properties have been linked to its unique phenolic and fatty acid composition (Seeram et al., 2006; Khoddami et al., 2014; Fernandes et al., 2015). Pomegranate oil carries a higher premium compared to other oils such as olive and avocado oil, the premium may be due to its unique fatty acid composition only found within pomegranates as well as its high phytochemical composition. Thus pomegranate oil, among others is highly susceptible to adulteration with cheaper alternatives (Uncu et al., 2020).

To evaluate the chemical constituents in oil products, standard analytical methods such as high-performance liquid chromatography and various colorimetric methods are used (Dieffenbacher and Pocklington, 1991; Aluyor et al., 2009). These methods are used to provide precise and accurate measurements of quality attributes. However, their approach is often time-consuming, expensive, and not always practical for large-scale commercial applications as it involves the use of trained sensory panelists or individuals. These drawbacks have promoted research interest in developing objective and non-invasive techniques for faster and less expensive assessment of oil quality attributes.

Due to its rapid, accurate, simple, and cost-effective way to evaluate chemical constituents, infrared (IR) spectroscopy in combination with chemometrics is one of the widely used non-destructive tools used by the food and beverage industry for quality testing and analysis (Sinelli et al., 2010; Becker and Yu, 2013; Shi and Yu, 2017). IR spectroscopy is appropriate for predicting compounds containing polar functional groups such as –OH, C–O, and N–H. In the agricultural industry, IR spectroscopy in the near-infrared (NIR, 12,500–4,000 cm^{-1}) and the mid-infrared (MIR, 4,000–400 cm^{-1}) spectral region has been applied as a non-destructive analytical tool. Fourier transform infrared spectroscopy (FT-IR) uses the mathematical process (Fourier transform) to translate the raw data (interferogram) into the actual spectrum. FT-IR spectrometers have recently replaced dispersive instruments, due to their superior speed and sensitivity. FT-IR spectrometers have several prominent advantages over dispersive IR spectrometers. A better signal-to-noise ratio of the spectrum compared to the previous generation infrared spectrometers. FT-IR spectrometers have a higher wavenumber accuracy and low error range (±0.01 cm^{-1}). Their scan time is short (approximately 1 s) and has a high resolution (0.1–0.005 cm^{-1}; Hsu, 1997).

In combination with chemometric tools, both Fourier transform near-infrared spectroscopy (FT-NIRs) and Fourier transform mid-infrared spectroscopy (FT-MIRs) has several advantages and limitations. For instance, FT-NIRs has inexpensive components due to low-cost materials such as glass and quartz compared to FT-MIRs. FT-NIRs also use more robust components, and it is easier to manufacture rugged instruments, involving no moving parts. FT-MIRs in contrast contain more spectral information due to the higher resolution of the fundamental vibrational absorption bands and can identify very complex or similar structures compared to the broad overtone and combination absorption bands in the NIR region (Socaciu et al., 2009; Manley, 2014; Shi and Yu, 2017). Another advantage of FT-MIRs includes fundamental vibrations of molecular bonds within a sample that occur in the "fingerprint" region, making the spectral profiles very sensitive; even very similar molecules can produce quite distinct spectral bands. Compared to FT-NIRs, the absorption bands of the spectra are very broad and overlapped as a result of many chemically different samples which give rise to almost indistinguishable spectral profiles. A detailed description of their advantages and limitations has been reviewed by Arendse et al. (2020).

FT-IR spectroscopy has been successfully used to classify geographical locations to classify geographical sources of oils (Lin et al., 2012) and detect adulteration in a variety of oil products (Yang et al., 2005; Gurdeniz and Ozen, 2009). Several studies have highlighted the application of IR spectroscopy for varying analytical quality attributes evaluation for a variety of oil products. Some of the major attributes accessed using IR spectroscopy include phenolic content, carotenoid content, peroxide value, refractive index, yellowness index, and fatty acids composition. These have been carried out for different oil products like olive oil (Inarejos-García et al., 2013; Cayuela and García, 2017), palm oil (Mba et al., 2014), maize oil (Kahrıman et al., 2019) and vegetable oil (Pereira et al., 2008).

Considering that the chemical composition of pomegranate oil may differ depending on the cultivar or growing region. To our knowledge, limited studies for the application of both FT-NIRs and FT-MIRs for evaluating quality attributes of pomegranate kernel oil, but also limited studies involved testing the robustness of PLS calibration models. The robustness of calibration models has become a critical issue in the application of vibrational spectroscopic techniques and an active area of research (Nicolaï et al., 2007; Magwaza et al., 2014). Our study attempts to evaluate the effects of cultivar differences on the robustness of calibration models and the ability of both FT-NIRs and FT-MIRs to qualitatively classify pomegranate oil based on different cultivars. The development of methods that combines FT-IR spectroscopy and chemometrics has the potential of providing novel input into non-destructive oil quality prediction for both authentication and adulteration application. Therefore, this study is aimed at investigating the feasibility of Fourier transform near-infrared and mid-infrared spectroscopy in evaluating pomegranate kernel oil quality both qualitatively [using principal component analysis (PCA) and orthogonal partial least squares discriminant analysis (OPLS-DA)] and quantitatively [*via* partial least squares regression (PLSr)]. However, very few studies on Vis/NIRS applications in fruit.

MATERIALS AND METHODS

Fruit Supply and Processing

Three different pomegranate cultivars (cv. Wonderful, Acco, Herskawitz) were procured from Sonlia pack-house, Wellington, Western Cape region. A total of 180 fruit or 60 fruit per cultivar was used for this study. At the research laboratory, fruit without any physical defects was sorted and manually cut open for the edible aril portion at ambient conditions (21°C ± 65% RH). Cheesecloth was employed to separate kernels from the arils. Kernels were extracted from arils and then washed with distilled water to eliminate the residual aril sacs before being dried at a temperature of 60°C for 24 h in a hot air oven (PROLAB, South Africa). Pomegranate kernels were dried to a moisture content of 1.7 wt. % (dry basis). After drying the seed the final seed weight averaged 12 ± 2.5 g per fruit. Dried pomegranate kernels were then packed in a polyethylene bag and stored at −20°C until further processing.

Oil Extraction and Yield

In this study, pomegranate oil was extracted using the solvent extraction method as described by Ampem (2017). Dried kernels were grinded into a powder with a particle size of 0.25 mm using a Sunbeam coffee grinder (Model SCG-250, 60 g capacity, South Africa) in preparation for oil extraction (Eikani et al., 2012). Hexane solvent was used to extract oil from the kernel powder. Pomegranate kernel powder (30 g) was weighed into a glass flask and extracted twice, respectively, with 300 ml of hexane solvent at a time, reaching a total volume of 600 ml solvent solution for each sample. The mixture (600 ml) was sonicated in an ultrasonic bath (Model DC 400H, Haifa, Israel) which was operated at 40°C for 40 min. The oil filtrates from repeated extractions were pooled and recovered through distillation using a rotary evaporator (Heidolph Instruments GmbH & Co. KG, Germany). Thereafter, samples were placed within a vacuum oven at 60°C for 1.5 h to remove any remaining hexane solution (Parashar et al., 2009). A total of 6 ml oil was obtained from each fruit and transferred into a 9 ml glass tube and stored in a dark environment at room temperature until further analysis. A total of 45 oil samples composed of 15 samples each from three different cultivars (Acco, Wonderful, Herskawitz) were used for this study.

Spectral Acquisition

The Alpha-P ATR FT-IR spectrometer (Bruker Optics, Ettlingen, Germany) and the Multi-purpose analyser (MPA) spectrometer (MPA, Bruker Optics, Ettlingen, Germany) were used for spectral data acquisition. Samples were kept in 8 mm glass vials, and sample temperature was maintained at ±50°C using a heating block before spectra recording. This was to ensure that sample temperature was stable as studies have shown temperature to impact the intensity of the bands (Jiang et al., 2008; Cayuela and García, 2017; Özdemir et al., 2018). The temperature of 50°C was chosen through preliminary trials and consultation with Bruker Optics, South Africa. For the MPA spectrometer, the spectral data were acquired over the range of 12,500 to 4,000 cm^{-1} (scanning resolution 4 cm^{-1}; scanner frequency 10 kHz; background with air, 128 scans). The spectral acquisition occurred almost immediately for the Multi-purpose analyser (MPA) spectrometer since the instrument does not have a temperature control system. For the Alpha-P ATR FT-IR spectrometer, sample spectral data were acquired over the range of 4,000–400 cm^{-1}. The Alpha-P spectrometer was equipped with a diamond crystal plate (area 2 mm^2) that maintained the sample temperature at 50°C. The temperature was monitored using OPUS software and spectral acquisition would only occur when the diamond crystal plate and sample reached a temperature of 50°C. The average time taken to acquire spectral data for one sample was 120 s using the following instrument settings: 4 cm^{-1} resolution scan, 10 kHz scanner frequency and 128 averaged scans per spectrum. The sample stage was cleaned in-between measurements with soft paper and undiluted methanol to avoid cross-contamination (Foudjo et al., 2013).

Reference Measurements

Refractive Index

The refractive index of pomegranate oil was measured at ambient temperature (21 ± 3°C) with a calibrated Abbé refractometer, Model 302 (ATAGO Co. Ltd., Japan). Three drops of pomegranate oil were loaded onto the refractometer prism, and refractive index values were reported as mean ± standard error (SE, $n = 3$) for each sample. After each measurement, the prism was cleaned with petroleum ether followed by distilled H_2O and dried with tissue paper.

Yellowness Index

Yellowness index indicates the degree of yellowness associated with scorching, soiling, and general product degradation by light, chemical exposure, and processing. The yellowness index of pomegranate oil was evaluated based on the CIE L*a*b* coordinates from a calibrated Minolta Chroma Meter, Model CR-400 (Japan). The yellowness index was calculated as described by Pathare et al. (2013).

$$YI = \frac{142.86 * b^*}{L^*} \quad (1)$$

Total Phenolic Content

Total phenolic content was measured using the Folin–Ciocalteau (Folin C) assay as reported by Makkar et al. (2007) with modification, according to Fawole et al. (2012). Briefly, pomegranate oil (0.5 ml) was dissolved in 14.5 ml of 50% aqueous methanol. An aliquot of 50 µl was diluted with 450 µl of 50% methanol (v/v) before the addition of 1 N Folin C (500 ml) and 2% sodium carbonate (2.5 ml). The mixture was vortexed and stored in a dark environment for 30 min before the absorbance was recorded at 760 nm against blank aqueous methanol. The total phenolic content of pomegranate kernel oil was extrapolated and reported as milligram gallic acid equivalent (mg GAE/g oil). The results for each sample were presented as mean ± SE ($n = 3$).

Total Carotenoid Content

Total carotenoid content was evaluated as decribed by Biehler et al. (2010) and Siano et al. (2015) with modification. In brief, pomegranate oil (0.1 ml) was dissolved in 10 ml dimethyl sulfoxide (DMSO). The total carotenoid content of the resulting mixture was recorded at 440 nm and 460 nm, against a blank DMSO solvent. A standard curve consisting of 0.02–0.15 mg/ml DMSO solution was prepared following the same procedure. The results for total carotenoid content were expressed as gram (g β-carotene/kg) of pomegranate oil, and the results for each sample were presented as mean ± SE ($n = 3$).

Peroxide Value

Peroxide value was performed as described by Ampem (2017). Briefly, pomegranate oil (0.2 ml) was dissolved in 9 ml of chloroform: methanol mixture (7:3 ratio) in screw-capped vials. The resultant solution was mixed with 50 µl of 10 Mm xylenol orange methanol solution and 50 µl of 36 Mm iron (II) chloride solution and vortexed, respectively. The peroxide value of the resulting mixture was estimated following absorbance reading at 560 nm. Peroxide value was expressed in milli-equivalents (meq) of active oxygen per kilogram of oil and calculated using the following equation:

$$PV = \frac{(A_S - A_B) \times mi}{W \times 55.84 \times 2} \quad (2)$$

Where

PV = peroxide value.

A_B = absorbance of the blank.

A_S = absorbance of the sample.

mi = the inverse of the slope (Obtained from calibration curve).

W = weight of the sample (g). 55.84 is the atomic weight of iron.

Chemicals and Reagents

All chemical reagents were obtained from Sigma–Aldrich–Fluka Co. Ltd. (South Africa) unless otherwise stated.

Chemometric Data Analysis

The spectral acquisition occurred with OPUS software (version 7.0), while data processing and analysis were achieved with SIMCA and OPUS software. Qualitative analysis (modeling of cultivar difference) was carried out using PCA and OPLS-DA using SIMCA software, and quantitative analysis (developing calibration models) was carried out with PLSr using OPUS software. For this study, several preprocessing methods were evaluated, baseline correction spectra were subjected to several filtering techniques, which included Savitzky–Golay transformation (first derivative), multiplicative scattering correction (MSC), and standard normal variate (SNV) correction. Separate OPLS-DA models were built for both NIR and MIR spectral data, each pair of two successive stages by using a dummy variable with a value of 1 assigned to samples that belonged to a specific group and a value of 0 to samples that did not belong to that group.

Partial Least Square (PLS) Regression Analysis of Spectral Data

For the quantitative analysis of spectral data, the spectral parameters used for multivariate analysis were optimized by subjecting spectral data to the software's "Optimise" function. This function provides a combination of parameters such as different pre-processing methods and wavenumber regions and ranks results based on the number of latent variables and root-mean-square error of cross-validation (RMSECV) values.

The development of calibration models for the infrared (NIR and MIR) spectra was performed by applying partial least squares regression analysis (including mean centering). Spectral outliers were identified as having high residual variance from the zero line. Concentration outliers present in the dataset were removed and successive rounds of PLSr were done with the reduced dataset. A total of three outliers were removed, and the resultant calibration models were validated with the test dataset. For PLSr analysis, cross-validation was applied by the Leave-one-out method, which calculates potential models excluding one observation at a time. Calibration models was developed by combining all three cultivars and then randomly splitting the dataset into 2:1 subsets, i.e., calibration (70%) and prediction (30%) sets, each subset containing sufficient samples of each cultivar.

The performance of PLS models was evaluated according to the following prediction statistics: coefficient of determination [R^2; Eq. (3)], root mean square error of validation [RMSEV; Eq. (4)] and root mean square error of prediction [RMSEP; Eq. (5)]. Other statistical indicators for this study include models bias [Eq. (6); which gives an indication of the systematic error in the predicted values and its calculated values] and the residual prediction deviation [RPD; Eq. (7)] value, which is defined as the ratio of the standard deviation of the reference data of the validation set to the RMSEP value (which indicates the efficiency of calibration models). RPD values can be used to evaluate the performance of the developed models (Williams, 2014). According to Nicolaï et al. (2007), models with RPD values below 1.5 is unreliable, while values between 1.5 and 2.0 indicate models can be used for rough prediction, while RPD values between 2.0 and 2.5 can be used for quantitative predictions, any values above 3 are considered satisfactory. The best-performing models were selected based on the best overall performance (low RMSEP, low RMSEV, high R^2, and higher RPD, and low bias).

$$R^2 = 1 - \frac{\sum (y_{cal} - y_{act})^2}{\sum (y_{cal} - y_{mean})^2} \quad (3)$$

$$RMSEE = \sqrt{\frac{1}{M - R - 1} \times SSE} \quad (4)$$

$$RMSEP = \sqrt{\sum \frac{(y_{pred} - y_{act})^2}{n}} \quad (5)$$

$$Bias = \frac{1}{n}\sqrt{\Sigma\left(y_{pred} - y_{act}\right)^2} \quad (6)$$

$$RPD = \frac{SD}{RMSEP} \quad (7)$$

Where n is number of spectra, y_{act} is actual value, y_{mean} is mean value, y_{cal} is calculated value, y_{pred} is the predicted value of the attribute, M is the number of calibration samples, R is the rank, SSE is the sum of squared error, SD is the standard deviation of reference values.

Statistical Analysis

To demonstrate that the prediction of the different selected quality parameters is from the actual IR spectra and not due to possible correlations with the other measured parameters, the reference data was subjected to Pearson's correlation test using Statistica software (Statistica 16.0, StatSoft Inc., Tulsa, OK, United States).

RESULTS AND DISCUSSION

Distribution of Calibration and Validation Reference Data

For this study, reference data for the different parameters were normally distributed around the mean (**Table 1**). According to Lu et al. (2006), the accuracy and validation of calibration models normally depend on large variation in the present within the sample set in the physical and biochemical reference data. However, reports have indicated superior model accuracies using NIR spectroscopy when data with a large sample variation within the calibration and validation set is being considered (Magwaza et al., 2013, 2014). **Table 2** presents the standard deviation, minimum-to-maximum range, and CV% statistics of most of the parameters. Most parameters had high CV% values of up to 43% for both calibration and validation data sets covering a wide range of values, aside from the refractive index. Pearson correlation was applied to investigate the interrelationships between selected reference data of pomegranate oil. From the result, it can be deduced that the prediction of these quality parameters (phenolics, carotenoids), and their concentrations should not correlate with one another. Correlation tests indicate that no correlation was observed between chemical indices such as phenolic and carotenoid content (0.227). Similarly, phenolic and carotenoid content showed no correlation with peroxide value (−0.009, 0.334) refractive index (0.260, 0.176) or oil yellowness index (0.172, 0.215). These results suggest that the prediction of the different studied parameters is actually from the IR spectra.

FT-NIR and FT-MIR Spectral Characteristics of Pomegranate Oil

NIR spectroscopy is a powerful non-destructive technique used for the detection of various compounds, the NIR spectrum provides information on the vibrational absorption of hydroxyl (O–H), amido (N–H), and C–H bonds. The average for both NIR and MIR spectra of pomegranate oil is presented in **Figure 1**. Pomegranate is highly abundant in punicic acid (C18:3-9c), linoleic acid (C18:2), and oleic acid (C18:1). Band assignment was done according to the literature (Foudjo et al., 2013; Inarejos-García et al., 2013; Özdemir et al., 2018). In the NIR region, bands around 8,451 cm^{-1} arise from second overtones of C–H stretching vibrations, while those at 7,502 and 7,498 cm^{-1} are due to the combination bands of C–H in fatty acids. The bands at 5,774 and 5,450 cm^{-1} can be ascribed, according to literature, from the first overtone of C–H stretching vibrations of methyl, methylene, and ethylene groups (Sinelli et al., 2011; Özdemir et al., 2018). Small bands at 4,659 and 4,597 cm^{-1} are associated with combination bands of C–H and C–O stretching vibration. Several bands dominate the MIR spectra at 2,918, 2,556, 1,837, 1,463, 1,377, 1,238, 1,163, 1,114, 1,099, and 721 cm^{-1}. The absorbance band at 3,013 cm^{-1} has been associated with the stretching of the functional group =C-H (cis-) found in unsaturated fatty acids such as punicic acid (Guillén and Cabo, 1997). Absorbance at 2,924 and 2,852 cm^{-1} are due to bands from asymmetric CH_2 stretching vibration of acyl chains and methylene chains in fatty acids (punicic acid, linoleic acid, and oleic acid; Guillén and Cabo, 1997; Sun, 2009). The major band at 1,743 cm^{-1} arises from C=O stretching vibrations of ν(C=O) ester in fatty acids (Guillén and Cabo, 1997, Sun, 2009). The band at 1,238, 1,163 and 1,114 cm^{-1} has been associated with C-O or CH_2 stretching or bending vibration out-of-plane of functional groups from fatty acids (Guillén and Cabo, 1997; Rohman and Che, 2011). The band at 721 cm^{-1} corresponds to the CH_2 rocking mode (Yang et al., 2005; Sinelli et al., 2010). The spectral profile for pomegranate oil is comparable to those reported for other oil

TABLE 1 | Mean, standard deviation (SD), range, and coefficient of variation (CV) for calibration and validation subsets for selected parameters of pomegranate kernel oil (sample number = 42).

Parameters	Calibration set				Validation set				Overall CV%
	Mean	SD	Min	Max	Mean	SD	Min	Max	
Peroxide value	7.311	4.219	1.745	16.342	7.478	3.873	1.943	13.517	54.758
Refractive index	1.520	0.0008	1.517	1.523	1.521	0.0010	1.519	1.522	0.0628
Total carotenoid content (g β-carotene/kg)	0.0977	0.0418	0.0640	0.270	0.100	0.0436	0.0650	0.232	43.158
Total phenolic content (mg GAE/g oil)	3.987	0.745	3.113	5.221	3.702	0.436	3.223	4.343	15.247
Yellowness index	54.226	18.540	23.141	97.280	55.690	21.842	23.946	96.416	36.706

TABLE 2 | Model evaluation statistics for quality parameters of pomegranate kernel oil as determined from FT-NIR and FT-MIR spectroscopy (sample number = 42).

Parameter	Acquisition mode	Pre-processing	Wavenumbers range (cm^{-1})	Calibration			Validation					
				LV	R^2	RMSEV	R^2	RMSEP	RPD	Bias	Slope	Corr.
Peroxide value	FT-NIRs	1st + MSC	7,500–6,098, 5,450–4,597	3	0.833	1.68	0.833	1.78	2.80	−0.866	0.823	0.935
	FT-MIRs	2nd	3,996–2,556	3	0.959	0.99	0.919	1.05	3.54	−0.036	0.829	0.965
Refractive index	FT-NIRs	2nd	9,400–6,098, 5,450–4,597	4	0.904	0.0003	0.863	0.0003	3.44	−0.000	0.906	0.956
	FT-MIRs	2nd	3,996–1,118	4	0.960	0.0002	0.912	0.0002	3.43	0.000	0.867	0.958
Total carotenoid content	FT-NIRs	SLS	7,498–940, 6,102–5,774	5	0.892	0.015	0.843	0.019	2.28	−0.003	0.893	0.944
	FT-MIRs	2nd	3,996–3,635, 2,558–1837, 760–399	3	0.958	0.002	0.632	0.007	1.72	0.002	0.543	0.836
Total phenolic content	FT-NIRs	SLS	7,502–4,597	2	0.332	0.85	0.185	1.39	1.26	0.657	0.226	0.774
	FT-MIRs	1st	3,996–3,965, 1,479–758	2	0.635	0.47	0.568	0.37	1.57	−0.066	0.879	0.814
Yellowness index	FT-NIRs	2nd	8,451–7,498, 6,102–4,597	5	0.556	13.60	0.531	14.30	1.49	2.64	0.543	0.740
	FT-MIRs	2nd	2,918–2,556, 1,120–758	1	0.307	11.90	0.205	15.00	1.15	−3.10	0.267	0.491

R^2, coefficient of determination; RMSEV, root mean square error of validation; RMSEP, root mean square error of prediction; RPD, residual predictive deviation; LV, latent variable; Corr., correlation coefficient; 1st, first derivative; 2nd, second derivative; MSC, multiplicative scattering correction; SLS, straight line subtraction.

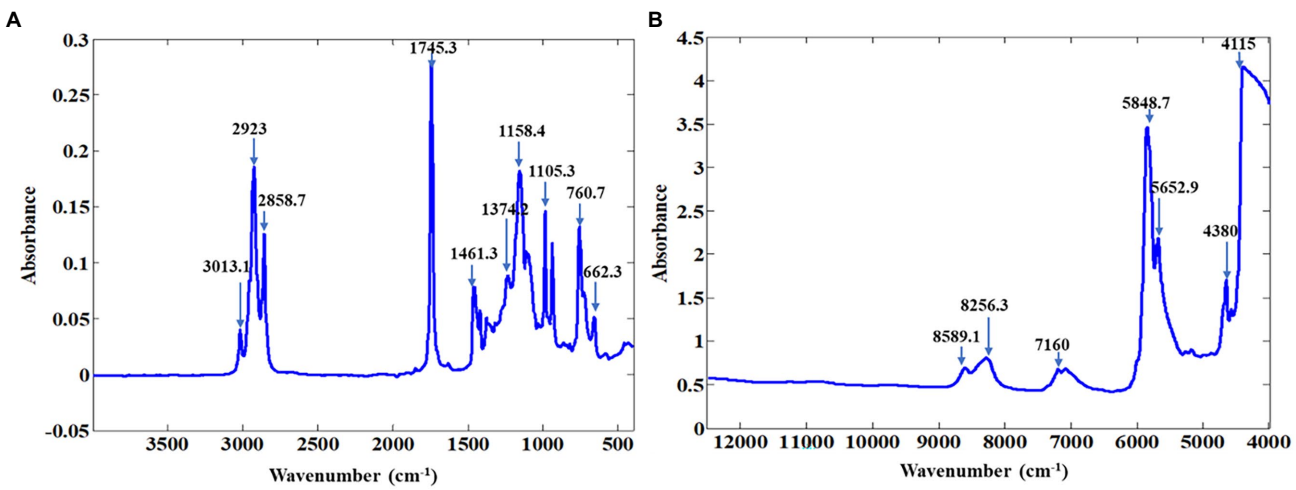

FIGURE 1 | Representative absorbance spectra for ATR-FT-MIR **(A)** and FT-NIR **(B)** of pomegranate kernel oil.

samples like avocado oil (Foudjo et al., 2013), virgin olive oil (Dupuy et al., 2010; Sinelli et al., 2010), rapeseed oil blend (Ma et al., 2014), and palm oil (Mba et al., 2014).

Qualitative Analysis of Pomegranate Oil Using PCA and OPLS-DA

Unsupervised Clustering (PCA)

PCA is, arguably, one of the most useful and widespread unsupervised methods used in chemometrics for its exploratory data analyses (Cozzolino et al., 2011; Jolliffe and Cadima, 2016). PCA was carried out to explore the possible clustering of samples and evaluate the influence of cultivar on oil quality. PCA is a statistical technique that is used to investigate the structure of a data set and attempts to model the total variance of the original data set *via* the uncorrelated principal components (Filzmoser and Todorov, 2011; Gautam et al., 2015). PCA maximizes the variation in the data set projects the main variation onto a few latent variables and presents sample groupings as clusters in PCA score plots with the corresponding loadings plots (Wold et al., 1987).

Preliminary assessment of both NIR and MIR spectra was performed using PCA, to examine the effects of cultivar differences on pomegranate oil quality. For NIR baseline-corrected spectra, the first two principal components (PC) were used in

relation to the chemical variation within the sample sets (**Supplementary Table 1**). By plotting all 45 data points, scores from the first two PC explained 100% (PC_1 = 99.97%, PC_2 = 0.0026%) of the total variation within the dataset. One dispersed group (cv. Herskawitz) was observed, which revealed that the first PC contributed most to the sample distribution, where samples were mainly stretched along the PC_1 region (**Figure 2A**). However, the PCA plot revealed no clear groupings according to chemical variation within the data set, with cultivar Acco co-clustering with cultivar Wonderful. The score plots from the FT-MIR spectra for oil samples showed that the first two PC explained a total of 91.38% (PC_1 = 91%, PC_2 = 0.38%) of the variation (**Supplementary Table 2**). Examination of the PCA scores plot generated from three cultivars showed well-defined sample clusters for both Acco and Wonderful cultivars with both co-clustered with cv. Herskawitz (**Figure 2B**). This observation showed that despite its simplified approach, IR spectroscopy could be used to differentiate between different cultivars based on spectral data.

Supervised Clustering/Discriminant Analysis (OPLS-DA)

Orthogonal projections to latent structures discriminant analysis (OPLS-DA) is a supervised classification technique that isolates a predictive component and integrates an orthogonal correction filter, to differentiate the variation within the dataset (Bylesjö et al., 2006). OPLS-DA is often used as an alternative method, where PCA cannot show clear clustering. OPLS-DA works through the projection of data and is guided by known class information, thus offering increased separation projection in comparison to PCA (Trygg et al., 2007). This is because OPLS-DA score plots are rotated so that between-class variation is projected on the predictive component, while within-class variation, is projected on the first y-orthogonal component (Wiklund et al., 2008). Therefore, several authors classify that OPLS-DA models are easier to interpret than PLS-DA models, although both methods have the same predictive power (Trygg and Wold, 2002; Trygg et al., 2007; Musingarabwi et al., 2016).

To see the effects of cultivar differences on the quality characteristics of pomegranate oil, OPLS-DA was performed on both FT-NIR and FT-MIR spectra (**Figure 3**). For FT-NIRs, the application of OPLS-DA showed two well-clustered groups (cv. Wonderful and Acco), while pomegranate cultivar Herskawitz remained dispersed and co-clustered with cultivar Wonderful (**Figure 3A**). Whereas, for FT-MIRs, the application of OPLS-DA successfully discriminated and separated all three cultivars into well-defined cluster groups (**Figure 3B**).

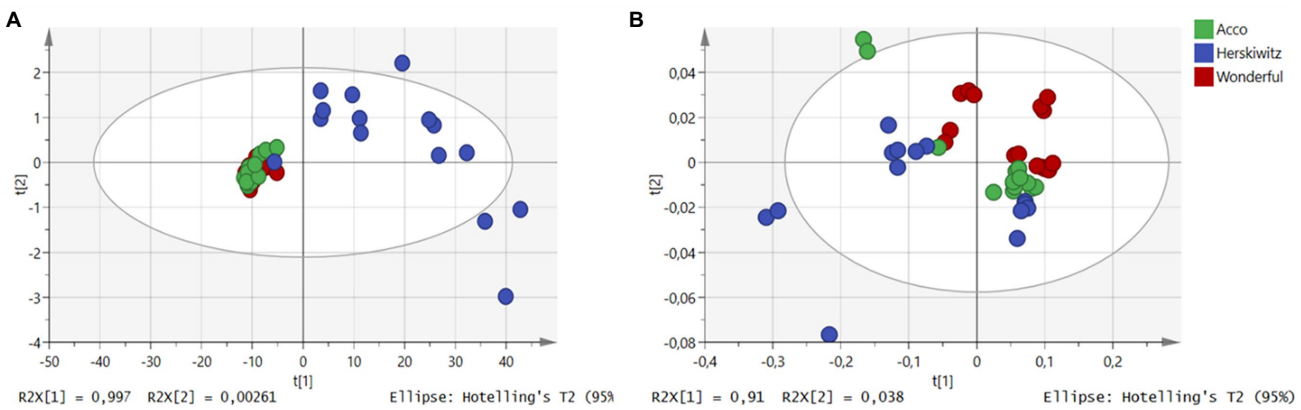

FIGURE 2 | PCA score plots for NIR spectral data **(A)** and MIR spectral data **(B)**. The colour represents different cultivars of extracted pomegranate oil, green (Acco), blue (Herskawitz), and red (Wonderful) (sample number = 42).

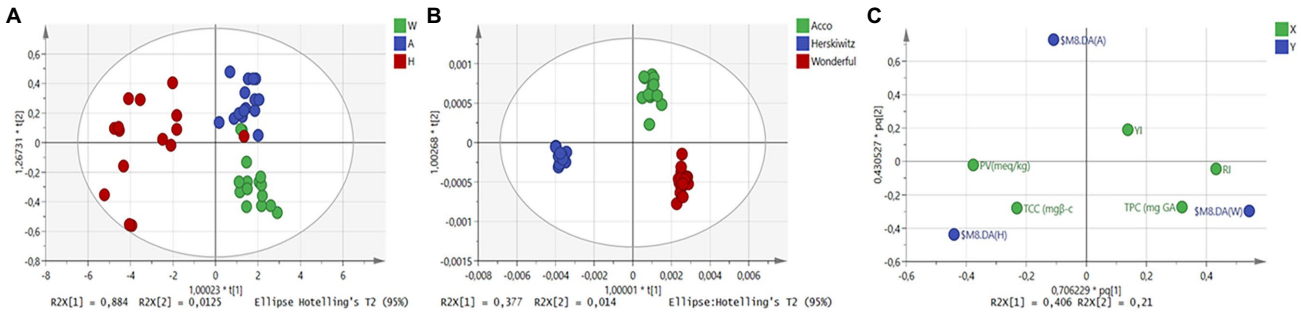

FIGURE 3 | OPLS-DA scores plots for NIR baseline-corrected spectra **(A)**, MIR baseline-corrected spectra **(B)**, and reference data plot **(C)**. The colour in **(A)** and **(B)** represents different cultivars (Acco, Wonderful, Herskawitz) of extracted pomegranate oil (sample number = 42).

A similar approach to qualitatively evaluate the quality of grape berries was performed by Musingarabwi et al. (2016). These authors reported that the application of PCA and OPLS-DA successfully discriminated against and separated different developmental stages of grape berries into well-defined cluster groups. The ability to successfully discriminate between different cultivars by both PCA and OPLS-DA using IR spectra has the potential for the application of authentication and adulteration assessment of pomegranate oil.

Interestingly, when plotting the reference data for each cultivar that is based on the reference measurements, the cultivar Herskawitz was highly associated with peroxide value and total carotenoid content (**Figure 3C**). The Wonderful cultivar has been grouped with total phenolic content and refractive index. While cv. Acco has shown an association with the yellowness index. These results suggest that the Wonderful cultivar has the highest concentration of unsaturation fatty acids since fatty acids are directly proportional to the refractive index of the oil. Similarly, pomegranate (cv. Wonderful) has the highest phenolic content, suggesting that fruit consumption for this particular cultivar, increases the intake of phenolic compounds which have been linked to antioxidant compounds. For color attributes, pomegranate oil obtained from Acco cultivar was the most suitable to assess the characteristic yellow coloration. While the cultivar Herskawitz has a high peroxide value suggesting that oil obtained from Herskawitz cultivar is more susceptible to oxidation. The differentiation between cultivars may be due to cultivar differences or fruit maturity status.

Quantitative Analysis of Pomegranate Oil Using PLS Regression

The best FT-NIRs and FT-MIRs models were developed using 17 points, first derivative, second derivative, and straight-line subtraction, respectively. The model for each parameter was selected based on the evaluation of statistical parameters that gave higher R^2, high RPD values, lowest RMSEV and RMSEP, and lowest number of latent variables. The overall performance of the developed models for all quality parameters is represented in **Table 2**. Scatter plots of FT-NIR and FT-MIR spectroscopy for predicted data plotted against measured reference data are presented in **Figure 4**. Models developed in the NIR and MIR spectral regions had a major influence on the regression statistics. All three cultivars were combined to create models with high robustness and variability.

The refractive index is an intrinsic property of oil measured based on light penetration through an oil sample (Aydeniz et al., 2014; Khoddami et al., 2014). Oil refractive index has been reported to be directly proportional to the degree of unsaturation of fatty acids and inversely related to its viscosity and can, therefore, be used to quantify the double bonds of fatty acids (Aydeniz et al., 2014; Khoddami et al., 2014). The statistical indicators for model fitness showed that both NIR

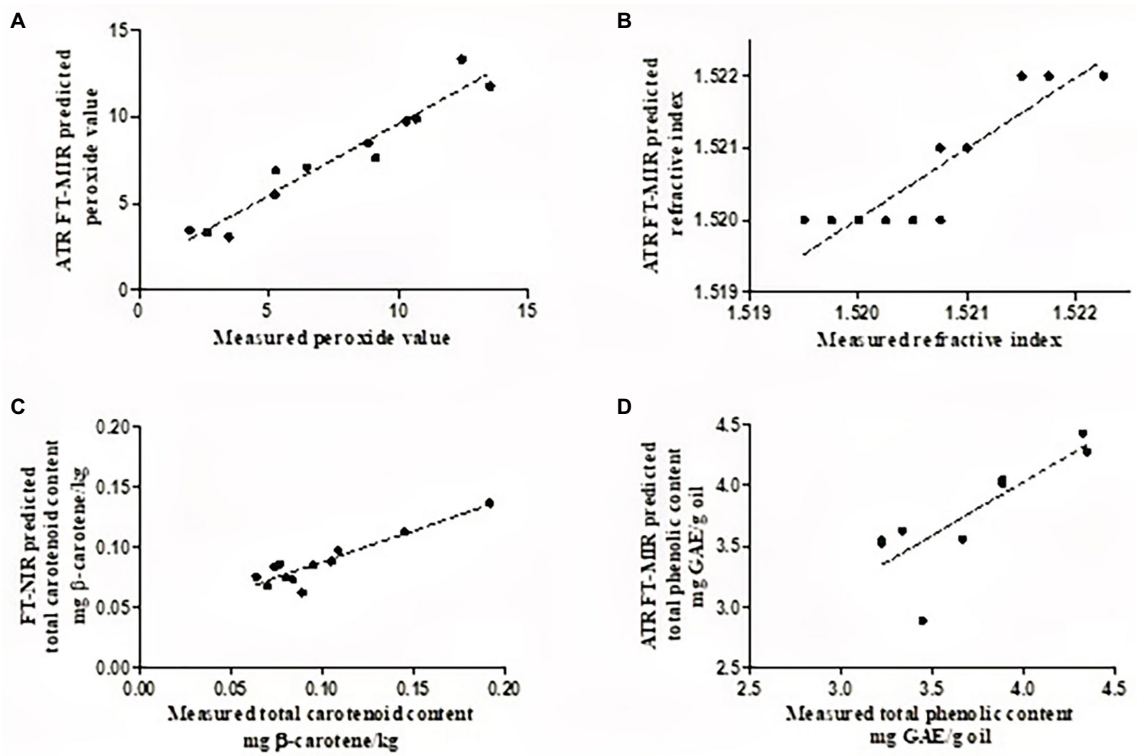

FIGURE 4 | Scatter plots of FT-NIR/FT-MIR predicted **(A)**, refractive index **(B)**, total carotenoid content **(C)**, and total phenolic content **(D)**, plotted against destructively acquired reference data (sample number = 42).

and MIR spectra yielded relatively accurate PLS models for refractive index. PLS model development in the FT-MIRs provided slightly better prediction statistics ($R^2 = 0.912$, RMSEP = 0.0002, and RPD = 3.43) compared to the FT-NIRs ($R^2 = 0.863$, RMSEP = 0.0003, and RPD = 3.44; **Table 2**). The wavenumber range used during the development of the PLSr model for the refractive index was between 3,996 and 1,118 cm^{-1}, which is within the range reported by Yang and Irudayaraj (2001) for olive oil. The RPD value suggests the model developed can provide a satisfactory prediction for refractive index, while the low bias (<0.0002) of the developed model suggests that the model was stable and non-sensitive to factors such as cultivar.

For quality control in edible fats and oils, oxidation is one of the main parameters used for oil products. Oxidation of fats and oils produces either primary (peroxides) or secondary oxidation products. The PLSr models developed for peroxide value has shown that the FT-MIRs provided better prediction statistics ($R^2 = 0.919$, RMSEP = 1.05 meq, and RPD = 3.54) compared to the FT-NIRs ($R^2 = 0.833$, RMSEP = 1.78 meq, and RPD = 2.80; **Table 2**). Similar values were observed for RMSEV and RMSEP, suggesting that the developed models were not overfitted. Furthermore, the developed models had low bias values (0.036–0.86) indicating robust fitting and stability. This indicates that the models were not sensitive to external factors such as different cultivars. The RPD value (3.54) for the developed model suggests that satisfactory predictions can be made with FT-MIRs.

FT-MIR spectroscopy has been used to evaluate the peroxide value of coconut oil, where the authors reported a high coefficient of determination ($R^2 = 0.982$) and low RMSEP values (0.4978 meq; Marina et al., 2013). The wavenumber range reported in this study for peroxide value is similar to those reported for the development of models for various oil products (Liang et al., 2013; Marina et al., 2015; Zahir et al., 2017). For total carotenoid content, the NIR region of 7,498–940 and 6,102–5,774 cm^{-1} provided better prediction statistics ($R^2 = 0.843$, RMSEP = 0.019 g β-carotene/kg) compared to FT-MIRs ($R^2 = 0.632$, RMSEP = 0.007 g β-carotene/kg), with RPD value of 2.28 suggesting that the model is fit for quantitative predictions. Similar prediction results for total carotenoid content were reported by Schulz et al. (1998) in essential oils, within the spectral region of 10,100 and 5,150 cm^{-1}. For total phenolic content, FT-MIRs in the region of 3,996 and 758 cm^{-1}, have been shown to provide rough predictions (RPD = 1.57), while those developed in the NIR region were shown to be unreliable (RPD = 1.26). Contrary to our results, Trapani et al. (2016) reported that the NIR spectral region of 12,500 to 4,000 cm^{-1} provided relatively good prediction statistics ($R^2 = 0.71$, RMSEP = 0.08 mg/kg dm) for total phenolic content in olive oil. Model development for the yellowness index gave relatively poor prediction statistics for both FT-NIRs and FT-MIRs (**Table 2**). Low RPD values and high bias characterized these models, suggesting that the developed models were unreliable, and overestimation may have occurred for these quality attributes. The developed calibration models were only performed using internal cross-validation and thus only applicable to the three selected cultivars. It is well known that the real challenge with calibration models is that their predictive performance almost always reduces when tested on unknown sources such as fruit maturity, seasonality, and growing regions. Thus future research should include more variability (growing regions and seasonality) to improve the model's robustness.

For this study, FT-MIRs were shown to be better suited for both qualitative and quantitative applications. The regression models developed within the MIR spectral region performed better than those developed within NIR spectral region. This can be because the mid-infrared spectrum contains wavenumbers for fundamental rotational molecular vibration, which is highly sensitive to specific chemical compositions. In contrast, the near-infrared spectrum is associated mainly with overtone and combination bands of fundamental transition, making it less reproducible and specific. Another advantage of ATR FT-MIR spectroscopy is temperature control *via* the ATR crystal, which reduces potential variation by maintaining constant sample temperature (Smyth and Cozzolino, 2011). However, FT-NIRS is more applicable to practical usage for online or inline implementation or the development of portable devices due to their relatively inexpensive instrumentation costs, more robust components, and it is easier to manufacture rugged instruments, involving no moving parts.

CONCLUSION

Classification of pomegranate oil quality according to their respective cultivars was possible with FT-IR spectroscopy. FT-MIRs spectra resulted in 100% discrimination between oil samples extracted from different cultivars using OPLS-DA. For quantitative prediction of various quality attributes, FT-MIRs predicted were able to predict three parameters (refractive index, peroxide value, total phenolic content) compared to FT-NIRS (refractive index, total carotenoid content). This study also revealed that pomegranate oil (cv. Wonderful) has been associated with a higher refractive index (indirect correlation with unsaturation fatty acids) and phenolic content compared to "Acco" and "Herskawitz." This studThe measurement of additional quality characteristics such as individual fatty acids will foreseeably improve the discrimination and prediction accuracy. Future research is required to improve the robustness of calibration models for both NIR and MIR spectroscopy by either increasing the sample size, including different growing locations and seasonality or by applying different chemometric techniques. The current knowledge obtained from this study has shown that chemical indices of pomegranate kernel oil differ even amongst cultivars and are detectable with both FT-NIR and FT-MIR spectroscopy. These chemical indices can not be used for quality evaluation but can be applied to effectively classify or discriminate between oil samples that have even slightly different chemical characteristics, making it a highly effective tool within the processing industry for authenticity and adulteration testing. The approach provides a powerful way to rapidly extract qualitative and quantitative information emanating from multiple spectral variables.

DATA AVAILABILITY STATEMENT

The original contributions presented in the study are included in the article/**Supplementary Material**, further inquiries can be directed to the corresponding author.

AUTHOR CONTRIBUTIONS

UO: conceptualization, methodology, funding acquisition, project administration, supervision, review, and editing. WP: project administration and supervision. HN: methodology, software and validation, review, and editing. EA: supervision, review, and editing. EO: data curation and writing—original draft preparation. All authors contributed to the article and approved the submitted version.

FUNDING

This work is based on the research supported wholly/in part by the National Research Foundation of South Africa (Grant Number: 64813). The opinions, findings, conclusions, or recommendations expressed are those of the author(s) alone, and the NRF accepts no liability whatsoever in this regard.

SUPPLEMENTARY MATERIAL

The Supplementary Material for this article can be found online at: https://www.frontiersin.org/articles/10.3389/fpls.2022.867555/full#supplementary-material

REFERENCES

Aluyor, E. O., Ozigagu, C. E., Oboh, O., and Aluyor, P. (2009). Chromatographic analysis of vegetable oils: a review. *Sci. Res. Essays* 4, 191–197. doi: 10.5897/SRE.9000267

Ampem, G. (2017). Quality attributes of pomegranate fruit and co-products relevant to processing and nutrition [dissertation/master's thesis], Stellenbosch, Stellenbosch University.

Arendse, E., Fawole, O. A., Magwaza, L. S., and Opara, U. L. (2016). Non-destructive characterization and volume estimation of pomegranate fruit external and internal morphological fractions using X-ray computed tomography. *J. Food Eng.* 186, 42–49. doi: 10.1016/j.jfoodeng.2016.04.011

Arendse, E., Nieuwoudt, H. H., Nturambirwe, J. F. I., Fawole, O. A., Magwaza, L. S., and Opara, U. L. (2020). Recent advancements on vibrational spectroscopic techniques for the detection of authenticity and adulteration in horticultural products with a specific focus on oils, juices, and powders. *Food Bioproc. Tech.* 14, 1–22. doi: 10.1007/s11947-020-02505-x

Aydeniz, B., Güneşer, O., and Yılmaz, E. (2014). Physico-chemical, sensory, and aromatic properties of cold press produced safflower oil. *J. Am. Oil Chem. Soc.* 91, 99–110. doi: 10.1007/s11746-013-2355-4

Becker, P. M., and Yu, P. (2013). What makes protein indigestible from tissue, cellular and molecular structure aspects. *Mol. Nutr. Food Res.* 57, 1695–1707. doi: 10.1002/mnfr.201200592

Biehler, E., Mayer, F., Hoffmann, L., Krause, E., and Bohn, T. (2010). Comparison of 3 spectrophotometric methods for carotenoid determination in frequently consumed fruits and vegetables. *J. Food Sci.* 75, C55–C61. doi: 10.1111/j.1750-3841.2009.01417.x

Bylesjö, M., Rantalainen, M., Cloarec, O., Nicholson, J. K., Holmes, E., and Trygg, J. (2006). OPLS discriminant analysis: combining the strengths of PLS-DA and SIMCA classification. *J. Chemometr.* 20, 341–351. doi: 10.1002/cem.1006

Cayuela, J. A., and García, J. F. (2017). Sorting olive oil based on alpha-tocopherol and total tocopherol content using near-infra-red spectroscopy (NIRS) analysis. *J. Food Eng.* 202, 79–88. doi: 10.1016/j.jfoodeng.2017.01.015

Cozzolino, D., Cynkar, W. U., Shah, N., and Smith, P. A. (2011). Multivariate data analysis applied to spectroscopy: potential application to juice and fruit quality. *Food Res. Int.* 44, 1888–1896. doi: 10.1016/j.foodres.2011.01.041

De Melo, I. L. P., de Carvalho, E. B. T., de Silva, A. M. O., Yoshime, L. T., Sattler, J. A. G., Pavan, R. T., et al. (2016). Characterisation of constituents, quality and stability of pomegranate seed oil (*Punica granatum* L.). *Food Sci. Technol.* 36, 132–139. doi: 10.1590/1678-457X.0069

Dieffenbacher, A., and Pocklington, W. D. (1991). "Standard methods for the analysis of oils, fats and derivatives," in *International Union of Pure and Applied Chemistry Division Commission on Oils, Fats, and Derivatives. 1st Supplement to the 7th Revised and Enlarged Edition* (Oxford, UK: Blackwell Scientific Publications), 2.303–2.801.

Dupuy, N., Galtier, O., Ollivier, D., Artaud, J., and Vanloota, P. (2010). Comparison between NIR, MIR, concatenated NIR and MIR analysis and hierarchical PLS model. Application to virgin olive oil analysis. *Anal. Chim. Acta* 666, 23–31. doi: 10.1016/j.aca.2010.03.034

Eikani, M. H., Golmohammad, F., and Homami, S. S. (2012). Extraction of pomegranate (*Punica granatum* L.) seed oil using superheated hexane. *Food Bioprod. Process.* 90, 32–36. doi: 10.1016/j.fbp.2011.01.002

Fawole, O. A., Opara, U. L., and Theron, K. I. (2012). Chemical and phytochemical properties and antioxidant activities of three pomegranate cultivars grown in South Africa. *Food Bioproc. Tech.* 5, 2934–2940. doi: 10.1007/s11947-011-0533-7

Fernandes, L., Pereira, J. A., Lopéz-Cortés, I., Salazar, D. M., Ramalhosa, E., and Casal, S. (2015). Fatty acid, vitamin E and sterols composition of seed oils from nine different pomegranate (*Punica granatum* L.) cultivars grown in Spain. *J. Food Compos. Anal.* 39, 13–22. doi: 10.1016/j.jfca.2014.11.006

Filzmoser, P., and Todorov, V. (2011). Review of robust multivariate statistical methods in high dimension. *Anal. Chim. Acta* 705, 2–14. doi: 10.1016/j.aca.2011.03.055

Foudjo, B. U. S., Kansci, G., Lazar, I. M., Lazar, G., Fokou, E., and Etoa, F. X. (2013). ATR-FTIR characterisation and classification of avocado oils from five Cameroon cultivars extracted with a friendly environmental process. *Environ. Eng. Manag. J.* 12, 97–103. doi: 10.30638/eemj.2013.012

Gautam, R., Vanga, S., Ariese, F., and Umapathy, S. (2015). Review of multidimensional data processing approaches for Raman and infrared spectroscopy. *EPJ Tech. Instrum.* 2, 1–38. doi: 10.1140/epjti/s40485-015-0018-6

Guillén, M. D., and Cabo, N. (1997). Infrared spectroscopy in the study of edible oils and fats. *J. Sci. Food Agric.* 75, 1–11. doi: 10.1002/(SICI)1097-0010(199709)75:1<1::AID-JSFA842>3.0.CO;2-R

Gurdeniz, G., and Ozen, B. (2009). Detection of adulteration of extra-virgin olive oil by chemometric analysis of mid-infrared spectral data. *Food Chem.* 116, 519–525. doi: 10.1016/j.foodchem.2009.02.068

Hsu, C. P. S. (1997). "Infrared spectroscopy," in *Handbook of Instrumental Techniques for Analytical Chemistry*. ed. F. A. Settle (Upper Saddle River, NJ: Prentice Hall PTR), 247–283.

Inarejos-García, A. M., Gómez-Alonso, S., Fregapane, G., and Salvador, M. D. (2013). Evaluation of minor components, sensory characteristics, and quality of virgin olive oil by near infrared (NIR) spectroscopy. *Food Res. Int.* 50, 250–258. doi: 10.1016/j.foodres.2012.10.029

Jiang, H. Y., Xie, L. J., Peng, Y. S., and Ying, Y. B. (2008). Study on the influence of temperature on near infrared spectra. *Spectrosc. Spect. Anal.* 28, 1510–1513.

Jing, P., Ye, T., Shi, H., Sheng, Y., Slavin, M., Gao, B., et al. (2012). Antioxidant properties and phytochemical composition of China-grown pomegranate seeds. *Food Chem.* 132, 1457–1464. doi: 10.1016/j.foodchem.2011.12.002

Jolliffe, I. T., and Cadima, J. (2016). Principal component analysis: a review and recent developments. Philosophical transactions. *Proc. Math. Phys. Eng. Sci.* 374:20150202. doi: 10.1098/rsta.2015.0202

Kahrıman, F., Onaç, I., Türk, F. M., Öner, F., and Egesel, C. O. (2019). Determination of carotenoid and tocopherol content in maize flour and oil samples using near-infrared spectroscopy. *Spectrosc. Lett.* 52, 473–481. doi: 10.1080/00387010.2019.1671872

Khoddami, A., Man, Y. B. C., and Roberts, T. H. (2014). Physico-chemical properties and fatty acid profile of seed oils from pomegranate (*Punica granatum* L.) extracted by cold pressing. *Eur. J. Lipid Sci. Technol.* 116, 553–562. doi: 10.1002/ejlt.201300416

Lansky, E. P., Jiang, W., Mo, H., Bravo, L., Froom, P., Yu, W., et al. (2005). Possible synergistic prostate cancer suppression by anatomically discrete pomegranate fractions. *Invest. New Drugs* 23, 11–20. doi: 10.1023/B:DRUG.0000047101.02178.07

Lansky, E. P., and Newman, R. A. (2007). *Punica granatum* (pomegranate) and its potential for prevention and treatment of inflammation and cancer. *J. Ethnopharmacol.* 109, 177–206. doi: 10.1016/j.jep.2006.09.006

Liang, P., Chen, C., Zhao, S., Ge, F., Liu, D., Liu, B., et al. (2013). Application of Fourier transform infrared spectroscopy for the oxidation and peroxide value evaluation in virgin walnut oil. *J. Spectrosc.* 2013:138728. doi: 10.1155/2013/138728

Lin, P., Chen, Y., and He, Y. (2012). Identification of geographical origin of olive oil using visible and near-infrared spectroscopy technique combined with chemometrics. *Food Bioproc. Tech.* 5, 235–242. doi: 10.1007/s11947-009-0302-z

Lu, H., Xu, H., Ying, Y., Fu, X., Yu, H., and Tian, H. (2006). Application Fourier transform near infrared spectrometer in rapid estimation of soluble solids content of intact citrus fruits. *J. Zhejiang Univ. Sci.* 7, 794–799. doi: 10.1631/jzus.2006.B0794

Ma, J., Zhang, H., Tuchiya, T., Miao, Y., and Chen, J. Y. (2014). Rapid determination of degradation of frying oil using near-infrared spectroscopy. *Food Sci. Technol.* 20, 217–223. doi: 10.3136/fstr.20.217

Magwaza, L. S., Opara, U. L., Cronje, P. J. R., Landahl, S., Nieuwoudt, H. H., Mouazen, A. M., et al. (2014). Assessment of rind quality of 'Nules Clementine' mandarin fruit during postharvest storage: 2. Robust Vis/NIRS PLS models for prediction of physico-chemical attributes. *Sci. Hortic.* 165, 421–432. doi: 10.1016/j.scienta.2013.09.050

Magwaza, L. S., Opara, U. L., Terry, L. A., Landahl, S., Cronje, P. J. R., Nieuwoudt, H. H., et al. (2013). Evaluation of Fourier transform-NIR spectroscopy for integrated external and internal quality assessment of Valencia oranges. *J. Food Compos. Anal.* 31, 144–154. doi: 10.1016/j.jfca.2013.05.007

Makkar, H. P. S., Siddhuraju, P., and Becker, K. (2007). Plant secondary metabolites. *Methods Mol. Biol.* 393, 1–122. doi: 10.1007/978-1-59745-425-4_1

Manley, M. (2014). Near-infrared spectroscopy and hyperspectral imaging: non-destructive analysis of biological materials. *Chem. Soc. Rev.* 43, 8200–8214. doi: 10.1039/c4cs00062e

Marina, A. M., Wan Rosli, W. I., and Noorhidayah, M. (2013). Quantitative analysis of peroxide value in virgin coconut oil by ATR-FT-IR spectroscopy. *Open Conf. Proc. J.* 4, 53–56. doi: 10.2174/2210289201304020053

Marina, A. M., Wan Rosli, W. I., and Noorhidayah, M. (2015). Rapid quantification of free fatty acids in virgin coconut oil by FTIR spectroscopy. *Malays. Appl. Biol.* 20, S790–S797. doi: 10.1080/10942912.2017.1312437

Mba, O., Adewale, P., Dumont, M. J., and Ngadi, M. (2014). Application of near-infrared spectroscopy to characterise binary blends of palm and canola oils. *Ind. Crop Prod.* 61, 472–478. doi: 10.1016/j.indcrop.2014.07.037

Musingarabwi, D. M., Nieuwoudt, H. H., Young, P. R., Eyéghè-Bickong, H. A., and Vivier, M. A. (2016). A rapid qualitative and quantitative evaluation of grape berries at various stages of development using Fourier-transform infrared spectroscopy and multivariate data analysis. *Food Chem.* 190, 253–262. doi: 10.1016/j.foodchem.2015.05.080

Nicolaï, B. M., Beullens, K., Bobelyn, E., Peirs, A., Saeys, W., Theron, K. I., et al. (2007). Non-destructive measurement of fruit and vegetable quality by means of NIR spectroscopy: a review. *Postharvest Biol. Technol.* 46, 99–118. doi: 10.1016/j.postharvbio.2007.06.024

O'Grady, L., Sigge, G., Caleb, O. J., and Opara, U. L. (2014). Effects of storage temperature and duration on chemical properties, proximate composition and selected bioactive components of pomegranate (*Punica granatum* L.) arils. *Food Sci. Technol.* 57, 508–515. doi: 10.1016/j.lwt.2014.02.030

Opara, L. U., Al-Ani, M. R., and Al-Shuaibi, Y. S. (2009). Physicochemical properties, vitamin C content, and antimicrobial properties of pomegranate fruit (*Punica granatum* L.). *Food Bioproc. Tech.* 2, 315–321. doi: 10.1007/s11947-008-0095-5

Özdemir, İ. S., Dağ, Ç., Özinanç, G., Sucsoran, O., Oznur, E., and Erdal, B. (2018). Quantification of sterols and fatty acids of extra virgin olive oils by FT-NIR spectroscopy and multivariate statistical analyses. *Food Sci. Technol.* 91, 125–132. doi: 10.1016/j.lwt.2018.01.045

Parashar, A., Gupta, S. K., and Kumar, A. (2009). Studies on separation techniques of pomegranate seeds and their effect on quality of anardana. *Afr. J. Biochem. Res.* 79, 671–674. doi: 10.1016/j.jfoodeng.2006.02.026

Pathare, P., Opara, U. L., and Al-Said, F. A. J. (2013). Colour measurement and analysis in fresh and processed foods: a review. *Food Bioproc. Tech.* 6, 36–60. doi: 10.1007/s11947-012-0867-9

Pereira, A. F. C., Pontes, M. J. C., Neto, F. F. G., Santos, S. R. B., Galvao, R. K. H., and Araujo, M. C. U. (2008). NIR spectrometric determination of quality parameters in vegetable oils using iPLS and variable selection. *Food Res. Int.* 41, 341–348. doi: 10.1016/j.foodres.2007.12.013

Rohman, A., and Che Man, Y. B. (2011). The use of Fourier transform mid infrared (FT-MIR) spectroscopy for detection and quantification of adulteration in virgin coconut oil. *Food Chem.* 129, 583–588. doi: 10.1016/j.foodchem.2011.04.070

Schulz, H., Drews, H. H., Quilitzsch, R., and Kruger, H. (1998). Application of near infrared spectroscopy for the quantification of quality parameters in selected vegetables and essential oil plants. *J. Near Infrared Spectrosc.* 6, A125–A130. doi: 10.1255/jnirs.179

Seeram, N. P., Zhang, Y., Reed, J. D., Krueger, C. G., and Vaya, J. (2006). "Pomegranate phytochemicals" in *Pomegranates: Ancient Roots to Modern Medicine*. ed. N. P. Seeram (Boca Raton, London, and New York: CRC Press Taylor and Francis Group), 3–29.

Shi, H., and Yu, P. (2017). Comparison of grating-based near-infrared (NIR) and Fourier transform mid-infrared (ATR-FT/MIR) spectroscopy based on spectral preprocessing and wavelength selection for the determination of crude protein and moisture content in wheat. *Food Control* 82, 57–65. doi: 10.1016/j.foodcont.2017.06.015

Siano, F., Straccia, M. C., Paolucci, M., Fasulo, G., Boscaino, F., and Volpe, M. G. (2015). Physico-chemical properties and fatty acid composition of pomegranate, cherry and pumpkin seed oils. *J. Sci. Food Agric.* 96, 1730–1735. doi: 10.1002/jsfa.7279

Sinelli, N., Casiraghi, E., Barzaghi, S., Brambilla, A., and Giovanelli, G. (2011). Near infrared (NIR) spectroscopy as a tool for monitoring blueberry osmo-air dehydration process. *Int. Food Res. J.* 44, 1427–1433. doi: 10.1016/j.foodres.2011.02.046

Sinelli, N., Cerretani, L., Egidio, V. D., Bendini, A., and Casiraghi, E. (2010). Application of near (NIR) infrared and mid (MIR) infrared spectroscopy as a rapid tool to classify extra virgin olive oil on the basis of fruity attribute intensity. *Food Res. Int.* 43, 369–375. doi: 10.1016/j.foodres.2009.10.008

Smyth, H. E., and Cozzolino, D. (2011). Application of infrared spectroscopy for quantitative analysis of volatile and secondary metabolites in plant materials. *Curr. Bioact. Compd.* 7, 66–74. doi: 10.2174/157340711796011160

Socaciu, C., Fetea, F., and Ranga, F. (2009). IR and Raman spectroscopy – advanced and versatile techniques for agrifood quality and authenticity assessment. *Bull. Univ. Agric. Sci. Vet. Med.* 66, 459–464. doi: 10.15835/buasvmcn-agr:4053

Sun, D. W. (2009). *Infrared Spectroscopy for Food Quality Analyses and Control*, New York, USA: Elsevier Inc.

Trapani, S., Migliorini, M., Cecchi, L., Giovenzana, V., Beghi, R., Canuti, V., et al. (2016). Feasibility of filter based NIR spectroscopy for the routine measurement of olive oil fruit ripening indices. *Eur. J. Lipid Sci. Technol.* 119, 1600239–1600234. doi: 10.1002/ejlt.201600239

Trygg, J., Holmes, E., and Lundstedt, T. (2007). Chemometrics in metabonomics. *J. Proteome Res.* 6, 469–479. doi: 10.1021/pr060594q

Trygg, J., and Wold, S. (2002). Orthogonal projections to latent structures (O-PLS). *J. Chemometr.* 16, 119–128. doi: 10.1002/cem.695

Uncu, O., Napiórkowska, A., Szajna, T. K., and Ozen, B. (2020). Evaluation of three spectroscopic techniques in determination of adulteration of cold pressed pomegranate seed oils. *Microchem. J.* 158:105128. doi: 10.1016/j.microc.2020.105128

Wiklund, S., Johansson, E., Sjöström, L., Mellerowicz, E. J., Edlund, U., Shockcor, J. P., et al. (2008). Visualisation of GC/TOF-MS-based metabolomics data for

identification of biochemically interesting compounds using OPLS class models. *Anal. Chem.* 80, 115–122. doi: 10.1021/ac0713510

Williams, P. (2014). The RPD statistic: a tutorial note. *NIR News* 25, 22–26. doi: 10.1255/nirn.1419

Wold, S., Esbensen, K., and Geladi, P. (1987). Principal component analysis. *Chemom. Intel. Lab. Syst.* 2, 37–52. doi: 10.1016/0169-7439(87)80084-9

Yang, H., and Irudayaraj, J. (2001). Comparison of near-infrared, Fourier transform-infrared, and Fourier transform-Raman methods for determining olive pomace oil adulteration in extra virgin olive oil. *J. Am. Oil Chem. Soc.* 78, 889–895. doi: 10.1007/s11746-001-0360-6

Yang, H., Irudayaraj, J., and Paradkar, M. M. (2005). Discriminant analysis of edible oils and fats by FTIR, FT-NIR and FT-Raman spectroscopy. *Food Chem.* 93, 25–32. doi: 10.1016/j.foodchem.2004.08.039

Zahir, E., Saeed, R., Hameed, M. A., and Yousuf, A. (2017). Study of physicochemical properties of edible oil and evaluation of frying oil quality by Fourier transform-infrared (FT-IR) spectroscopy. *Arab. J. Chem.* 10, S3870–S3876. doi: 10.1016/j.arabjc.2014.05.025

Conflict of Interest: The authors declare that the research was conducted in the absence of any commercial or financial relationships that could be construed as a potential conflict of interest.

Publisher's Note: All claims expressed in this article are solely those of the authors and do not necessarily represent those of their affiliated organizations, or those of the publisher, the editors and the reviewers. Any product that may be evaluated in this article, or claim that may be made by its manufacturer, is not guaranteed or endorsed by the publisher.

frontiers | Frontiers in Plant Science

ORIGINAL RESEARCH
published: 14 July 2022
doi: 10.3389/fpls.2022.942040

Surface Defect Detection of Cabbage Based on Curvature Features of 3D Point Cloud

Jin Gu[1], Yawei Zhang[1], Yanxin Yin[2,3], Ruixue Wang[4], Junwen Deng[1] and Bin Zhang[1]*

[1] College of Engineering, China Agricultural University, Beijing, China, [2] Research Center of Intelligent Equipment, Beijing Academy of Agriculture and Forestry Sciences, Beijing, China, [3] National Research Center of Intelligent Equipment for Agriculture, Beijing, China, [4] Chinese Academy of Agricultural Mechanization Sciences Group Co., Ltd., Beijing, China

The dents and cracks of cabbage caused by mechanical damage during transportation have a direct impact on both commercial value and storage time. In this study, a method for surface defect detection of cabbage is proposed based on the curvature feature of the 3D point cloud. First, the red-green-blue (RGB) images and depth images are collected using a RealSense-D455 depth camera for 3D point cloud reconstruction. Then, the region of interest (ROI) is extracted by statistical filtering and Euclidean clustering segmentation algorithm, and the 3D point cloud of cabbage is segmented from background noise. Then, the curvature features of the 3D point cloud are calculated using the estimated normal vector based on the least square plane fitting method. Finally, the curvature threshold is determined according to the curvature characteristic parameters, and the surface defect type and area can be detected. The flat-headed cabbage and round-headed cabbage are selected to test the surface damage of dents and cracks. The test results show that the average detection accuracy of this proposed method is 96.25%, in which, the average detection accuracy of dents is 93.3% and the average detection accuracy of cracks is 96.67%, suggesting high detection accuracy and good adaptability for various cabbages. This study provides important technical support for automatic and non-destructive detection of cabbage surface defects.

Keywords: defect detection, cabbage, curvature features, 3D point cloud, depth camera

OPEN ACCESS

Edited by:
Jianwei Qin,
Agricultural Research Service (USDA), United States

Reviewed by:
Leiqing Pan,
Nanjing Agricultural University, China
Pibo Ma,
Jiangnan University, China

***Correspondence:**
Yanxin Yin
yinyx@nercita.org.cn

Specialty section:
This article was submitted to Crop and Product Physiology, a section of the journal Frontiers in Plant Science

Received: *12 May 2022*
Accepted: *14 June 2022*
Published: *14 July 2022*

Citation:
Gu J, Zhang Y, Yin Y, Wang R, Deng J and Zhang B (2022) Surface Defect Detection of Cabbage Based on Curvature Features of 3D Point Cloud. Front. Plant Sci. 13:942040. doi: 10.3389/fpls.2022.942040

INTRODUCTION

As one of the economically important vegetable products, cabbage occupies a crucial position in agricultural products. The dents and cracks of cabbage caused by extrusion and collection during transportation have a direct impact both on the commercial value and storage time (Li and Thomas, 2014). The vegetable non-destructive system is a recent trend for quality evaluation, post-harvest classification, and grading (Fathizadeh et al., 2020; Zhang et al., 2021).

The non-destructive testing means mainly include near-infrared spectroscopy and machine vision. The near-infrared spectroscopy-based non-destructive testing is an advanced method, and hyperspectral reflectance imaging can be used to detect the quality of fresh-cut lettuce (Mo et al., 2017). However, it is limited in engineering applications due to the high cost of equipment and slow data processing process (Lu and Lu, 2017; Chen et al., 2021). Machine vision-based non-destructive testing is fast and of low cost, and it identifies the dents and cracks of vegetables according to

the color features, texture features, and geometric features. It has achieved good results in tomato defect detection (da Costa et al., 2020), apple defect detection (Zhang et al., 2017), and litchi surface micro-damage detection (Wang et al., 2016). The machine vision algorithm combined with the deep learning model has predominant robustness in carrot defect detection (Xie et al., 2021). Choosing the appropriate learning algorithm for a specific problem is crucial for vegetable defect detection based on the deep learning algorithm. This particularity makes the deep learning technology can only build a standardized detection system for specific targets (Nturambirwe and Opara, 2020). In recent years, the RGB-D depth cameras represented by Intel RealSense series have developed rapidly. It integrates the RGB images and depth images to provide richer information. On this basis, a 3D point cloud based on destructive testing technology provides a fast, convenient, and applicable solution for target detection and surface 3D reconstruction (Jiang et al., 2018; Wu et al., 2019; Das Choudhury et al., 2020). It has been successfully used to detail road surface defects, composite wrinkle defects, and seamless steel pipe wear defects (Zhang et al., 2018; Hu and Furukawa, 2020; Zong et al., 2021). The 3D point cloud technology has an excellent performance in object detection (Ying et al., 2013). Therefore, it is meaningful to build a cabbage surface defect detection system based on 3D point cloud for presale testing applications.

Curvature is an important basis for feature recognition. The variation of edge curvature of dents and cracks usually fluctuates obviously. In this study, we took the RealSense-D455 depth camera as the sensor to rebuild the 3D point cloud of the image, and the target 3D point cloud of cabbage is segmented from the background noise through preprocessing and region of interest (ROI) extraction. The normal vector is estimated based on the least-squares plane fitting method, and the curvature threshold is defined in agreement with the curvature character parameters. The surface defect detection is realized according to the curvature difference between the normal area and the defective area on the cabbage surface.

MATERIALS AND METHODS

3D Point Cloud Reconstruction System

The 3D point cloud reconstruction system was built using a RealSense-D455 depth camera, a rotating platform, and a computer, as shown in **Figure 1**. The RealSense-D455 depth camera was used as a sensor to get a 3D point cloud of the cabbage surface, and its parameters are shown in **Table 1**. The rotating platform rotated at 45° intervals to record the images from different angles; therefore, for each cabbage, 8 frames of point clouds could be obtained. The computer was used for collecting and analyzing the RGB images and depth images from the camera and reconstructing the 3D point clouds. As the most common cabbage, the flat-headed cabbage and round-headed cabbage were selected to conduct experiments.

TABLE 1 | Parameters of the D455 depth camera.

Parameters	Values
RGB frame resolution/(pixels)	1280 × 800
Depth output resolution/(pixels)	1280 × 720
RGB frame rate/(frame/s)	30
Depth field of view/(°)	87 × 58
Ideal range/(m)	0.6 ∼ 6
Depth Accuracy	<2% at 4 m

To ensure the consistency of cabbage samples, the diameter of the cabbage was in the range of 150–200 mm, and the mass of the cabbage was in the range of 0.8–1.2 kg. The two varieties of cabbage samples contain three types, namely, intact cabbage, crack cabbage, and dent cabbage, as shown in **Figure 2**. In experiments, the cabbage was placed in the center of the rotating platform. The distance between the camera and the top of the rotating platform was 0.4 m, and the height between the camera and the center of the rotating platform was 0.24 m. The computer is configured as Intel (R) Core (TM) i5-8265 CPU @ 1.6 GHz, 8 GB RAM, NVIDIA GeForce MX150 graphics card. All algorithms of surface defect detection method were written in C++, using RealSense SDK 2.0 provided by Intel Corporation and open source library PCL 1.8.1.

Point Cloud Denoising

The camera fuses the collected RGB images with the depth images to obtain the point cloud data in the view (Condotta et al., 2020). **Figure 3** shows the RGB image of the cabbage in one view, the corresponding depth image, and the 3D point cloud image after aligning and fusing the RGB image with the depth image.

The original point cloud contains a large number of background noises and redundant outliers, which affects the processing effect of subsequent clustering segmentation. In this study, statistical filters were used to remove outliers with sparse edge distribution of point cloud. The principle of statistical filtering is to calculate the average value of the distances from each point to the points in the neighbor according to the sparse degree of points in space. Then, the points whose average distance is outside the standard range are removed. **Figure 4** shows the point cloud statistical filtering process.

First, the average value of distances from each point to i points in the neighbor was calculated. The average values constituted a Gaussian distribution, and its shape was determined by mean value μ and standard deviation σ. The coordinate of one point was removed $Pn\,(Xn, Yn, Zn)$. The distance from the point $Pn\,(Xn, Yn, Zn)$ to the other point $Pm\,(Xm, Ym, Zm)$ could be calculated as follows:

$$S_i = \sqrt{(X_n - X_m)^2 + (Y_n - Y_m)^2 + (Z_n - Z_m)^2} \quad (1)$$

The average value of the distances between all the points could be calculated as follows:

$$\mu = \frac{1}{n}\sum_{i=1}^{n} S_i \quad (2)$$

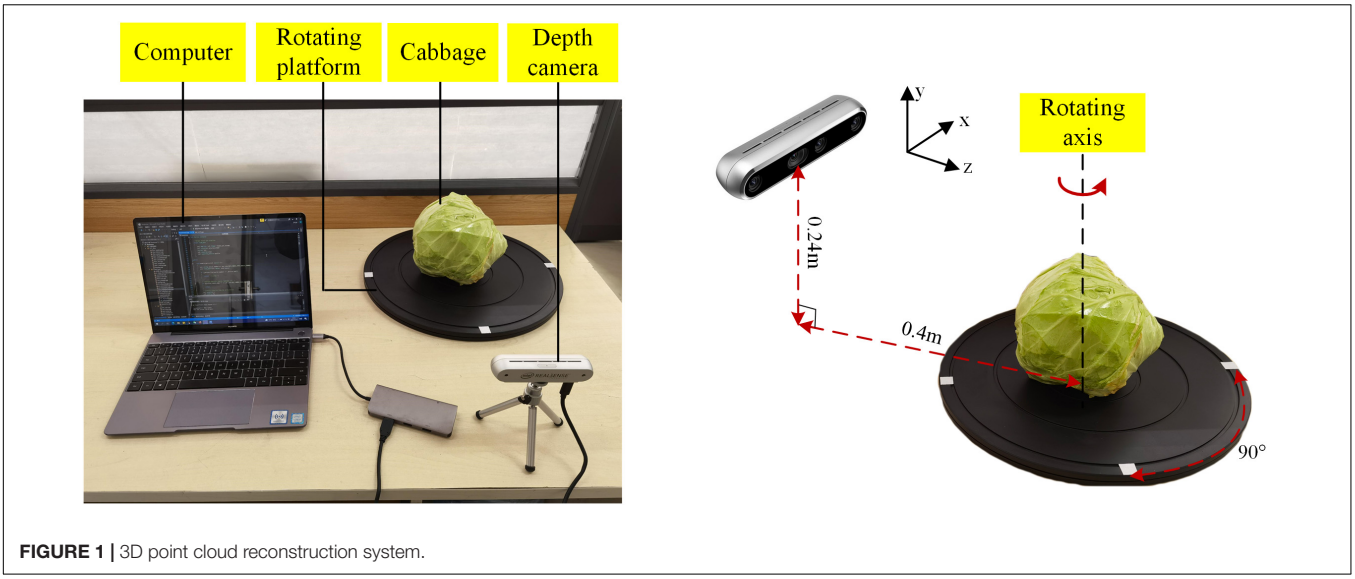

FIGURE 1 | 3D point cloud reconstruction system.

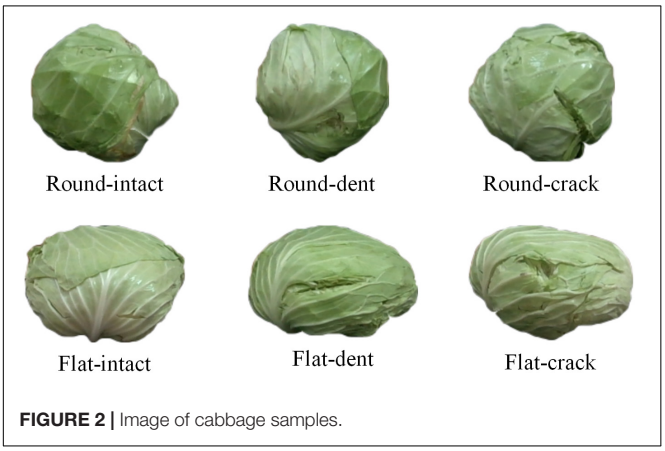

FIGURE 2 | Image of cabbage samples.

The standard deviation of distance could be calculated as follows:

$$\sigma = \sqrt{\frac{1}{n}\sum_{i=1}^{n}(S_i - \mu)^2} \tag{3}$$

When the average value of distances was beyond the range $(\mu - \sigma, \mu + \sigma)$, this point is regarded as an outlier. In this algorithm, i was set to the threshold. When $i = 50$, the point cloud after statistical filtering is shown in **Figure 5**. The points in blue circles are outliers. The outliers were effectively eliminated from the origin point cloud after statistical filtering.

Extract the Region of Interest

To extract the point cloud of target cabbage from the point cloud containing background information, it is necessary to segment the point cloud data to extract the ROI. The principle of point cloud clustering segmentation is to classify the point cloud according to geometric and texture features. The point clouds with similar features are clustered into one class. Common point cloud segmentation methods are the Random Sampling Consistency (RANSAC) algorithm, region growing algorithm, and Euclidean clustering segmentation algorithm (Xu et al., 2015; Wu et al., 2020; Luo et al., 2021). Considering processing time and segmentation effect, the Euclidean clustering segmentation algorithm was used to extract the ROI of the point cloud.

The Euclidean clustering segmentation algorithm is a distance measure clustering algorithm based on k-dimensional (KD)-tree nearest neighbor search, which takes Euclidean distance as the judgment criterion (Li et al., 2021).

Step 1: For a point p, the n points of the nearest neighbor by KD-tree were searched, and the distances between the points to the point p were calculated, respectively.

$$d_i(p, q_i) = \sqrt{\sum_{i=1}^{n}(p - q_i)^2} \tag{4}$$

Step 2: The threshold was set to r. If the distance di was less than the set threshold r, the point qi was clustered in the database Q. Until the number of points in Q no longer increased, indicating that the clustering of points in this category is completed.

Step 3: Continue to select another point in the space and repeat the above operation, until the number of point cloud category sets was no longer increasing.

Figure 6A shows the point cloud clustering results using the European clustering segmentation algorithm. **Figure 6B** shows the target cabbage point cloud. It can be seen that the target cabbage is effectively clustered from the background noises, and the processing time of this algorithm was 3.648 s.

Point Cloud Subsampling

The point cloud after clustering segmentation extraction contained a mass of data. To speed up the subsequent processing, it was necessary to minimize the amount of data without losing point cloud features. In this study, a voxel filter was used to subsample the point cloud of cabbage.

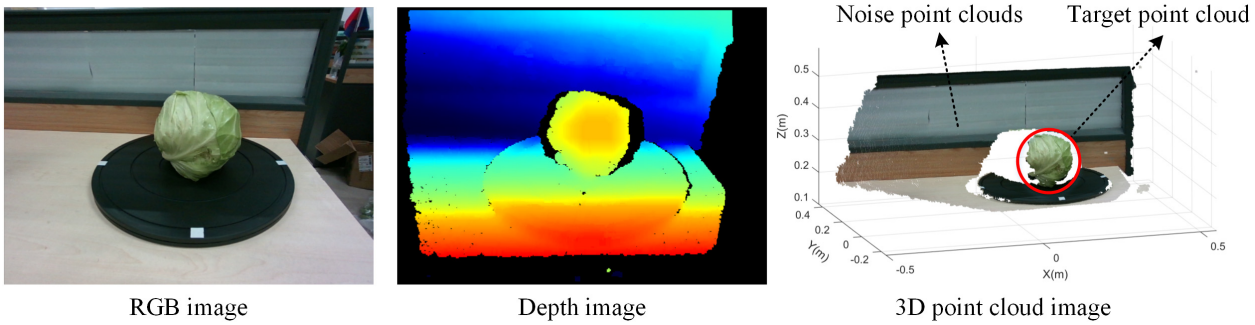

FIGURE 3 | Image fusion.

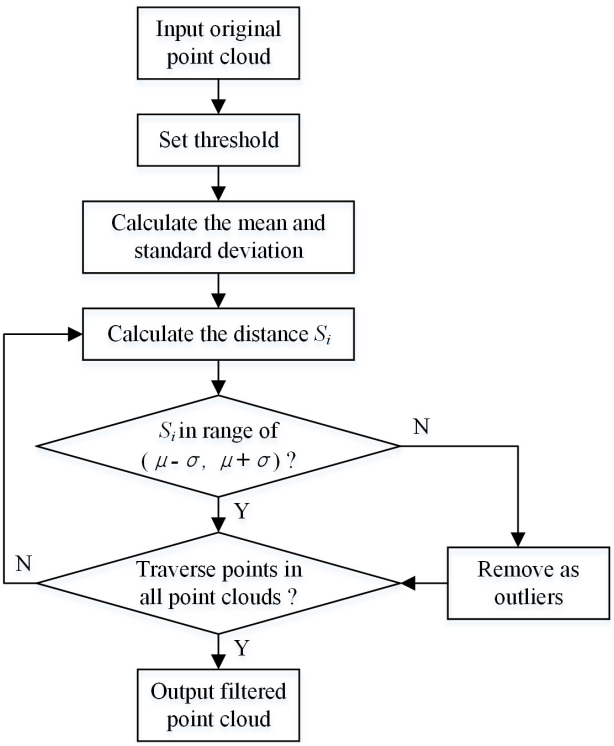

FIGURE 4 | Flowchart of statistical filtering.

The principle of the algorithm for the voxel filter was to create tiny three-dimensional cubes in space, namely, voxel grid, and divide the point cloud using the voxel grid (Xiong et al., 2021). In each voxel, the centroid of all the points was used to replace all the points to minimize the amount of point cloud. The size of the three-dimensional voxel grid was set to 1 mm. **Figure 7** shows the point distribution histogram of a frame of cabbage before and after subsampling.

Figure 7A shows the point cloud before subsampling, which contains 16,484 points in total. The distribution on the *Z*-axis of all the points is expressed as Gaussian distribution, with the mean value of $\mu 1 = 0.371$ and the standard deviation of $\sigma_1 = 0.013$. **Figure 7B** shows the point cloud after subsampling, and the number of points drops to 9,396. The distribution on the *Z*-axis of all the points is expressed as the Gaussian distribution, with the mean value of $\mu_2 = 0.374$ and the standard deviation of $\sigma 2 = 0.015$ after subsampling. From Gaussian distributions, it can be seen that the rate of changes in mean value and the standard deviation are less than 2% when the number of point clouds decreases by 42.9%. It shows that the spatial distribution characteristics of point clouds before and after subsampling are very similar. Therefore, it can be concluded that the selection of the voxel filter grid size is relatively accurate.

Cabbage Surface Defect Detection Method

Normal Vector Estimation and Curvature Calculation

Surface curvature describes the change degree of point cloud by the eigenvalue. The curvature at a certain point can be obtained by estimating the normal vector of each point in the point cloud. The normal vector can be calculated using the normal of the tangent line of the surface at that point. According to the least square method (LSM), the quadratic surface can be used to characterize the local region, and the normal vector can be estimated using the local region surface fitting method.

Each point in the point cloud has a neighborhood point cloud, which is approached using a certain surface. The curvature of a certain point can be expressed by the curvature of the local surface fitted by the point and its neighborhood points. By taking the point *Pi* as a central point, *k* points were uniformly selected in the neighborhood of point *Pi*.

The quadratic surface equation can be expressed as follows:

$$z(x, y) = ax^2 + bxy + cy^2 \tag{5}$$

According to the principle of least squares, the sum of the squares of *zi* can be expressed as follows:

$$Q^2 = \sum_i \left(ax_i^2 + bx_i y_i + cy_i^2 = z_i\right)^2, j \in (0, k) \tag{6}$$

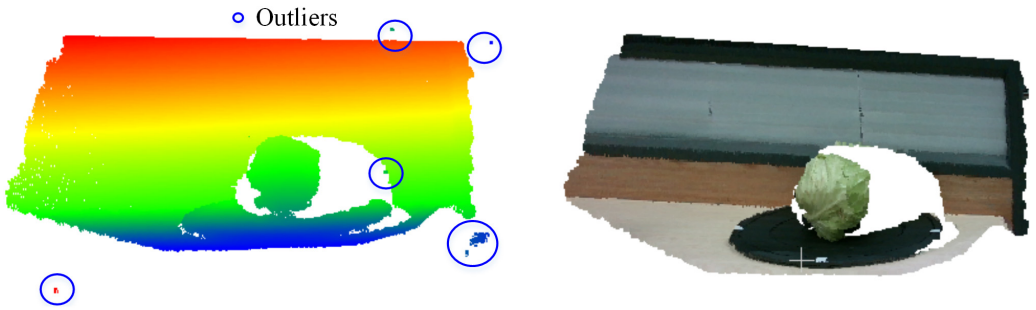

FIGURE 5 | Statistical filtering result of the point cloud.

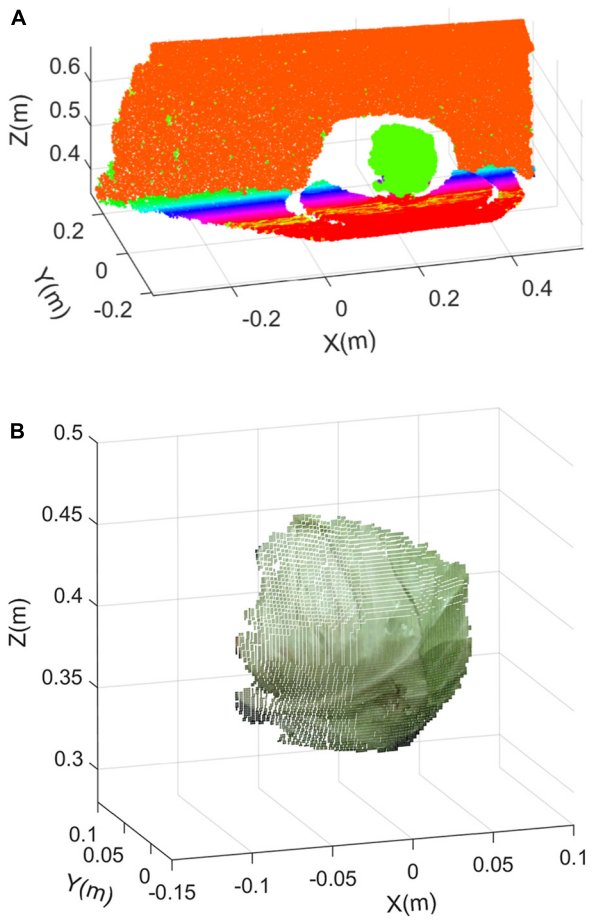

FIGURE 6 | Clustering segmentation extraction result: **(A)** result of the European clustering segmentation algorithm and **(B)** the target cabbage point cloud.

where, *xi*, *yi*, and *zi* are points in the neighbor of point *Pi*. The derivative of the coefficient is obtained in Eq. 6.

$$\begin{cases} \frac{\partial Q^2}{\partial a} = \sum_i 2x_i^2 \left(ax_i^2 + bx_iy_i + cy_i^2 - z_i\right) = 0 \\ \frac{\partial Q^2}{\partial b} = \sum_i 2x_iy_i \left(ax_i^2 + bx_iy_i + cy_i^2 - z_i\right) = 0 \\ \frac{\partial Q^2}{\partial c} = \sum_i 2y_i^2 \left(ax_i^2 + bx_iy_i + cy_i^2 - z_i\right) = 0 \end{cases}, i \in (0, k) \quad (7)$$

From this, the values of the coefficients *a*, *b*, and *c* of the quadratic surface equation can be solved. Equation 6 is expressed as a parametric form.

$$r(x, y) = \begin{cases} X(x, y) = x \\ Y(x, y) = y \\ Z(x, y) = ax^2 + bxy + cy^2 \end{cases} \quad (8)$$

Then, a curve on the surface can be expressed as follows:

$$r = r\left(x(t), y(t)\right) \quad (9)$$

The arc length differential equation of the curve can be obtained by derivation.

$$(ds)^2 = r_x^2 (dx)^2 + 2r_x r_y dxdy + r_y^2 (dy)^2 \quad (10)$$

The unit normal vector at point *Pi* can be expressed as follows:

$$n_i = \frac{r_x \times r_y}{|r_x \times r_y|} \quad (11)$$

Considering the normal vector at the point *Pi* as the normal vector of the local surface in the neighborhood, then the covariance matrix of the points in the neighborhood was as follows:

$$C = \frac{1}{k} \sum_{i=1}^{k} (P_i - P_0)(P_i - P_0)^T \quad (12)$$

$$C \cdot X_j = \lambda_j \cdot X_j, j = 1, 2, 3 \quad (13)$$

where *P*0 is the centroid of points in the neighborhood, *k* is the number of points in the neighborhood, and λ*j* and *Xj* represent the eigenvalue and eigenvector of *C*, respectively.

The eigenvector corresponding to the smallest eigenvalue of matrix *C* was the normal vector of point *Pi*. The covariance matrix was constructed, and the eigenvalues of the matrix were calculated by eigenvalue decomposition.

If the eigenvalues satisfied the condition λ0 ≤ λ1 ≤ λ2, the curvature of the neighborhood points can be expressed as follows:

$$\kappa_i = \frac{\lambda_0}{\lambda_0 + \lambda_1 + \lambda_2} \quad (14)$$

Neighborhood curvature represents the degree of curvature of the neighborhood surface. The curvature values of all points in the point cloud are calculated. The curvature features were used to determine the surface concavity of the cabbage point cloud to improve the accuracy of damage detection.

Cabbage Defect Detection Algorithm Based on Curvature

Cabbage surface damage generally manifests itself in the form of dents and cracks. The dent damage is mainly due to extrusion or falling, and the edges are generally round or oval with shallow internal depressions. The crack damage is mainly due to growth cracking or scratching by sharp objects, which leads to multilayered fracture of cabbage. The edges are generally narrow-shaped and have deep internal depressions. Since the curvature of the edges of the damaged area would change significantly compared with the normal area, the damaged area could be extracted according to the surface type represented by different curvatures.

Taking one frame of cabbage point clouds as an example, **Figure 8** shows the extraction process of cabbage surface defective area. It can be seen from the curvature image that the curvature of the edge of the damaged area is significantly higher than that of the normal area of cabbage, so the defective area can be extracted by setting the curvature threshold and segmenting the curvature of the point cloud according to the threshold.

From the curvature calculation results, it can be seen that although the cabbage curvature image shows the surface damaged area, it is mistakenly segmented as a damaged area due to the curvature gradient at the edge of the point cloud. However, the curvature change caused by the protrusion of cabbage leaf stalk and cabbage itself dents will also interfere with the detection results. To solve these problems, the defect extraction results can be segmented twice by optimizing the curvature threshold.

According to the definition proposed by Chen and Bhanu (2007), the point with the largest curvature change on the surface of the point cloud is considered the feature point. Whether the current pointP_i is a feature point should be checked. The formula for the curvature characteristic parameter can be expressed as follows:

$$S(P_i) = \frac{1}{2} - \frac{1}{\pi} \arctan \frac{k_1(P_i) + k_2(P_i)}{k_1(P_i) - k_2(P_i)} \tag{15}$$

where $k1$ and $k2$ are the maximum principal curvature and the minimum principal curvature, respectively, which can be obtained by calculating the two roots of normal curvature according to the second basic formula of the surface.

The criteria to determine whether the current sampling point is a feature point is as follows: if $S(Pi) > \max\left(S(Pi1), S(Pi2), \ldots, S\left(Pik\right)\right)$, the point Pi is a curvature feature point.

The curvature parameter at the feature points was taken as the threshold value, and the final point cloud that satisfies the conditions was extracted as the correct damaged area. It can be seen from the extracted image of the cabbage damaged area that this method effectively eliminates the influence of curvature change caused by the shape of the cabbage surface on the test results and accurately extracts the damaged area of the cabbage.

RESULTS AND DISCUSSION

Accuracy Analysis of Point Cloud Detection Methods

The detection effect of this algorithm was evaluated by selecting different varieties and different defect types of cabbage samples. **Figure 9** shows four visualization results of this method, including round-headed cabbage dent damage, round-headed cabbage crack damage, flat-headed cabbage dent damage, and flat-headed cabbage crack damage. The original cabbage image, the point cloud image including the defects' part, the curvature threshold calculation result, and the defect point cloud extraction result are, respectively, shown in the figure. Based on the curvature statistics of the point cloud samples, the curvature threshold was determined as 0.08. The point cloud area of cracking damage is larger than that of denting damage, but the curvature mutation of denting damage is more obvious. It shows that the algorithm has good adaptability to two varieties and two damaged types of cabbage.

To evaluate the performance of the proposed algorithm in detecting different types of cabbage damage, 80 cabbage point cloud samples collected were tested for detection. It includes 30 samples of dent damage (15 samples per variety), 30 samples of crack damage (15 samples per variety), and 20 intact samples (10 samples per variety). The correct classification accuracies were calculated and evaluated for dent damaged samples, crack damaged samples, and intact samples of different varieties of cabbage, respectively, and the results are shown in **Table 2**.

Table 2 shows the test results of all samples. In terms of dent damage detection, the accuracy of the point cloud detection method for round-headed cabbage and flat-headed cabbage is 93.3%. In terms of crack damage detection, the detection accuracy of the point cloud detection method for round-headed cabbage is 100%, that of flat-headed cabbage is 93.3%, and the average detection accuracy of the two varieties is 96.67%. The detection accuracy of cracked damaged samples is higher than that of dented damaged samples. From the overall test results, the average detection accuracy of the point cloud detection method is 96.25%, and it appears that this method could effectively detect dent-damaged cabbage, crack-damaged cabbage, and intact cabbage samples. The detection accuracy of

TABLE 2 | Detection results of point cloud defect detection method.

Samples	Types	Number	Correct detection	Accuracy (%)
Denting cabbages	Round-headed	15	14	93.3
	Flat-headed	15	14	93.3
Cracking cabbages	Round-headed	15	15	100
	Flat-headed	15	14	93.3
Intact cabbages	Round-headed	10	10	100
	Flat-headed	10	10	100
Total	6	80	77	96.25

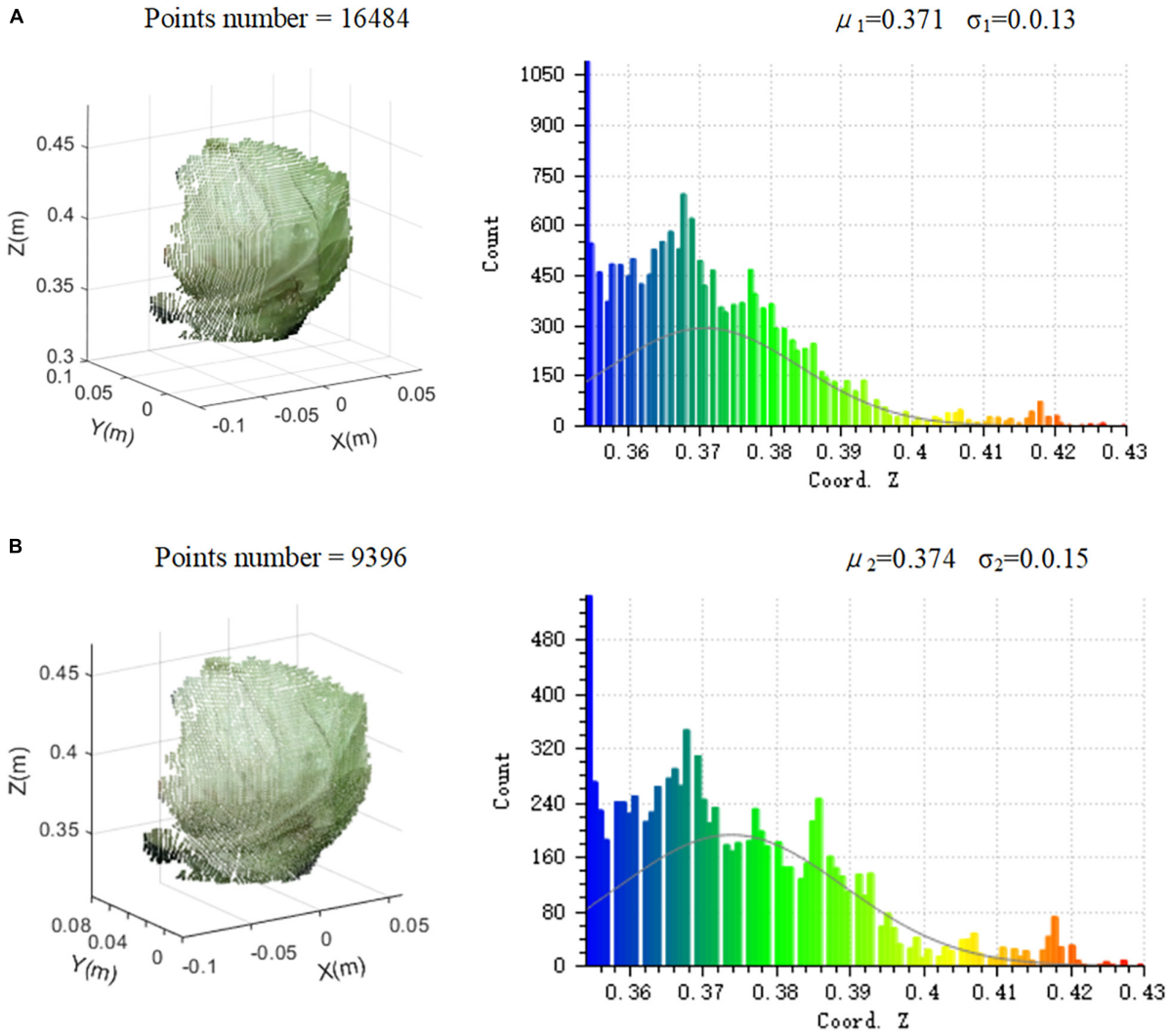

FIGURE 7 | The point distribution histogram before and after subsampling: **(A)** the point cloud before subsampling and **(B)** the point cloud after subsampling.

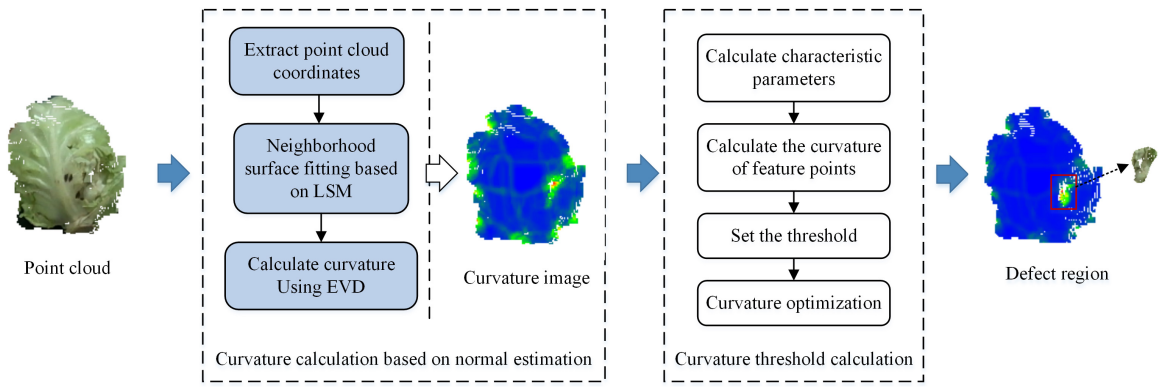

FIGURE 8 | Defective area extraction process.

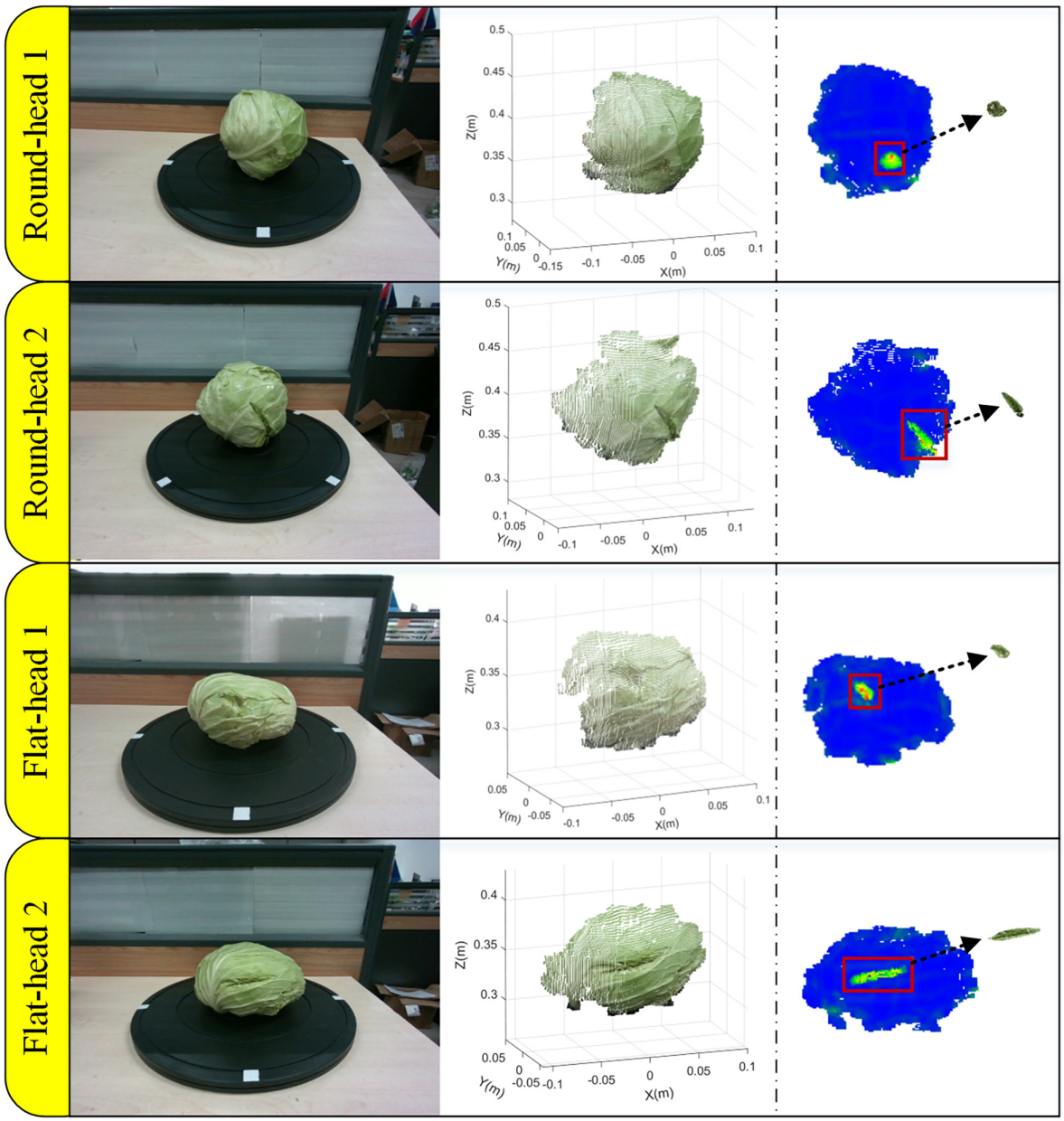

FIGURE 9 | Defective area extraction results.

the intact cabbages is 100%, indicating that the detection method can distinguish the cabbage itself dents from other defects, and the detection error of intact cabbage is low. The detection error in the test mainly occurs in the detection of defective samples, and the detection accuracy of the defect cabbages is 95%. It indicates that this method has good detection performance.

Misjudgment Analysis of Detection Results

To further analyze the reasons for the higher misjudgment rate of dent samples, the curvature calculation results of representative cabbage sample point clouds were extracted and represented as curvature curves according to the point cloud index values. **Figure 10** shows the comparison results.

Figure 10A shows the curvature curve of a correctly detected dent sample, and **Figure 10B** shows the curvature curve of a dent sample misjudged as non-damaging. It can be seen that the curvature of the defective area varies less due to the smaller area and shallow depth of the depressed area of the sample in **Figure 10B**. The extreme value of curvature is 0.043, which is very close to the curvature size of interference regions such as leaf stems, and it is difficult to be accurately segmented by a single curvature threshold so the correct detection rate is low.

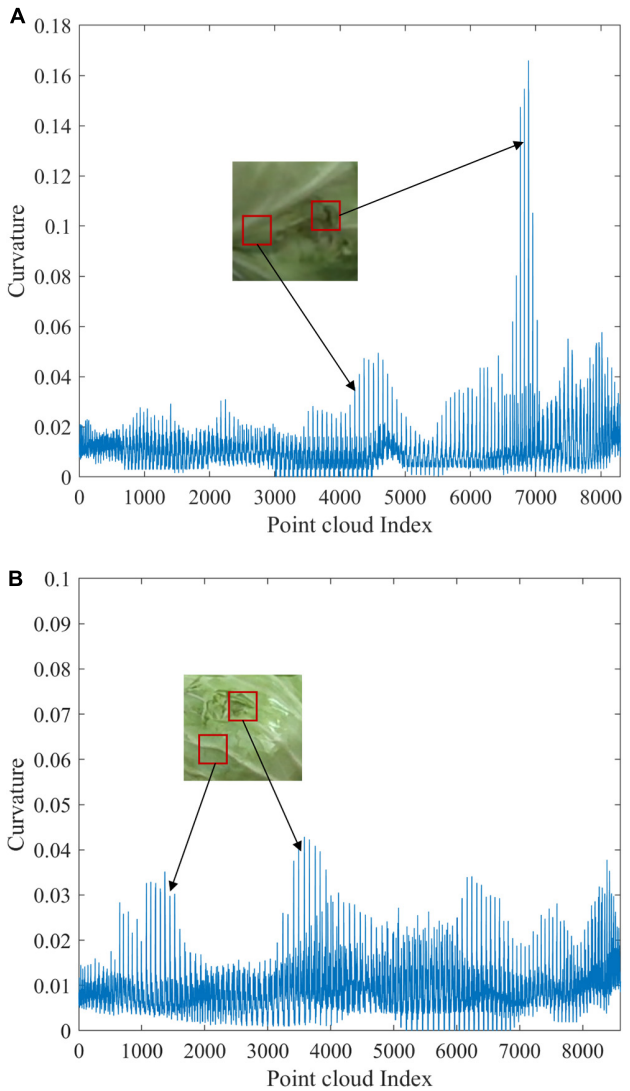

FIGURE 10 | Curvature curves of dent detection of cabbage: **(A)** the curvature curve of a correctly detected dent sample and **(B)** the curvature curve of a dent sample misjudged as non-maging.

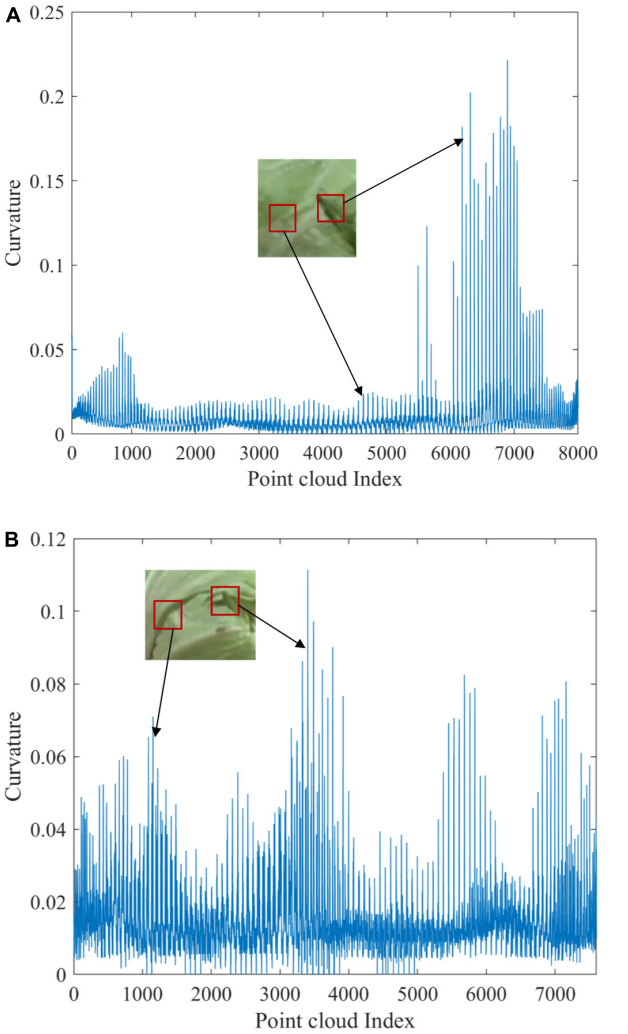

FIGURE 11 | Curvature curves of different variables of cabbage: **(A)** the curvature curve of the cracked sample of round-headed cabbage and **(B)** the curvature curve of the cracked sample of flat-headed cabbage.

In contrast, the area of damage in the depressed sample in **Figure 10A** is larger, the abrupt change of edge curvature is more obvious, the extreme value of curvature in the defective area reaches 0.167, and the surface curvature distribution of other parts is relatively uniform except for the defective area. The curvature fluctuation mainly appears at the leaf stem position, in which the maximum value of curvature is 0.059, much lower than that in the defective area. Therefore, the defective area can be easily extracted by curvature threshold segmentation.

It is also found that different varieties of cabbage had differences in detection accuracy in this study. According to the point cloud detection results of all defect types, the average detection accuracy of round-headed cabbage is 97.5%, and that of flat-headed cabbage is 95%. It is inferred that the cabbage type may be one of the reasons affecting the detection accuracy. To further analyze the reasons for the misjudgment, the curvature calculation results of representative cabbage sample point clouds were extracted and represented as curvature curves according to the point cloud index values. **Figure 11** shows the comparison results.

Figure 11A shows the curvature curve of the cracked sample of round-headed cabbage, and **Figure 11B** shows the curvature curve of the cracked sample of flat-headed cabbage. By analyzing the point cloud curvature curve of the two varieties of cabbage, it was concluded that the difference in detection accuracy was caused by the difference in the surface shape of the cabbage. From **Figure 11A**, it can be seen that the curvature fluctuation is smaller in the undamaged area due to the tighter wrapping of round-headed cabbage, while the cracked area usually has a more pronounced edge curvature mutation. The curvature extreme value of the selected sample in the cracked area is 0.227, which is much higher than that in the undamaged area. As

for **Figure 11B**, the curvature of flat-headed cabbage fluctuates greatly as a whole, mainly because there are many leaf edge bulges forming curvature mutation, which makes the curvature value of these areas close to the defective area, making the detection algorithm easy to misjudge and causing the recognition rate to decrease.

CONCLUSION

To provide an effective means of detecting mechanical damages such as dents and cracks on the surface of cabbage, this study proposes a method for surface defect detection of cabbage that is proposed based on the curvature feature of the 3D point cloud. The experimental results show that this method has high accuracy and good robustness in detecting surface depression damage and cracking damage of flat-headed cabbage and round-headed cabbage. The conclusion of this study were as follows:

1. The cabbage point cloud collection platform was built based on the D455 depth camera. The ROI of cabbage samples was extracted by statistical filtering and the European clustering segmentation method, and the invalid information of the point cloud was removed. The data amount of point cloud was reduced by voxel down sampling. Based on the least square plane method, the normal vector was estimated, and the curvature of the point cloud was calculated. According to the curvature characteristic parameters, the curvature threshold was determined, and the interference factors on the surface of the cabbage were eliminated to accurately obtain the defective area.
2. In total, 80 point cloud samples of cabbage (including flat-headed cabbage and round-headed cabbage) were tested in the laboratory. It includes 30 samples of dent damage, 30 samples of crack damage, and 20 intact samples. The experimental results show that the average detection accuracy of the point cloud detection method for 80 samples was 96.25%. The average detection accuracy was 93.3% for dent cabbage samples and 96.67% for crack cabbage samples. In terms of the detection effect of two varieties of cabbage, the average detection accuracy of this method for round-headed cabbage was 97.5%, and the average detection accuracy of flat-headed cabbage was 95%. The results showed that the method had an excellent detection effect on two varieties and two defect types of cabbage.
3. In this study, a consumer-grade D455 depth camera was used to detect the defective area of cabbage, which provided an inexpensive automatic solution for the cabbage quality screening. In some cases, the detection accuracy decreased when the leaf edge bumps and dents were shallow. It is difficult to completely solve the problem by a single detection means. In the future, the detection accuracy and robustness can be improved by enhancing the hardware acquisition accuracy and developing the fusion of multiple detection means and multi-threshold discrimination.

DATA AVAILABILITY STATEMENT

The original contributions presented in this study are included in the article/supplementary material, further inquiries can be directed to the corresponding author.

AUTHOR CONTRIBUTIONS

JG, YZ, RW, and JD built the system, conducted experiments, and wrote the manuscript. BZ and YY designed the detection method. All authors discussed the detection method, designed the experiments, contributed to the article, and approved the submitted version.

FUNDING

This study was supported by the Key Research and Development Plan of Shandong Province (2022CXGC010608) and the Modern Agricultural Equipments and Technology Demonstration and Promotion Project of Jiangsu Province (NJ2020-08). We thank the team of the Beijing Research Center of Intelligent Equipment for Agriculture for financial support of the research.

ACKNOWLEDGMENTS

We thank Taiyu Wu, Lin Gui, Xiao Su, and Hanrong Lai for helpful discussion and assistance of the research.

REFERENCES

Chen, H., and Bhanu, B. (2007). 3D free-form object recognition in range images using local surface patches. *Pattern Recognit. Lett.* 28, 1252–1262. doi: 10.1016/j.patrec.2007.02.009

Chen, Y. H., An, X. S., Gao, S. M., Li, S. J., and Kang, H. W. (2021). A deep learning-based vision system combining detection and tracking for fast on-line citrus sorting. *Front. Plant Sci.* 12:622062. doi: 10.3389/fpls.2021.622062

Condotta, I., Brown-Brandl, T. M., Pitla, S. K., Stinn, J. P., and Silva-Miranda, K. O. (2020). Evaluation of low-cost depth cameras for agricultural applications. *Comput. Electron. Agric.* 173:105394. doi: 10.1016/j.compag.2020.105394

da Costa, A. Z., Figueroa, H. E. H., and Fracarolli, J. A. (2020). Computer vision based detection of external defects on tomatoes using deep learning. *Biosyst. Eng.* 190, 131–144. doi: 10.1016/j.biosystemseng.2019.12.003

Das Choudhury, S., Maturu, S., Samal, A., Stoerger, V., and Awada, T. (2020). Leveraging image analysis to compute 3D plant phenotypes based on voxel-grid plant reconstruction. *Front. Plant Sci.* 11:521431. doi: 10.3389/fpls.2020.521431

Fathizadeh, Z., Aboonajmi, M., and Beygi, S. R. H. (2020). Nondestructive firmness prediction of apple fruit using acoustic vibration response. *Sci. Hortic.* 262:109073. doi: 10.1016/j.scienta.2019.109073

Hu, Y. Z., and Furukawa, T. (2020). Degenerate near-planar 3D reconstruction from two overlapped images for road defects detection. *Sensors* 20:1640. doi: 10.3390/s20061640

Jiang, Y., Li, C. Y., Paterson, A. H., Sun, S. P., Xu, R., and Robertson, J. (2018). Quantitative analysis of cotton canopy size in field conditions using a consumer-grade RGB-D camera. *Front. Plant Sci.* 8:2233. doi: 10.3389/fpls.2017.02233

Li, Y., He, L., Jia, J., Lv, J., Chen, J., Qiao, X., et al. (2021). In-field tea shoot detection and 3D localization using an RGB-D camera. *Comput. Electron. Agric.* 185:106149. doi: 10.1016/j.compag.2021.106149

Li, Z., and Thomas, C. (2014). Quantitative evaluation of mechanical damage to fresh fruits. *Trends Food Sci. Technol.* 35, 138–150. doi: 10.1016/j.tifs.2013.12.001

Lu, Y. Z., and Lu, R. F. (2017). Histogram-based automatic thresholding for bruise detection of apples by structured-illumination reflectance imaging. *Biosyst. Eng.* 160, 30–41. doi: 10.1016/j.biosystemseng.2017.05.005

Luo, N., Jiang, Y. Y., and Wang, Q. (2021). Supervoxel-based region growing segmentation for point cloud data. *Intern. J. Pattern Recognit. Artif. Intell.* 35:2154007. doi: 10.1142/s0218001421540070

Mo, C., Kim, G., Kim, M. S., Lim, J., Lee, K., Lee, W. H., et al. (2017). On-line fresh-cut lettuce quality measurement system using hyperspectral imaging. *Biosyst. Eng.* 156, 38–50.

Nturambirwe, J. F. I., and Opara, U. L. (2020). Machine learning applications to non-destructive defect detection in horticultural products. *Biosyst. Eng.* 189, 60–83. doi: 10.1016/j.biosystemseng.2019.11.011

Wang, C. L., Zou, X. J., Tang, Y. C., Luo, L. F., and Feng, W. X. (2016). Localisation of litchi in an unstructured environment using binocular stereo vision. *Biosyst. Eng.* 145, 39–51. doi: 10.1016/j.biosystemseng.2016.02.004

Wu, G., Li, B., Zhu, Q., Huang, M., and Guo, Y. (2020). Using color and 3D geometry features to segment fruit point cloud and improve fruit recognition accuracy. *Comput. Electron. Agric.* 174:105475. doi: 10.1016/j.compag.2020.105475

Wu, S., Wen, W. L., Xiao, B. X., Guo, X. Y., Du, J. J., Wang, C. Y., et al. (2019). An accurate skeleton extraction approach from 3D point clouds of maize plants. *Front. Plant Sci.* 10:248. doi: 10.3389/fpls.2019.00248

Xie, W., Wei, S., Zheng, Z., and Engineering, D. Y. J. B. (2021). A CNN-based lightweight ensemble model for detecting defective carrots. *Biosyst. Eng.* 208, 287–299.

Xiong, B. A., Jiang, W. Z., Li, D. K., and Qi, M. (2021). Voxel grid-based fast registration of terrestrial point cloud. *Remote Sens.* 13:1905. doi: 10.3390/rs13101905

Xu, B., Jiang, W., Shan, J., Zhang, J., and Li, L. (2015). Investigation on the weighted RANSAC approaches for building roof plane segmentation from LiDAR point clouds. *Remote Sens.* 8:5. doi: 10.3390/rs8010005

Ying, W., Cuiyun, J., and Yanhui, Z. (2013). Pipe defect detection and deconstruction based on 3D points acquired by the circular structured Light Vision. *Adv. Mech. Eng.* 5:7. doi: 10.1155/2013/670487

Zhang, C., Zhao, C. J., Huang, W. Q., Wang, Q. Y., Liu, S. G., Li, J. B., et al. (2017). Automatic detection of defective apples using NIR coded structured light and fast lightness correction. *J. Food Eng.* 203, 69–82. doi: 10.1016/j.jfoodeng.2017.02.008

Zhang, D. J., Zou, Q., Lin, H., Xu, X., He, L., Gui, R., et al. (2018). Automatic pavement defect detection using 3D laser profiling technology. *Autom. Constr.* 96, 350–365. doi: 10.1016/j.autcon.2018.09.019

Zhang, J., Wang, J., Zheng, C. Y., Guo, H., and Shan, F. K. (2021). Nondestructive evaluation of chinese cabbage quality using mechanical vibration response. *Comput. Electron. Agric.* 188:106317. doi: 10.1016/j.compag.2021.106317

Zong, Y. L., Liang, J., Wang, H., Ren, M. D., Zhang, M. K., Li, W. P., et al. (2021). An intelligent and automated 3D surface defect detection system for quantitative 3D estimation and feature classification of material surface defects. *Opt. Lasers Eng.* 144:106633. doi: 10.1016/j.optlaseng.2021.106633

Conflict of Interest: RW was employed by Chinese Academy of Agricultural Mechanization Sciences Group Co., Ltd.

The remaining authors declare that the research was conducted in the absence of any commercial or financial relationships that could be construed as a potential conflict of interest.

Publisher's Note: All claims expressed in this article are solely those of the authors and do not necessarily represent those of their affiliated organizations, or those of the publisher, the editors and the reviewers. Any product that may be evaluated in this article, or claim that may be made by its manufacturer, is not guaranteed or endorsed by the publisher.

frontiers | Frontiers in Plant Science

TYPE Original Research
PUBLISHED 04 August 2022
DOI 10.3389/fpls.2022.967706

OPEN ACCESS

EDITED BY
Jiangbo Li,
Beijing Academy of Agriculture and Forestry Sciences, China

REVIEWED BY
Zhenguo Zhang,
Xinjiang Agricultural University, China
Yang Chuanhua,
Jiamusi University, China

*CORRESPONDENCE
Xinwu Du
du_xinwu@sina.com.cn

SPECIALTY SECTION
This article was submitted to Technical Advances in Plant Science, a section of the journal Frontiers in Plant Science

RECEIVED 16 June 2022
ACCEPTED 11 July 2022
PUBLISHED 04 August 2022

CITATION
Du X, Si L, Jin X, Li P, Yun Z and Gao K (2022) Classification of plug seedling quality by improved convolutional neural network with an attention mechanism.
Front. Plant Sci. 13:967706.
doi: 10.3389/fpls.2022.967706

Classification of plug seedling quality by improved convolutional neural network with an attention mechanism

Xinwu Du[1,2]*, Laiqiang Si[1], Xin Jin[1,3], Pengfei Li[1], Zhihao Yun[1] and Kaihang Gao[1]

[1]College of Agricultural Equipment Engineering, Henan University of Science and Technology, Luoyang, China, [2]Science & Technology Innovation Center for Completed Set Equipment, Longmen Laboratory, Luoyang, China, [3]Collaborative Innovation Center of Machinery Equipment Advanced Manufacturing of Henan Province, Luoyang, China

The classification of plug seedling quality plays an active role in enhancing the quality of seedlings. The EfficientNet-B7-CBAM model, an improved convolutional neural network (CNN) model, was proposed to improve classification efficiency and reduce high cost. To ensure that the EfficientNet-B7 model simultaneously learns crucial channel and spatial location information, the convolutional block attention module (CBAM) has been incorporated. To improve the model's ability to generalize, a transfer learning strategy and Adam optimization algorithm were introduced. A system for image acquisition collected 8,109 images of pepper plug seedlings, and data augmentation techniques improved the resulting data set. The proposed EfficientNet-B7-CBAM model achieved an average accuracy of 97.99% on the test set, 7.32% higher than before the improvement. Under the same experimental conditions, the classification accuracy increased by 8.88–20.05% to classical network models such as AlexNet, VGG16, InceptionV3, ResNet50, and DenseNet121. The proposed method had high accuracy in the plug seedling quality classification task. It was well-adapted to numerous types of plug seedlings, providing a reference for developing a fast and accurate algorithm for plug seedling quality classification.

KEYWORDS

plug seedlings, convolutional neural network, EfficientNet-B7-CBAM model, transfer learning, quality classification

Introduction

China is the world's leading producer of vegetables. China's vegetable cultivated area sowing area in 2020 was 2148.54 × 10^4 hm^2, and its production was 74912.90 × 10^4 t (Meng et al., 2021; Zhang et al., 2022). In order to meet the increasing demand for vegetable planting and ensure a safe and efficient supply of seedlings, vegetable

seedling production has adopted an intensive plug seedling cultivation method which is characterized by a high survival rate, low labor costs, and convenient transportation. Approximately 60% of the world's vegetable varieties currently use plug seedling technology (Li et al., 2021; Shao et al., 2021; Han et al., 2022). The plug seedlings enhanced the quality of vegetable seedlings as a whole. However, due to the sowing accuracy, seed quality, and seedling environment, the nursery tray contained empty plug cells, seedlings with poor growing conditions, and dead seedlings. About 5–10% of the total number of seedlings were comprised of these empty plug cells and weak seedlings. If they are not eradicated, they will not only cause economic losses but also hinder future machine transplantation operations. For the quality of plug seedlings, it is necessary to remove empty plug cells and weak seedlings from the tray cells and replant them with strong seedlings (Jin et al., 2020; Wen et al., 2021; Yang et al., 2021).

In intensive plug seedlings, classification of seedling quality is necessary to ensure overall seedling quality. Currently, this process relies heavily on manual labor. Manual classification is time-consuming, laborious, inefficient, and prone to error, making it challenging to meet the demands of large-scale seedling production. Consequently, it is essential to investigate the automated plug seedling quality classification technology, and machine vision is a crucial component of this technology (He et al., 2019; Yang et al., 2020; Tong et al., 2021). Early identification of plug seedlings using machine vision and conventional image processing techniques. Tong et al. (2018) presented a skewness correction algorithm for images of plug seedlings based on the canny operator and hough transform. The method is based on the watershed algorithm and the center of gravity method to extract leaf area and seedling leaf number from images of plug seedlings for quality evaluation; the results showed that the average accuracy of empty plug cells and weak seedlings reached 98%. Wang et al. (2018) developed a device for automatically supplementing vegetable plug seedlings to obtain accurate information about plug seedlings. By obtaining information on the vegetation statistics values of each cell, the method achieved a 100% accurate classification of plug cells and seedling cells. Jin et al. (2021) proposed a computer vision-based architecture to identify seedlings accurately. The method extracts leaf area information from plug seedlings using a genetic algorithm and a three-dimensional block matching algorithm with optimal threshold segmentation. Based on the results, the detection accuracy for healthy seedlings reached 94.33%. Wang et al. (2021) proposed a non-destructive monitoring method for the growth process of plug seedlings based on a Kinect camera, which determines the germination rate in trays by reconstructing leaf area analysis with an error of less than 1.56%. To determine the growth status of plug seedlings, the primary research used the threshold pre-processing method for threshold segmentation and statistical pixel value information. The technology is relatively mature. Nonetheless, the following problems remain. (1) Following segmentation, seedling growth data is lost. (2) To obtain the proper segmentation threshold, a large number of human tuning parameters are required. (3) More complex algorithms must be developed to increase the precision of leaf area segmentation.

The application of deep CNN models in agriculture has achieved significant results in recent years, including disease detection (Sharma et al., 2022), weed identification (Wang et al., 2022), and crop condition monitoring (Zhao L. et al., 2021; Tan et al., 2022). Using deep learning techniques to classify the quality of plug seedlings can better meet the development requirements of seedling production. Namin et al. (2018) proposed a robust AlexNet-CNN-LSTM architecture for classifying the various growth states of plants. This method improved model performance by embedding long short-term memory network (LSTM) units and achieved 93% recognition accuracy by reducing model parameters. Xiao et al. (2019) developed a transfer learning CNN for the plug seedling classification model. Based on a limited sample of empty plug cells, weak seedlings, and strong seedlings, the final classification accuracy was 95.50%. Perugachi-Diaz et al. (2021) used an AlexNet network to predict the growth of cabbage seedlings. According to the results, the method provided a reliable and effective classification of cabbage seedlings with an optimal recognition accuracy of 94%. Garbouge et al. (2021) proposed a method for tracking the growth of seedlings that combines RGB with deep learning. As a result of the method, seedlings grown in plug cells, seedlings at the cotyledon stage, and seedlings at the true leaf stage performed with an average classification accuracy of 94%. Compared to other models discussed in the paper, Kolhar and Jagtap (2021) proposed a CNN-ConvLSTM-based model for seedling quality classification of Arabidopsis thaliana that achieved 97.97% classification accuracy with very few trainable parameters. According to the appeal study, CNNs had a higher accuracy rate and more excellent stability than conventional image processing methods without requiring threshold segmentation. However, the following issues persist: (1) The majority of current CNN have high computational complexity and a large number of parameters, making it difficult to directly deploy and apply them in this paper's quality classification of plug seedlings. (2) Due to the variability between different task goals, CNN models required a certain amount of target data for adaptive learning. Constructing the desired data set required much human time and effort.

Using pepper plug seedlings as the research object, a new and more effective CNN model, EfficientNet-B7-CBAM, is presented for seedling quality classification. Following is a summary of the main contributions and innovations.

1. A classification standard for various qualities of plug seedlings is developed. On the basis of this standard, an 8109-image dataset of plug seedlings is compiled to aid in developing a plug seedling quality classification model.

2. A novel attention-based recognition model for plug seedling quality classification, the EfficientNet-B7-CBAM model, is proposed. By deeply integrating the CBAM module and the EfficientNet-B7 model, the model can simultaneously acquire feature channel information and spatial information attention and enhance the model's ability to learn important information about the plug seedling region.
3. The lightweight and high-performance EfficientNet-B7-CBAM model can provide technical support for developing the automated classification of plug seedling quality equipment.

Experimental data

Data acquisition

Pepper plug seedlings were grown from Oct to Nov 2021 in a multi-span seedling nursery at the Academy of Agricultural Sciences, Luoyang City, Henan Province, China (34°39′55″N, 112°21′58″E), as shown in **Figure 1**. The temperature in the greenhouse was kept between 20–25°C during the day and 10–15°C at night. The chosen pepper variety was the stress-resistant Luo Jiao 308 variety. The seeds were sterilized before being sown with a single hole and seed. Approximately 9,000 pepper seeds were planted in 540 mm × 280 mm, 32-cell nursery trays that contained a mixture of peat, vermiculite, and perlite (at a 3:1:1 ratio).

Image the tops of pepper plug seedlings using the selected data acquisition equipment Hikvision MV-CE200-10UC color sensor camera with a frame rate of 14 fps and a resolution of 5472 × 3648 pixels. The USB3.0 port connects the camera to the computer. The lens was the MVL-HF1224M-10MP model with a focal length of 12 mm. When shooting, the camera was mounted vertically above the nursery trays at the height of H = 545.4 mm, effectively encompassing the standard nursery trays area. Three light-emitting diodes (LED) with a power of 5.76 W/m were installed on the inner wall of the lightbox to supplement the light during image capture, thereby enabling the camera to capture the fine details of the seedlings in the nursery trays. The image capture system is shown in **Figure 2**.

Data preprocessing

Pepper seedlings at approximately 21 days after emergence are shown in **Figure 3**. Within the same batch of pepper plug seedlings, there are empty plug cells caused by non-germinating seeds, weak seedlings with slow growth, and strong seedlings for transplantation due to biological differences between individual seedlings. Leaf area characteristics were obtained to classify three distinct types of plug seedlings with varying qualities to construct image data sets of empty plug cells, weak seedlings, and strong seedlings.

Leaf area is a popular gauge employed in agricultural cultivation and breeding techniques, and it is one of the most important indicators for determining crop yield and quality. For the purpose of categorizing the quality of pepper seedlings, leaf area parameters were extracted from pepper seedlings. The leaf area extraction procedure for pepper seedlings is shown in **Figure 4**.

The distribution of pixel values for the leaf area of 21-day-old pepper plug seedlings is shown in **Figure 5**. Leaf areas were 0 in empty plug cells, less than 100 in weak seedlings, and at least 100 in strong seedlings.

In order to construct training data set, empty plug cells, weak seedlings, and strong seedlings were extracted from the original RGB image based on their pixel value distributions. Pepper plug seedlings of differing qualities are shown in **Figure 6**. After the reduction, 2,210 empty plug cells, 3,381 weak seedlings, and 2,518 strong seedlings were obtained. Using the Albumentations library to expand data, the original data for pepper plug seedlings were enhanced to include additional image data. The data were clipped, rotated, and inverted to generate a data set containing 19,603 images, as shown in **Table 1**.

Methodology

This study chose the lightweight, high-precision, and simple-to-deploy EfficientNet-B7 model as the benchmark network for the application of intelligent recognition algorithms to images of plug seedlings in agriculture. To increase the network model's recognition accuracy, the CBAM module was introduced to optimize and enhance the EfficientNet-B7 model, which was then renamed EfficientNet-B7-CBAM.

Efficientnet-B7 network structure

To improve the performance of the CNN model, we increased the input image's resolution as well as the network's depth and width. However, the concurrent use of the three methods may result in severe issues, such as the loss of model gradients and the degradation of models. The emergence of EfficientNet is characterized by a balance between depth, width, and resolution. There were B0-B7 EfficientNet versions. Mobile Inverted Bottleneck Convolution (MBConv) was the core structure of the network (Zhang et al., 2020; Liu et al., 2021; Bhupendra et al., 2022). This module introduces the Squeeze-and-Excitation Network (SE)'s core concept to optimize the Network's structure, as shown in **Figure 7**. The MBConv module first uses 1 × 1 convolutions to up-dimension the feature

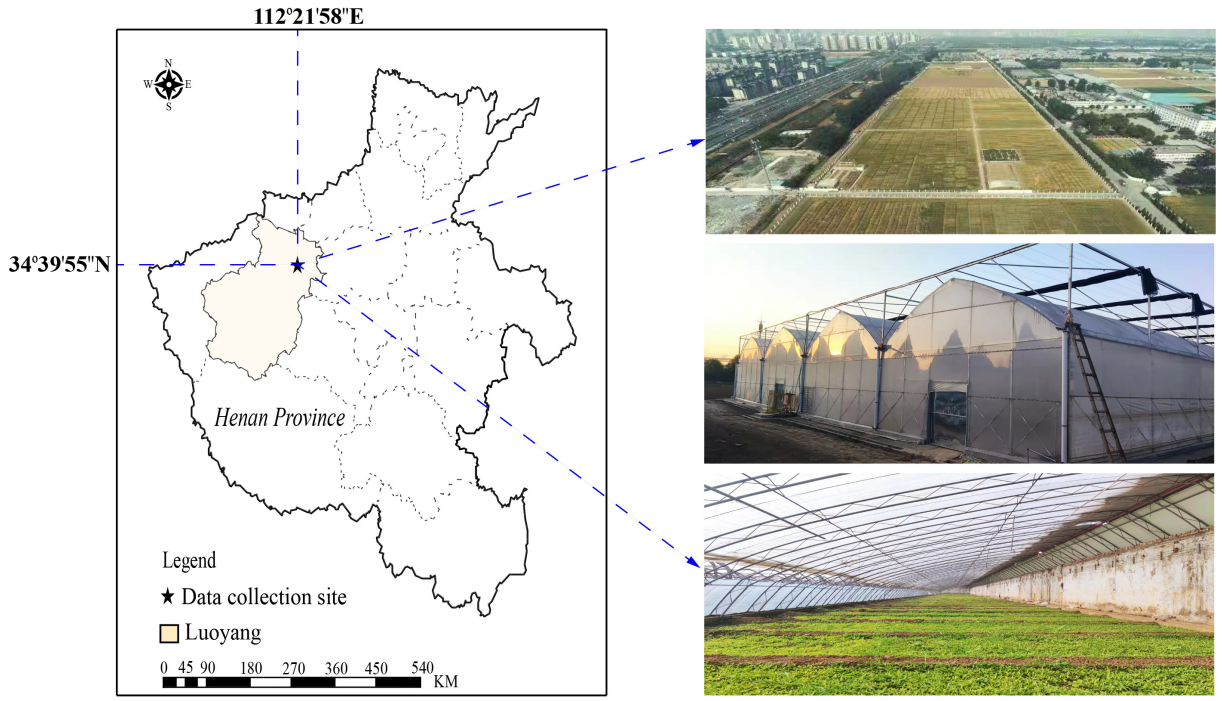

FIGURE 1
Location of data collecting and multi-span seedling greenhouses.

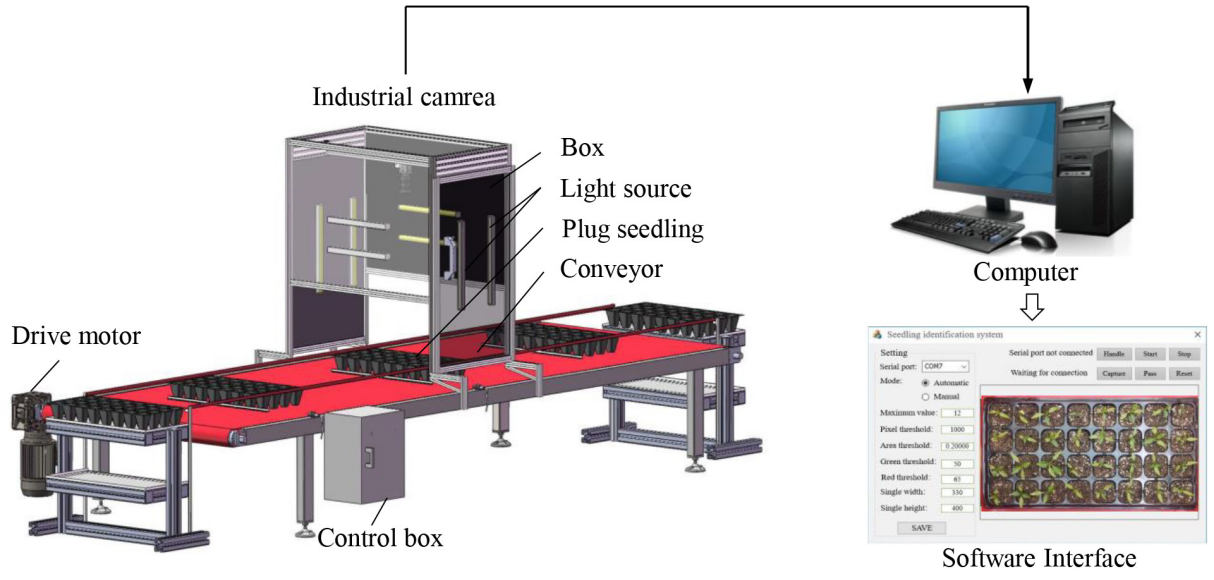

FIGURE 2
Picture capture system.

map, followed by $k \times k$ depthwise convolutions. After that, SE modules adjust the feature map matrix, and eventually, 1×1 convolutions to down-dimension the feature map. When the input and output feature maps have the same shape, the MBConv module is also capable of performing short-cut concatenation. This structure reduces model training time. A typical Efficientnet-B7 model consists of 55 layers of MBConvs modules, 2 layers of Convs modules, 1 layer of global average pool, and 1 layer of FC classification. The network architecture of EfficientNet-B7 is shown in Figure 8.

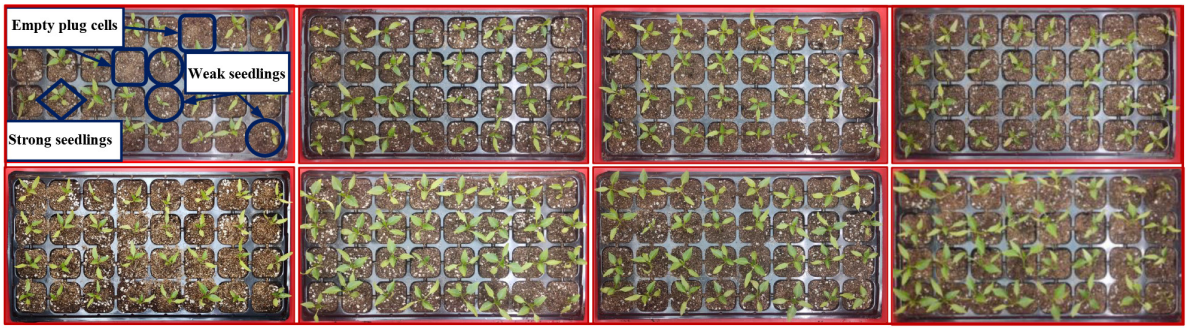

FIGURE 3
Sample of pepper seedlings growing for 21 days.

Convolutional block attention module model

This section will provide an overview of the CBAM attention mechanism. Woo proposed CBAM, which would be comprised of two modules: the channel attention module and the space attention module (Bao et al., 2021; Gao et al., 2021; Zhao Y. et al., 2021). The CBAM module is shown in **Figure 9**. The CBAM module first generates the feature map F' *via* the channel attention module, then the feature map F'' *via* the spatial attention module, given a middle layer feature map F as input, as shown in **Figure 9A**. The process of calculation can be expressed as Equation 1.

$$\begin{cases} F' = M_c(F) \otimes F \\ F'' = M_s(F') \otimes F' \end{cases} \quad (1)$$

where $\otimes$ represents the multiplication operation between the corresponding elements. F ($\in R^{C\times H\times W}$) represents the input feature map. M_c ($\in R^{C\times 1\times 1}$) represents the output weight of F' through the channel attention. M_s ($\in R^{1\times H\times W}$) represents the output weight of F'' through the spatial attention.

The module of the channel attention mechanism is shown in **Figure 9B**. In the first step of the channel attention mechanism, the average pooling and maximum pooling operations are performed based on width and height to generate two layers of $C \times 1 \times 1$ feature maps. Then, they are fed to the shared MLP layer for summation and activated by the sigmoid to produce the final channel attention feature weights M_c. The channel attention calculation procedure can be expressed as Equation 2.

$$M_c(F) = \sigma[MLP(AvgPool(F)] + MLP[MaxPool(F)] \quad (2)$$

where σ represents a sigmoid function; MLP represents a multilayer perceptron.

The module of the spatial attention mechanism is shown in **Figure 9C**. As input to the spatial attention mechanism is the feature map F'. First, the average pooling and maximum pooling operations are performed on the channel to generate a two-layer $1 \times H \times W$ feature map, which is then subject to the Concatenate operation. The dimension of the feature map is then reduced using a 7×7 convolution kernel, and the Sigmoid function is used to generate the spatial attention weights M_s. The spatial attention calculation procedure can be expressed as Equation 3.

$$M_s(F) = \sigma\{f^{7\times 7}[AvgPool(Mc); MaxPool(Mac)]\} \quad (3)$$

Where $f^{7\times 7}$ is the convolution operation with a convolution kernel size of 7×7, which is used to extract the spatial features of the target.

EfficientNet-B7-CBAM model

EfficientNet-B7 is composed of the MBConv stack, with each MBConv module containing a SE module. The SE module controls the focus or gating of channel dimensions. The model can emphasize the channel characteristics that contain the most information while ignoring the channel characteristics that are unimportant. However, this operation only considered the information of the channels and lost the spatial information, which played a crucial role in the visual recognition task of seedlings, which negatively impacted the classification performance of seedlings. CBAM was added to Efficientnet-B7 in this study to improve the model's ability to extract features. The improved EfficientNet-B7-CBAM network structure is shown in **Figure 10**. The following enhancements have been made relative to the original Efficientnet-B7 network model:

(1) The SE module within each MBConv module of the original EfficientNet-B7 model was replaced with a CBAM module. This allowed the network to acquire channel information without losing crucial spatial information regarding the pepper plug seedlings.

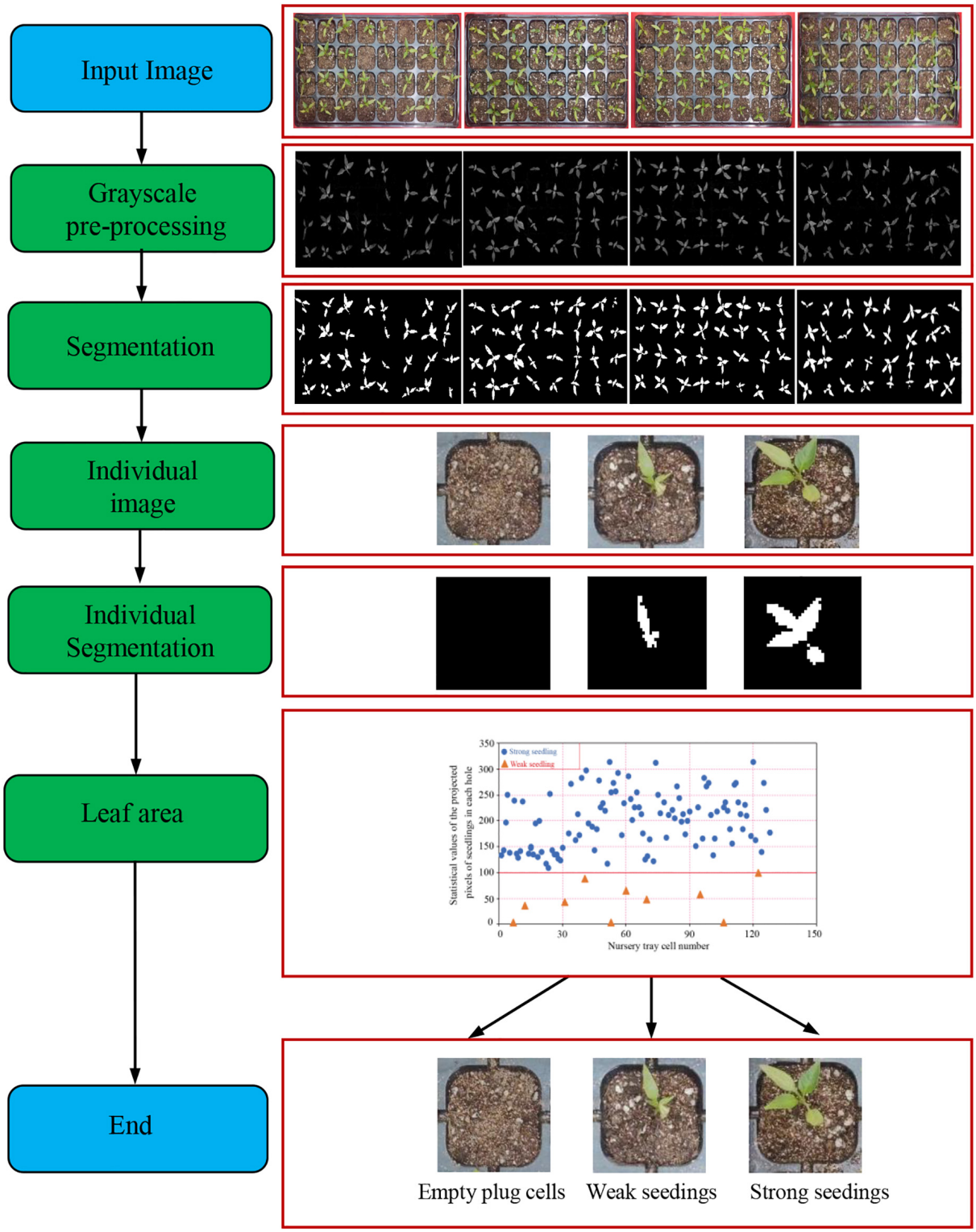

FIGURE 4
The image processing flow of the leaf area of pepper seedlings.

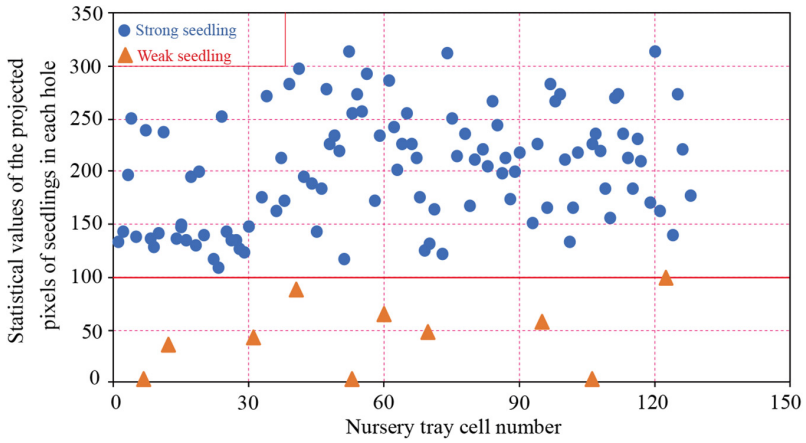

FIGURE 5
Pixel statistical scatter plot of seedling leaf area.

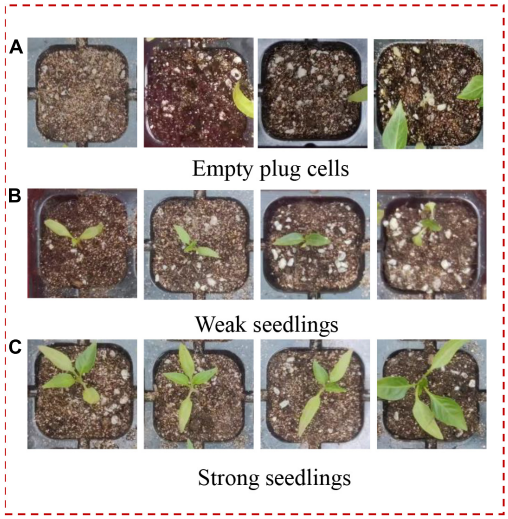

FIGURE 6
Plug seedlings of different qualities. **(A)** Empty plug cells. **(B)** Weak seedlings. **(C)** Strong seedlings.

(2) The CBAM module was embedded in the EfficientNet-B7-CBAM model after the second convolutional layer. It improved the model's ability to classify different quality plug seedlings by refining the extracted feature information and enhancing the model's classification capability.

Adam optimization algorithm

A classical optimization algorithm is used to optimize the EfficientNet-B7 model: Stochastic Gradient Descent (SGD). Due to the same learning rate for each parameter, it was difficult to obtain a suitable learning rate for the SGD algorithm. In addition, the SGD optimization algorithm converges rapidly to a local optimum when training the model, which causes the model to be unable to obtain an optimal training model when performing different quality pepper plug seedling classification tasks. In order to solve the above problem, this paper employed the Adam optimization algorithm. Each parameter of the Adam algorithm maintained a learning rate and was adjusted individually as a result of training. Additionally, each learning rate adjustment was bias-corrected in order to reduce the fluctuations in parameter updates and enhance the smoothness of the model convergence. In the Adam optimization algorithm, momentum updates are combined with learning rate adjustments, and the learning rates of each parameter are dynamically adjusted by the first and second moments of the gradient (Yu and Liu, 2019; Ilboudo et al., 2020; Cheng et al., 2021). The calculation process can be expressed as Equation 4.

TABLE 1 The sample size of the training set and validation set.

Class	Training dataset	Validation dataset	Total
Strong seedlings	5,042	843	5,885
Weak seedlings	6,230	1,037	7,267
Empty plug cells	5,480	971	6,451

$$\begin{cases} \theta_t = \theta_{t-1} - \alpha \cdot \frac{\hat{m}_t}{\sqrt{\hat{v}_t}+\varepsilon} \\ \hat{m}_t = \frac{m_t}{1-\beta_1^t} \\ \hat{v}_t = \frac{v_t}{1-\beta_2^t} \\ m_t = \beta_1 \cdot m_{t-1} + (1-\beta_1) \cdot g_t \\ v_t = \beta_2 \cdot v_{t-1} + (1-\beta_2) \cdot g_t^2 \\ g_t = \nabla_\theta f_t(\theta_{t-1}) \end{cases} \quad (4)$$

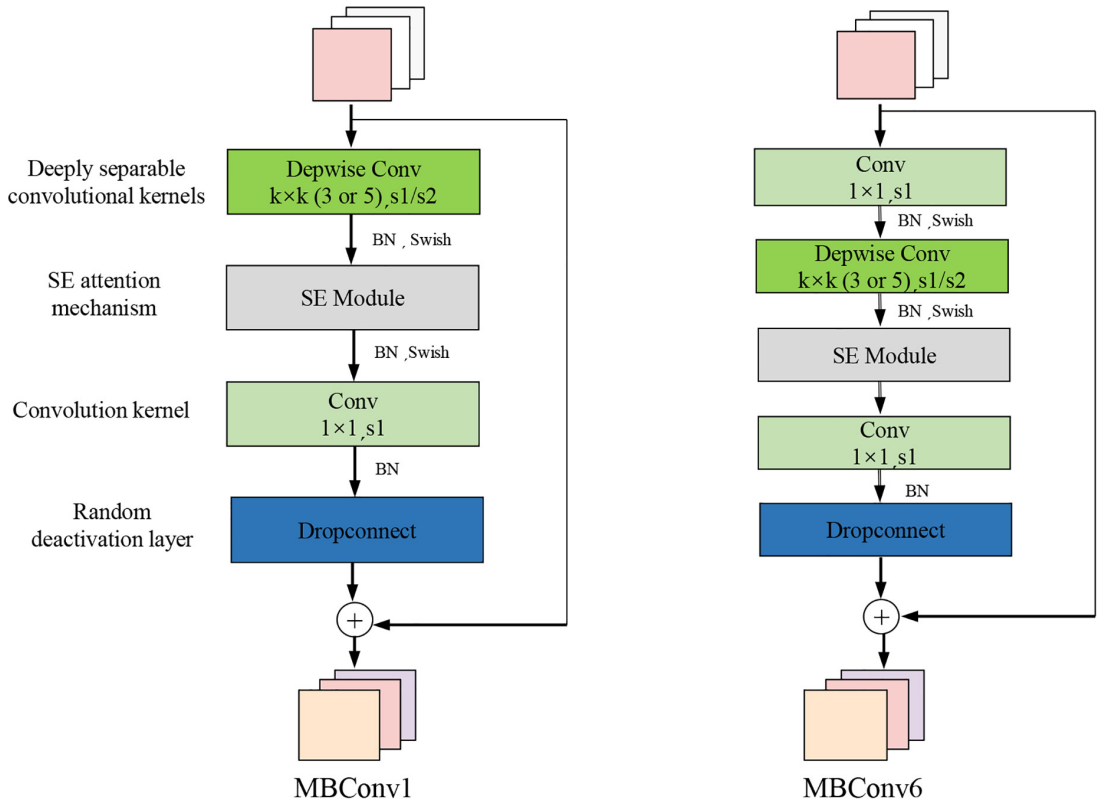

FIGURE 7
Mobile inverted bottleneck convolution.

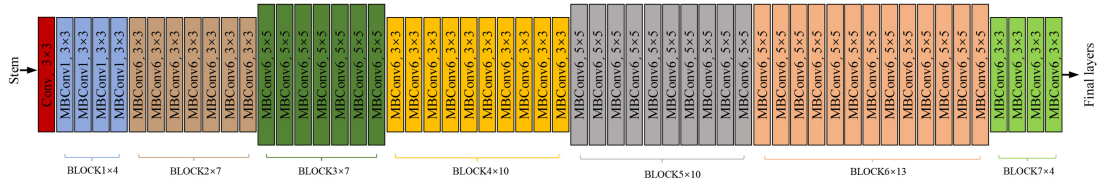

FIGURE 8
The network structure of EfficientNet-B7.

where θ_t and θ_{t-1} represents the parameter values of the tth and t-1th updates. m_t represents the exponentially shifted mean of the gradient. v_t represents the squared gradient. $\hat{m}_t$ represents the updated value of m_t. $\hat{v}_t$ represents the updated value of v_t. β_1 and β_2 represent the constants used to control the exponential decay. g_t represents th first-order derivative. The default values for each of the parameters are: $\alpha = 0.001, \beta_1 = 0.9, \beta_2 = 0.999$, and $\varepsilon = 10^{-8}$.

Transfer learning

Given that images from different domains contain common underlying features among them, transfer learning makes the training more stable by transferring knowledge of common features in the convolutional layer, thus improving the training efficiency (Espejo-Garcia et al., 2022; Zhao X. et al., 2022). Inspired by this, this study is based on transfer learning to train the EfficientNet-B7-CBAM network.

All models utilized in this study were pretrained on the ImageNet dataset. The pre-trained weights were used only for initialization. All models were fully trained using the previously created plug seedling data. Due to the fact that there were only three types of plug seedlings, the final fully connected layer in each network was reduced from 1,000 to 3. SoftMax activation was implemented in the final layer. Using the Adam optimization algorithm and categorical cross-entropy

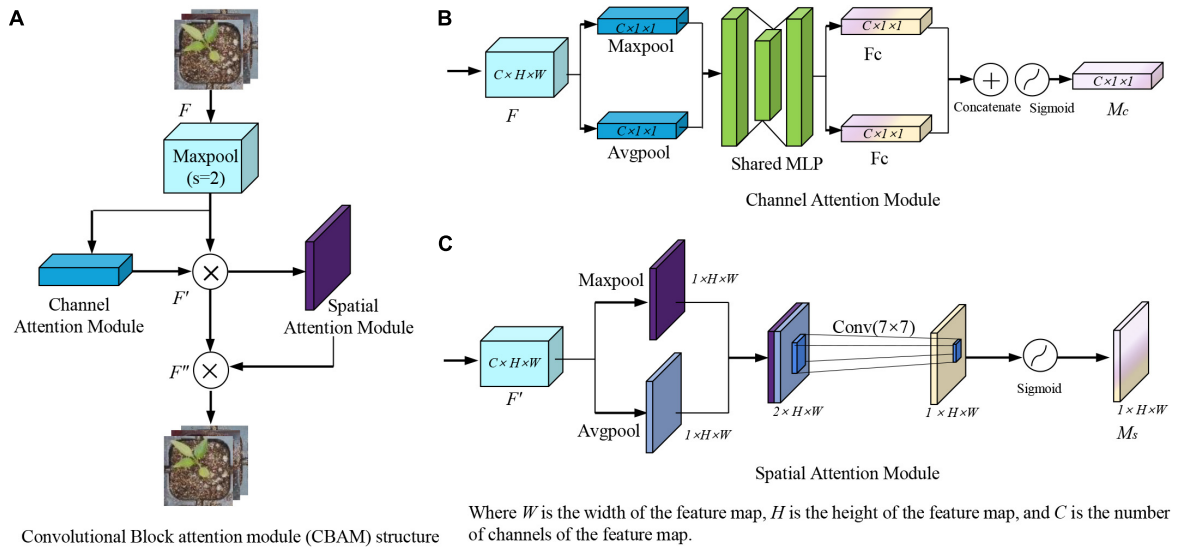

FIGURE 9
CBAM attention module. **(A)** Convolutional block attention module (CBAM) structure. **(B)** Channel attention module. **(C)** Spatial attention module. Where *W* is the width of the feature map, *H* is the height of the feature map, and *C* is the number of channels of the feature map.

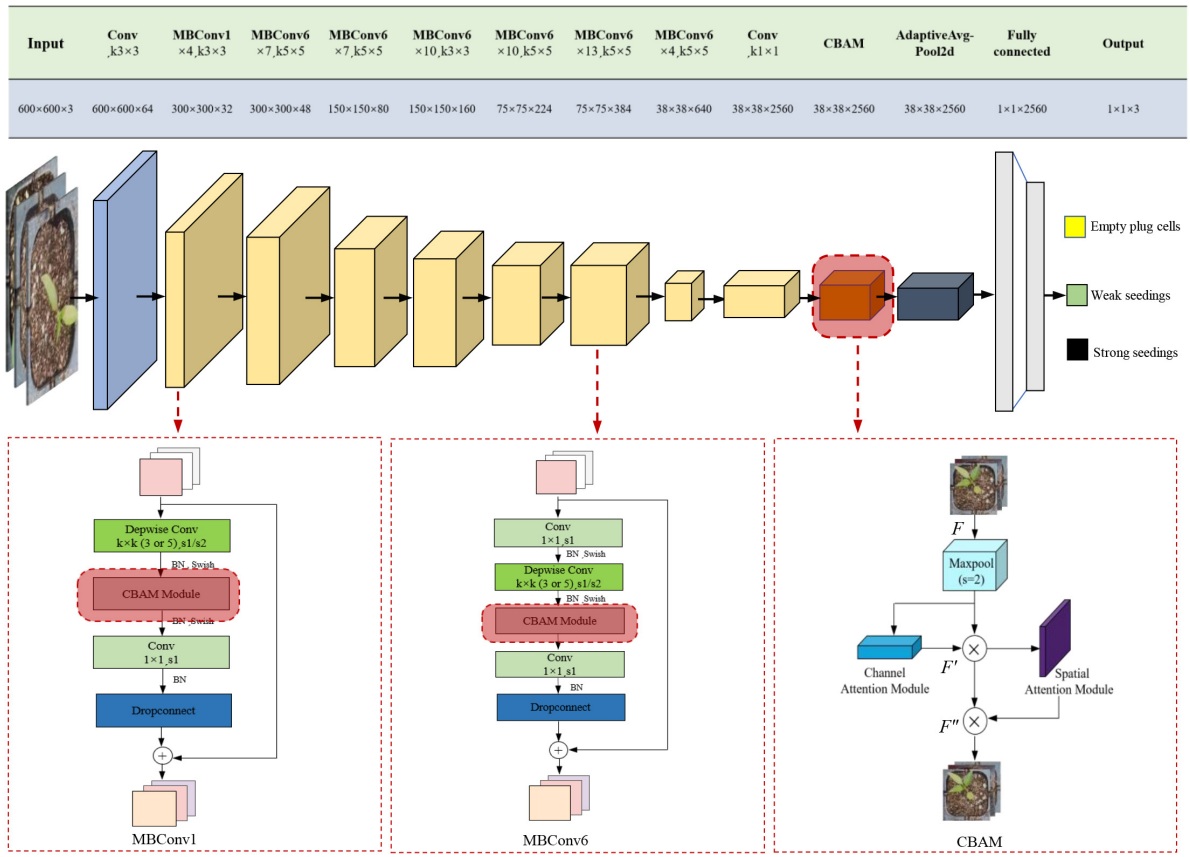

FIGURE 10
EfficientNet-B7-CBAM model.

TABLE 2 Results of ablation experiment.

No.	Average A_{cc}/%	Average P_r/%	Average R_e/%	Average F_1/%	Times of training (min)
1	90.67	91.03	90.66	90.84	96.7
2	94.66	94.82	94.67	94.75	73.2
3	95.33	95.41	95.33	95.37	52.5
4	96.66	96.76	96.67	96.72	40.9
5	97.99	98.01	98.00	98.01	36.5

as a loss, the models were trained. The Adam optimization algorithm's parameters were as described as: $\alpha = 0.001$, $\beta_1 = 0.9$, $\beta_2 = 0.999$, and $\varepsilon = 10^{-8}$. There was a maximum of 300 iterations. The initial learning was set to 0.001, and the learning rate decayed to the original 0.8 for every 10 training epochs. The batch size was limited to 16 due to hardware limitations. We used dropout before the last layer of each model. A dropout rate of 0.45 was observed in this paper's model.

Experimental results and analysis

Experimental configuration

Configuration of the hardware: GPU: GeForce GTX 1080Ti with 12 GB of video memory. The NVIDIA graphics drivers installed were CUDA 10.1 and CUDNNV7.6. It was NVIDIA's GPU parallel computing framework that enabled users to solve complex computing problems using GPUs. CuDNN was a GPU accelerator developed by NVIDIA for deep neural networks. Windows 10 was the operating system of the software, and Python 3.8.5 was used to create the Pytorch deep learning framework and Opencv open-source visual library.

Model evaluation index

The confusion matrix is an effective tool for evaluating the classification model's merit and performance (Gajjar et al., 2022; Zhao Y. et al., 2022). Typically, the measures of model performance in the confusion matrix are Recall (R_e), F1-Score (F_1), Precision (P_r), and Accuracy (A_{cc}). The above formula for the four indexes can be expressed as Equations 5, 8.

$$R_e = \frac{TP}{TP + FN} \tag{5}$$

$$P_r = \frac{TP}{TP + FP} \tag{6}$$

$$F_1 = 2 \cdot \frac{Precision \times Recall}{Precision + Recall} \tag{7}$$

$$A_{cc} = \frac{TP + TN}{TP + TN + FP + FN} \tag{8}$$

where TP represents the number of samples predicted by the model to be in a positive class that were actually in a positive class, whereas FP represents the number of samples predicted to be in a positive class that were actually in a negative class. TN is the number of samples predicted by the model to be in the negative class that are in the negative class. FN indicates the number of samples that the model predicted to be in a negative class but were actually in a positive class.

Results and analysis

In this section, all models were validated on the re-collected data set of 450 unlabeled images of pepper plug seedlings (150 images of each plug seedling type). Concurrently, the evaluation index was the proposed confusion matrix from Section "Model evaluation index."

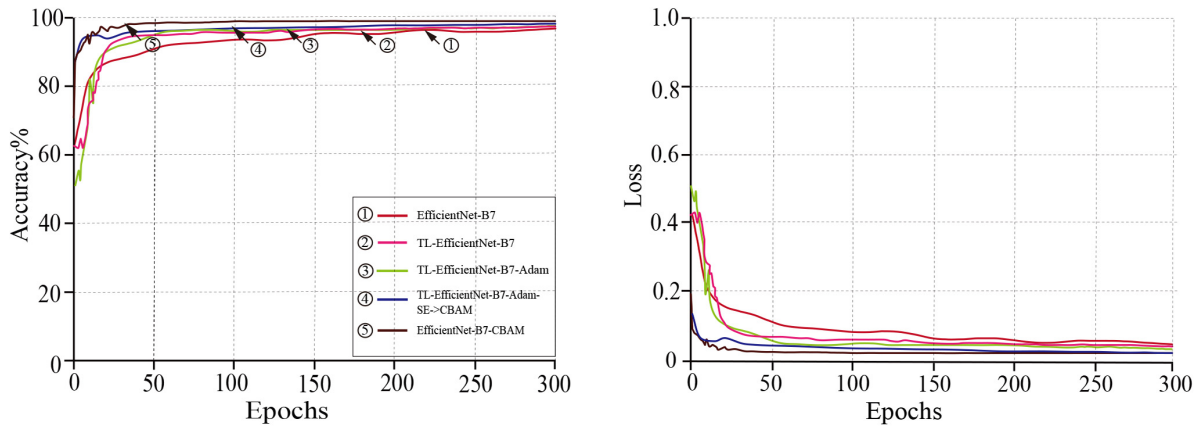

FIGURE 11
The training curves of the models.

TABLE 3 Performance of the model before and after data augmentation.

Data set	Class	P_r/%	R_e/%	F_1/%	Acc/%
Original	Empty plug cells	95.45	98.00	96.71	96.45
	Weak seedlings	95.36	95.33	95.01	
	Strong seedlings	94.70	96.00	97.63	
Data augmentation	Empty plug cells	97.40	100.00	98.68	97.99
	Weak seedlings	97.31	96.67	96.99	
	Strong seedlings	99.32	97.33	98.31	

TABLE 4 Performance comparison with other models.

Model	Average A_{cc}/%	Average P_r/%	Average R_e/%	Average F_1/%	Times of training (min)
AlexNet	77.94	78.92	78.67	78.79	80.9
VGG16	81.98	82.75	81.78	82.27	220.9
InceptionV3	85.60	86.24	85.55	85.89	60.3
ResNet50	88.92	82.93	88.89	85.91	48.5
DenseNet121	89.11	89.56	89.11	89.34	42.2
EfficientNet-B7-CBAM	97.99	98.01	98.00	98.01	36.5

Ablation experiments

In order to verify the effectiveness of the EfficientNet-B7-CBAM model, the following five abatement experiments were set up. (1) The original EfficientNet-B7 model. (2) In scheme 1 based on EfficientNet-B7 model trained using transfer learning, which constructed TL-EfficientNet-B7 model. (3) Used Adam's optimization algorithm to train the TL-EfficientNet-B7 model, which constructed the TL-EfficientNet-B7-Adam model. (4) Replaced the SE module with the CBAM module in the TL-EfficientNet-B7-Adam model, which constructed the TL-EfficientNet-B7-Adam+SE- > CBAM model. (5) The EfficientNet-B7-CBAM model in this paper.

The training results of the models for the five schemes described above are shown in Table 2. Compared to the experimental results of schemes 1 and 2, the average classification accuracy of the TL-EfficientNet-B7 model for plug seedlings reached 94.66%, which was 3.99% higher than that of the model in scheme 1. Additionally, the model's training time was reduced by 23.5 min, and the transfer learning method effectively enhanced the model's generalization ability. Compared to the experimental results of schemes 2 and 3, the average classification accuracy of the TL-EfficientNet-B7-Adam model was 95.33%, a 0.67% improvement over the scheme 2 models, and its training time was reduced by 20.7 min. The Adam optimization algorithm could hasten the model's convergence and enhance its performance. The effectiveness of the scheme improvement was demonstrated by the fact that the overall accuracy of the TL-EfficientNet-B7-Adam model increased by 4.66%, and the training time was reduced by 44.2 min using both transfer learning and Adam optimization algorithms. In addition, experiments comparing schemes 3 and 4 demonstrated that the CBAM module possessed superior attention learning capability to the SE module. Compared to the experimental results of schemes 4 and 5, the addition of the CBAM module after the second convolutional layer improves the model's ability to extract information. The experimental

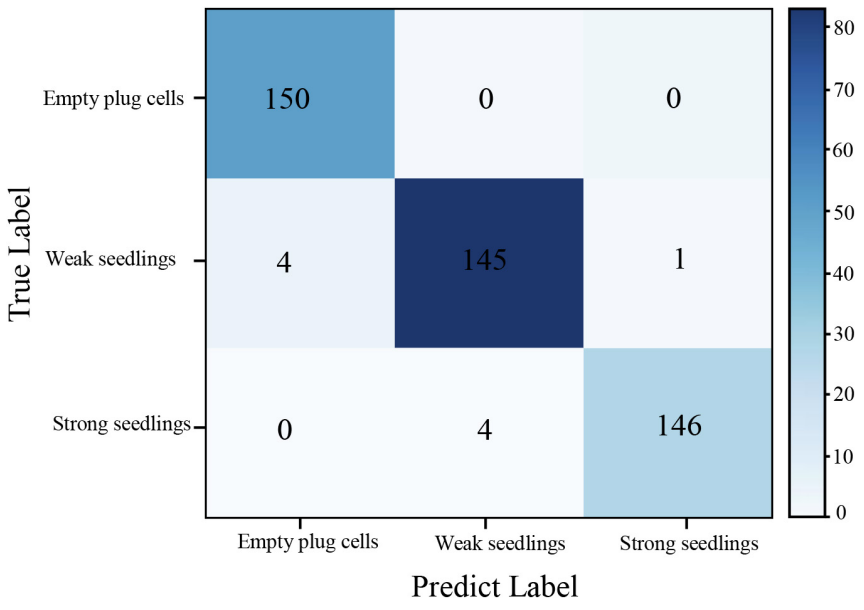

FIGURE 12
The EfficientNet-B7-CBAM model confusion matrix.

results shown in Table 2 demonstrated that the enhanced EfficientNet-B7-CBAM model achieved a classification accuracy of 97.99% on the previously constructed plug seedling dataset, which was 7.32% better than before the enhancement, and that the model training time was reduced by 60.2 min. The training curves of the models proposed by the five schemes are shown in Figure 11. According to Figure 11, the EfficientNet-B7-CBAM model converged around the 40th iteration, which was the quickest convergence speed of all models.

In combination with the above findings, the model training scheme's feasibility and effectiveness could be determined. The improved EfficientNet-B7-CBAM model performed the classification of plug seedling quality with high accuracy and robustness.

The impact of data enhancement on model performance

Data augmentation was performed on the plug seedling images to increase the EfficientNet-B7-CBAM model's resistance to interference in complex environments and prevent overfitting issues. A series of comparison experiments were designed to demonstrate the effect of data augmentation on model performance improvement in order to verify the effect of data augmentation. The experimental results before and after model data enhancement is shown in Table 3. By comparing the model's A_{cc}, R_e, P_r, and F_1 performance metrics for each category on the plug seedling test set. On the test set, the classification recognition accuracy of the model trained on the original plug seedling data was 96.45%, which was 1.54% than the classification accuracy of the model after data enhancement. The experimental results demonstrated that data augmentation can improve model performance and contribute to the classification of plug seedlings.

The performance comparison of different convolutional neural network model

Several classical CNN models AlexNet, VGG16, InceptionV3, ResNet50, and DenseNet121 were used to classify datasets of different quality cavity seedlings in order to demonstrate the efficacy of EfficientNet-B7-CBAM Mode. In addition, the performance was compared to the EfficientNet-B7-CBAM model. To ensure the fairness of the experiment, the above CNN models and EfficientNet-B7-CBAM Mode were trained using the same strategy and hardware configuration. The classification performance of several models is shown in Table 4.

As shown in Table 4, the EfficientNet-B7-CBAM model had the highest average classification accuracy of 97.99% on the test set of different quality pepper plug seedlings, which was 20.05, 16.01, 12.39, 9.07, and 8.88% higher than the average classification accuracy of a number of other models, respectively. Additionally, the EfficientNet-B7-CBAM model's training time was only 36.5 min. In summary, the EfficientNet-B7-CBAM model had a significant advantage in terms of accuracy and training time, and was better able to meet the classification requirements for plug seedling quality.

Confusion matrix of the model

The confusion matrix of the EfficientNet-B7-CBAM model applied to the test set of plug seedlings, as shown in Figure 12. The average classification accuracy of the EfficientNet-B7-CBAM model for the three types of plug seedlings was 97.99%, the average P_r was 98.01%, the average R_e was 98.00%, and the overall index F_1 was 98.01%, as determined by the confusion matrix. From the confusion matrix, it was evident that empty plug cells, weak seedlings, and Strong seedlings were misclassified as one another. Empty plug cells were misclassified as weak seedlings due to the presence of shed leaves; weak seedlings were misclassified as strong seedlings due to the interference of leaves protruding from seedlings in adjacent cells; and strong seedlings were misclassified as weak seedlings due to the incorrect angle of the plug seedlings and the low resolution of the images in this category.

Conclusion

In order to support effective management of seedlings, an improved convolutional neural network with an attention mechanism was proposed in this work. The device acquisition system was used to collect a total of 8,109 images of plug seedlings for the model training process. Image augmentation was used to expand the dataset during the data preparation stage. The original EfficientNet-B7 model and the CBAM module were thoroughly integrated to acquire feature channels and spatial location data simultaneously. To hasten the model's convergence, a transfer learning technique and the Adam optimization algorithm were also applied. The suggested model underwent extensive training, testing, and comparative experimentation. The proposed method in this study reaches recognition accuracy of 97.99%, which is better than other deep learning techniques currently in use, according to experimental results. The method's competitive performance on the task of classifying the quality of plug seedlings served as a benchmark for the use of deep learning techniques in plug seedling classification. Our follow-up studies aim to expand the dataset and enhance the model's ability to generalize in challenging situations. Additionally, by quantizing and pruning the model to reduce the number of parameters, and speed up the model convergence.

Data availability statement

The raw data supporting the conclusions of this article will be made available by the authors, without undue reservation.

Author contributions

XD: guidance on thesis writing and funding. LS: original writing. XJ: supervision, revision, and funding. PL: helped to set up the test bench and organize the data. ZY: helped to build the test bench and organize data. KG: helped to build the testbed and organize the data. All authors contributed to the article and approved the submitted version.

Funding

This work was supported in part by the National Natural Science Foundation of China (52075150) and in part by the Natural Science Foundation of Henan Province (No. 202300410124) and Guangdong Key R&D Program (No. 2019B020222004).

Conflict of interest

The authors declare that the research was conducted in the absence of any commercial or financial relationships that could be construed as a potential conflict of interest.

Publisher's note

All claims expressed in this article are solely those of the authors and do not necessarily represent those of their affiliated organizations, or those of the publisher, the editors and the reviewers. Any product that may be evaluated in this article, or claim that may be made by its manufacturer, is not guaranteed or endorsed by the publisher.

References

Bao, W., Yang, X., Liang, D., Hu, G., and Yang, X. (2021). Lightweight convolutional neural network model for field wheat ear disease identification. *Comput. Electron. Agric*. 189:106367. doi: 10.1016/j.compag.2021.106367

Bhupendra, Moses, K., Miglani, A., and Kankar, P. (2022). Deep CNN-based damage classification of milled rice grains using a high-magnification image dataset. *Comput. Electron. Agric.* 195:106811. doi: 10.1016/j.compag.2022.106811

Cheng, D., Li, S., Zhang, H., Xia, F., and Zhang, Y. (2021). Why Dataset Properties Bound the Scalability of Parallel Machine Learning Training Algorithms. *IEEE Trans. Parallel Distrib. Syst*. 32, 1702–1712. doi: 10.1109/TPDS.2020.3048836

Espejo-Garcia, B., Malounas, I., Mylonas, N., Kasimati, A., and Fountas, S. (2022). Using EfficientNet and transfer learning for image-based diagnosis of nutrient deficiencies. *Comput. Electron. Agric.* 196:106868. doi: 10.1016/j.compag.2022.106868

Gajjar, V., Nambisan, A., and Kosbar, K. (2022). Plant Identification in a Combined-Imbalanced Leaf Dataset. *IEEE Access* 10, 37882–37891. doi: 10.1109/ACCESS.2022.3165583

Gao, R., Wang, R., Feng, L., Li, Q., and Wu, H. (2021). Dual-branch, efficient, channel attention-based crop disease identification. *Comput. Electron. Agric.* 190:106410. doi: 10.1016/j.compag.2021.106410

Garbouge, H., Rasti, P., and Rousseau, D. (2021). Enhancing the Tracking of Seedling Growth Using RGB-Depth Fusion and Deep Learning. *Sensors* 21:8425. doi: 10.3390/s21248425

Han, L., Mo, M., Gao, Y., Ma, H., Xiang, D., Ma, G., et al. (2022). Effects of New Compounds into Substrates on Seedling Qualities for Efficient Transplanting. *Agronomy* 12:983. doi: 10.3390/agronomy12050983

He, Y., Wang, R., Wang, Y., and Wu, C. (2019). Fourier Descriptors Based Expert Decision Classification of Plug Seedlings. *Math. Probl. Eng.* 2019, 1–10. doi: 10.1155/2019/5078735

Ilboudo, W. E. L., Kobayashi, T., and Sugimoto, K. (2020). Robust stochastic gradient descent with student-t distribution based first-order momentum. *IEEE Trans. Neural Netw. Learn. Syst.* 33, 1324–1337. doi: 10.1109/TNNLS.2020.3041755

Jin, X., Wang, C., Chen, K., Ji, J., Liu, S., and Wang, Y. (2021). A Framework for Identification of Healthy Potted Seedlings in Automatic Transplanting System Using Computer Vision. *Front. Plant Sci.* 12:691753. doi: 10.3389/fpls.2021.691753

Jin, X., Yuan, Y., Ji, J., Zhao, K., Li, M., and Chen, K. (2020). Design and implementation of anti-leakage planting system for transplanting machine based on fuzzy information. *Comput. Electron. Agric.* 169:105204. doi: 10.1016/j.compag.2019.105204

Kolhar, S., and Jagtap, J. (2021). Spatio-temporal deep neural networks for accession classification of Arabidopsis plants using image sequences. *Ecol. Inform.* 64:101334. doi: 10.1016/j.ecoinf.2021.101334

Li, M., Jin, X., Ji, J., Li, P., and Du, X. (2021). Design and experiment of intelligent sorting and transplanting system for healthy vegetable seedlings. *Int. J. Agric. Biol. Eng.* 14, 208–216. doi: 10.25165/j.ijabe.20211404.6169

Liu, C., Zhu, H., Guo, W., Han, X., Chen, C., and Wu, H. (2021). EFDet: an efficient detection method for cucumber disease under natural complex environments. *Comput. Electron. Agric.* 189:106378. doi: 10.1016/j.compag.2021.106378

Meng, Q., Zhang, M., Ye, J., Du, Z., Song, M., and Zhang, Z. (2021). Identification of Multiple Vegetable Seedlings Based on Two-stage Lightweight Detection Model. *Trans. Chin. Soc. Agric. Mach.* 52, 282–290. doi: 10.6041/j.issn.1000-1298.2021.10.029

Namin, S. T., Esmaeilzadeh, M., Najafi, M., Brown, T. B., and Borevitz, J. O. (2018). Deep phenotyping: deep learning for temporal phenotype/genotype classification. *Plant Methods* 14:66. doi: 10.1186/s13007-018-0333-4

Perugachi-Diaz, Y., Tomczak, J. M., and Bhulai, S. (2021). Deep learning for white cabbage seedling prediction. *Comput. Electron. Agric.* 184:106059. doi: 10.1016/j.compag.2021.106059

Shao, Y., Han, X., Xuan, G., Liu, Y., Gao, C., Wang, G., et al. (2021). Development of a multi-adaptive feeding device for automated plug seedling transplanter. *Int. J. Agric. Biol. Eng.* 14, 91–96. doi: 10.25165/j.ijabe.2021

Sharma, R., Singh, A., Kavita, Jhanjhi, N. Z., Masud, M., Jaha, E. S., et al. (2022). Plant Disease Diagnosis and Image Classification Using Deep Learning. *CMC-Comput. Mat. Contin.* 71, 2125–2140. doi: 10.32604/cmc.2022.020017

Tan, S., Liu, J., Lu, H., Lan, M., Yu, J., Liao, G., et al. (2022). Machine Learning Approaches for Rice Seedling Growth Stages Detection. *Front. Plant Sci.* 13:914771. doi: 10.3389/fpls.2022.914771

Tong, J., Shi, H., Wu, C., Jiang, H., and Yang, T. (2018). Skewness correction and quality evaluation of plug seedling images based on Canny operator and Hough transform. *Comput. Electron. Agric.* 155, 461–472. doi: 10.1016/j.compag.2018.10.035

Tong, J., Yu, J., Wu, C., Yu, G., Du, X., and Shi, H. (2021). Health information acquisition and position calculation of plug seedling in greenhouse seedling bed. *Comput. Electron. Agric.* 185:106146. doi: 10.1016/j.compag.2021.106146

Wang, J., Gu, R., Sun, L., and Zhang, Y. (2021). Non-destructive Monitoring of Plug Seedling Growth Process Based on Kinect Camera. *Trans. Chin. Soc. Agric. Mach.* 52, 227–235. doi: 10.6041/j.issn.1000-1298.2021.02.021

Wang, Y., Xiao, X., Liang, X., Wang, J., Wu, C., and Xu, J. (2018). Plug hole positioning and seedling shortage detecting system on automatic seedling supplementing test-bed for vegetable plug seedlings. *Trans. Chin. Soc. Agric. Eng.* 26, 206–211. doi: 10.11975/j.issn.1002-6819.2018.12.005

Wang, Z., Guo, J., and Zhang, S. (2022). Lightweight Convolution Neural Network Based on Multi-Scale Parallel Fusion for Weed Identification. *Int. J. Pattern Recognit. Artif. Intell.* 36:2250028. doi: 10.1142/S0218001422500288

Wen, Y., Zhang, L., Huang, X., Yuan, T., Zhang, J., Tan, Y., et al. (2021). Design of and Experiment with Seedling Selection System for Automatic Transplanter for Vegetable Plug Seedlings. *Agronomy* 11:2031. doi: 10.3390/agronomy1110 2031

Xiao, Z., Tan, Y., Liu, X., and Yang, S. (2019). Classification method of plug seedlings based on transfer learning. *Appl. Sci. Basel* 9:2725. doi: 10.3390/app9132725

Yang, S., Zheng, L., Gao, W., Wang, B., Hao, X., Mi, J., et al. (2020). An efficient processing approach for colored point cloud-based high-throughput seedling phenotyping. *Remote Sens.* 12:1540. doi: 10.3390/rs12101540

Yang, Y., Fan, K., Han, J., Yang, Y., Chu, Q., Zhou, Z. M., et al. (2021). Quality inspection of Spathiphyllum plug seedlings based on the side view images of the seedling stem under the leaves. *Trans. Chin. Soc. Agric. Eng.* 37, 194–201. doi: 10.11975/j.issn.1002-6819.2021.20.022

Yu, Y., and Liu, F. (2019). Effective neural network training with a new weighting mechanism-based optimization algorithm. *IEEE Access* 7, 72403–72410. doi: 10.1109/ACCESS.2019.2919987

Zhang, P., Yang, L., and Li, D. (2020). EfficientNet-B4-Ranger: a novel method for greenhouse cucumber disease recognition under natural complex environment. *Comput. Electron. Agric.* 176:105652. doi: 10.1016/j.compag.2020.105652

Zhang, X., Jing, M., Yuan, Y., Yin, Y., Li, K., and Wang, C. (2022). Tomato seedling classification detection using improved YOLOv3-Tiny. *Trans. Chin. Soc. Agric. Eng.* 38, 221–229. doi: 10.11975/j.issn.1002-6819.2022.01.025

Zhao, L., Guo, W., Wang, J., Wang, H., Duan, Y., Wang, C., et al. (2021). An efficient method for estimating wheat heading dates using uav images. *Remote Sens.* 13:3067. doi: 10.3390/rs13163067

Zhao, X., Li, K., Li, Y., Ma, J., and Zhang, L. (2022). Identification method of vegetable diseases based on transfer learning and attention mechanism. *Comput. Electron. Agric.* 193:106703. doi: 10.1016/j.compag.2022.106703

Zhao, Y., Chen, J., Xu, X., Lei, J., and Zhou, W. (2021). SEV-Net: residual network embedded with attention mechanism for plant disease severity detection. *Concurr. Comput. Pract. Exp.* 33:e6161. doi: 10.1002/cpe.6161

Zhao, Y., Sun, C., Xu, X., and Chen, J. (2022). RIC-Net: a plant disease classification model based on the fusion of Inception and residual structure and embedded attention mechanism. *Comput. Electron. Agric.* 193:106644. doi: 10.1016/j.compag.2021.106644

frontiers | Frontiers in Plant Science

TYPE Original Research
PUBLISHED 15 September 2022
DOI 10.3389/fpls.2022.956636

OPEN ACCESS

EDITED BY
Yanbei Zhu,
National Institute of Advanced Industrial Science and Technology (AIST), Japan

REVIEWED BY
Zhiming Guo,
Jiangsu University, China
Leiqing Pan,
Nanjing Agricultural University, China

*CORRESPONDENCE
Liping Chen
chenlp@nercita.org.cn
Qingyan Wang
wangqy@nercita.org.cn

SPECIALTY SECTION
This article was submitted to Technical Advances in Plant Science, a section of the journal Frontiers in Plant Science

RECEIVED 31 May 2022
ACCEPTED 28 July 2022
PUBLISHED 15 September 2022

CITATION
Zhang C, Huang W, Liang X, He X, Tian X, Chen L and Wang Q (2022) Slight crack identification of cottonseed using air-coupled ultrasound with sound to image encoding. *Front. Plant Sci.* 13:956636. doi: 10.3389/fpls.2022.956636

Slight crack identification of cottonseed using air-coupled ultrasound with sound to image encoding

Chi Zhang[1], Wenqian Huang[1], Xiaoting Liang[1,2], Xin He[1], Xi Tian[1], Liping Chen[1]* and Qingyan Wang[1]*

[1]Intelligent Equipment Research Center, Beijing Academy of Agriculture and Forestry Sciences, Beijing, China, [2]College of Information Technology, Shanghai Ocean University, Shanghai, China

Slight crack of cottonseed is a critical factor influencing the germination rate of cotton due to foamed acid or water entering cottonseed through testa. However, it is very difficult to detect cottonseed with slight crack using common non-destructive detection methods, such as machine vision, optical spectroscopy, and thermal imaging, because slight crack has little effect on morphology, chemical substances or temperature. By contrast, the acoustic method shows a sensitivity to fine structure defects and demonstrates potential application in seed detection. This paper presents a novel method to detect slightly cracked cottonseed using air-coupled ultrasound with a light-weight vision transformer (ViT) and a sound-to-image encoding method. The echo signal of air-coupled ultrasound from cottonseed is obtained by non-contact and non-destructive methods. The intrinsic mode functions (IMFs) of ultrasound signal are obtained as the sound features using variational mode decomposition (VMD) approach. Then the sound features are converted into colorful images by a color encoding method. This method uses different colored lines to represent the changes of different values of IMFs according to the specified encoding period. A light-weight MobileViT method is utilized to identify the slightly cracked cottonseeds using encoding colorful images corresponding to cottonseeds. The experimental results show an average overall recognition accuracy of 90.7% for slightly cracked cottonseed from normal cottonseed, which indicates that the proposed method is reliable to applications in detection task of cottonseed with slight crack.

KEYWORDS

crack cottonseed identification, variational mode decomposition, sound to image encoding, vision transformer, deep learning, air-coupled ultrasound

Introduction

Cotton is an important economic crop throughout the world. The quality of cottonseed is an important factor in determining the yield and quality of cotton. Cotton seed will go through a series of processes such as ginning and stripping, which will cause a lot of damage to cotton seed. However, in the process of removing excess linters of

cottonseed, the foamed acid will enter the cottonseed through the cracks and diminish the germination of the cotton seed. After sowing, water will also enter cottonseed through cracks, further reducing the germination of cottonseed. Therefore, cracked cottonseeds will decrease cotton yield.

To reduce the amount of cottonseed wasted, the automation system of cotton precision seeding is often applied in practical production. After precision seeding, there is no need for thinning seedlings or avoiding inconsistency of individual growth and development in cotton field. Therefore, cotton precision seeding can significantly decrease the production cost of cotton, improve the efficiency of field management, and consequently, realize standardized planting. However, this technology puts forward higher requirements for the quality of cottonseeds, which makes the quality detection of cottonseeds crucial. The traditional seed detection method is destructive, inefficient, time-consuming, and non-automated. Developing fast and high-throughput non-destructive detection methods for seed quality is urgently needed for agricultural production. In recent years, non-destructive detection technologies, such as machine vision, optical spectroscopy, thermal imaging, and acoustics, have gradually become new ways to detect seed quality.

Machine vision is a rapid and non-destructive technology and has been applied to detect the quality and safety of seed. Based on morphological and color features extracted from images acquired by camera with high resolution, morphology (Rodríguez-Pulido et al., 2012), color (Tu et al., 2018), shape (Li et al., 2016), size, texture, and exterior defects (Huang et al., 2019) of seed can be evaluated. Severely damaged and broken cottonseeds can also be identified effectively by extracting morphological characteristics from image (Bai et al., 2018). However, injuries recognition and location are still major difficulties in using machine vision for seed surface defect detection (Huang et al., 2015). Slight injuries such as small cracks in cottonseed are hardly distinguished by vision. Moreover, it is particularly difficult for imaging the injuries on the edge and the back side of seed that are hidden from the camera's field of view.

Optical spectroscopy is also a powerful tool to inspect seed, especially in characterizing internal quality. Based on the interactions between light and material molecular groups, the information of corresponding chemical compositions can be extracted from the changes of optical spectra. According to the form of interaction, spectroscopic techniques are mainly based on light absorption (e.g., near-infrared spectroscopy), light scattering (e.g., Raman spectroscopy) and light emission (e.g., fluorescence spectroscopy). Most of them have been used to determine seed quality and safety, including internal compositions (Sunoj et al., 2016), moisture (Zhang and Guo, 2020), germination (Fan Y. et al., 2020) and infection (Tao et al., 2019). Hyperspectral imaging technique incorporates optical spectroscopy and imaging technology to obtain spatial and spectroscopic information simultaneously. Combined with machine learning methods, such as linear discriminant analysis (LDA), partial least-squares discriminant analysis (PLS-DA), support vector machine (SVM), and artificial neural networks (ANN), a hyperspectral imaging data cube can provide the information of chemical compositions and their distributions, which makes this a potential technology in the seed industry, especially in variety identification (Zhou et al., 2020), classification (Barboza da Silva et al., 2021) and chemical composition determination (Yang et al., 2018; Hu et al., 2021). Spectroscopic technology also does a good job in damage detection of seed, such as insect damage (Chelladurai et al., 2014), fungi damage (Baek et al., 2019), frost damage, and sprout damage, because all these types of damage can lead to the change of chemical compositions of seed, which could change the spectral features. Nevertheless, it is still challenging to distinguish pure physical damage with little chemical change, such as slight crack in cottonseed.

Thermal imaging is a non-destructive technique for converting the invisible infrared radiation pattern of an object into visible images for feature extraction and analysis (Rahman and Cho, 2016). Based on the changes of surface temperature, the infrared radiation profile of seed can be mapped and analyzed. Unlike above-mentioned methods, no illumination sources are required in this system, and a thermal imaging camera along with its data acquisition system is enough to provide information of object. Thermal imaging technology has found its way in estimating seed quality, including determination of morphological features, detection of diseases and insect infestation, evaluation of viability (Belin et al., 2018) and germination performance (Fang et al., 2016), distinguishing aged or dead seeds from healthy ones (Kim et al., 2014), and monitoring seed quality during storage (Xia et al., 2019). In addition, thermal imaging has the capability of sensing all possible physical damage of seed, since there is a significant relationship between seed temperature and degree of damage (ElMasry et al., 2020). But the difficulties of detecting slight physical injuries, which are hard to recognize by machine vision and even human vision, still exist for the thermal imaging method.

An acoustic method is also developed for non-destructive detection of agricultural products. Among acoustic technology, ultrasonic testing is an important method. With the advantages of short wavelength, high frequency, and good directional property, ultrasound possesses better penetrability than audible sound and subsonic wave, and consequently becomes a powerful tool in non-destructive testing of seed. Ultrasound signal produced by impacting seed can be used to evaluate seed quality. When crack appears on seed testa, the structural strength and damping coefficient of the seed will change, which leads to the variations of frequency and intensity of the impacting ultrasound signal. Depending on the differences in echo signals between healthy seed and defective seed, the acoustic method shows more superiority in recognizing fine surface crack than

common non-destructive detection methods. The approach was first proposed to distinguish pistachio nuts with open shells from those with closed shells (Pearson, 2001), and the results showed that the detection accuracy of pistachio nuts was ∼97%. Combined with signal processing and identifying algorithm, the acoustic method is applied to detect insect damage (Pearson et al., 2007; Yanyun et al., 2016) and mildew damage (Sun et al., 2018) of seed. The potential to identify fine defects with this method is expected and verified. However, detecting light crack of cottonseed with smaller size than most seeds is rarely reported.

In this paper, a non-destructive detection method based on an air-coupled ultrasonic inspection system is developed to distinguish cottonseed with slight crack from intact kernel. VMD is utilized to decompose an ultrasonic signal into band-limited multiple IMFs. These IMFs are used to construct the feature matrix of ultrasonic signal. Then the feature matrix is converted into the colorful image using a color encoding method. A deep learning-based method combining Transformer model with CNN model is used to classify the color images generated from air-coupled ultrasonic cottonseeds. Finally, the performance of the proposed method is compared with other detection methods.

Materials and methods

Samples

A total of 600 cottonseeds named Xinluzhong52 are used in this study. The total cottonseeds consisted of 296 intact kernels and 304 kernels with slight crack. Cracked cottonseed is damaged cottonseed showing the obvious white endosperm inside. For slightly cracked cottonseed, it is difficult to detect the endosperm inside, but there is crack on testa of cottonseed. Physical images of cottonseed are shown in Figure 1. The cottonseed with severe crack that shows the white endosperm can be identified by machine vision method. This research focuses on the method of distinguishing cottonseed with slight crack from intact cottonseed. Therefore, the samples only include the two classes of cottonseeds.

Detection system based on air-coupled ultrasound

To maintain sufficient energy transmission, liquid couplant, such as water, oil etc. is used to immerse samples in a traditional ultrasonic technique. The mode of contact coupling may cause damage or pollution on the surface of sample. The air-coupled ultrasonic technique emerges as a novel approach for non-destructive, non-contact, and rapid inspection (Fang et al., 2017). The surrounding air is used as the couplant between transmitting transducer and materials or between receiving transducer and materials in air-coupled ultrasonic techniques. The significant advantage of an air-coupled ultrasonic technique is avoiding the use of traditional couplant. Therefore, it becomes a reliable and effective non-destructive detection method. The air-coupled ultrasonic technique is suitable for industrial detection applications, such as the natural defects in wood (Tiitta et al., 2020), corn seed with hole (Yanyun et al., 2016) and food engineering (Fariñas et al., 2021a,b).

The air-coupled ultrasonic detection system is used to obtain the ultrasonic echo signal. The inspection system is shown in Figure 2. The signal acquisition system consists of a pair of transducers (400K-20N-R50-T and 400K-20N-R50-R, PR, China), a preamplifier (400K, PR, China), an air-coupled ultrasonic inspection instrument (PRACUT-111, PR, China), and an industrial computer. The center frequency of the transducer is 400 *kHz*. The diameter of the piezoelectric ceramic disc is 20 mm. The focal length of the transducer is 50 mm. The normal through-transmission mode is applied to two transducers. In order to obtain accurate ultrasonic signals, the two transducers need to be strictly aligned. The cottonseed is placed as the focus between transmitting transducer and receiving transducer. To meet the requirement of cottonseed placement, an aluminum plate with a thickness of 0.2 mm as a holder is fixed in the middle of two transducers. The thin aluminum plate can guarantee that the air-coupled ultrasonic signal transmitted by the transmitting transducer can be received by the receiving transducer as much as possible. The preamplifier with the amplification factor of 60 dB is used to amplify and filter the ultrasonic signal received by the air-coupling receiver transducer (400K-20N-R50-R), and then input the processed ultrasonic signal to the air-coupled ultrasonic inspection instrument. The ultrasonic inspection instrument outputs 400 V excitation signal to drive the transmitting transducer and converts the received ultrasonic signal into digital signal. The industrial computer mainly consists of Intel i7-6700 CPU @3.4 GHz, 512G SSD hard drive, 16 GB RAM and a GPU (Geforce RTX 2080 WindForce OC 8G, GIGABYTE). The computer sends the control command to the ultrasonic inspection instrument through the USB interface, and receives the ultrasonic data sent by the ultrasonic inspection instrument through a LAN interface. The ultrasonic data are stored in the computer using PRACUT software (Suzhou Phaserise Technology Co., Ltd., China). Although Python language and Pytorch deep learning framework are used to realize the signal processing and the identification of cottonseed with slight crack, real-time detection can be realized by C++ language with the standard dynamic link library provided by PRACUT software.

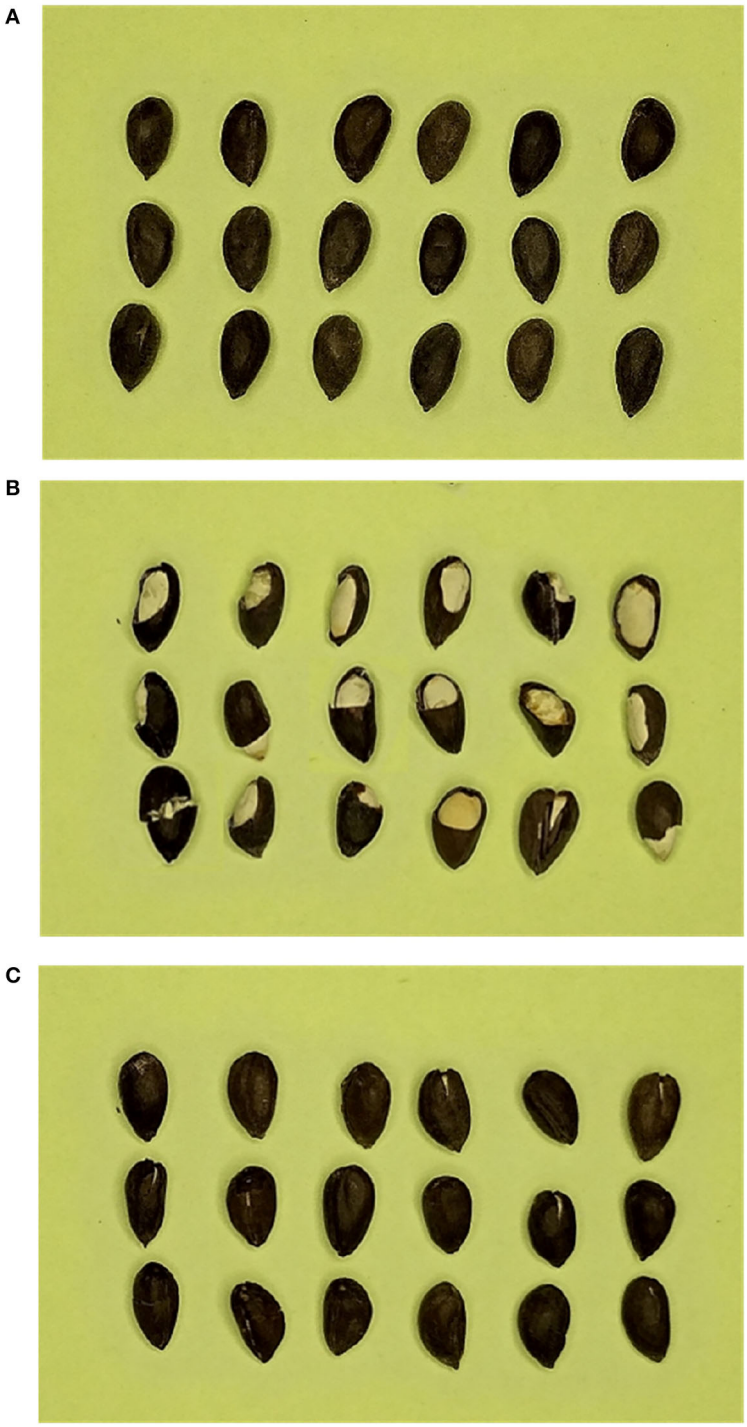

FIGURE 1
Cottonseed kernels. **(A)** Intact cottonseeds. **(B)** Cottonseeds with severe cracks. **(C)** Cottonseeds with slight cracks.

Ultrasonic signal acquisition

A-scan mode of the air-coupled ultrasonic inspection instrument is used to identify cottonseed with slight crack. In A-scan mode, damaged cottonseeds are detected through changes in air-coupled ultrasonic signal passing through them. In order to generate the ultrasonic signal data set, first, the cottonseed sample is placed on the aluminum plate so that it

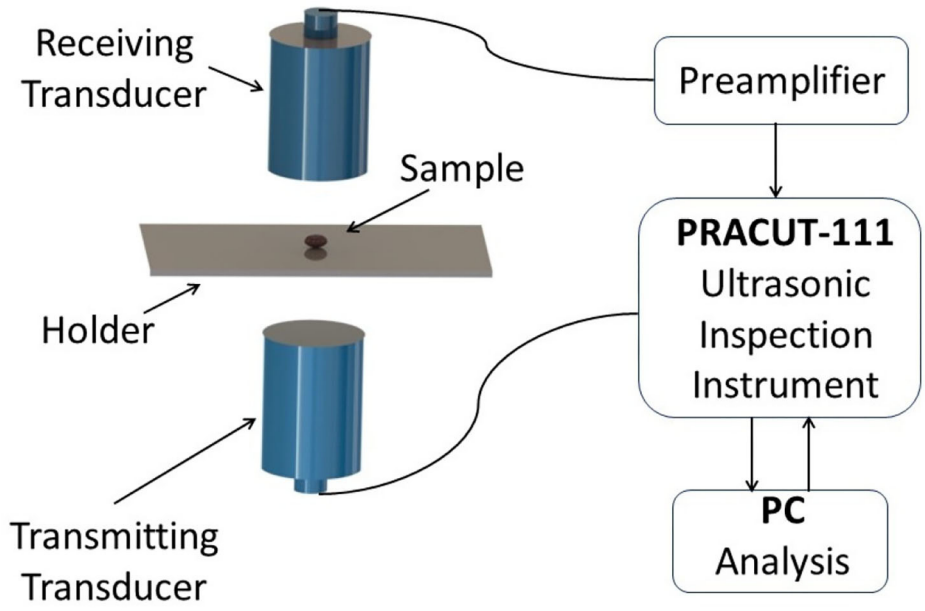

FIGURE 2
Scheme of air-coupled ultrasonic inspection system set-up.

coincides with the focus position of the transducers. Then the ultrasonic signal is obtained after the ultrasonic signal passes through the cottonseed. The ultrasonic signal data is exported and saved as a CSV format file. Finally, the category label (1 or 0) corresponding to each sample is appended to the end of CSV file, where "1" represents the normal cottonseed and "0" represents the cottonseed with slight crack. Each cottonseed sample corresponds to a CSV file, and all CSV files constitute the data set used in this study. The typical ultrasonic signals from intact cottonseed and cottonseed with slight crack are shown in Figure 3 respectively. The amplitude fluctuations of the two types of ultrasonic signals are very similar, so it is very important to extract effective features for classification from these signals.

Identification of slight crack cottonseed

Variational mode decomposition method

Variational mode decomposition (VMD) (Dragomiretskiy and Zosso, 2013) is one of novel non-stationary signal decomposition techniques and has been recently applied in wind speed forecasting and many other fields (Dibaj et al., 2021; Yildiz et al., 2021). The original non-stationary signal can be decomposed into different band-limited intrinsic mode functions (IMFs) using VMD, similar to empirical mode decomposition (EMD). A non-recursive method is used to decompose original signal $X(t)$ into M modes or subsequences $u_m(m = 1, 2, ..., M)$. These IMFs have different central frequencies with finite bandwidths. The purpose of the transformation is to minimize the sum of the estimated frequency bandwidth of each IMF, and the constraint condition is that the sum of each IMF is equal to the input signal $X(t)$. The objective function and constraint condition corresponding to the variational constraint model can be represented by the following Equation 1:

$$\begin{cases} \min\limits_{\{u_m\},\{\omega_m\}} \sum_{m=1}^{M} \left\| \partial \left[\left(\delta(t) + \frac{j}{\pi t} \right) * u_m(t) e^{-j\omega_k t} \right] \right\|_2^2 \\ s.t.\ X(t) = \sum_{m=1}^{M} u_m \end{cases} \quad (1)$$

where $\delta(t)$ is Dirac function; $*$ denotes the convolution operation in signal processing; j is an imaginary number; $\| \cdot \|$ denotes the L^2- norm; $\{u_m\} = \{u_1, u_2, ..., u_M\}$ is the set of all IMFs; $\{\omega_m\} = \{\omega_1, \omega_2, ..., \omega_M\}$ is the set of central frequencies corresponding to all IMFs.

In order to resolve the constrained variational optimization problem, quadratic penalty factor term α and Lagrange multipliers $\lambda(t)$ are defined, so the optimization problem can be transformed into an unconstrained variational problem. The constructed unconstrained form can be presented in Equation 2.

$$\begin{aligned} &\mathcal{L}(\{u_m\}, \{\omega_m\}, \{\lambda(t)\}) \\ &= \alpha \sum_{m=1}^{M} \left\| \partial \left[\left(\delta(t) + \frac{j}{\pi t} \right) * u_m(t) e^{-j\omega_k t} \right] \right\|_2^2 \\ &+ \left\| X(t) - \sum_{m=1}^{M} u_m \right\|_2^2 + \left\langle \{\lambda(t)\}, X(t) - \sum_{m=1}^{M} u_m \right\rangle \end{aligned} \quad (2)$$

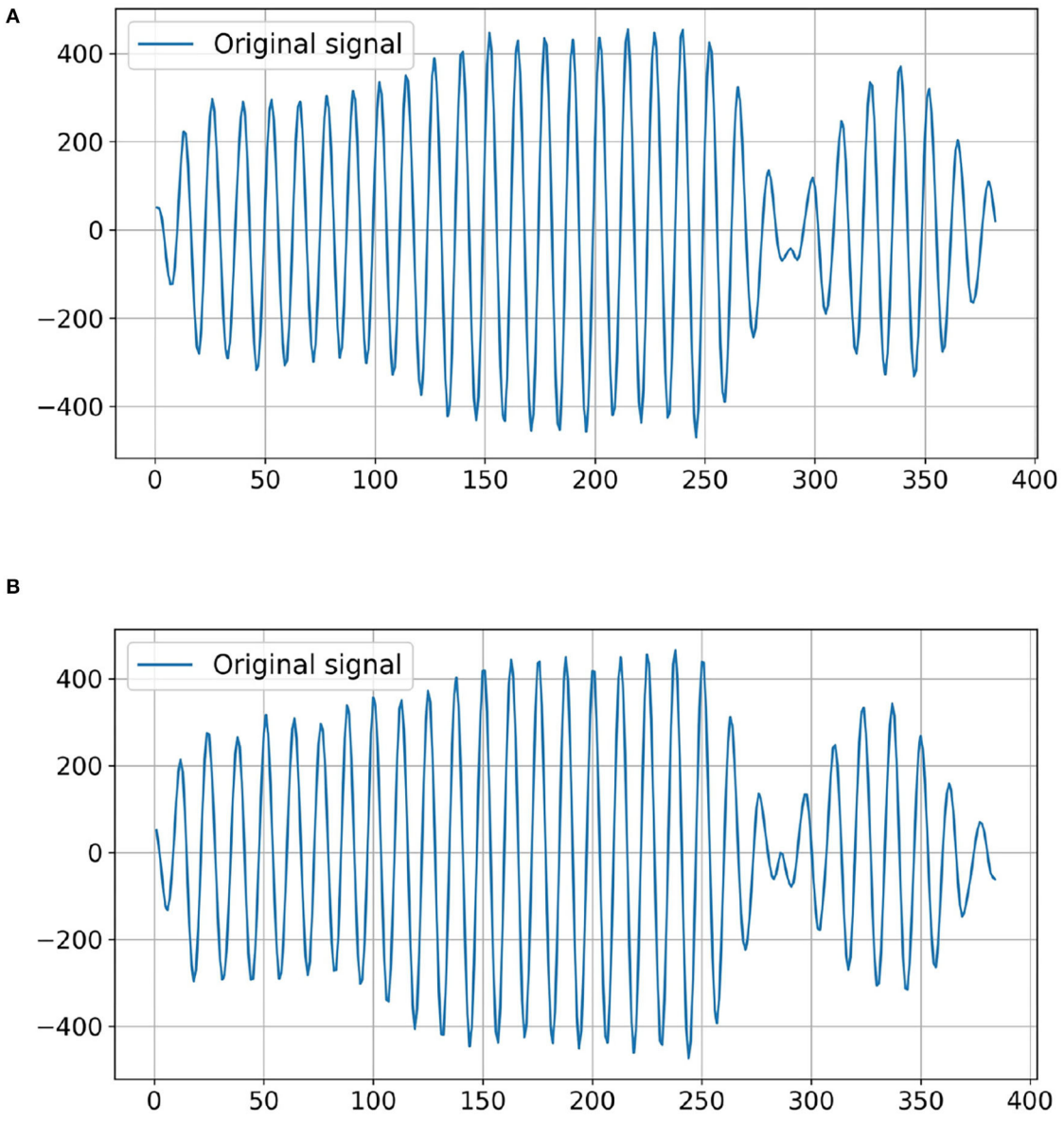

FIGURE 3
Examples of the original ultrasonic signals of cottonseed. **(A)** Intact cottonseed. **(B)** Cottonseed with slight crack.

where α is used to ensure high reconstruction fidelity even in the presence of additive Gaussian white noise; $\lambda(t)$ is used to strictly ensure the constraints.

To solve the unconstrained optimization problem in Equation 2, the alternating direction multiplier method (ADMM) (Hong and Luo, 2017) is used to find the saddle point of the optimization problem. The minimax point of the augmented Lagrangian function $\mathcal{L}$ can be obtained by updating u_m, ω_m and λ alternately. The iteration process of u_m, ω_m and λ are as following Equation 3, 4, 5:

$$\hat{u}_m^{n+1}(\omega) = \frac{\hat{f}(\omega) - \sum_{i \neq m} \hat{u}_i(\omega) + \frac{\hat{\lambda}(\omega)}{2}}{1 + 2\alpha(\omega - \omega_m)^2} \tag{3}$$

$$\omega_m^{n+1} = \frac{\int_0^\infty \omega \left|\hat{u}_m(\omega)\right|^2 d\omega}{\int_0^\infty \left|\hat{u}_m(\omega)\right|^2 d\omega} \tag{4}$$

$$\hat{\lambda}^{n+1}(\omega) = \hat{\lambda}^n(\omega) + \tau(\hat{X}(\omega) - \sum_m \hat{u}_m^{n+1}(\omega)) \tag{5}$$

where n is the number of iterations; $\hat{X}(\omega)$, $\hat{u}_m^{n+1}(\omega)$, $\hat{u}_i(\omega)$ and $\hat{\lambda}(\omega)$ can be obtained from $X(t)$, $u_m^{n+1}(t)$, $u_i(t)$ and $\lambda(t)$ by the Fourier transforms. If the convergence condition shown in Equation 6 is satisfied, the iteration will be terminated. Finally, through the inverse Fourier transform of $\hat{u}_m^{n+1}(t)$, the real part of the result is taken as the mode functions $u_m^{n+1}(t)$.

$$\sum_{m=1}^{M} \frac{\left\| \hat{u}_m^{n+1} - \hat{u}_m^n \right\|_2^2}{\left\| \hat{u}_m^n \right\|_2^2} < \epsilon \tag{6}$$

The optimization process for VMD is as follows:

Step 1: Initialize u_m^1, ω_m^1, λ^1 and n, where $n = 1$.
Step 2: Set n to $n + 1$ and update $\hat{u}_m^{n+1}(\omega)$, ω_m^{n+1} and $\hat{\lambda}^{n+1}$ according to Equation 3, 4, 5.
Step 3: Repeat step 2 until the iteration convergence condition in Equation 6 is satisfied. M narrowband IMF $u_m^{n+1}(t)$ can be obtained by using inverse Fourier transform.

The air-coupled ultrasonic signal of a cottonseed with slight crack is used as the examples for VMD decomposition. The results of VMD decomposition are shown in Figure 4. Because of the similarity between air-coupled ultrasonic signal of intact cottonseed and that of cottonseed with slight crack, it is important to extract the air-coupled ultrasonic signal features from these intrinsic mode functions.

Encoding from ultrasound to image

The ultrasonic signal $X(n)$ acquired from air-coupled ultrasonic detection system are decomposed to M intrinsic mode functions u_m, $m \in \{1, 2, ..., M\}$ using VMD transformation. M IMFs are stacked to generate the intrinsic mode functions matrix S of air-coupled ultrasonic signal $X(n)$ according to Equation 7:

$$S = \begin{bmatrix} u_1 \\ u_2 \\ \vdots \\ u_M \end{bmatrix} = [s_1, s_2, \cdots, s_L] \tag{7}$$

where $S \in \mathbb{R}^{M \times L}$ and L is the length of the air-coupled ultrasonic signal $X(n)$. u_m is composed of L discrete values with the same length as the ultrasonic signal, which can be represented as $u_m \in \mathbb{R}^{1 \times L}$. Vector s_l is composed of M discrete values in the column direction of the matrix S which can be represented as $s_l \in \mathbb{R}^{M \times 1}$. In order to convert the ultrasonic signal $X(n)$ into a color-coded image I_C, the color set C is defined for color coding, $C = \{c_1, c_2, \cdots, c_B\}$, where c_i represents different colors and B is the number of different colors in the color set C. First, vector s_1 at the first column of the intrinsic mode functions matrix S is selected and converted into a part of colorful image I_C. Here, $s_1 = \{u_{11}, u_{12}, \cdots, u_{1M}\}$. Color c_1 in set C is chosen and used to draw a polyline in the image I_C according to the value of s_1. Then vector s_2 at the second column of matrix S and color c_2 are selected to draw the second polyline in the image I_C to represent s_2. According to this method, color c_1 is used to draw the next polyline again after completing the drawing of B colorful polylines. Finally, B is considered as the cycle to complete the drawing of L colorful polylines. Image I_C is generated from the air-coupled ultrasonic signal $X(n)$ using the above color encoding method.

In order to accurately convert the ultrasonic signal into a colorful image, first, the drawing ranges W_S, H_S in image I_C and the coordinates $(x_{O_S}, y_{O_S})$of the image origin O_S are defined. Then the coordinates required to draw polylines are calculated according to Equation 8:

$$\begin{cases} x_{s_{lm}} = x_{O_S} + \frac{(m-1)W_S}{M-1} & m \in \{1, 2, \cdots, M\} \\ y_{s_{lm}} = y_{O_S} + \frac{(H_S - y_{O_S})(S_{\max} - S_{lm})}{(S_{\max} - S_{\min})} & l \in \{1, 2, \cdots, L\} \end{cases} \tag{8}$$

where $S_{\max}$ and $S_{\min}$ are respectively the maximum and minimum values in the matrix S composed of M intrinsic mode functions after VMD decomposition of each ultrasonic signal. The position of each column vector of matrix S in the image I_C is determined by Equation 8, and then the corresponding position is connected with the same color to complete the drawing of polylines. For each vector s_l, M – 1 colorful lines need to be drawn. In this study, let $M = 3$, $L = 450$, $B = 10$, the size of the generated image I_C is 1,800 × 1,200 and the origin coordinate of the encoding image part on image I_C is (288,1010). The process of generating images from the ultrasonic signals of intact cottonseed and slight cracked cottonseed is shown in Figure 5. As seen in Figure 5, the coding representation of ultrasonic signals from one-dimensional ultrasonic signal to two-dimensional images can be realized by polylines with different colors according to the results of VMD decomposition of ultrasonic signals.

In practical application, in order to obtain the optimal detection effect, the air-coupled ultrasonic data of 30 intact cottonseeds and 30 cottonseeds with slight crack are randomly selected from the air-coupled ultrasonic data set, the background image is generated according to the above method, and then the air-coupled ultrasonic data of the remaining 540 cottonseeds are used to generate colorful encoding images on the background image. So, the conversion from sound to image is completed. Finally, the image data set including 266 images generated from intact kernels and 274 images generated from slight crack kernels is obtained. In this study, 80% of the data set is used to train the model and 20% is used to test the effect of the training model.

MobileVIT vision transformer model

The ransformer-based model achieves great success in the natural language processing (NLP) field (Vaswani et al., 2017).

10.3389/fpls.2022.956636

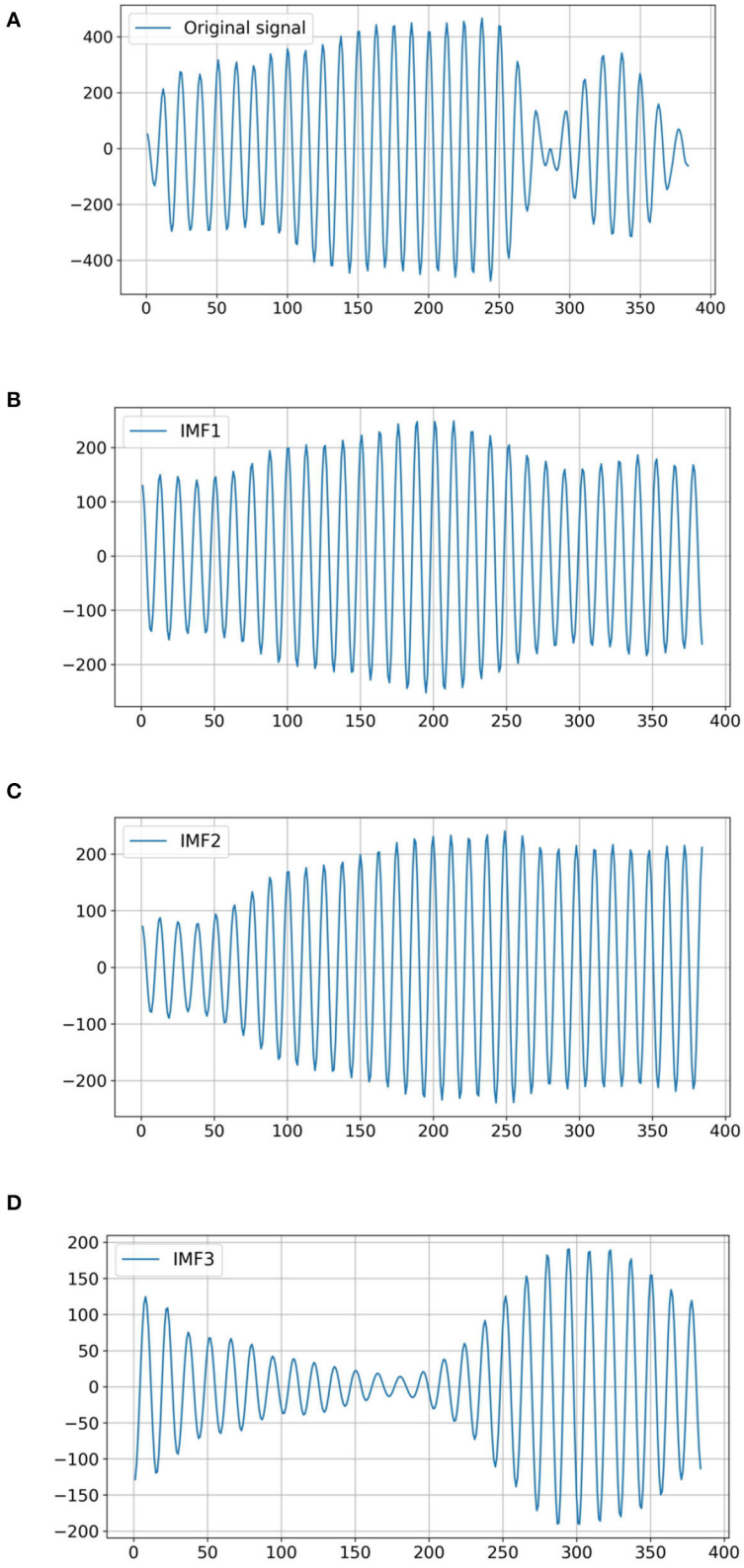

FIGURE 4
The VMD decomposition from the air-coupled ultrasonic signal of a cottonseed with slight crack. **(A)** Original signal. **(B)** IMF1. **(C)** IMF2. **(D)** IMF3.

10.3389/fpls.2022.956636

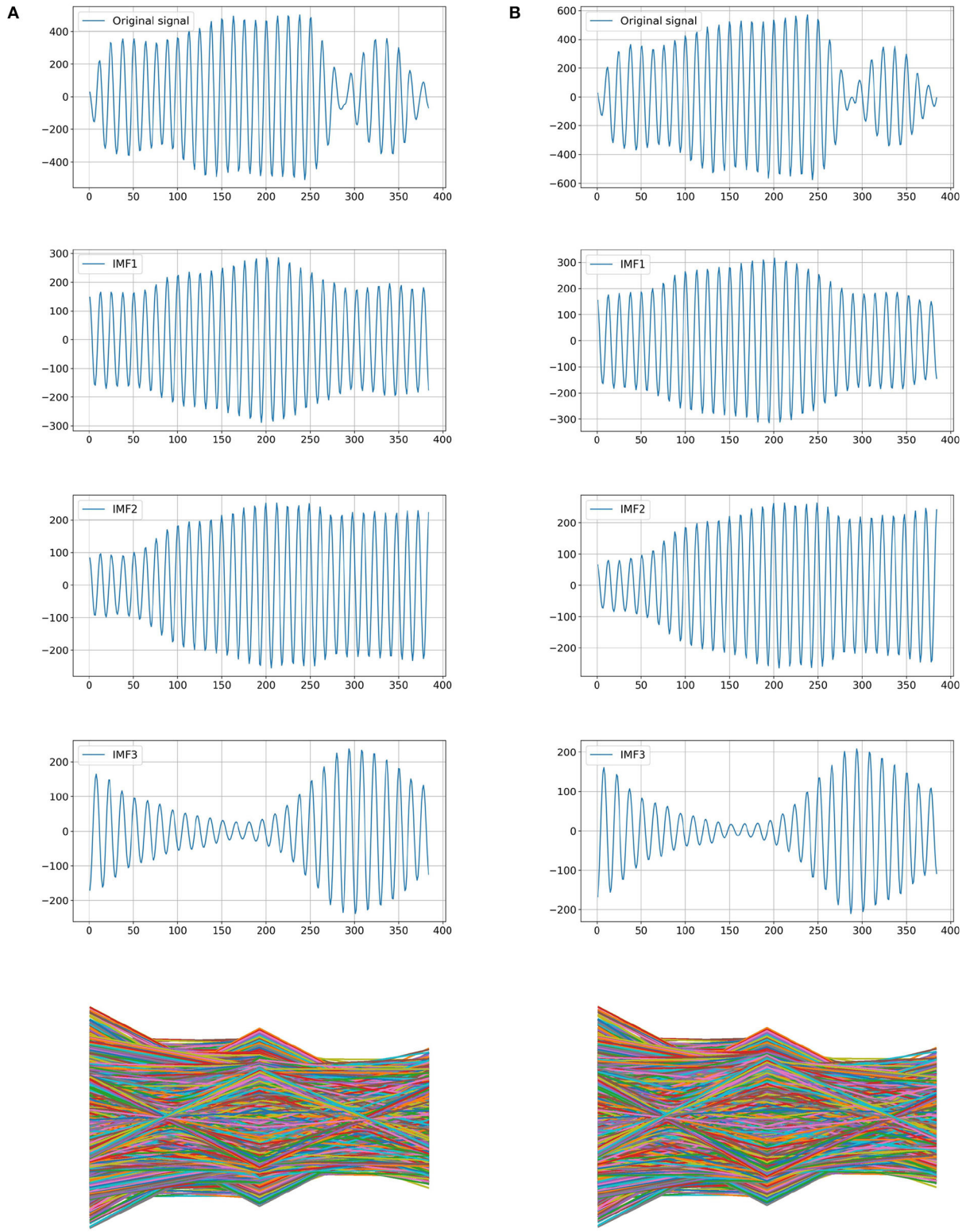

FIGURE 5
Colorful images generated from the ultrasonic signals. **(A)** The process of generating image from the ultrasonic signal of intact cottonseed. **(B)** The process of generating image from the ultrasonic signal of slightly cracked cottonseed.

Transformer has a layer stacking architecture, which only uses the multi-Head self-attention mechanism without convolution and recursion. Inspired by the successful application of transformer in NLP field, Dosovitskiy et al. (2020) propose Vision Transformer (ViT) model which employed a standard Transformer directly to visual tasks. In this method, the image is divided into a sequence of patches, and the linear embedding sequence of these image patches are taken as the input of the Transformer. The processing method of image patches is the same as that of tokens in NLP application, and excellent results are achieved on massive data sets. Liu et al. (2021), proposed the Swin Transformer (Shifted Window Transformer) model that could replace the classic convolutional neural network (CNN) architecture and become a general backbone in the field of computer vision. This model is based on the idea of ViT model and shows the effectiveness on different vision problems using patch merging and the shifted window with self-attention.

Although Vision Transformer-based model can be an alternative to CNNs in computer vision field, the large model size, high requirement for training data, and latency of Vision Transformer limits its practice application, especially for resource constrained equipment. In order to obtain a lightweight and efficient architecture of Vision Transformer model, MobileViT (Mehta and Rastegari, 2021) is proposed for mobile vision applications. MobileViT combines the advantages of transformers and convolutions, so it can encode the local information obtained from convolutions and global information obtained from transformers in tensors without lacking in inductive bias. The model structure of MobileViT is shown in Figure 6, where MV2 block represents MobileNetV2 block with inverted residual structure. ↓2 refers to down-sampling operation. A standard 3×3 convolution operation is represented by *Conv*-3×3 block in MobileViT model. MobileViT block combines convolutions with transformers to learn the global and local information from input tensor respectively. Tensor $X_T \in \mathbb{R}^{H \times W \times D}$passes through a series of convolution operations and tensor $X_{L_T} \in \mathbb{R}^{H \times W \times d}$ is obtained. Then tensor X_{L_T} is divided into N patches with width w and height h and $X_{U_T} \in \mathbb{R}^{P \times N \times d}$ can be obtained by unfolding X_{L_T}. For example, the X_{L_T} in Figure 6 is equally divided into 4×4 small patches, then a d-dimensional vector is extracted at the same position of each patch. The corresponding vectors from the same position $p \in \{1, \cdots, P\}$are combined and used to generate tokens. The inter-path relationships $X_{G_T} \in \mathbb{R}^{P \times N \times d}$ can be obtained by encoding operation with Transformers as Equation 9:

$$X_{G_T} = Transformer\left(X_{U_T}(p)\right), 1 \leq p \leq P \tag{9}$$

where local information can be encoded by $X_{U_T}(p)$ and global information passing through *p-th* position in P patches can be encoded by $X_{U_G}(p)$. The output Y_T of MobileViT block can be obtained after convolution and concatenation operations.

The computation of self-attention in above Transformer is realized using scale dot-product attention according to Equation 10:

$$Attention\,(Q, K, V) = SoftMax(\frac{QK^T}{\sqrt{d_k}})V \tag{10}$$

where Q, K and V represent the query, key, and value matrices respectively. d_k refers to the dimension of Q and K. The *SoftMax* function is used to obtain the weights of V. Spatial order of pixels will be ignored in standard ViTs. But both the spatial order of pixels and the path order will be obtained in MobileViT model.

Results and discussion

Cottonseed germination test

It is important to guarantee the safety of air-coupled ultrasonic detection for cottonseed. In order to verify the safety of ultrasonic detection, the germination test of cottonseeds is used as the verification method. First, two batches of intact cottonseeds are randomly selected, then the cottonseeds are divided into two groups. One group is not used to ultrasonic testing, and the other group is passed through air-coupled ultrasonic at the same frequency and intensity in detection experiment. For each germination test, 1,000 cottonseeds after ultrasonic testing and 1,000 cottonseeds without ultrasonic testing are selected respectively. Then the two groups of cottonseeds are used in cottonseed germination tests at the same time. It is determined whether air-coupled ultrasonic detection will cause damage to the cottonseeds by the comparison of the germination rates.

Table 1 shows the comparative results of the cottonseed germination rate. By comparing the results in Table 1, it can be seen that air-coupled ultrasonic detection does not affect the germination rate of cottonseeds. At the same time, the germination rate of seeds tends to decrease with the increase of time. This trend may be due to the storage environment of cottonseeds not in accordance with the storage standards, which affects the germination rate of cottonseeds. Therefore, in this study, the air-coupled ultrasound with frequency of 400 kHz and voltage of 200 V is used to detect the slight crack of cottonseed, which will not damage the cottonseeds or reduce the germination rate of cottonseeds. This is a safe non-destructive detection method.

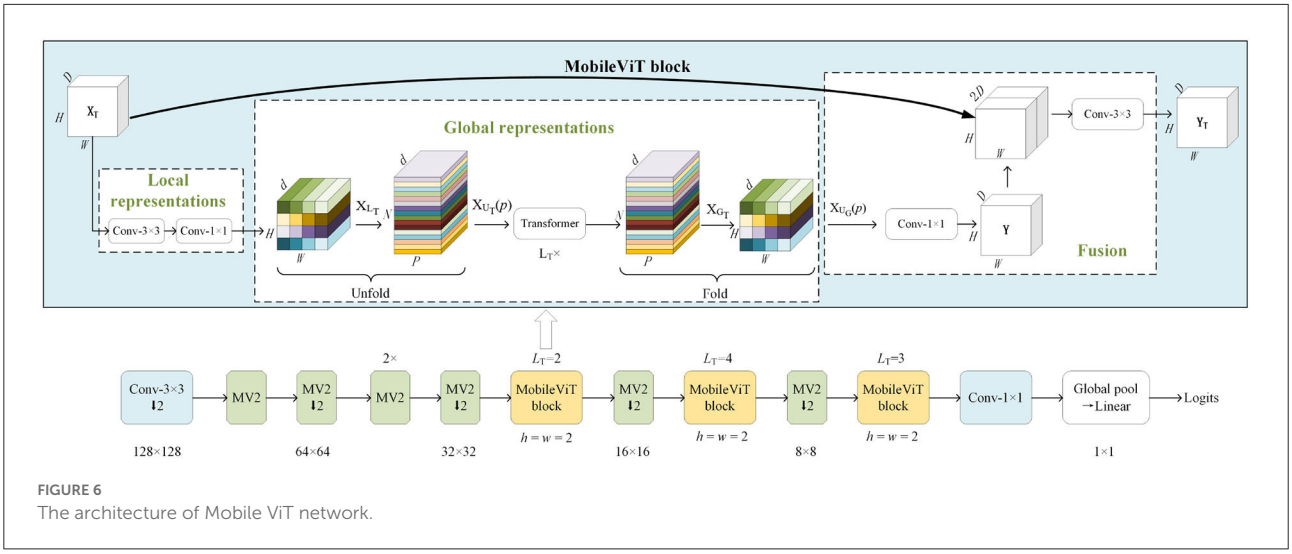

FIGURE 6
The architecture of Mobile ViT network.

TABLE 1 The results of cottonseeds germination test.

Cottonseed category	Storage for 2 months	Storage 1 year
Cottonseeds after ultrasonic testing	83.5%	72.2%
Cottonseeds without ultrasonic testing	86.1%	70.6%

Determination of decomposition number *M* using sample entropy

The ultrasonic signal $X(n)$ is decomposed to M intrinsic mode functions using VMD decomposition. The number M of intrinsic mode functions needs to be determined artificially. Sample entropy is proposed to measure the complexity of time series by Richman and Moorman (2000). Complex time series signals have large sample entropy, while time series signals with strong selfsimilarity have small sample entropy. Zhang et al. (2020) proposed a method to select the number M of intrinsic mode functions by computing the sample entropy of time series. For an appropriate M value of VMD decomposition operation, it will correspond to smaller sample entropy of the time sequence signal. Therefore, on the condition of effectively limiting the computational complexity, the M value is determined by calculating the sample entropy of the intrinsic mode functions.

For one-dimensional time series signal $\{X_{SE}(i), i = 1, 2, \ldots, L\}$, z-dimensional vector is reconstructed and represented by $\{Y_{SE}(i), i = 1, 2, \ldots, Z, Z = L - z + 1\}$ according to Equation 11:

$$Y_{SE}(i) = \{X_{SE}(i), X_{SE}(i+1), X_{SE}(i+2), \cdots, X_{SE}(i+m-1)\} \quad (11)$$

Then the maximum value of Euclidean distance between any component of vectors $Y_{SE}(i)$ and $Y_{SE}(j)$ is calculated according to Equation 12 and represented as $D_{SE}(Y_{SE}(i), Y_{SE}(j))$.

$$D_{SE}(Y_{SE}(i), Y_{SE}(j)) = \max\left[\left|Y_{SE}(i+k) - Y_{SE}(j+k)\right|\right] \quad (12)$$

where $i, j \in \{1, 2, \ldots, Z - z + 1\}$ and $k \in \{0, 1, \ldots, z - 1\}$. Then $A_i^z(r)$ is calculated according to Equation 13, where r is tolerance threshold and A_i^z is the number that the distance between $Y_{SE}(i)$ and $Y_{SE}(i)$ is not greater than r.

$$\overline{A}_i^z(r) = \frac{1}{L - z + 1} A_i^z \quad (13)$$

Then $A_i^z(r)$ is used to calculate $\overline{A}_i^z(r) \cdot \overline{A}_i^z(r) = \frac{1}{L-z}\sum_{i=1}^{L-z} A_i^z(r)$. Finally, the sample entropy of time series signal is calculated according to the following to Equation 14:

$$SampleEn(m, r) = -\ln \frac{A_i^{z+1}(r)}{A_i^z(r)} \quad (14)$$

The original air-coupled ultrasonic signal is decomposed using VMD with different parameter M. Then the sample entropy corresponding to each M is calculated accordance to Equation 14. In order to obtain an appropriate detection speed, M is set to 2, 3, 4, 5, 6 in the experiment respectively. It can be seen from Figure 7 that the sample entropy has the smallest value when M is equal to 3. Therefore, $M = 3$ is determined as the number of intrinsic mode functions of VMD decomposition in this study.

Influence of the number of encoding colors

The conversion from air-coupled ultrasonic data to image data is realized through a specific number of color encoding sets. In order to determine the optimal number of encoding

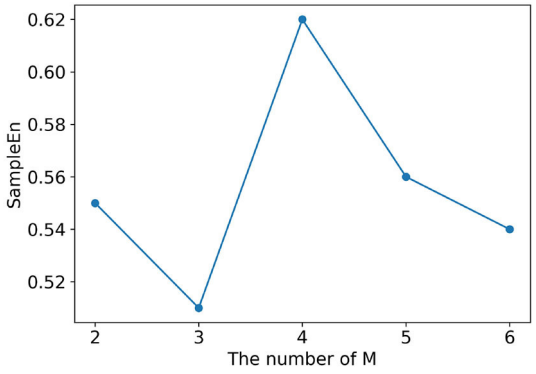

FIGURE 7
The value of the sample entropy with different numbers M of IMFs.

colors for ultrasound to image conversion, a color set for encoding including 12 colors is constructed. The air-coupled ultrasonic signal decomposed by VMD method is encoded by two to 12 colors respectively. Eleven image data sets are constructed using the original air-coupled ultrasonic data. The MobileViT model is trained by using each image data set. The training data sets and test data sets from 11 image data sets are divided in the same proportion respectively. The initialization parameters of MobileViT in this study are shown in Table 2. These initialization parameters are mainly determined according to GPU performance and characteristics of encoding image. The comparison results of the MobileViT model obtained on the test sets of colorful images generated by different numbers of encoding colors are shown in Figure 8. The colorful image sets for tests come from the same air-coupled ultrasonic data test set, but different test sets are generated according to the corresponding color encoding method. It can be seen from Figure 8 that with the increase of encoding colors, the classification accuracy increases gradually. When the number of encoding colors is equal to 10, the classification accuracy reaches the maximum. Then the classification accuracy decreases with the increase of the encoding color number. This is mainly because, with the increase of the encoding colors number and the types of colors, the image generated from the air-coupled ultrasound becomes more complex. It is difficult for the classification algorithm to extract effective features from the complex image. Therefore, to realize the conversion from sound to image, 10 colors are selected to encode the intrinsic mode functions of the original air-coupled ultrasonic signal.

Comparison of different methods

In order to compare the detection effects of the method proposed in this study with those of other methods, eight

TABLE 2 Parameters of MobileViT for cottonseed with slight crack.

Parameters	Value
Input size	256 × 256
Classes	2
Batch size	16
Learning rate	1.0×10^{-3}
Iterations	10

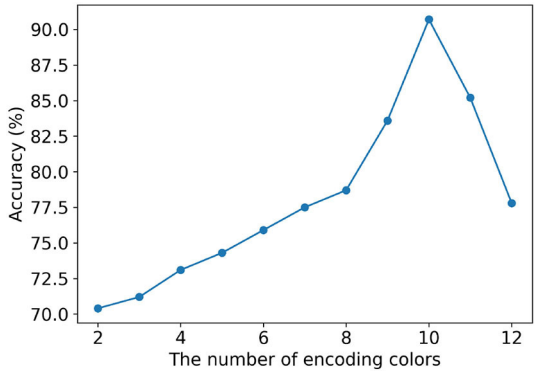

FIGURE 8
Accuracy of slight crack detection of cottonseed with different numbers of encoding colors.

detection methods are proposed for the comparison experiment. The long short-term memory (LSTM) network is a special kind of recurrent neural network that can store and retrieve information from sequence data by memory cells (Hochreiter and Schmidhuber, 1997). LSTM network is an effective classifier for dealing with one-dimensional time-series and sequential data. The original air-coupled ultrasonic signal, wavelet features, and the results of VMD decomposition are used as input data respectively, and then combined with LSTM classifier to obtain four methods for the comparison. The wavelet transformer can be used to obtain the time-frequency domain features of original air-coupled ultrasonic signal.

The color images used to train deep learning classifiers are shown in Figure 9. For the data set obtained by the color encoding (CE) method from sound to image, different classifiers are used to compare the detection of cottonseed with slight crack. The traditional convolutional neural network (CNN) (Fan S. et al., 2020), residual network (ResNet18) (He et al., 2016) and Swin Transformer (Liu et al., 2021) are chosen as the classifier for the comparison respectively. The shortcut connections in ResNet18 make deeper neural networks to realize complex classification tasks. These models use a cross-entropy function as a loss function. Meanwhile, the training iterations of all models is set to 10.

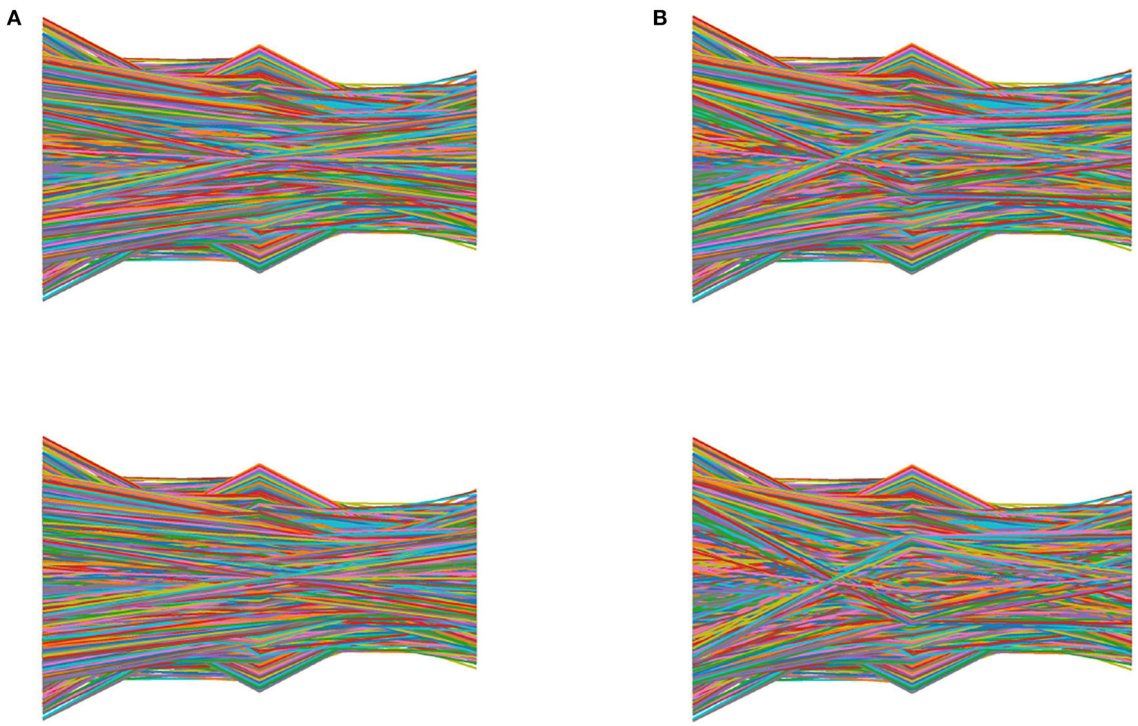

FIGURE 9
Color images generated from air-coupled ultrasound of cottonseeds. **(A)** Intact cottonseeds. **(B)** Cottonseeds with slight cracks.

TABLE 3 The comparison of different methods for the detection of cottonseed with slight crack.

Method	Precision	Recall	F1 score	Accuracy
1D raw data - LSTM	80%	65.5%	72%	74%
Wavelet - LSTM	64.1%	92.6%	78.5%	70.4%
VMD- LSTM	75.5%	68.5%	71.8%	73.1%
VMD- CE - CNN	94.4%	61.8%	74.7%	78.7%
VMD- CE - ResNet18	82.8%	96.4%	89.1%	88%
VMD- CE – Swin Transformer	73.1%	89.1%	80.3%	77.8%
VMD- CE – MobileViT (proposed method)	86.9%	96.4%	91.4%	90.7%

The experimental results are shown in Table 3. From the experimental results, it can be seen that the two-dimensional image can better reflect the features of air-coupled ultrasonic signal than the features of one-dimensional signal. Because the MobileVIT model can combine the local analysis ability of convolutional neural network with the global analysis ability of Transformer, the classification performance of MobileViT is better than that of convolutional neural network and Swin Transformer model. Due to the vast amount of parameters in the Swin Transformer model and the requirement for a large number of training data, the training and learning of non-large data sets can't show the advantages of the Swin Transformer model. Therefore, VMD-CE–MobileViT approach proposed in this study can distinguish normal cottonseed from cottonseed with slight crack effectively.

Conclusion

In this paper, a detection method based on air-coupled ultrasound and sound to image encoding is proposed for slight crack identification of cottonseed. The traditional ultrasound detection method is not suitable for the requirements of non-destructive detection of cottonseed quality, and it is very difficult to detect cottonseed with slight crack using machine vision and other non-destructive detection technologies. To distinguish kernels with slight crack from intact kernels, a non-destructive, non-contact detection method based on air-coupled ultrasound is developed. VMD decomposition is used to obtain the IMFs of air-coupled ultrasonic signal. Then the feature matrix from the IMFs is applied to generate colorful image by a color encoding method. This method of converting sound into image can help

the MobileViT classifier to obtain higher detection accuracy. The experimental results show that slightly cracked cottonseed can be distinguished from normal cottonseed precisely. The average accuracy of slightly cracked cottonseed identification test is 90.7%. The presented method can be extended to other signal recognition domain, such as distinguishing premature heartbeat signal from normal heartbeat signal in electrocardiogram (ECG) domain. In the future, we will combine the method proposed in this study with hyperspectral image processing technology to improve the detection accuracy further.

Data availability statement

The original contributions presented in the study are included in the article/supplementary material, further inquiries can be directed to the corresponding authors.

Author contributions

CZ proposed the idea, designed the methodology and prepared the manuscript. WH managed and coordinated the research activity planning and execution. XL conducted the experiment and maintained the research data. XH designed the experimental system. XT assisted in analyzing experimental data. LC provided oversight and leadership responsibility for the research. QW reviewed, edited the manuscript, and is responsible for ensuring that the descriptions are accurate and agreed by all authors. All authors contributed to the article and approved the submitted version.

Funding

This work was supported by the National Natural Science Foundation of China (NSFC No. 31871523), Young Elite Scientists Sponsorship Program by CAST (2019QNRC001), and National Natural Science Foundation of China (NSFC No. 31901402).

Conflict of interest

The authors declare that the research was conducted in the absence of any commercial or financial relationships that could be construed as a potential conflict of interest.

Publisher's note

All claims expressed in this article are solely those of the authors and do not necessarily represent those of their affiliated organizations, or those of the publisher, the editors and the reviewers. Any product that may be evaluated in this article, or claim that may be made by its manufacturer, is not guaranteed or endorsed by the publisher.

References

Baek, I., Kim, M. S., Cho, B.-K., Mo, C., Barnaby, J. Y., et al. (2019). Selection of optimal hyperspectral wavebands for detection of discolored, diseased rice seeds. *Applied Sciences* 9, 1027. doi: 10.3390/app9051027

Bai, X., Wang, W., Jiang, H., Chu, X., Zhao, X., Wang, B., et al. (2018). "Research on classification method of cotton seeds on machine vision," in: *2018 ASABE Annual International* Meeting (American Society of 385 Agricultural and Biological Engineers), Detroit, 1. doi: 10.13031/aim.201800810

Barboza da Silva, C., Oliveira, N. M., de Carvalho, M. E. A., de Medeiros, A. D., de Lima Nogueira, M., and Dos Reis, A. R. (2021). Autofluorescence-spectral imaging as an innovative method for rapid, non-destructive and reliable assessing of soybean seed quality. *Sci. Rep.* 11, 17834. doi: 10.1038/s41598-021-97223-5

Belin, E., Douarre, C., Gillard, N., Franconi, F., Rojas-Varela, J., Chapeau-Blondeau, F., et al. (2018). Evaluation of 3d/2d imaging and image processing techniques for the monitoring of seed imbibition. *J. Imaging* 4, 83. doi: 10.3390/jimaging4070083

Chelladurai, V., Karuppiah, K., Jayas, D., Fields, P., and White, N. (2014). Detection of *Callosobruchus maculatus* (f.) infestation in soybean using soft X-ray and NIR hyperspectral imaging techniques. *J. Stored Prod. Res.* 57, 43–48. doi: 10.1016/j.jspr.2013.12.005

Dibaj, Ali, Ettefagh, M. M., Hassannejad, R., and Ehghaghi, M. B. (2021). A hybrid fine-tuned VMD and CNN scheme for untrained compound fault diagnosis of rotating machinery with unequal-severity faults. *Expert Syst. Appl.* 167, 114094. doi: 10.1016/j.eswa.2020.114094

Dosovitskiy, A., Beyer, L., Kolesnikov, A., Weissenborn, D., Zhai, X., Unterthiner, T., et al. (2020). An image is worth 16x16 words: transformers for image recognition at scale. *arXiv*. preprint arXiv:2010.11929. doi: 10.48550/arXiv.2010.11929

Dragomiretskiy, K., and Zosso, D. (2013). Variational mode decomposition. *IEEE Trans. Signal Proces.* 62, 531–544. doi: 10.1109/TSP.2013.2288675

ElMasry, G., ElGamal, R., Mandour, N., Gou, P., Al-Rejaie, S., Belin, E., et al. (2020). Emerging thermal imaging techniques for seed quality evaluation: principles and applications. *Food Res. Int.* 131, 109025. doi: 10.1016/j.foodres.2020.109025

Fan, S., Li, J., Zhang, Y., Tian, X., Wang, Q., He, X., et al. (2020). On line detection of defective apples using computer vision system combined with deep learning methods. *J. Food Eng.* 286, 110102. doi: 10.1016/j.jfoodeng.2020.110102

Fan, Y., Ma, S., and Wu, T. (2020). Individual wheat kernels vigor assessment based on NIR spectroscopy coupled with machine learning methodologies. *Infrared Phy. Technol.* 105, 103213. doi: 10.1016/j.infrared.2020.103213

Fang, W., Lu, W., Xu, H., Hong, D., and Liang, K. (2016). Study on the detection of rice seed germination rate based on infrared thermal imaging technology combined with generalized regression neural network. *Spectrosc. Spectr. Anal.* 36, 2692–2697. doi: 10.3964/j.issn.1000-0593(2016)08-2692-06

Fang, Y., Lin, L., Feng, H., Lu, Z., and Emms, G. W. (2017). Review of the use of air-coupled ultrasonic technologies for nondestructive testing of wood and wood products. *Comput. Electr. Agric.* 137, 79–87. doi: 10.1016/j.compag.2017.03.015

Fariñas, L., Contreras, M., Sanchez-Jimenez, V., Benedito, J., and Garcia-Perez, J. V. (2021a). Use of air-coupled ultrasound for the non-invasive characterization of the textural properties of pork burger patties. *J. Food Eng.* 297, 110481. doi: 10.1016/j.jfoodeng.2021.110481

Fariñas, L., Sanchez-Torres, E. A., Sanchez-Jimenez, V., Diaz, R., Benedito, J., Garcia-Perez, J. V., et al. (2021b). Assessment of avocado textural changes during

ripening by using contactless air-coupled ultrasound. *J. Food Eng.* 289, 110266. doi: 10.1016/j.jfoodeng.2020.110266

He, K., Zhang, X., Ren, S., and Sun, J. (2016). Deep residual learning for image recognition. *In Proceedings of the IEEE Conference on Computer Vision and Pattern Recognition* 770–778. doi: 10.1109/CVPR.2016.90

Hochreiter, S., and Schmidhuber, J. (1997). Long short-term memory. *Neural Comput.* 9, 1735–1780. doi: 10.1162/neco.1997.9.8.1735

Hong, M., and Luo, Z.-Q. (2017). On the linear convergence of the alternating direction method of multipliers. *Math. Program.* 162, 165–199. doi: 10.1007/s10107-016-1034-2

Hu, N., Li, W., Du, C., Zhang, Z., Gao, Y., Sun, Z., et al. (2021). Predicting micronutrients of wheat using hyperspectral imaging. *Food Chem.* 343, 128473. doi: 10.1016/j.foodchem.2020.128473

Huang, M., Wang, Q., Zhu, Q., Qin, J., and Huang, G. (2015). Review of seed quality and safety tests using optical sensing technologies. *Seed Sci. Technol.* 43, 337–366. doi: 10.15258/sst.2015.43.3.16

Huang, S., Fan, X., Sun, L., Shen, Y., and Suo, X. (2019). Research on classification method of maize seed defect based on machine vision. *J. Sens.* 2019, 1–9. doi: 10.1155/2019/2716975

Kim, G., Kim, G-., H., Lohumi, S., Kang, J-, S., Cho, B-., et al. (2014). Viability estimation of pepper seeds using time-resolved photothermal signal characterization. *Infrared Phys. Technol.* 67, 214–221. doi: 10.1016/j.infrared.2014.07.025

Li, D., and Liu, Y., and Gao,. L. (2016). Research of maize seeds classification recognition based on the image processing. *Int. J. Signal Proces. Image Proces. Pattern Recognit.* 9, 181–190. doi: 10.14257/ijsip.2016.9.11.16

Liu, Z., Lin, Y., Cao, Y., Hu, H., Wei, Y., Zhang, Z., et al. (2021). "Swin transformer: Hierarchical vision transformer using shifted windows," in: *Proceedings of the IEEE/CVF International Conference on Computer Vision*, Montreal, 10012–10022. doi: 10.1109/ICCV48922.2021.00986

Mehta, S., and Rastegari, M. (2021). Mobilevit: light-weight, general-purpose, and mobile-friendly vision transformer. *arXiv.* preprint arXiv:2110.02178. doi: 10.48550/arXiv.2110.02178

Pearson, T. (2001). Detection of pistachio nuts with closed shells using impact acoustics. *Appl. Eng. Agric.* 17, 249. doi: 10.13031/2013.5450

Pearson, T. C., Cetin, A. E., Tewfik, A. H., and Haff, R. P. (2007). Feasibility of impact-acoustic emissions for detection of damaged wheat kernels. *Digit. Signal Process.* 17, 617–633. doi: 10.1016/j.dsp.2005.08.002

Rahman, A., and Cho, B.-K. (2016). Assessment of seed quality using non-destructive measurement techniques: a review. *Seed Sci. Res.* 26, 285–305. doi: 10.1017/S0960258516000234

Richman, J. S., and Moorman, J. R. (2000). Physiological time-series analysis using approximate entropy and sample entropy. *Am. J. Physiol. Heart Circ. Physiol.* 278, H2039–49. doi: 10.1152/ajpheart.2000.278.6.H2039

Rodríguez-Pulido, F. J., and Ferrer-Gallego, R., González -Miret, M. L., Rivas-Gonzalo, J. C., Escribano-Bailón's, M. T., and Heredia, F. J. (2012). Preliminary study to determine the phenolic maturity stage of grape seeds by computer vision. *Anal. Chim. Acta* 732, 78–82. doi: 10.1016/j.aca.2012.01.005

Sun, X., Guo, M., Ma, M., and Mankin, R. W. (2018). Identification and classification of damaged corn kernels with impact acoustics multi-domain patterns. *Comput. Electron. Agric.* 150, 152–161. doi: 10.1016/j.compag.2018.04.008

Sunoj, S., Igathinathane, C., and Visvanathan, R. (2016). Nondestructive determination of cocoa bean quality using FT-NIR spectroscopy. *Comput. Electron. Agric.* 124, 234–242. doi: 10.1016/j.compag.2016.04.012

Tao, F., Yao, H., Hruska, Z., Liu, Y., Rajasekaran, K., Bhatnagar, D., et al. (2019). Use of visible–near-infrared (Vis-NIR) spectroscopy to detect aflatoxin B1 on peanut kernels. *Appl. Spectrosc.* 73, 415–423. doi: 10.1177/0003702819829725

Tiitta, M., Tiitta, V., Gaal, M., Heikkinen, J., Lappalainen, R., Tomppo, L., et al. (2020). Air-coupled ultrasound detection of natural defects in wood using ferroelectret and piezoelectric sensors. *Wood Sci. Technol.* 54, 1051–1064. doi: 10.1007/s00226-020-01189-y

Tu, K.-l., Li, L.-j., Yang, L.-m., Wang, J.-h., and Qun, S. (2018). Selection for high quality pepper seeds by machine vision and classifiers. *J. Integr. Agric.* 17, 1999–2006. doi: 10.1016/S2095-3119(18)62031-3

Vaswani, A., Shazeer, N., Parmar, N., Uszkoreit, J., Jones, L., Gomez, A. N., et al. (2017). "Attention is all you need," in: *31st Conference on Neural Information Processing Systems (NIPS 2017).* Long Beach, CA 30, 5998–6008.

Xia, Y., Xu, Y., Li, J., Zhang, C., and Fan, S. (2019). Recent advances in emerging techniques for non-destructive detection of seed viability: A review. *Artif. Intell. Agri.* 1, 35–47. doi: 10.1016/j.aiia.2019.05.001

Yang, G., Wang, Q., Liu, C., Wang, X., Fan, S., Huang, W., et al. (2018). Rapid and visual detection of the main chemical compositions in maize seeds based on Raman hyperspectral imaging. *Spectrochim. Acta A Mol. Biomol. Spectrosc.* 200, 186–194. doi: 10.1016/j.saa.2018.04.026

Yanyun, J., Wanlin, G., Han, Z., Dong, A., Sihan, G., Ahmed, S. I., et al. (2016). Identification of damaged corn seeds using air-coupled ultrasound. *Int. J. Agric. Biol. Eng.* 9, 63–70. doi: 10.3965/j.ijabe.20160901.1880

Yildiz, C., Acikgoz, H., Korkmaz, D., and Budak, U. (2021). An improved residual-based convolutional neural network for very short-term wind power forecasting. *Energy Convers. Manage.* 228, 113731. doi: 10.1016/j.enconman.2020.113731

Zhang, Y., and Guo, W. (2020). Moisture content detection of maize seed based on visible/near-infrared and near-infrared hyperspectral imaging technology. *Int. J. Food Sci. Technol.* 55, 631–640. doi: 10.1111/ijfs.14317

Zhang, Y., Pan, G., Chen, B., Han, J., Zhao, Y., Zhang, C., et al. (2020). Short-term wind speed prediction model based on GA-ANN improved by VMD. *Renew. Energy* 156, 1373–1388. doi: 10.1016/j.renene.2019.12.047

Zhou, Q., Huang, W., Fan, S., Zhao, F., Liang, D., Tian, X., et al. (2020). Non-destructive discrimination of the variety of sweet maize seeds based on hyperspectral image coupled with wavelength selection algorithm. *Infrared Phys. Technol.* 109, 103418. doi: 10.1016/j.infrared.2020.103418

frontiers | Frontiers in Plant Science

TYPE Original Research
PUBLISHED 11 October 2022
DOI 10.3389/fpls.2022.991883

OPEN ACCESS

EDITED BY
Jianwei Qin,
Agricultural Research Service (USDA),
United States

REVIEWED BY
Leiqing Pan,
Nanjing Agricultural University, China
Julio Nogales-Bueno,
Universidad de Sevilla, Spain

*CORRESPONDENCE
Leizi Jiao
jiaolz@nercita.org.cn

SPECIALTY SECTION
This article was submitted to Crop and Product Physiology, a section of the journal Frontiers in Plant Science

RECEIVED 12 July 2022
ACCEPTED 26 September 2022
PUBLISHED 11 October 2022

CITATION
Zhou Y, Gu Y, Guo R, Jiao L, Wang K, Zhu Q and Dong D (2022) *In situ* detection of fruit spoilage based on volatile compounds using the mid-infrared fiber-optic evanescent wave spectroscopy.
Front. Plant Sci. 13:991883.
doi: 10.3389/fpls.2022.991883

In situ detection of fruit spoilage based on volatile compounds using the mid-infrared fiber-optic evanescent wave spectroscopy

Yunhai Zhou[1,2], Yifan Gu[2], Rui Guo[2], Leizi Jiao[1,2]*, Ke Wang[2], Qingzhen Zhu[1] and Daming Dong[1,2]

[1]School of Agricultural Engineering, Jiangsu University, Zhenjiang, China, [2]National Research Center of Intelligent Equipment for Agriculture, Beijing Academy of Agriculture and Forestry Sciences, Beijing, China

Volatile compounds such as ethanol released from fruit can be rapidly detected using Fourier Transform Infrared spectroscopy based on a long-path gas cell. However, this method relies on a long optical path length and requires pumping fruit volatiles into the gas cell. This can lead to the volatile compounds being contaminated and not detectable *in situ*. Fiber optic evanescent wave spectroscopy (FOEW) is not influenced by the path length so can detect materials (solid, liquid and gas phase) rapidly *in situ*, using only a few millimeters of optical fiber. In the present study, a spiral silver halide FOEW sensor with a length of approximately 21 mm was used to replace a long-path gas cell to explore the feasibility of identifying volatile compounds released from grapes *in situ*. The absorption peaks of ethanol in the volatile compounds were clearly found in the FOEW spectra and their intensity gradually increased as the storage time of the grapes increased. PCA analysis of these spectra showed clear clustering at different storage times (1-3, 4-5 and 6-7 d), revealing that the concentration of the ethanol released from the grapes changed significantly with time. The qualitative model established by PLS-DA algorithm could accurately classify grape samples as "Fresh," "Slight spoilage," or "Severe spoilage". The accuracy of the calibration and validation sets both were 100.00%. These changes can therefore be used for rapidly identifying fruit deterioration. Compared with the method used in a previous study by the authors, this method avoids using a pumping process and can thus identify volatile compounds and hence monitor deterioration *in situ* and on-line by placing a very short optical fiber near the fruit.

KEYWORDS

***in situ* detection, fruit spoilage, volatile compounds, ethanol, FOEW spectroscopy, FTIR**

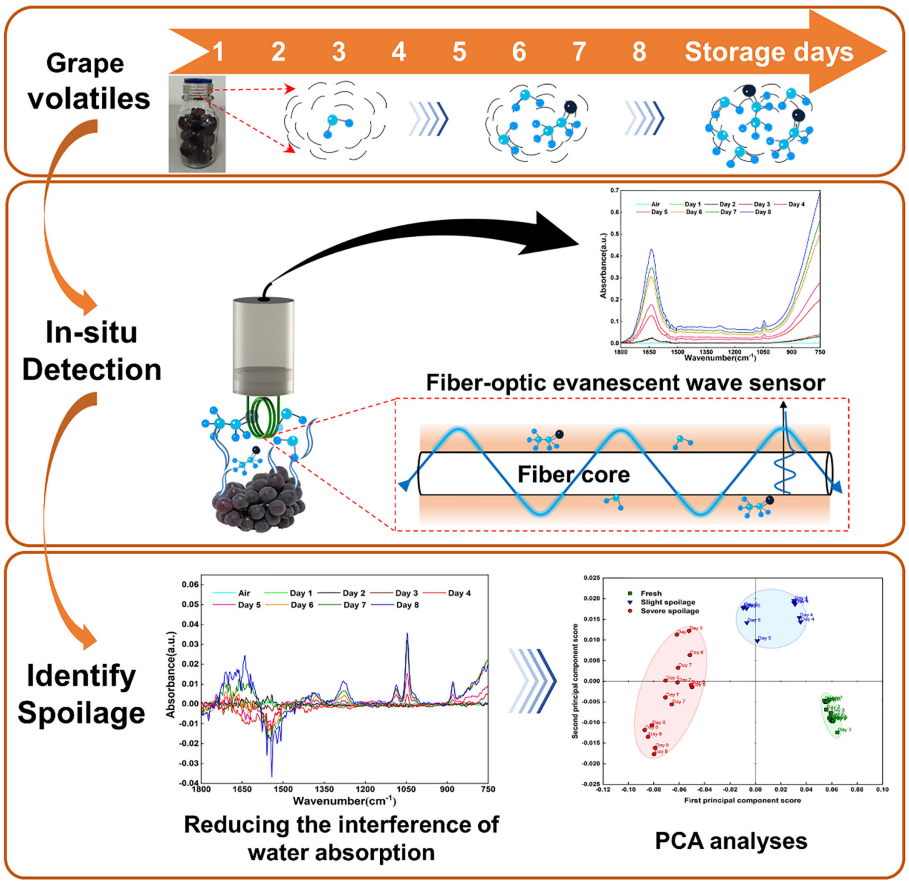

GRAPHICAL ABSTRACT

Highlights

- Sensitive detection of volatile compounds using a FOEW sensor to replace a long-path gas cell.
- Sensitive detection of volatile compounds can be achieved independently of long optic path.
- *In situ* and on-line detection of ethanol by placing a short FOEW sensor near the fruits.
- Fruit spoilage can be identified *in situ* by a FOEW sensor and FTIR spectrometer.

1 Introduction

Fruit is essential for human health with its high contents of vitamins, minerals, antioxidants and many phytonutrients (Rice-Evans and Miller, 1995). However, fruit is frequently transported over long distances, allowing time for it to spoil easily, with the consequent food safety concerns and heavy economic losses. It has been estimated that approximately 20% of all fruit produced for human consumption is lost each year because of spoilage (Jahun et al., 2021). Therefore, the rapid identification of fruit spoilage *in situ* is of great significance for ensuring food safety, reducing economic losses and improving human living standards. The volatile compounds released from fruit reflect their particular status during storage. Several studies have reported that the concentrations of volatile compounds emitted from fruit, such as alcohols, esters, terpenes and ethylene, are closely related to their quality (Zhu et al., 2018a; Cai et al., 2019; Wu et al., 2020). Thus, the qualitative and quantitative analyses of these volatile compounds are critical for rapidly assessing the quality of fruit.

Gas Chromatography (GC) and Gas Chromatography Mass Spectrometry (GC-MS) are commonly used in most research

studies for accurately detecting volatiles released from fruit (Sánchez-Palomo et al., 2005; Giannetti et al., 2017; Zhu et al., 2018b). These methods detect differences in the adsorption capacity of adsorbents in the chromatographic column for the qualitative and quantitative detection of fruit volatiles. Although these laboratory physical and chemical analysis methods are sensitive and accurate, they require complex sampling, preparation and analysis processes. This method requires time and effort compared to spectroscopy, which does not necessitate sample preparation. For fruit volatiles, a rapid detection method is required. Stimulated by this demand, Proton Transfer Reaction Mass Spectrometry (PTR-MS) (Hewitt et al., 2003; Franke and Beauchamp, 2016), which can be linked to a quadrupole (PTR-(Quad)MS) or time-of-flight mass spectrometer (PTR-TOF-MS) (Liu et al., 2018), has been used to detect fruit volatiles on-line (Cappellin et al., 2012; Li et al., 2021). However, the equipment must be calibrated with a standard gas for quantitative analysis, and requires several minutes to stabilize for reagent ion switching. It is also important to note that PTR-MS only provides molecular weight information (mass-to-charge ratio) on the volatile compounds and cannot be used for the qualitative analysis of isomers. It can not achieve the recognition accurate of spectroscopy. Compared with these complex laboratory analysis methods, an electronic nose (E-nose) based on electrochemical reactions has the advantages of low cost, portability and ease of use. It can quickly generate a superimposed signal response of the volatile compounds almost in real time. Some studies have used the E-nose to determine the stages of fruit spoilage and assess the physical and chemical properties of fruit (Chen et al., 2018; Tatli et al., 2021). However, the data generated by the E-nose is complex and must be processed by multivariate statistical methods for their accurate interpretation, compared with spectroscopy, its reproducibility, resolution and robustness still needing to be resolved.

Based on the specific excitation of rotation and vibrational transitions of most molecular compounds, mid-infrared (MIR) spectroscopy provides quantitative information on the unique chemical and structural properties of molecules and has been widely used in medicine (Tiernan et al., 2020), agriculture (Volkov et al., 2021) and general industry as a rapid and sensitive technique for obtaining molecular fingerprints (Ke et al., 2018). Most volatile compounds released from food have specific infrared absorption characteristics and can be analyzed qualitatively and quantitatively using these specific infrared absorption peaks, with many studies demonstrating the feasibility of this technique (Cubero-Leon et al., 2014; Jahromi et al., 2021). Since 2013, this research group has been studying MIR spectroscopy methods to detect the volatile compounds released from food during storage as it matures and spoils (Dong et al., 2019). The volatile compounds released from fruit, such as grapes, strawberries and mangoes, have been measured using Fourier Transform Infrared (FTIR) spectrometry using a long-path gas cell for predicting the stages of fruit spoilage and ripeness (Dong et al., 2013; Jiao et al., 2017; Jiao et al., 2019). This method is clearly useful but depends on the optical path length. A large long-path gas cell (up to 20 m) was necessary for the sensitive detection of volatile compounds. This method required a blower to pump the volatile compounds into the gas cell, leading to their possible contamination and thus not detectable *in situ*.

Fiber optic evanescent wave (FOEW) sensing technology was first developed by Paul and Kychakoff (Paul and Kychakoff, 1987). Its mode of detection is based on the interaction between evanescent waves and the absorbing medium surrounding the fiber core (Alvarez-ordóñez et al., 2011; Blum and John, 2012; Sharma et al., 2019). Using only a few centimeters of optical fiber, it can detect volatile compounds in solution (Lu et al., 2016; Memon et al., 2017; Dettenrieder et al., 2019; Jiao et al., 2020), *in situ* and on-line, and also where limited space is available. However, the density of gas is low compared with that of a liquid, meaning that the number of molecules on the optical fiber core surface is low at any given time. Therefore, detecting volatile compounds in air using MIR FOEW spectroscopy is not common and remains a challenging technique. Recently, using a single mode chalcogenide glass optical waveguide, Jin et al. (2019) have verified the feasibility of using evanescent wave spectroscopy for selectively detecting ethanol in air (Jin et al., 2019), which provided a basis for detecting fruit volatiles in air based on FOEW spectroscopy as used in the present study. To the best of our knowledge, there have been no reports on using FOEW spectroscopy to detect fruit volatiles, and its feasibility needs to be verified.

The present study, based on previous studies, aims to use a spiral silver halide FOEW sensor with a length of approximately 21 mm to replace the long-path gas cell to check the feasibility of identifying the ethanol in volatile compounds released from fruit *in situ*. The major advantages and innovations of the proposed method are that it requires no sample pretreatment, the identification *in situ* does not require the volatile compounds to be pumped into the gas cell so does not rely on a long optical path length, thus allowing it to be used in practical food storage situations.

2 Materials and methods

2.1 Materials

Fresh grapes (Kyoho, Tianjin, China) were purchased from a local supermarket in Beijing, China. These grapes were carefully separated one by one to ensure that their surfaces were free of mechanical damage. The experiment used 5 independent samples of grapes, each consisting of 150 g. Five glass bottles were cleaned and pasteurized to store the grape samples to

collect their volatile compounds during storage. The same glass bottles were later used to hold different concentrations of ethanol standard gases. Plastic wrap was used to seal these bottles and contain the volatiles. Plastic tubes with a volume of 60 ml were used to store ethanol and deionized solutions to produce the headspace volatile compounds for analysis.

2.2 Instruments

The schematic diagram for detecting the volatile compounds of grapes based on the FOEW sensor is shown in Figure 1. The FTIR spectrometer (Vertex 70, Bruker Ltd., Karlsruhe, Germany) was equipped with a MIR source, an interferometer and an infrared (IR) detector. It could obtain infrared spectra in the range of 4000–600 cm^{-1} with high levels of stability and sensitivity by cooling the detector with liquid nitrogen. The spectral resolution, diaphragm and sampling frequency of the FTIR spectrometer were set to 4 cm^{-1}, 8 mm and 20 Hz, respectively. The time to acquire an infrared spectrum was approximately 1 s under these parameters. A silver halide FOEW sensor (Fiber Optic ATR Loop Probe, Flexispec@ Art Photonics, Berlin, Germany) consisted of a transmission fiber optic with a length of 1000 mm and a spiral FOEW tip with a length of approximately 21 mm. This tip could easily be replaced and connected to the transmission fiber optic when needed. The light beam between the silver halide FOEW sensor and the FTIR spectrometer was connected using a fiber optic coupler (Universal Fiber Probe Coupler, Flexispec@ Art Photonics). This coupler could be directly mounted on a pedestal in the sample chamber of the FTIR spectrometer. The silver halide FOEW sensor was then connected to the coupler using two SMA905 interfaces. The IR spectra of the volatile compounds were collected using OPUS 7.0 software (Bruker Ltd.) by connecting a computer (PC) to the FTIR spectrometer with a data cable.

2.3 Methods

2.3.1 Feasibility of detecting volatile ethanol in air using an FOEW sensor

Detecting volatile compounds in air using MIR FOEW spectroscopy is challenging (Dong et al., 2019). Therefore, an experiment to verify the feasibility of our proposed method was first carried out. First, the FTIR spectrometer was set to the single measurement mode to acquire the FOEW infrared spectra of the air and headspace volatiles of 10% and 30% ethanol

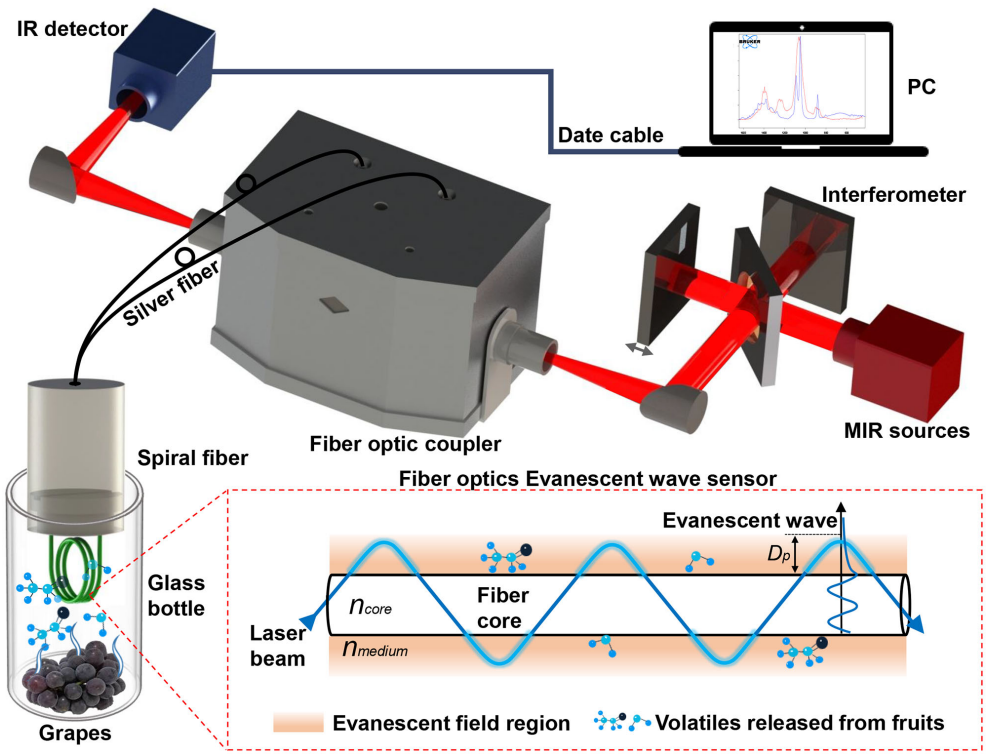

FIGURE 1
Schematic diagram for detecting volatile compounds released from grapes *in situ* based on the MIR FOEW spectrum.

solutions. In this mode, a FOEW infrared spectrum was obtained by averaging 16 spectra. The FTIR spectrometer was then set to the repeated measurement mode to continuously acquire the FOEW infrared spectra alternately between the air and headspace volatiles of the 30% ethanol solution. Three consecutive measurements between air and volatiles were made alternately. The infrared spectra of water and ethanol in the National Institute of Standards and Technology (NIST) Reference Database were used for a comparative analysis with those of air and headspace volatiles. The dynamic response characteristics of the detection system are very important during the on-line measurement of fruit volatiles. Therefore, the absorbance of the ethanol at the 1045 cm^{-1} peak was extracted from the obtained spectra to analyze the response and recovery times of the FOEW sensor.

2.3.2 Quantitation of ethanol in air based on the FOEW spectra

To quantify the concentration of ethanol released from grapes during storage, we acquired the FOEW spectra of standard gas of ethanol at different concentrations in nitrogen using the FTIR spectrometer in the single measurement mode. In this mode, a FOEW infrared spectrum was obtained from the average of 16 spectra. A calibration curve between the absorbance at 1045 cm^{-1} was then extracted from these FOEW spectra and the ethanol concentrations were established based on a chemometrics method. The analytical curves were performed using standard gas of ethanol at 12 different concentrations. Standard gas was analyzed in triplicate by FOEW spectra, and the intensity of characteristic absorption peak for each replica of standard gas were observed and averaged to obtain the calibration curves. We could then quantitatively analyze the concentration of ethanol released from the grapes from this curve.

2.3.3 Analysis of FOEW spectra of grape volatiles and identification of grape spoilage

When detecting the grape volatiles, the FTIR spectrometer was set to the single measurement mode. In this mode, an FOEW infrared spectrum was obtained from the average of 16 spectra. To allow the grapes to decay gradually, five glass bottles containing samples of fresh grapes were stored for 8 d at 22°C and 50% relative humidity. The bottles were sealed for 5 hours from 9 a.m. every day. An infrared background spectrum of the indoor air was acquired as a reference spectrum before opening these bottles. The bottles were then opened in sequence at 2 p.m. every day and immediately placed under the spiral silver halide FOEW sensor to obtain the infrared spectra of the volatile compounds from the grapes. Forty FOEW infrared spectra of the grape volatiles were obtained during the whole experiment. To take account of the strong absorption interference of water in the MIR spectral region (Raichlin and Katzir, 2008), the infrared spectra of the headspace volatiles of deionized water in air were obtained and used as reference spectra for the differential spectral treatment for the grapes. Using the mathematical difference between the absorbance at 1045 cm^{-1} from the ethanol standard gases concentration, the ethanol contained in the grape volatiles was quantified. From the visible light images of the grapes during storage and an analysis of changes in the absorption peak intensity and concentration of ethanol, principal component analysis (PCA) of the infrared spectra of the grape volatiles was used to identify grape spoilage using Unscrambler X software (CAMO Software AS, Oslo, Norway). Partial least squares discriminant analysis (PLS-DA) was used to predict the process of grape spoilage using Matlab (Matlab2019a, MathWorks, Natick, USA), among which the Kennard-Stone sampling algorithm was used to divide the data matrices of grape samples into the calibration and prediction sets and applied using Matlab.

3 Results and discussion

3.1 Detection of ethanol in air by the MIR FOEW spectrum

In this study, the FOEW spectra of the headspace volatiles of 30 mL 10% and 30% ethanol solutions in plastic tubes were obtained in air (Figure 2C). By comparison with the infrared absorption spectra of gaseous and aqueous ethanol in the NIST Reference Database (Figure 2B), the absorption peaks of aqueous ethanol at 880, 1045 and 1088 cm^{-1} were clearly detected in our experiments (Figure 2C). A similar comparison (Figure 2A) also revealed a distinct absorption peak of aqueous water at 1640 cm^{-1}, with a strong absorption band from 1000 to 750 cm^{-1} in Figure 2C. However, in previous studies on the detection of food volatiles based on a long-path gas cell, the absorption spectra of water and ethanol exhibited gaseous absorption peaks (Dong et al., 2013; Dong et al., 2014b; Jiao et al., 2017), possibly because of the interaction of the water and ethanol molecules surrounding the fiber core surface thus forming aqueous ethanol. Generally, the penetration depth of evanescent field region is very small (Sharma et al., 2019). Over such a small range of action, the ethanol molecules surrounding the core surface and the water volatilized by the ethanol solution formed aqueous ethanol which absorbed the evanescent waves on the core surface of the optical fiber. Therefore, the sensor developed based on FOEW was able to detect volatile compounds in air.

As well as verifying the sensor sensitivity, other performance characteristics such as dynamic response, are very important. To demonstrate the reversibility of the sensor's response, we conducted time-dependent measurements by repeatedly exposing the sensor to indoor air and the headspace volatiles of the 30% ethanol solution. Figure 2D shows the absorbance of ethanol at 1045 cm^{-1} when switching from indoor air to the

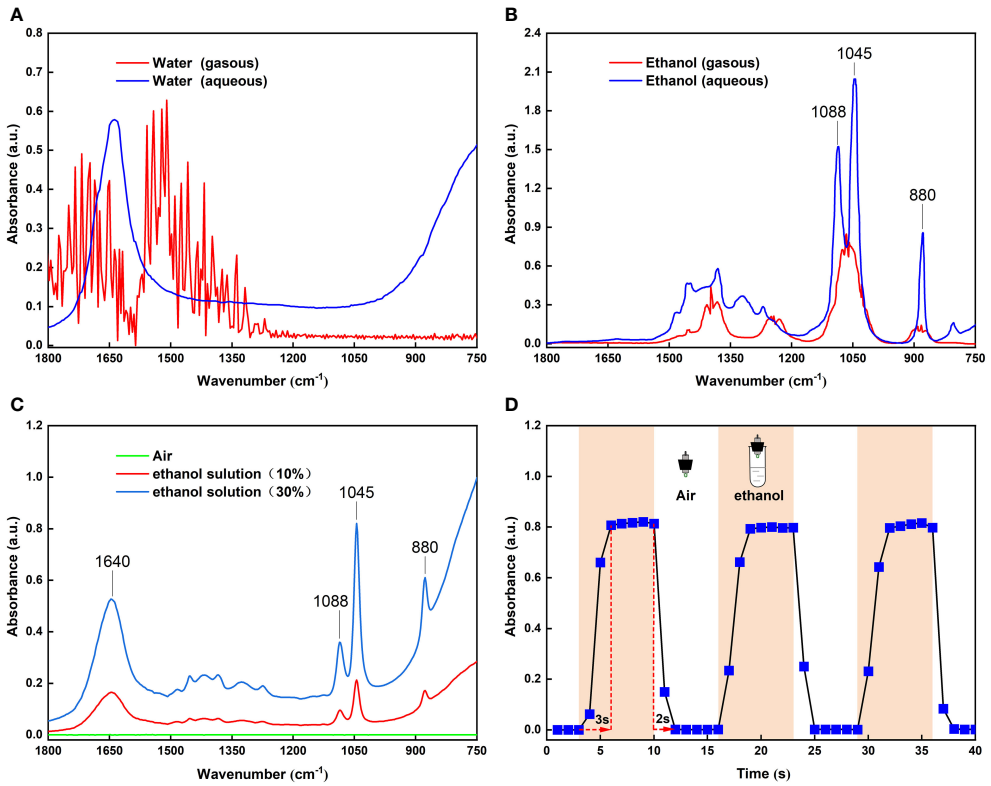

FIGURE 2
(A) Infrared spectra of gaseous and aqueous water from the NIST standard reference database; **(B)** Infrared spectra of gaseous and aqueous ethanol from the NIST standard reference database; **(C)** FOEW infrared spectra of headspace volatiles from 10% and 30% ethanol solutions in test tubes; **(D)** Changes in absorbance at 1045 cm^{-1} peak with time when FOEW sensor was alternately placed in the air and headspace volatiles of the 30% ethanol solution.

headspace volatiles of the 30% ethanol solution three times. It can be seen that the absorbance signal returned to the original baseline level, meaning that the sensor exhibited good reversibility. The dynamic response characteristics showed a response time of approximately 3 s and a recovery time of approximately 2 s. These advantages lead to the possibility of its use for detecting ethanol in fruit volatiles *in situ* and on-line, which are urgently demanded in today's industry (Xia et al., 2016).

3.2 Quantitative analysis by the MIR FOEW spectrum

The absorbance of ethanol increased with increasing concentration of the ethanol standard gases (Figure 2C). This indicated the potential for using the FOEW sensor for the quantitative detection of the concentration of ethanol by the absorbance of the ethanol volatiles. To quantify the concentration of ethanol volatiles, we acquired the FOEW spectra of standard gases of ethanol at different concentrations in nitrogen. The relationship between the absorbance of the ethanol volatiles in the glass bottle and the concentrations of ethanol standard gases was then calculated. The absorbance at 1045 cm^{-1} extracted from these FOEW spectra could then be used to determine the concentration of ethanol. The calibration curve analyzed using linear regression ($y = 0.1062x - 0.0017$) was developed (Figure 3), exhibited a good linearity ($R^2 = 0.9854$).

3.3 Detection of ethanol of grapes in air by the MIR FOEW spectrum

The FOEW infrared spectra of the grape volatiles during storage are shown in Figure 4B. In the first three days, we observed the weak absorption peaks of aqueous water at 1640 and 900–750 cm^{-1} in the grape volatiles. Figure 4A also showed that there were no changes in the grape skin during the first three days, with the grapes appearing fresh. On the fourth day, a weak absorption peak was detected at 1045 cm^{-1}, indicating that there was a small amount of ethanol in the grape volatiles. The water absorbed in the grape volatiles also increased greatly. These

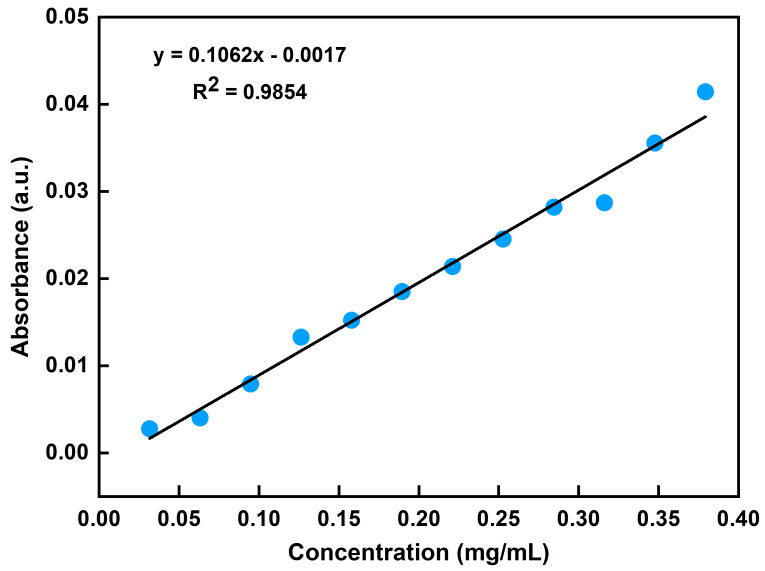

FIGURE 3
FOEW calibration curve of absorption at 1045 cm^{-1} corresponding to different concentrations of ethanol standard gases.

trends in the amounts of ethanol and water in the grape volatiles agreed with previous results (Dong et al., 2014a; Ding et al., 2017; Jiao et al., 2019). Figure 4A also showed that some slightly white hyphae appeared on the grape surface on the fourth day. This became more apparent on the eighth day, possibly indicating a large change in the physiological activity of the grapes (Ding et al., 2017). On the fourth day and on every day thereafter, the absorbance of aqueous water and ethanol both gradually increased, which was entirely consistent with the previous results (Dong et al., 2014a; Ding et al., 2017; Jiao et al., 2019). This indicated that the grape volatiles contained greater amounts of water and ethanol and that the deterioration of the grapes had increased.

In previous studies using methods based on MIR spectroscopy, one of the major difficulties for detecting volatiles released from fruits is the high-water content (Raichlin and Katzir, 2008; Dong et al., 2019). Water has strong absorption in the MIR FOEW (Raichlin and Katzir, 2008). Therefore, it is difficult to measure the absorbance of samples that contain water, a problem confirmed in this study. In the present study, there was serious interference in the detection of ethanol in the range of 900–750 cm^{-1} when a large amount of water was present in the volatiles (Figure 2C). This is the reason for the absorption peaks at 880 cm^{-1} showing unobvious changes (Figure 4B). To reduce the strong interference due to water absorption, previous studies collected data using deionized water as the background spectrum or used the difference spectroscopy method to mitigate the effects of moisture on the FOEW sensors (Lu et al., 2016; Bančič, et al., 2018; Zhang et al., 2018). In the present study, the infrared spectra of the headspace volatiles of deionized water in air were obtained then used as reference spectra to be subtracted from those of the grape volatiles (Figure 5A). In comparison with Figure 4B, the characteristic absorption peak at 880 cm^{-1} was clearly present after the difference spectra and showed a similar pattern of change to that at 1045 cm^{-1} (Figure 5C). Therefore, the strong interference from water absorption could be effectively reduced and the signal-to-noise of this system could also be increased (Jahromi et al., 2021).

Using this method, 40 sets of spectra from grape volatiles obtained during the 8 days of storage (5 sets of spectra per day) were processed. The absorbances at 1088, 1045 and 881 cm^{-1} were extracted from these spectra. The curves of those absorbances with error bands are shown in Figure 5B. The overall pattern of change of the absorbance for the three peaks was basically the same. The slope of these curves began to increase during the 3rd and 4th days, indicating that the grapes had begun to emit ethanol during this period. The maximum slopes were observed between the 4th and 6th days of storage, implying that the rate of ethanol release increased as the grapes deteriorated, which agreed with the previous results (Dong et al., 2014a; Ding et al., 2017; Jiao et al., 2019). The decrease in the slope between the 6th and 8th days was caused by the loss of water from the grapes. This might have arisen from poor physiological activity in the grapes or the dissolution of ethanol in the juice at the bottom of the bottle as shown in the visible light image of the grape on the 8th day (Figure 4A). The greatest error band appeared between the 3th and 5th days, particularly on the 4th day, indicating that the rate of ethanol release was unstable during this period. This could therefore

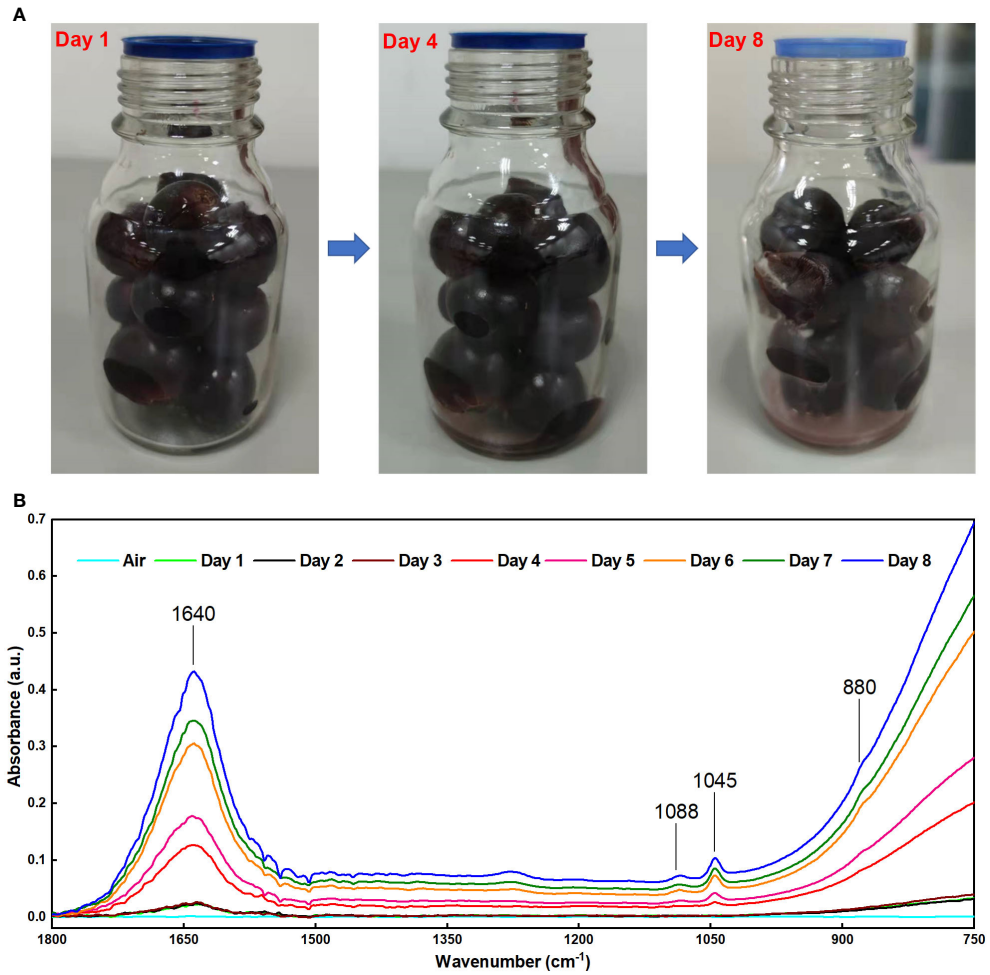

FIGURE 4
(A) Visible light images of grapes at different storage times; **(B)** FOEW infrared absorption spectrum of the grape volatiles at different storage times.

suggest that during the transition period from fresh to spoiled grapes, the physiological activity of the grapes or of the microorganisms was highly variable, which was consistent with our previous study (Dong et al., 2014a). Subsequently, in combination with quantification from the FOEW sensor calibration curve of the absorption at 1045 cm^{-1}, the ethanol concentration in volatiles released from the grapes were analyzed quantitatively (Figure 6A).

3.4 Analyzing spoilage of grapes by the MIR FOEW spectrum

Grapes are one of the most perishable fruits (Shen and Yang, 2017), with post-harvest losses caused by decay and from water loss after harvest and during storage (Leng et al., 2022). Previous study found that 'Kyoho' grapes began to spoil at the room temperature at approximately the 4th day and defined three freshness categories: "Fresh," "Slight spoilage," and "Severe spoilage" (Dong et al., 2014a; Ding et al., 2017; Jiao et al., 2019). After observing the visible light images of the grapes in Figure 4A and the analysis of the infrared spectra of the grape volatiles, we suggest that the grapes were fresh between the 1st and 3rd days of storage, with the FOEW sensor not detecting obvious ethanol volatiles during this period; slight spoilage between the 4th and 5th days, at which point the sensor detected between 0.088 and 0.252 mg ethanol per g of grape volatiles; then severe spoilage after 6th to 8th days, at which time the sensor detected between 0.471 and 0.591 mg ethanol per g of grape volatiles. The data obtained from the ethanol concentration of grape volatiles provided crucial criteria for distinguishing the three stages of grape spoilage.

Principal component analysis (PCA) can be performed as an unsupervised classification method to visualize the resemblances

10.3389/fpls.2022.991883

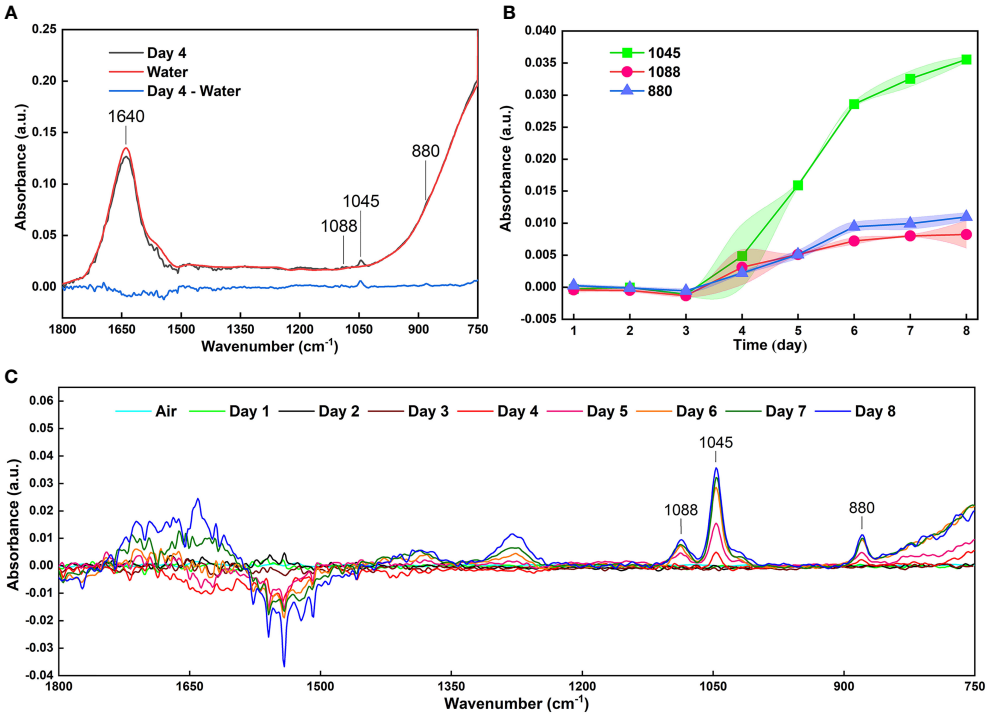

FIGURE 5
(A) Reducing the interference of water absorption by the difference spectra; **(B)** The curves of the absorbance with an error band at absorption peaks of 1088, 1045 and 881 cm^{-1} of 40 infrared spectra of grape volatiles after reducing the interference from water absorption; **(C)** Infrared spectra of grape volatiles after subtracting the interference from water absorption.

and differences between different measurements. After subtracting the interference from water absorption, 40 infrared spectra of grape volatiles corresponding to different storage times were used for PCA analysis (Figure 6B). PCA analysis used data from the 1800–750 cm^{-1} wavelength bands, with contributions of 92% and 4% from PC1 and PC2, respectively. The grape samples were separated along the first PC which described 92% of the peak variation and showed three defined

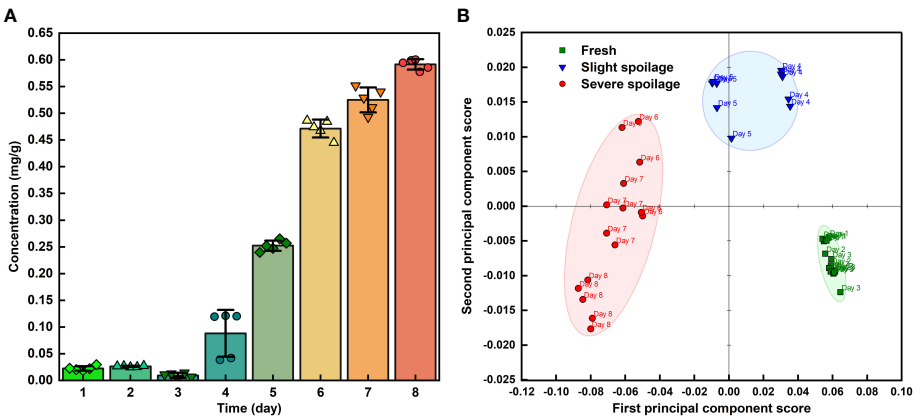

FIGURE 6
(A) The ethanol concentration in volatiles released from grapes during storage; **(B)** PCA analysis of 40 infrared spectra of grape volatiles corresponding to different storage times.

groups. Along the PC1 axis, the storage times of grapes showed obvious clustering at 1-3, 4-5 and 6-8 days of storage. The analysis of the infrared spectra of the grape volatiles suggested that the grapes were fresh between the 1st and 3rd days of storage, slightly spoiled at between the 4th and 5th days then severely spoiled after 6 to 8 days of storage. This was basically consistent with the PCA analysis, indicating that this method based on the FOEW sensor can be used to accurately detect grape spoilage by monitoring the spoilage odors from the volatile substances when the grapes were stored.

The results of PCA cluster analysis served as a reference for establishing a qualitative model based on FOEW spectral data sets combined with a PLS-DA algorithm. The data matrices produced for the grape samples during storage were divided into the calibration and prediction sets in a ratio of 3–1, using the Kennard-Stone method. Of the 40 spectral data from grape samples used for classification, 30 samples were in the calibration set, and 10 samples in the validation set. The accuracies of the calibration and validation sets both were 100%, which indicated that the model had good stability and predictability. It therefore appears that FOEW spectra could reliably predict the process of grape spoilage.

4 Conclusions

This study has used a method based on the FOEW sensor and FTIR spectrometer to detect grape volatiles in air *in situ* and has identified a marker volatile compound (ethanol) that indicates grape spoilage. When combined with chemometric analysis, grape spoilage could be accurately identified. Compared with the method used in previous study based on the long-path gas cell, this method uses a miniature FOEW sensor placed directly near the fruit without the need to sample the fruit itself. This not only eliminates the potential pollution of the gas source used for injection into the FTIR spectrometer, but also achieves a practical method for detecting the volatile compounds released by fruit *in situ*. Fiber optic sensing technology is not affected by electromagnetic interference and can be distributed over long distances for on-line measurement. The proposed technique is expected to provide a new method for the long-distance, *in situ* and on-line detection of the volatile compounds released from fruit. This will allow the rapid identification of fruit deterioration. In addition, the sensitivity and specificity of the FOEW sensor could be greatly improved by coating a thin film (nanoparticles, metal-organic frameworks and so on) on the fiber core to accumulate the volatiles, which will be applied in our future work.

Data availability statement

The raw data supporting the conclusions of this article will be made available by the authors, without undue reservation.

Author contributions

YZ: conceptualization, drafted the manuscript and revised it. LJ: contributed to the funding acquisition, and supervision of the study and made substantial contributions to the revision of the manuscript. YG, RG, KW, and QZ: some experiments, performed the data acquisition and analysis. DD: conceptualization, writing the manuscript, read, and agreed to the submitted version. All authors contributed to the article and approved the submitted version.

Funding

This research was funded by the National Natural Science Foundation of China (31972148, 32101609), Financial special project of Beijing Academy of Agriculture and Forestry Sciences (CZZJ202204), and Beijing Innovation Consortium of Agriculture Research System (BAIC08-2022).

Acknowledgments

The authors are grateful to reviewers for their valuable comments and suggestions.

Conflict of interest

The authors declare that the research was conducted in the absence of any commercial or financial relationships that could be construed as a potential conflict of interest.

Publisher's note

References

Alvarez-ordóñez, A., Mouwen, D. J. M., López, M., and Prieto, M. (2011). Fourier Transform infrared spectroscopy as a tool to characterize molecular composition and stress response in foodborne pathogenic bacteria. *J. Microbiol. Methods* 84 (3), 369–378. doi: 10.1016/j.mimet.2011.01.009

Bančič, T., Bitenc, J., Pirnat, K., Lautar, A. K., Grdadolnik, J., Vitanova, A. R., et al. (2018). Electrochemical performance and redox mechanism of naphthalene-hydrazine diimide polymer as a cathode in magnesium battery. *J. Power Sources* 395, 25–30. doi: 10.1016/j.jpowsour.2018.05.051

Blum, M. M., and John, H. (2012). Historical perspective and modern applications of attenuated total reflectance-Fourier transform infrared spectroscopy (ATR-FTIR). *Drug test. Anal.* 4 (3-4), 298–302. doi: 10.1002/dta.374

Cai, H., Han, S., Jiang, L., Yu, M., Ma, R., and Yu, Z. (2019). 1-MCP treatment affects peach fruit aroma metabolism as revealed by transcriptomics and metabolite analyses. *Food Res. Int.* 122, 573–584. doi: 10.1016/j.foodres.2019.01.026

Cappellin, L., Soukoulis, C., Aprea, E., Granitto, P., Dallabetta, N., Costa, F., et al. (2012). PTR-ToF-MS and data mining methods: A new tool for fruit metabolomics. *Metabolomics* 8 (5), 761–770. doi: 10.1007/s11306-012-0405-9

Chen, Q., Song, J., Bi, J., Meng, X., and Wu, X. (2018). Characterization of volatile profile from ten different varieties of Chinese jujubes by HS-SPME/GC-MS coupled with e-nose. *Food Res. Int.* 105, 605–615. doi: 10.1016/j.foodres.2017.11.054

Cubero-Leon, E., Peñalver, R., and Maquet, A. (2014). Review on metabolomics for food authentication. *Food Res. Int.* 60, 95–107. doi: 10.1016/j.foodres.2013.11.041

Dettenrieder, C., Raichlin, Y., Katzir, A., and Mizaikoff, B. (2019). Toward the required detection limits for volatile organic constituents in marine environments with infrared evanescent field chemical sensors. *Sens. (Basel)* 19 (17), 3644. doi: 10.3390/s19173644

Ding, L., Dong, D., Jiao, L., and Zheng, W. (2017). Potential using of infrared thermal imaging to detect volatile compounds released from decayed grapes. *PloS One* 12 (6), e0180649. doi: 10.1371/journal.pone.0180649

Dong, D., Jiao, L., Li, C., and Zhao, C. (2019). Rapid and real-time analysis of volatile compounds released from food using infrared and laser spectroscopy. *TrAC Trends Anal. Chem.* 110, 410–416. doi: 10.1016/j.trac.2018.11.039

Dong, D., Zhao, C., Zheng, W., Wang, W., Zhao, X., and Jiao, L. (2013). Analyzing strawberry spoilage *via* its volatile compounds using longpath Fourier transform infrared spectroscopy. *Sci. Rep.* 3, 2585. doi: 10.1038/srep02585

Dong, D., Zheng, W., Wang, W., Zhao, X., Jiao, L. , and Zhao, C. (2014a). Analysis and discrimination of grape spoilage *via* volatiles: a comparison between long optical path Fourier-transform-infrared spectroscopy and sensor arrays. *Analyst* 139 (19), 5028–5034. doi: 10.1039/c4an00586d

Dong, D., Zheng, W., Wang, W., Zhao, X., Jiao, L. , and Zhao, C. (2014b). A new volatiles-based differentiation method of Chinese spirits using longpath gas-phase infrared spectroscopy. *Food Chem.* 155, 45–49. doi: 10.1016/j.foodchem.2014.01.025

Franke, C., and Beauchamp, J. (2016). Real-time detection of volatiles released during meat spoilage: a case study of modified atmosphere-packaged chicken breast fillets inoculated with br. thermosphacta. *Food Anal. Methods* 10 (2), 310–319. doi: 10.1007/s12161-016-0585-4

Giannetti, V., Boccacci Mariani, M., Mannino, P., and Marini, F. (2017). Volatile fraction analysis by HS-SPME/GC-MS and chemometric modeling for traceability of apples cultivated in the northeast Italy. *Food Control* 78, 215–221. doi: 10.1016/j.foodcont.2017.02.036

Hewitt, C. N., Hayward, S., and Tani, A. (2003). The application of proton transfer reaction-mass spectrometry (PTR-MS) to the monitoring and analysis of volatile organic compounds in the atmosphere. *J. Environ. Monit.* 5 (1), 1–7. doi: 10.1039/b204712h

Jahromi, K. E., Nematollahi, M., Krebbers, R., Abbas, M. A., Khodabakhsh, A., and Harren, F. J. M. (2021). Fourier Transform and grating-based spectroscopy with a mid-infrared supercontinuum source for trace gas detection in fruit quality monitoring. *Opt. Express* 29 (8), 12381–12397. doi: 10.1364/OE.418072

Jahun, B. M., Ilu, K. J., Yahaya, S. M., Ahmed, B., and Salami, K. D. (2021). Fungi causing post-harvest spoilage carica papaya Linn fruits of two selected markets in Kano state, Nigeria. *J. Appl. Sci. Environ. Manage.* 25 (5), 727–731. doi: 10.4314/jasem.v25i5.6

Jiao, L., Dong, D., Han, P., Zhao, X., and Du, X. (2017). Identification of the mango maturity level by the analysis of volatiles based on long optical-path FTIR spectroscopy and a molecular sieve. *Anal. Methods* 9 (16), 2458–2463. doi: 10.1039/c7ay00149e

Jiao, L., Guo, Y., Chen, J., Zhao, X., and Dong, D. (2019). Detecting volatile compounds in food by open-path Fourier-transform infrared spectroscopy. *Food Res. Int.* 119, 968–973. doi: 10.1016/j.foodres.2018.11.042

Jiao, L., Zhong, N., Zhao, X., Ma, S., Fu, X., and Dong, D. (2020). Recent advances in fiber-optic evanescent wave sensors for monitoring organic and inorganic pollutants in water. *TrAC Trends Anal. Chem.* 127, 115892. doi: 10.1016/j.trac.2020.115892

Jin, T., Zhou, J., Lin, H. G., and Lin, P. T. (2019). Mid-infrared chalcogenide waveguides for real-time and nondestructive volatile organic compound detection. *Anal. Chem.* 91 (1), 817–822. doi: 10.1021/acs.analchem.8b03004

Ke, Z.-J., Tang, D.-L., Lai, X., Dai, Z.-Y., and Zhang, Q. (2018). Optical fiber evanescent-wave sensing technology of hydrogen sulfide gas concentration in oil and gas fields. *Optik* 157, 1094–1100. doi: 10.1016/j.ijleo.2017.11.130

Leng, F., Wang, C., Sun, L., Li, P., Cao, J., Wang, Y., et al. (2022). Effects of different treatments on physicochemical characteristics of 'Kyoho' grapes during storage at low temperature. *Horticulturae* 8 (2), 94. doi: 10.3390/horticulturae8020094

Li, H., Brouwer, B., Oud, N., Verdonk, J. C., Tikunov, Y., Woltering, E., et al. (2021). Sensory, GC-MS and PTR-ToF-MS profiling of strawberries varying in maturity at harvest with subsequent cold storage. *Postharvest Biol. Technol.* 182, 111719. doi: 10.1016/j.postharvbio.2021.111719

Liu, N., Koot, A., Hettinga, K., De Jong, J., and van Ruth, S. M. (2018). Portraying and tracing the impact of different production systems on the volatile organic compound composition of milk by PTR-(Quad)MS and PTR-(ToF)MS. *Food Chem.* 239, 201–207. doi: 10.1016/j.foodchem.2017.06.099

Lu, R., Li, W. W., Mizaikoff, B., Katzir, A., Raichlin, Y., Sheng, G. P., et al. (2016). High-sensitivity infrared attenuated total reflectance sensors for *in situ* multicomponent detection of volatile organic compounds in water. *Nat. Protoc.* 11 (2), 377–386. doi: 10.1038/nprot.2016.013

Memon, S. F., Lewis, E., Ali, M. M., Pembroke, J. T., and Chowdhry, B. S. (2017). "U-Bend evanescent wave plastic optical fibre sensor for minute level concentration detection of ethanol corresponding to biofuel production rate," in 2017 IEEE Sensors Applications Symposium (SAS). (Glassboro, NJ: IEEE) 1-5 . doi: 10.1109/SAS.2017.7894101

Paul, P. H., and Kychakoff, G. (1987). Fiber-optic evanescent field absorption sensor. *Appl. Phys. Lett.* 51 (1), 12–14. doi: 10.1063/1.98888

Raichlin, Y., and Katzir, A. (2008). Fiber-optic evanescent wave spectroscopy in the middle infrared. applied spectroscopy. *Appl. Spectrosc.* 62 (2), 55A–72A. doi: 10.1366/000370208783575456

Rice-Evans, C., and Miller, N. J. (1995). Antioxidants – the case for fruit and vegetables in the diet. *Br. Food J.* 97 (9), 35–40. doi: 10.1108/00070709510100163

Sánchez-Palomo, E., Diaz-Maroto, M. C., and Perez-Coello, M. S. (2005). Rapid determination of volatile compounds in grapes by HS-SPME coupled with GC-MS. *Talanta* 66 (5), 1152–1157. doi: 10.1016/j.talanta.2005.01.015

Sharma, A. K., Gupta, J. , and Sharma, I. (2019). Fiber optic evanescent wave absorption-based sensors: A detailed review of advancements in the last decaddecade, (2007–18). *Optik* 183, 1008–1025. doi: 10.1016/j.ijleo.2019.02.104

Shen, Y., and Yang, H. (2017). Effect of preharvest chitosan- g -salicylic acid treatment on postharvest table grape quality, shelf life, and resistance to botrytis cinerea -induced spoilage. *Sci. Hortic.* 224, 367–373. doi: 10.1016/j.scienta.2017.06.046

Tatli, S., Mirzaee-Ghaleh, E., Rabbani, H., Karami, H., and Wilson, A. D. (2021). Rapid detection of urea fertilizer effects on VOC emissions from cucumber fruits using a MOS e-nose sensor array. *Agronomy* 12 (1), 35. doi: 10.3390/agronomy12010035

Tiernan, H., Byrne, B., and Kazarian, S. G. (2020).). ATR-FTIR spectroscopy and spectroscopic imaging for the analysis of biopharmaceuticals. spectrochimica acta part a. *Mol. Biomol. Spectrosc.* 241, 118636. doi: 10.1016/j.saa.2020.118636

Volkov, D., Rogova, O., and Proskurnin, M. (2021). Organic matter and mineral composition of silicate soils: FTIR comparison study by photoacoustic, diffuse reflectance, and attenuated total reflection modalities. *Agronomy* 11 (9), 1879. doi: 10.3390/agronomy11091879

Wu, Y., Zhang, W., Song, S., Xu, W., Zhang, C., Ma, C., et al. (2020). Evolution of volatile compounds during the development of Muscat grape 'Shine muscat' (Vitis labruscaxV. vinifera). *Food Chem.* 309, 125778. doi: 10.1016/j.foodchem.2019.125778

Xia, X., Wu, W., Wang, Z., Bao, Y., Huang, Z., and Gao, Y. (2016). A hydrogen sensor based on orientation aligned TiO2 thin films with low concentration detecting limit and short response time. sensors and actuators b. *Chemical* 234, 192–200. doi: 10.1016/j.snb.2016.04.110

Zhang, S. Y., Jensen, S., Tan, K., Wojtas, L., Roveto, M., Cure, J., et al. (2018). Modulation of water vapor sorption by a fourth-generation metal-organic material with a rigid framework and self-switching pores. *J. Am. Chem. Soc.* 140 (39), 12545–12552. doi: 10.1021/jacs.8b07290

Zhu, X., Li, Q., Li, J., Luo, J., Chen, W., and Li, X. (2018a). Comparative study of volatile compounds in the fruit of two banana cultivars at different ripening stages. *Molecules* 23 (10), 2456. doi: 10.3390/molecules23102456

Zhu, J., Wang, L., Xiao, Z., and Niu, Y. (2018b). Characterization of the key aroma compounds in mulberry fruits by application of gas chromatography-olfactometry (GC-O), odor activity value (OAV), gas chromatography-mass spectrometry (GC-MS) and flame photometric detection (FPD). *Food Chem.* 245, 775–785. doi: 10.1016/j.foodchem.2017.11.112

Frontiers in
Plant Science

Cultivates the science of plant biology and its applications

The most cited plant science journal, which advances our understanding of plant biology for sustainable food security, functional ecosystems and human health.

Discover the latest Research Topics

See more →

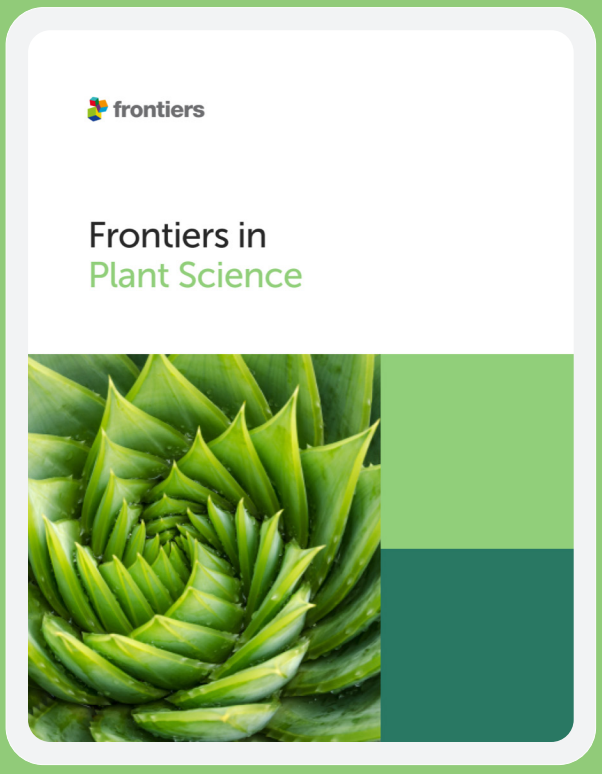

Frontiers

Avenue du Tribunal-Fédéral 34
1005 Lausanne, Switzerland
frontiersin.org

Contact us

+41 (0)21 510 17 00
frontiersin.org/about/contact